University of Southampton

Faculty of Engineering and the Environment

national Centre for Advanced Tribology at Southampton (nCATS)

Electrodeposited Nanocrystalline Ni-Co and Co-Ni-P Coatings for Hard Chromium Replacement

by

Chao Ma

Thesis for the degree of Doctor of Philosophy

June 2013

UNIVERSITY OF SOUTHAMPTON

ABSTRACT

Faculty of Engineering and the Environment

national Centre for Advanced Tribology at Southampton (nCATS)

Thesis for the degree of Doctor of Philosophy

ELECTRODEPOSITED NANOCRYSTALLINE Ni-Co AND Co-Ni-P COATINGS FOR HARD CHROMIUM REPLACEMENT

Chao Ma

This thesis describes the preparation and characterisation of environmentally friendly and low-cost nanocrystalline Ni-Co coatings and Co-Ni-P coatings to replace hard chromium coatings for anti-wear and anti-corrosion applications.

The nanocrystalline Ni–Co coatings with different cobalt contents were electrodeposited. The investigation on the role of tribofilms and wear debris in the tribological behaviour sliding against AISI-52100 stainless steel under unlubricated conditions shows that the tribofilms containing iron from the counterparts were formed on the worn surface of the coatings (less than 60 at.% Co), which exhibited high coefficients of friction and wear rates. In contrast, no tribofilm or iron transfer from the pin was found on the Co-rich coatings (more than 70 at.% Co), which exhibited a dramatic friction reduction of 50 % and improved wear resistance. The wear debris contains a mixture of face-centred cubic (fcc) metallic phase and fcc oxidised phase, irrespective of the coating composition. The oxidised debris cannot form an efficient lubricative film to promote separation of the sliding surfaces. Ni-Co coatings exhibited the active-passive polarisation behaviour in 3.5 % NaCl solution. The corrosion resistance of Ni-Co coatings needs to be further improved in order to replace hard chromium for anti-corrosion applications.

A new approach to fabricate single-layer Ni-Co coatings with high cobalt content onto mild steel substrates has been developed by optimising of additives (saccharin and 2-butin-1,4-diol (BD)). The present method is more feasible in industry with a competitive cost compared to other techniques, e.g. developing graded coatings and applying pulse current waveforms. The effect of saccharin and BD on the properties of the coatings were investigated, including surface morphology, grain size, crystalline texture, hardness and tribological performance against a steel counterpart. The coating microstrain could be manipulated from tensile to compressive and the fibre texture could be modified from the $(10\bar{1}0)$ for hexagonal close-packed (hcp) structure to $(0002)_{\mathrm{hcp}}$ / $(111)_{\mathrm{fcc}}$. The inhibition effect of absorbed species on electrodeposited nanocrystalline coatings is explained via grain size and texture analyses. The coating from the bath with an optimised additive content had high hardness (500 HV) due to its reduced grain size (11±2 nm) and improved tribological properties due to the high proportion of hcp structure.

The Hall-Petch relationship can fail when the grain size is below a critical value of tens of nanometres. This occurs particularly for coatings having porous surfaces. In this study, electrodeposited nanostructured Ni-Co coatings with different porosities were obtained by controlling the concentration of nickel sulphate and nickel chloride within electroplating baths. The coatings with the grain size in the range of 11-23 nm had varying surface morphologies and different porosities. A cluster-pore mixture model has been proposed by considering no contribution from pores to the hardness. As the porosity effect is taken into consideration, the calculated pore-free hardness is in agreement with the ordinary Hall-Petch relationship even when the grain size is reduced to 11 nm for the Ni-Co coatings with 77±2 at% cobalt. The present model has been applied to other porous nanocrystalline coatings, and the Hall-Petch relationship is maintained.

In order to further improve the microhardness, wear resistance and corrosion resistance of Ni-Co coatings to match the properties of hard chromium, a new Co-Ni-P coating has been developed by combining the precipitation hardening of Ni-P alloys with the lubricity of cobalt-rich Ni-Co coatings. The evolution of composition and microstructure, hardness, thermal stability and tribological properties have been investigated. The local pH near the cathode played an important role in the change of the microstructure from nanocrystalline to amorphous along the growth direction as the phosphorus content increased from 7 at.% to 26 at.%. The highest microhardness (980 HV) and the lowest wear rate (an order of magnitude lower than that of hard chrome coatings under the same dry sliding conditions) were achieved by annealing the coatings at 400 °C facilitating precipitation hardening. Furthermore, the coefficients of friction of both the as-deposited Co-Ni-P coating and the heat-treated samples were approximately 0.3, only half of that of hard chrome coatings. The roll-like debris found on the worn surfaces of the coating annealed at 500 °C were oriented perpendicularly to the sliding direction. The Co-Ni-P coating annealed at 400 °C exhibited improved anti-corrosion properties, which can be attributed to the formation of a protective oxide layer.

Contents

List of Tables

List of Figures

Declaration of Authorship

I, Chao Ma
declare that the thesis entitled

Electrodeposited Nanocrystalline Ni-Co and Co-Ni-P Coatings for Hard Chromium Replacement

and the work presented in the thesis and the work presented in the thesis are both my own, and have been generated by me as the result of my own original research. I confirm that:

- this work was done wholly or mainly while in candidature for a research degree at this University;
- this work was done wholly or mainly while in candidature for a research degree at this University; where any part of this thesis has previously been submitted for a degree or any other qualification at this University or any other institution, this has been clearly stated;
- where I have consulted the published work of others, this is always clearly attributed;
- where I have quoted from the work of others, the source is always given. With the exception of such quotations, this thesis is entirely my own work;
- I have acknowledged all main sources of help;
- where the thesis is based on work done by myself jointly with others, I have made clear exactly what was done by others and what I have contributed myself;
- parts of this work have been published as journal papers listed in Appendix: B.

Signed: ....

Date:..

Acknowledgements

First of all, I would like to express my sincere gratitude to Dr. Shuncai Wang and Prof. Frank C Walsh for them to offer me the opportunity to pursue my research under their invaluable guidance. I am deeply indebted to Dr. Shuncai Wang for his continuous encouragement, kind support and inspiration for research.

Moreover, special thanks are due to Prof. Robert J K Wood for his constructive advice throughout my PhD studies.

I would like to thank my colleagues in Faculty of Engineering and the Environment: Dr. Julian A Wharton, Dr. Xiaohong Li, Dr. Chee Tong Low, Dr. Mengyan Nie, Dr. Jurgita Zekonyte, Dr. Terry J Harvey and Dr. John Walker, who bring me the help as and when required.

I acknowledge and appreciate Ekaterin Minev in University of Cardiff for technical support on FIB and financial support from the EPSRC Nanoaccess programme.

I am also immensely grateful to Dr. Liping Wang of Lanzhou Institute of Chemical Physics in China and Dr. Quanshun Luo of Sheffield Hallam University, for their useful advice and help.

A big THANK YOU goes to everyone who shared with me this path: my parents and family, Martin Evans, Chuanting Wang, Intan Othman, Richard Critchley, Liping Fang, Ying Chen, Yang He, Feifei Zhang, Stefano Neodo, Fanfan Sun and Mihaela Stevar.

The completion of the thesis would not be possible without a mention of the whole-hearted support given by my beloved soulmate, Liang. I would like to thank you all most sincerely, for always being there for me.

Dedication

This thesis is dedicated to to my dear father, mother, and my dear husband.

Nomenclature

Roman Symbols

a	lattice constant
a'	contact radius
B	full width at half maximum height of the peak
B_{ε}	peak broadening caused by internal strain
c	lattice constant in a hcp structure
C_b	metal ion concentration in bulk solution
C_i	metal ion concentration at the interface
d	grain size in Hall-Petch relationship
d_0	lattice spacing at stress-free condition
d'	grain size obtained by TEM
d''	grain size obtained by XRD
d_{cl}	size of the cluster
D_i	diffusivity of metal ion
$d_{\phi\psi}$	d-spacing of the (hkl) lattice plane
E^*	reduced modulus
E	Young's modulus
E_b	breakdown potential
E_{corr}	corrosion potential

E_{ED}	electrodeposition potential
f	volume fraction
F	Faraday constant
H	hardness in Hall-Petch relationship
H_0	intrinsic hardness
H_c	hardness contribution of clusters
H_{com}	composite hardness
H_m	measured hardness
H_p	hardness contribution of pores
i_{corr}	corrosion current density
i	plating current density
J_{lim}	limiting current density
K	wear rate
k	constant in Hall-Petch relatioship
M	Metal (Ni or Co)
M^{Z+}	metals ions
N	normal load
N'	number of clusters
p	porosity
P_0	peak contact pressure
R	linear correlation coefficient
R'	effective radius
r_1, r_2	equatorial radius of an ellipsoid
r_3	polar radius radii of an ellipsoid

R_a	surface roughness
S	total sliding distance
t	time
V	wear volume
V_t	total deposit volume of the top surface
W	crystalline nucleus formation probability
z	number of electrons

Acronyms

AFM	atomic force microscopy
bcc	body centred cubic
BD	2-butin-1,4-diol
BEI	backscattered electrons images
CVD	chemical vapour deposition
DLC	diamond-like carbon
EDS	energy dispersive X-ray spectroscopy
EPA	Environmental Protection Agency
fcc	face centred cubic
FIB	focused ion beam
hcp	hexagonal close-packed
HVOF	high velocity oxy-fuel
PVD	physical vapour deposition
SAED	selected area electron diffraction
SCE	saturated calomel electrode
SEM	scanning electron microscopy

TEM	transmission electron microscopy
XRD	X-ray Diffraction

Greek Symbols

δ	thickness of the diffusion layer
η_k	overpotential
λ	wavelength of the X-rays
ν	Poisson's ratio
Φ_{mini}	minimum internal diameter
ψ	off-axis angle with respect to the sample surface normal
σ	internal stress
θ	Bragg diffraction angle
ε	microstrain

Subscripts and Superscripts

ads	adsorption
cr	crystallites
gb	grain boundary
qn	quadratic node
tj	triple line junction
*	Axis normal to a crystal plane

Chapter 1

Introduction

1.1 General Introduction

For over a century, chromium plating has been widely used to produce decorative and functional coatings. In 2003, the world wide output value of decorative chromium plating was approximately \$16 billion and \$3.2 billion for functional chromium plating [1]. Decorative chromium coatings, typically with a thickness of less than 250 nm, are plated over the layer of electrodeposited nickel or copper depending on the intended use. They provide an attractive blue-white metallic lustre and are resistant to corrosion, tarnishing and scratch [2]. Functional or hard chromium plating with the thickness of 2.5 µm to 500 µm delivers high hardness (typically 850-1100 HV), excellent wear and corrosion resistance. It has been widely used as a fundamental coating in aerospace, automotive and general engineering industries, e.g. aircraft engines, automobile valve components, piston rings, oil well equipment, dies and hydraulic cylinders [3, 4]. However, chrome plating solution consists of chromic acid with hexavalent chromium, which is extremely toxic and carcinogenic. A large amount of chromic acid mist at the surface of the plating tank results in the exposure of workers to hexavalent chromium due to the inhalation and skin contact, which can cause liver and kidney damage or failure, burns, and anaemia [5]. Moreover, the presence of hexavalent chromium ions in the environment is toxic to organisms. Therefore, it has been identified as one of the 17 chemicals posing the greatest threat to humans by the United States Environmental Protection Agency (EPA) [6]. Due to both work safety and environmental issues, hard chromium coatings are facing strict regulations [1, 7]. For many years, the permissible exposure limit for hexavalent chromium compounds in workplace air addressed by United States Occupational Safety and Health Administration was 52 µg m^{-3}. It has been reported that the US Department of Defence spent over \$10 million dollars per year in hazardous material disposal costs associated with hard chromium deposition [8]. The standard has been set to a much lower value at 5 µg m^{-3} in 2006 [4], which further increases the cost of chromium plating. In the European Union, the directive 2002/95/EC to restrict the use of certain hazardous substances including hexavalent chromium in electrical and electronic equipment became effective on the 1st July, 2006 [7]. The hexavalent chromium eliminations in car manufacture were in operation on the 1st July 2007 in USA [1]. Besides, hard chromium plating has inherent disadvantages, including poor coverage power, poor throwing power and requiring high average cathode current densities [9]. Therefore, there is currently tremendous pressure to develop environmentally friendly and cost-effective coatings to replace hard chromium. Substitutable materials, alternative technologies and new designs have attracted increasing scientific and industrial attention, including thermal spray [10], vapour deposition [11], functional trivalent chromium plating [12], electroless nickel-based coatings [13], non-chromium electrodeposited nanocrystalline coatings [14] and welding facing methods [15]. Among these current methods, chromium-free electrodeposition is versatile, technologically feasible and economically competitive. It allows the use of existing hard chromium plating infrastructure, which can significantly reduce the cost. Additionally, numerous benefits associated with hard chromium plating are retained, e.g. non-line-of-sight application, dimensional consistency, good coating adhesion and surface finish [8]. Various electrodeposited nickel-based and cobalt-based coatings have been considered as possible replacements for hard chromium [14, 16, 17].

Electrodeposited Ni-Co alloys exhibit enhanced tribological properties, high strength, excellent magnetic properties and unique electrocatalytic activity, which have the potential to be used in aerospace, automobile and general engineering industries [18, 19]. Previous studies showed that experimental variables, such as cobalt ions concentration, current density, additive type and bath temperature, can influence the cobalt content and grain size, thus determining the microstructure and mechanical properties [20–22]. Electrodeposited nanocrystalline Ni coatings and nickel-rich Ni-Co coatings have an fcc structure. With a further increase in the cobalt content, the hcp structure is formed [23, 24]. Recent findings showed that cobalt-rich alloys with hcp structure exhibited a reduced coefficient of friction and improved wear resistance against an AISI-52100 stainless steel ball compared to the nickel-rich coatings [24]. However, the coating hardness is relatively low (below 350 HV) due to its large grain size (above 1.5 µm measured by X-ray Diffraction (XRD)). It has been found that the hcp structure of cobalt-based alloys (Co-Re, Co-Mo and Co-Cr) leads to lower coefficient of friction and wear rate than their counterparts with fcc structure [25, 26]. Inman et al. [27, 28] reported that the presence of hcp structure in a Co-Cr alloy (Stellite 6) restricted material removal and reduced material transfer when sliding against body centred cubic (bcc) structured Incolony MA956. Moreover, Persson et al. [29] suggested that the excellent low friction properties and galling resistance of Stellite 21 were attributed to the transformation from fcc structure to easily sheared hcp structure in the tribofilm which is enriched with Co. The switch in tribological performance between nickel-rich and cobalt-rich Ni-Co coatings [24] was thought to be related to the formation of a tribofilm. However, there has been no further investigation of the participation of tribofilms and wear debris in the friction and wear of Ni-Co coatings that could explain such behaviour.

If the generated wear debris is not simultaneously removed from the contact surfaces, it can form a three-body contact which results in physical and chemical interactions [30]. The layer of compacted wear debris, referred to as a tribofilm, may be inadvertently formed on the rubbing surfaces. A majority of studies show that the formation of stable tribofilms leads to a significant reduction in the coefficient of friction and the wear rate by redistributing contact stresses and establishing mild wear with the oxide films as solid lubricants [31, 32]. For example, for a TiAlN/VN coating [33], the presence of a thin hydrated tribofilm resulted in a relatively low coefficient of friction (0.53) at room temperature (compared to those obtained at elevated temperatures). However, quite a number of inconsistent experiments have also been reported. For example, the coefficient of friction of the TiAlN/VN coating increased to approximately 1 at 300 °C due to the breaking of the -OH bonds and the transformation of the monohydrate to an amorphous (TiAlV)N_xO_y with higher inherent friction [33]. Luo et al. [34] reported that the coefficient of friction of TiAlCrYN coatings increased from less than 0.2 to a high value of 0.6-0.7 after the formation of an adhesive tribofilm. Olofsson and Jacobson [35] found the coefficient of friction was under 0.4 during the sliding contact between two alumina smooth surfaces where no tribofilm was formed. It increased to above 0.7 after surface treatment by grit blasting, which contributed to the formation of the tribofilm by building up the agglomerated wear particles. This was explained by lower hardness of the tribofilm compared to the alumina counterpart. As the role of tribofilm is disputed and poorly understood, it is interesting to study the function of tribofilms on Ni-Co coatings with varied triboloigical properties under the same tribological conditions.

The electrodeposition of cobalt-rich nanocrystalline coatings onto steel is challenging since the coating can be highly stressed (tensile or compressive) during crystal builtup. Also, the mismatch of crystal lattice between the coating and substrate can cause the development of cracks within the coatings and even delamination from the substrates. The internal stress in the coating has been reported to change from compressive to tensile stress as the cobalt content increases [18]. A number of strategies have been employed to combat internal stress in cobalt-rich coatings. Examples include (a) graded Ni-Co coating by gradually changing the composition of alloys from nickel-rich to cobalt-rich via a number of baths, but the deposition process is complex for industrial uses [18] and (b) pulse current waveforms to electrodeposit coatings, but this method has only been successful in depositing a low-cobalt content alloy on steel and needs to employ a sophisticated, pulsed current power supply [36–38]. Additionally, recent findings showed that cobalt-rich coatings with hcp structure exhibit low coefficient of friction, but still need further improvement to enhance their tribological properties and microhardness [24]. Industry expects a simpler electrodeposition approach, which avoids the need to develop a graded coating or employ a sophisticated power supply.

Nickel coatings commonly deposited from the baths containing one or two types of nickel salts - sulphate and chloride for different applications. For example, coatings deposited from a nickel chloride bath can be used in the decorative industry for anti-corrosion applications but not in engineering applications as a high internal stress limits the coating thickness (less than 2.5 µm). Although the effect of baths with different nickel salts on mechanical properties has been studied on coarse-grained (grain size of the order of microns) nickel coatings with a low hardness, typically below 300 HV [39], there are few comparable studies for nanocrystalline Ni-Co coatings. Polycrystalline metals show an increase of yield stress with the decrease of grain size. This effect is known as the Hall-Petch effect [40]. It can be applied to Vickers hardness which is approximately three times the compressive yield stress if a small amount work-hardening occurs. Nanocrystalline materials (grain size below 100 nm) can show enhanced physical, mechanical and chemical properties compared with their coarse-grained counterparts [41]. However, with a further refined grain size of nanocrystals, it has been reported that the Hall-Petch slope becomes smaller or even negative when the grain size is reduced to a threshold value [42]. Previous studies indicated that a deviation from the conventional Hall-Petch relationship occurs when the grain size is below 50 - 60 nm for both electrodeposited Ni and Co [43, 44]. Many mechanisms have been proposed, including increasing porosity of deposits with small grain size [45], larger fraction of atoms at grain boundaries [42], suppression of dislocation pile-ups [46] and the thermally-activated grain boundary shearing model [47]. Although electrodeposition was claimed to produce porosity-free products [48], it has been noticed that the as-deposited nickel and cobalt coatings [43, 44] consist of a mixture of clusters and pores, in which a cluster contains tens and hundreds of nanocrystalline grains. Deviation from the Hall-Petch relationship may derive from the porosity, which needs to be clarified.

Although cobalt-rich Ni-Co coatings prepared from electrolytes with optimised amount of additives exhibit low coefficient of friction and improved anti-wear resistance, their microhardness and corrosion resistance need to be substantially improved to match the properties of hard chromium. It has been reported that the as-plated Ni-P coatings had high hardness (more than 640 HV) [49], which could further reach 1000 HV after heat treatment at 400 °C due to the precipitation strengthening which resulted in a lower wear rate than that of hard chromium coatings [14]. However, the coefficient of friction of Ni-P is in the range of 0.45-0.7 on dry sliding conditions against different counterface materials, including carbon steel, TiN-coated tool steel and Si_3N_4 [14, 50, 51]. Therefore, by alloying Co into Ni-P, Co-Ni-P coatings are expected to exhibit a lower coefficient of friction and improved wear resistance. Thin Co-Ni-P films (from 10 nm to 10 µm thick) are generally used as magnetic recording media, and as hard magnetic materials for microelectromechanical systems (MEMS) applications due to their unique magnetic properties [52, 53]. In the engineering industry, they have been applied as anti-corrosion coatings [54], microwave absorptive materials [55] and electrocatalytic materials for water electrolysis [56]. However, few researchers have addressed the tribological properties of the Co-Ni-P coatings. Co-Ni-P films can be electroplated from a sulphate bath [54], a Brenner type chloride bath [57, 58], or a sulphamate bath [59]. The experimental parameters, such as pH, current density and electrolyte compositions, have been reported to affect the surface morphology, composition, microstructure, microhardness and their magnetic properties. Pattanaik et al. [57] reported that the Co-Ni-P film with the P content more than 12 at.% had an amorphous structure. Djokić et al. [60] found that Co-Ni-P coatings exhibited an amorphous structure on the top surface but a crystalline structure at the beginning of electrodeposition. It was suggested that the P content controlled the transition. However, its mechanism needs to be further investigated.

1.2 Objectives

The current work aims to develop environmentally friendly and low-cost nanocrystalline Ni-Co coatings and Co-Ni-P coatings to replace hard chromium coatings for anti-wear and anti-corrosion applications. The key performance characteristics for hard chromium include: the hardness of 850-1100 HV, the coefficient of friction 0.6-0.8 when sliding against an AISI-52100 stainless steel counterpart, the wear rate of 2.1×10^{-5}- 4×10^{-5} mm^3 N^{-1} m^{-1} obtained by the reciprocating sliding wear tests [61–64], the corrosion potential (E_{corr}) vs. saturated calomel electrode (SCE) of -299 mV and corrosion current (i_{corr}) of 3.3×10^{-6} A cm^{-2} in 3.5 wt.% NaCl [62]. In order to match or exceed the unique properties of hard chromium, the effects of electroplating variables on Ni-Co coatings as well as the preparation and heat treatment of Co-Ni-P coatings have been investigated.

The objects of the present research are to:

(1) electrodeposit Ni-Co coatings with different cobalt contents and examine their wear and corrosion resistance;

(2) study the participation of tribofilms and wear debris in the friction and wear of Ni–Co coatings with different cobalt contents by chemical and structural characterisations of the worn surfaces and debris;

(3) electrodeposit single layer Ni-Co coatings with high cobalt content on steel substrates by selecting and optimising electrolyte additives to control the internal stress;

(4) investigate the effect of additives on the grain size and texture of Ni-Co coatings with high cobalt content;

(5) study the microhardness of nanocrystalline Ni-Co coatings with different porosities obtained by controlling the concentration of nickel sulphate and nickel chloride within electroplating baths;

(6) propose a cluster-pore mixture model to explain the deviation from Hall-Petch relationship for porous materials;

(7) fabricate novel Co-Ni-P deposits with acceptable thickness as anti-wear and anti-corrosion coatings;

(8) clarify the evolution of composition and microstructure, hardness, thermal stability and tribological properties of Co-Ni-P coatings.

1.3 Thesis Outline

Chapter 1 introduces the background, motivations and objectives of the present research. Chapter 2 presents the literature review on surface engineering, hard chromium replacement, electrodeposited nanocrystalline nickel, cobalt, Ni-Co binary alloys and Co-Ni-P ternary coatings. Chapter 3 lists the experimental methodologies. Chapter 4 presents the wear and corrosion properties of nanocrystalline Ni-Co Coatings with different cobalt contents. The role of tribofilms and wear debris in the tribological behaviour has been discussed. Chapter 5 investigates the effects of additives on the microstructure and properties of electrodeposited nanocrystalline Ni-Co coatings with high cobalt content. Chapter 6 studies the effect of porosity on the hardness of nanocrystalline Ni-Co coatings plated from baths containing different nickel salts (nickel sulphate and/or nickel chloride). Chapter 7 presents the preparation and characterisation of the novel Co-Ni-P coatings for anti-wear and anti-corrosion applications. Subsequently, the conclusions, novelties and future work are shown in Chapter 8.

Chapter 2

Literature Review

2.1 Introduction of Surface Engineering Techniques

High performance coatings provide an effective approach to control wear and corrosion, which is an important topic from an economic point of view as illustrated in Fig. 2.1. Surface deterioration represents the predominant factor of the materials degradation [65]. Surface engineering intends to tailor the properties of the surface and near-surface regions of a material to meet the anti-wear and anti-corrosion requirements. The properties can be enhanced metallurgically, mechanically, chemically, or by developing a coating [66].

2.1.1 Surface Coating Methods

Coatings can be applied by numerous processes in order to enhance the properties of the surface, illustrated in Fig. 2.2 [67]. Surface coatings can be produced by depositing films onto substrates or by reactions involving substrate materials. Hard chromium plating

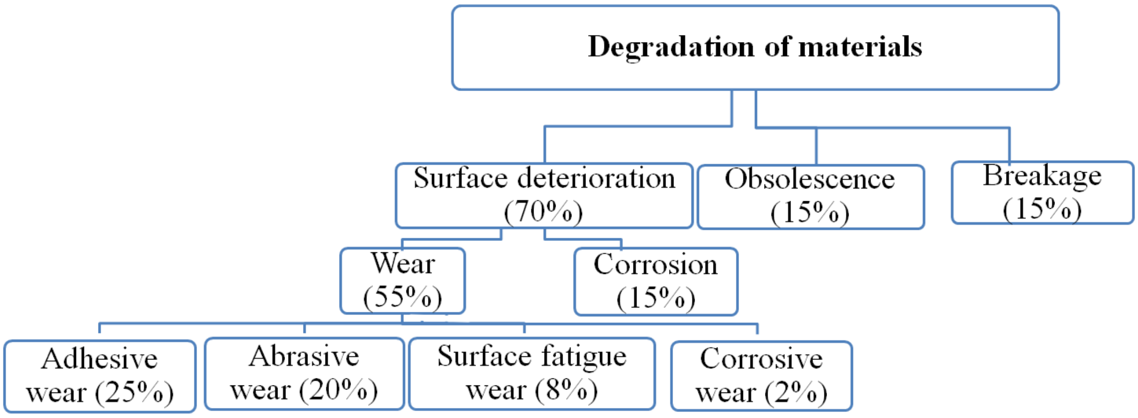

Fig. 2.1. The causes of materials degradation showing a percentage estimate of the economic importance of each [65].

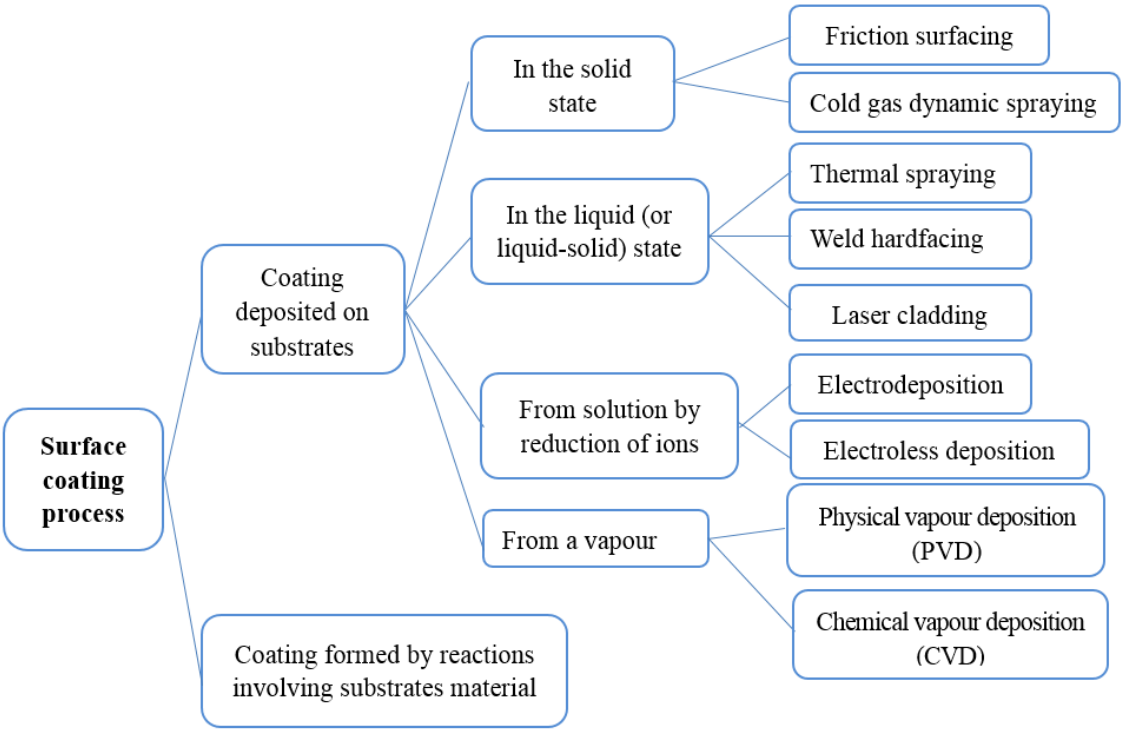

Fig. 2.2. Classification of coatings types [67].

and electrodeposited nanocrystalline coatings are classified to the coatings produced from solutions by the reduction of ions.

Electrolytic deposition is a versatile and powerful method to synthesise dense coatings with improved properties, such as good wear and corrosion resistance, high hardness and excellent ductility. A coating can be built up on an electrically conductive surface by using the electrolytic cell as represented in Fig. 2.3. A metal M is deposited from a solution of its ions M^{z+}:

$$M^{z+} + ze^{-} \rightarrow M \tag{2.1}$$

In addition to pure metals, alloys and composites containing co-deposited particles can be formed by electroplating, which is easy to control the thickness as well as the rate of deposition and to produce different types of deposits for various applications, as demonstrated in Fig. 2.4. The properties of electrodeposited metallic coatings (Fig. 2.4(a)) can be favourably tailored by changing the experimental variables, e.g. current density, plating temperature, electrolyte composition, additives and bath agitation. Composite coatings as shown in Fig. 2.4(b) consist of a metal or alloy matrix with a dispersion of second phase particles, which can be hard particles (e.g. Al_2O_3, SiC, WC and diamond), solid lubricants (e.g. PTFE, graphite and MoS_2), or nanotubes to improve wear and corrosion resistance

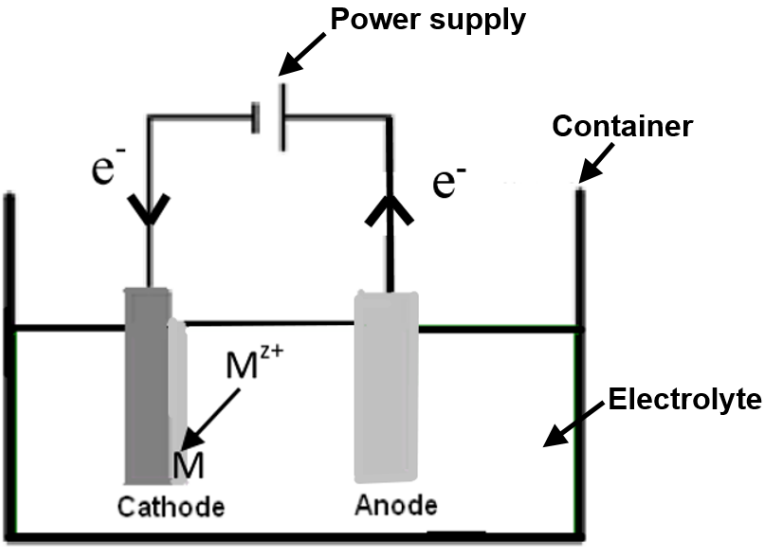

Fig. 2.3. Schematic illustration of electrodeposition.

[66]. The deposition of the sub-layers and gradient coatings shown in Figs. 2.4(c, e) can reduce the stress between coatings and substrates. In the meantime, the anti-wear and anti-corrosion properties can be significantly improved [18, 68]. The patterned films shown in Fig. 2.4(d) have a wide range of applications, such as optoelectronic devices, magnetic storage media, gas sensors, and micro fluidic systems [69].

2.1.2 Surface Nanocrystallisation Technologies

Nanocrystalline coatings with the grain size below 100 nm exhibit unique properties due to a large number of grain boundaries, which attract increasing scientific and industrial interests [70]. Surface nanocrystallites can be produced by the following approaches as illustrated in Fig. 2.5 [71]: (a) Surface coating or deposition. The coated materials, which can be either nano-sized isolated particles or polycrystalline powders with nano-sized grains, are consolidated by means of various techniques such as PVD, CVD, sputtering and electrochemical methods. The adhesion between the coated layer and the substrate is crucial to the properties of the coating. (b) Surface self-nanocrystallisation. The surface layers of the materials can be transformed into nanocrystalline states without changing the overall composition and/or phases after mechanical or thermal treatment, such as ball-milling and high strain rate deformation [72]. (c) Hybrid surface nanocrystallisation. It is a combination of two processes mentioned above, which includes the formation of a nanostructured transformable layer and a chemical, thermal or metallurgical process to produce a nanocrystalline layer with different compositions or phases.

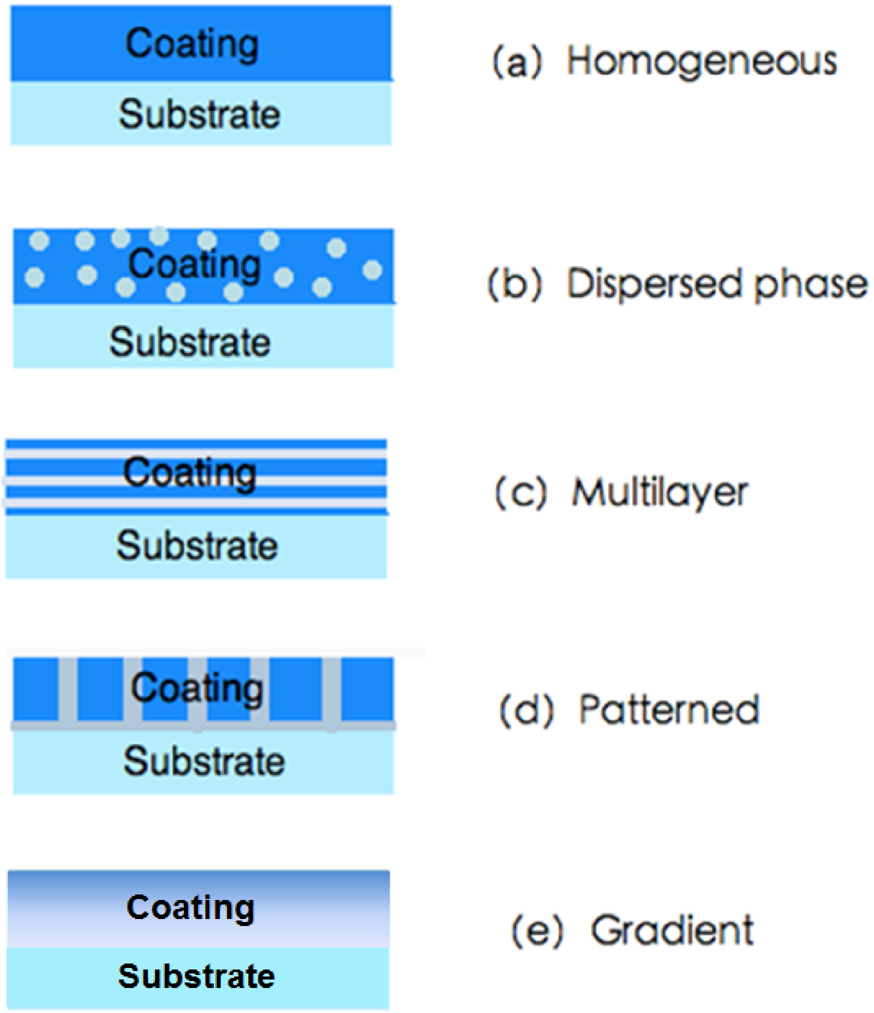

Fig. 2.4. Various types of electrodeposited coatings [67].

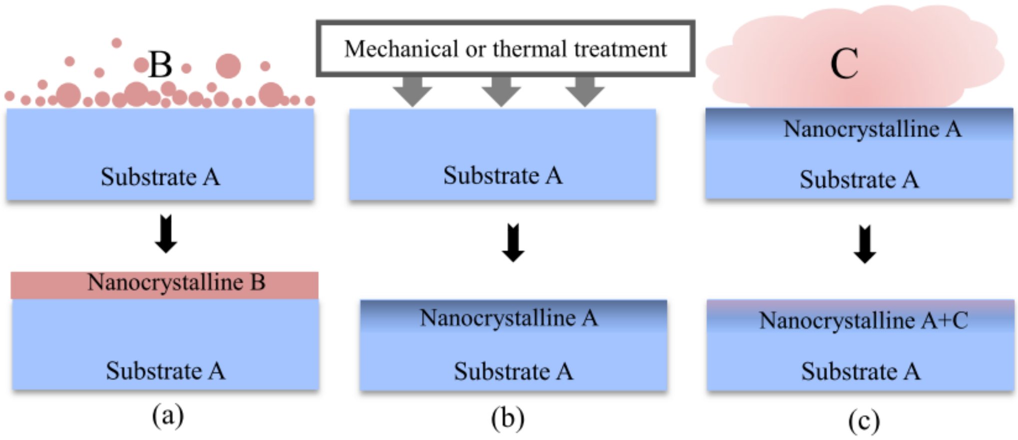

Fig. 2.5. Schematic illustration of three types of surface nanocrystallisation processes: (a) surface coating or deposition, (b) surface self-nanocrystallisation and (c) hybrid surface nanocrystallisation [71].

2.1.3 Nanocomposite Coatings

In order to further optimise the properties of coatings, the second phase, particularly nanoparticles, are added or formed in nanocrystalline deposits to produce various types of composite nanostructures [73] where the size of nanoparticles and nanotubes is comparable to the grain size of coatings. The intragranular dispersions can be achieved by adding nanoparticles or nanotubes in order to anchor dislocations during processing, annealing, cooling and to control the size and shape of matrix grains. Dispersing second-phase particles, whiskers and nanotubes can improve the mechanical properties. The magnetic, electric and optical properties can also be tailored in the composites. Electrodeposited nanocomposite materials can be synthesised by two approaches. The first approach is the same as the process to produce polycrystalline composite deposits used for many years by adding particles, nanotubes or whiskers to electroplating solutions for the codeposition of second phase particles and the nanocrystalline metal matrix. However, the particles tend to easily agglomerate. The second approach is an in-situ two-step process. Firstly, the nanocrystalline matrix is deposited as a supersaturated solid solution, which is followed by an annealing step in which the second phase is precipitated. Meanwhile, little change in the matrix grain size may occur [73].

2.2 Replacement of Hexavalent Chromium Plating

For over a century, hard chrome coatings have been applied in a wide range of industries but are facing strict regulations due to both work safety and environmental issues [1, 7]. The chrome plating solution consists of chromic acid with hexavalent chromium, which is extremely toxic and carcinogenic [5]. Substitutable materials, alternative technologies and new designs have attracted increasing scientific and industrial attention, including thermal spray, vapour deposition, functional trivalent chromium plating, electroless nickel-based coatings, non-chromium electrodeposited nanocrystalline coatings and welding facing methods, which are discussed as follows.

2.2.1 Thermal Spray

2.2.1.1 High Velocity Oxy-Fuel (HVOF) Thermal Spray

HVOF thermal spray process, developed by James Browning in 1982, has been considered as one of the most promising candidates for the replacement of hard chromium [10, 74]. As illustrated in Fig. 2.6, the coating material in powder form of micrometre size is fed into the gun of the combustion chamber, where pure oxygen is mixed with fuels, such as kerosene, propylene, acetylene, propane and hydrogen. The combustion propellant generates the supersonic stream with an extremely high velocity which can reach to 2000 m/s at the temperature of 3000 °C [75]. The powder particles with the high kinetic energy are sprayed on the substrates, producing coatings with low porosity (<1%), high bond strength (>80 MPa) and low oxide content (<1%) [10, 76]. Tungsten carbides and chromium carbides based coatings are the most common systems manufactured by HVOF for replacing hard chromium. As listed in Table 2.1, WC-Co coatings exhibit much higher hardness and superior wear resistance than hard chromium coatings [77–80]. Wood [81] found the erosion resistance of 86WC-10Co-4Cr (wt.%) coatings was significantly improved compared to hard chromium. Fedrizzi et al. [75] reported that the addition of Cr enhanced the tribocorrosion behaviour of WC-based coatings. However, their applications at elevated temperatures above 450 °C are limited due to the decarburisation of WC to W_2C, W_3C and/or W. At high temperatures up to 900 °C, Cr_3C_2-NiCr coatings with higher thermal stability can be used for reducing corrosion and wear, although the hardness is lower than WC-Co systems [76, 80]. It was found that the use of nano-sized powders could improve the tribo-corrosion properties of HVOF coatings due to the reduced interconnected porosity, lower roughness and better distribution of chromium carbides in the matrix [82]. Picas et al. [76] also reported that by using the 75 wt.% Cr_3C_2-25 wt.% NiCr powder with smaller size in the range of 1-12 µm, the wear rate of the coating was reduced by 50% compared to the coatings developed from the powder with the size of 10-30 µm. It can be attributed to a better distribution and cohesion of smaller carbide particles in the NiCr binder phase, which reduced the pullout of hard particles and decreased the abrasive wear. The properties of the HVOF coatings can be further optimised by tailoring process parameters, such as combustion pressure, fuel/oxygen ratio, spraying distance and substrate temperature [83, 84].

As one of the leading candidates for replacement of hard chromium, HVOF coatings have been applied on more than one hundred components of Boeing aircraft, including landing gear, hydraulic actuators as well as flap and slat tracks, especially for overhaul and repair [74, 85]. Compared to hard chromium plating, the HVOF process has some advantages including [4, 86]:

- Can be applied to almost any material without causing hydrogen embrittlement
- Better fatigue performance
- Improved wear and corrosion resistance

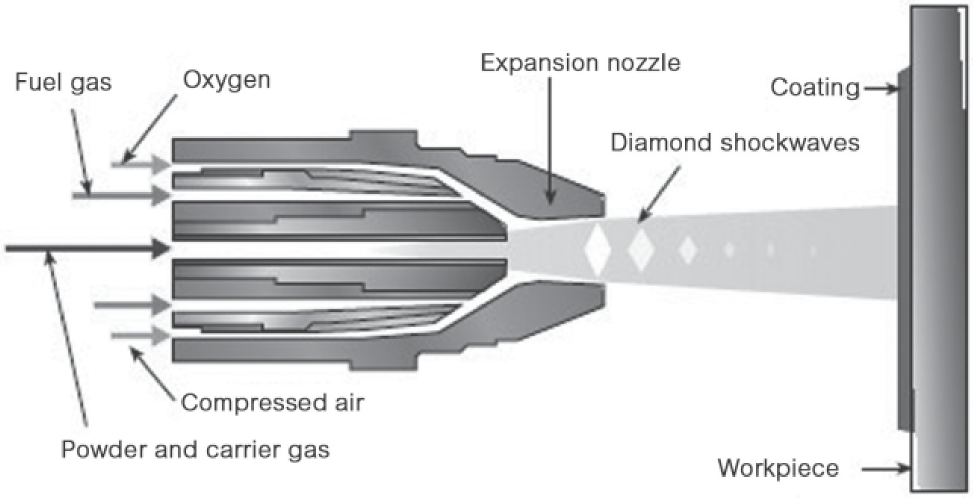

Fig. 2.6. Schematic diagram of HVOF process [86].

- Clean process without environmental costs associated with electroplating, such as rinse water treatment, waste disposal and ventilation
- Reduced amount of rework/replacement costs and lower operating cost

However, there are some limitations, which are summarised as follows [4, 77, 78, 86, 87]:

- Line-of-sight.
- Limitations in the minimum internal diameter of a cylinder that can be coated (i.e., Φ_{mini} = 40–80 mm) .
- Low-strain-to-failure, and spalling can occur at high load.
- Cause more wear on adjacent components.
- More complex process which needs much higher capital and installation expense.

2.2.1.2 Plasma Spray

As one of thermal spray techniques, plasma spray requires a plasma generator powered by an arc or a high frequency discharge. The melted powder in the plasma jet is propelled towards a substrate and forms a deposit. The coating materials include metals, alloys, ceramics and cermets [93]. Compared with HVOF, the principle advantage of plasma spray is the ability to coat the components with non-line-of-sight geometries such as internal diameters. By optimising the spray gun, the minimum diameter down to approximately

Table 2.1. Summaries of HVOF coatings as alternatives to hard chromium

Powders	Specific applications	Properties compared to hard chromium	Ref.
WC-12Co	Repair of Gas turbine shafts (heavy duty)	Higher hardness (>1000 HV), better performance in fatigue tests, superior performances in wear resistance, lower salt spray resistance	[77, 78]
WC-17Co	Aircraft components	Higher hardness (1300 HV), less loss of properties in fatigue testing, lower abrasive wear rate, comparable performance in salt fog testing, better performance in atmospheric corrosion tests, less resistance on aluminium alloy substrates	[79, 80, 88]
86WC-10Co-4Cr	Aircraft components	Higher hardness (>1300 HV), better anti-wear properties	[80, 88]
$75Cr_3C_2$-25NiCr	Piston rings and valves	Comparable hardness (>700 HV), better wear resistance, improved resistance to tribo-corrosion in NaCl solutions, better corrosion resistance in salt spray test, higher fatigue strength	[76, 77, 82, 89]
$80Cr_3C_2$-20NiCr	N/A	Better performance against corrosion in chloride solutions, but corrosion resistance is less stable as immersion time increases	[90]
WC-CrC-Ni	N/A	Comparable hardness, enhance fatigue strength, better abrasive wear resistance, worse corrosion resistance	[91]
NiCrBCSi	N/A	Comparable hardness and wear resistance after cyclic heat treatment	[92]
Tribaloy 400 (60% Co, 28% Mo, 9% Cr, 3% Si)	Aircraft landing gear	Comparable hardness (700-1150 HV), superior wear resistance, slightly inferior performance in salt fog testing, comparable performance in atmospheric corrosion tests	[77, 87]

6.5 mm can be coated, which is small enough for any landing gear outer cylinders, most utility actuators, and flight surface actuators [94]. Heydarzadeh Sohi and Ghadami [95] reported that the wear rate of air plasma sprayed WC-12Co coating against a sintered alumina disc was three times lower than that of hard chromium coatings. However, the limitations of plasma spray are listed as follows [94]:

- Minimum diameter cannot be lower than 6.5 mm. The limitation is due to the need for an adequate gun-surface distance.
- Higher porosity (typically 2-10%) than HVOF.
- Not suitable for heat-sensitive materials.

2.2.2 Vapour Deposition

As a dry and clean technology, the PVD process starts from creating a vapourised coating material by an electric arc or an electron beam from a solid or liquid source, and then the material is transported through a vacuum, low pressure gas or plasma (which accelerates the ions) followed by condensing on the substrate surface to form a thin and hard layer. PVD processes can be classified with respect to the following types of evaporation: vacuum evaporation (thermal evaporation), sputter deposition, arc evaporation and ion plating [96]. Various coating materials can be applied, including CrN, TiN, Ni, Cr, TiAlN, ZrN, CrC, SiC and diamond-like carbon (DLC) coatings [97]. PVD films can provide equivalent or superior performance with respect to hardness, wear and corrosion resistance compared to hard chromium coatings. Hurkmans et al. [98] have deposited a CrN_x coating with the thicknesses up to 50 µm by the unbalanced magnetron sputtering technique with high bias voltages (>200 V). The coating exhibited the super hardness of 2700-3100 HV and excellent tribological and electrochemical properties. Groshart [11] reported that PVD titanium nitride coatings could be used to protect cutting tools as their lifetime was three times longer than that of hard chromium. Brondum [99] developed chromium and chromium nitride coatings by low temperature arc vapour deposition using a plasma created from a mixture of evaporated metal, metal ions and gases. The hardness of PVD Cr was in the range of 800-1400 HV and that of PVD CrN reached 2200 HV. Both of the coatings had equivalent or better abrasion and corrosion characteristics than hard chromium. It was found that multilayer PVD coatings, such as TiN/Ti/TiN, CrN/Cr/CrN and ZrN/Zr/ZrN, exhibited better corrosion resistance than binary nitrides [97]. Additionally, DLC film can be deposited by plasma process using a mixture of hydrocarbons and inert gases. The thin coating can be used as a protective coating on fatigue sensitive components [100].

Although the PVD process is versatile and environmentally friendly, it has the following disadvantages [4]:

- Complex equipment and high capital cost.
- Line-of-sight restrictions for complex substrates.
- Not suitable for rebuilding.
- Limited by the reactor size.

Another vapour deposition method is CVD. In this process, the volatile precursors react and/or decompose on the hot substrate surface to form the coatings. It can create the same hard nitride and DLC coatings as PVD. However, the substrate needs to be heated to at least 500 °C, which is unsuitable for heat-sensitive alloys. Unlike PVD, CVD can coat complex objects [4].

2.2.3 Functional Trivalent Chromium Plating

Trivalent chromium plating with significantly fewer potential human health effects has been considered to be a promising replacement technology for hexavalent chromium for decorative applications since 1970s. Compared to hard chromium plating, the trivalent process has the advantages in terms of the cathode efficiency, throwing power and disposal cost. However, the maximum thickness of the coatings plated from commercial trivalent baths is less than 10 µm, which restricts their applications for anti-wear and other functional purposes [1, 101]. The inability of depositing thick coatings from trivalent chromium baths can be ascribed to the formation of chromium hydroxides and a stable olation production ($[(H_2O)Cr(OH)Cr(OH)Cr(H_2O)_4]$), which inhibit the trivalent Cr from discharging [102]. It can be minimised by adding complexants and decreasing the pH. With the presence of complexants (e.g. formate and glycine), olation reactions are competed with complexation reactions [103]. Zeng et al. [12] plated Cr-C alloys with the thickness of 50 µm from the trivalent chromium bath containing formic acid. The doping of C was attributed to the presence of organic substances. The as-deposited Cr-C alloy with crack-free surface and amorphous/microcrystalline structure had the microhardness of 800 HV, which increased to approximately 1400 HV after heat treatment in Ar_2 atmosphere for 1 h due to the crystallisation of chromium and precipitation of new phases. The Cr-C coatings annealed at 200 °C exhibited better wear resistance against a steel ball under unlubricated conditions than conventional hard chromium and as-deposited Cr-C alloys, but the corrosion resistance in 0.1 M H_2SO_4 was reduced by introducing crystal interfaces and cracks. Edigaryan et al. [104] added aluminium ions as a strong buffer in trivalent chromium electrolytes in order to prevent the formation of chromium hydroxide. The thickness of the coating was claimed to be at least 100 µm and the hardness was 1000 HV. Another attempt to overcome the limitation of thickness is by applying pulsed current. Chromium hydroxides can be dissolved under the countercurrent and the hydrogen film can also be reduced [1]. Kagajwala et al. [105] developed an additive free trivalent chromium plating process though the use of sophisticated waveforms. The coatings exhibited equivalent functional properties to the coatings produced from hexavalent chromium baths. Although the process has been demonstrated as a drop-in replacement for hard chromium, it has not been applied to produce hard thick chromium coatings at an industrial scale. Besides, the trivalent chromium baths are more sensitive to foreign ions contamination than hexavalent chromium plating. Impurities need to be removed by adding precipitating agents or using ion exchange, which increases the cost [102].

2.2.4 Electroless Nickel-based Coatings

Electroless nickel based coatings, formed by an autocatalytic reduction reaction with reducing agents, exhibit good corrosion and wear resistance and provide another cost effective solution to replace hard chromium coatings [13]. Actually, an intermediate electroless nickel layer is used to prevent the corrosion of base metals through the characteristic cracks of hard chromium [106]. Ni-P alloys turn out to be one of the most common autocatalytic nickel deposits, which have various applications in aircraft, automotive, marine and electronics industries. The hardness of as-deposited Ni-P coatings ranges from 490 HV to 660 HV depending on the phosphorus content, which can be significantly increased to the comparable value to hard chromium after annealing at 400 °C due to precipitation hardening by intermetallic compound Ni_3P as shown in Table 2.2 [107]. Thanks to their high hardness and good ductility, the wear resistance is equivalent to hard chromium [108]. Boron electroless nickel plating is another process which can produce coatings with higher hardness, typically between 650-750 HV. After heat treatment, the hardness of 1200 HV can be obtained by precipitating Ni_3B intermetallic compound. The Ni-B coatings also exhibit lower coefficient of friction and wear rates against steel ball in lubricated wear tests [109]. In order to further improve the corrosion and wear resistance, electroless composite coatings have been developed by co-depositing particles , for example, boron nitride, sil-

Table 2.2. Hardness of as-deposited and annealed electroless Ni-P coatings with different phosphorus content [107]

Phosphorus content / wt.%	Hardness of as-coated samples / HV	Hardness of heat-treated samples / HV
2-3	660	1080
6-9	520	940
10-12	490	880

icon carbide, alumina, MoS_2 and PTFE [107]. Another advantage for electroless plating is maintaining the uniformity of thickness, especially for products with complex geometry and deep pores [108]. However, the process requires high standards of quality control of surface preparation and plating solution because of unstable baths [107].

2.2.5 Non-chromium Electrodeposited Nanocrystalline Coatings

Nanocrystalline materials (grain size below 100 nm) exhibit enhanced physical, mechanical and chemical properties compared with their coarse-grained counterparts [41]. Nanocrystalline coatings can be synthesised by numerous techniques as mentioned in Section 2.1.2. Among them, nano-electrodepostion is one of the most widely applied methods due to its capability to produce dense metals, alloys and metal-matrix composites at a relatively low cost in a single-step process [110]. Various electrodeposited cobalt-based and nickel-based coatings have been considered as potential replacements for hard chromium. Weston et al. [17] deposited 16 at.% W-Co coatings with the hardness of approximately 900 HV. The Co-W coatings demonstrated lower coefficient of friction and wear rate than hard chromium in the dry sliding wear tests against stainless steel balls. By adding ferrous sulphate to the Co-W baths, the hardness of the as-deposited Co-W-Fe ternary alloy containing 30 wt.% Fe was 840 HV, close to that of hard chromium. The Co-W-Fe coatings had better corrosion resistance but lower wear resistance [111]. Facchini et al. [112] investigated nanocrystalline Co-P coatings with average grain size in the range of 5 to 15 nm, which compared favourably with hard chromium in most respects as listed in Table 2.3. Moreover, the Co-P plating process had greater efficiency and higher deposition rate than its counterpart. Wang et al. [14, 16] produced a novel Ni-P coating with a graded change of phosphorus content in the direction of thickness by controlling current density during electrodeposition. The coatings exhibited better wear and corrosion wear resistance than hard chromium. However, similar to Co-P coatings, the high hardness (more

Table 2.3. Properties of electrodeposited nanocrystalline Co-P coatings compared to hard chromium [112]

Properties	Nanocrystalline Co-P coatings	Hard chromium
Hardness (as-deposited)	530-600 HV	800-1200 HV
Hardness (annealed at 350 °C)	600-700 HV	-
Ductility	2-7% elongation	<0.1%
Pin-on-disk wear tests against Al_2O_3 balls	Coefficient of friction: 0.48-0.5	Coefficient of friction: 0.7
	Wear Volume: 6-7×10^{-6} mm^3 N^{-1} m^{-1}	Wear Volume: 9-11×10^{-6} mm^3 N^{-1} m^{-1}
Corrosion (salt spray)$^{\#}$	Protection ranking 8 @ 1000 hours	Protection ranking 2 @ 1000 hours
Hydrogen embrittlement	None	Yes

$^{\#}$ The protection ranking numbers of the coatings exposed in salt-spray cabinets were determined by ASTM B537 (Standard Practice for Rating of Electroplated Panels Subjected to Atmospheric Exposure).

than 1000 HV) of Ni-P deposits was only obtained after heat treatment at 400 °C, while the hardness of the as-deposited coatings was approximately 550 HV. It may limit their ability to replace hard chromium. Additionally, the co-deposition of particles, such as SiC, TiO_2 and Al_2O_3, can further improve the anti-wear and anti-corrosion properties, which broadens the prospect of their applications [113].

2.2.6 Welding Facing Methods

Laser cladding is one of the welding facing methods to join melting metallic power on to substrates using a high energy laser beam. The generated heat during the process can be localised at the surface of the substrate, but it is still unsuitable for high strength steel used in aerospace which is quite heat sensitive [114]. Serres et al. [115] produced NiCrBSi coatings by laser cladding, which were claimed to be a good alternative to hard chromium for anti-wear applications. Electro-spark deposition is a pulsed-arc micro-welding process to deposit the consumable electrode materials on a metallic substrate [4]. Johnson et al. [15] studied several electro-spark deposits as replacement candidates. The hardness of the as-deposited cobalt-based coating (Stellite 21) was equal to the lower range of that of hard chromium, and it also exhibited better corrosion resistance. The WC-25TaC-13Co coating had lower wear rate than hard chromium. Due to the very low deposition rate, the method has been used for repairing small damage areas of moulds, dies and some aircraft engine components which are not fatigue-critical [116].

2.3 Electrodeposited Nanocrystalline Ni, Co and Their Alloys

2.3.1 Mechanism of Electrodepositing Nanocrystalline Coatings

Electrocrystallisation is a result of competition between the buildup of existing crystals and the formation of new ones, which are influenced by the rate of charge transfer at the electrode surface and the surface diffusion of adions on the crystal surface. Electrodeposited nanocrystalline coatings allow the use of existing hard chromium plating infrastructure with some modest modification. The grain dimension strongly depends on the surface diffusion and overpotential. A low surface diffusion rate and high overpotential promote the formation of new nuclei resulting in refined grain size. The former can be achieved by adsorption of foreign species on the growing surface, such as grain refiners. Saccharin has been proven to be an effective additive on grain refinement for nickel electrodeposition [117]. The overpotential can be experimentally tailored by changing the current density provided by the power supply [73].

2.3.2 Texture of Electrodeposits

The preferred orientation of electrodeposited metals depends mainly on the crystal structure of the substrate and the bath conditions. When the difference in lattice parameter between the substrate and deposit exceeds 15%, the texture is independent from the substrate structure [118]. The bath condition includes bath composition, current density, temperature, type of anions, presence of impurities and pH [119]. Since the bath condition can be varied over a wide range, it is hard to predict the texture based on the existing studies. However, Pangarov [120] drew several conclusions about the effect of certain bath conditions. Firstly, low current densities and high deposition temperatures lead to the most densely packed crystallographic planes parallel to the substrate. The axis of preferred orientation of the fcc metal is (111)*, (110)* for bcc structure and (0001)* for hcp structure. In contrast, if the deposition is carried at high current density and low temperature, the direction having the maximum atomic packing of the deposits is perpendicular to the substrate. The axis of preferred orientation of fcc metal is (220)*, for bcc (222)* and for hcp $(11\bar{2}0)^*$. In many cases the preferred orientation does not comply with the above conclusions. The absorbed substance on the electrode can change the axis of preferred orientation of deposits. Pangarov developed the two-dimensional nuclei theory which gives an explanation of the preferred orientation as the function of overvoltage.

However, it is not in agreement with all the experimental results [121].

2.3.3 Health Risks of Nickel and Cobalt Compared to Hexavalent Chromium

EPA has designated 17 chemicals as extremely hazardous substances, including chromium and its compounds as well as nickel and its compounds [122]. As mentioned before there is no doubt that hexavalent chromium is carcinogenic and can cause serious damage to health by prolonged exposure through inhalation. The carcinogenic potency of various nickel compounds varies widely on the basis of solubility and the route of exposure. EPA classified nickel refinery dust and nickel subsulfide as Group A (carcinogenic to humans) and nickel carbonyl as Group B (likely to be carcinogenic to humans), whereas it has not evaluated soluble salts of nickel as a class of compounds for potential human carcinogenicity. Nickel sulphate via inhalation is not carcinogenic in either rats or mice [123]. Although nickel-refinery workers exposed primarily to soluble nickel compounds had a significant excess risk of lung cancer, and injection of soluble nickel salts followed by barbital exposure caused kidney cancer [124], there is no sufficient evidence to convince that inhalation of a mist containing nickel during electroplating can cause cancer. Nickel sulphate is classified as Category 2 (suspected human carcinogens) or even lower grade Category 3 according to REGULATION (EC) No 1272/2008 [125]. Cobalt sulphate is not on the list of carcinogenic chemicals created by EPA, but is classified as Category 2 (suspected human carcinogens) according to REGULATION (EC) No 1272/2008 [125]. Although the categories are inconsistent, it is generally accepted that nickel and cobalt solute salts used in the electroplating industry have much less carcinogenic potency than hexavalent chromium. For nickel plating, it is more concerned about asthma caused by inhaling the mist and skin sensitisation caused by skin contact [126, 127]. At present it is unrealistic to substitute chromium for a non-hazardous material at low cost. Therefore, nickel [128] and cobalt is a reasonable choice to fill the gap between chromium plating and future non-hazardous coatings.

2.3.4 Electrodeposited Nanocrystalline Nickel

2.3.4.1 Plating Baths

The first bath to deposit nickel is formulated by Watts in 1916, which contains nickel sulphate to provide nickel ions, nickel chloride or sodium chloride to assist the dissolution of nickel anode and boric acid as buffering agent. Controlled current density and specific

Table 2.4. Nickel electroplating baths [129].

Baths	Source of Ni^{2+}	Advantages	Disadvantages
Nickel sulphate bath	$NiSO_4$ with small quantities of $NiCl_2$	Less expensive Less corrosive to equipment Easy to use and maintain Lower internal stress in deposits	N/A
Nickel sulphamate bath	$Ni(NH_2SO_3)_2$ with small quantities of $NiCl_2$	High rate of deposition Lower internal stress in deposits	High sensitivity to impurities High cost of chemicals
Nickel chloride bath	$NiCl_2$	Higher electrical conductivity	High cost High corrosion Higher internal stress in deposits
Nickel fluoborate bath	$Ni(BF_4)_2$	Deposits obtained similar to those from nickel sulphate bath	High cost of chemicals

additives are used to refine the grain size. Three other baths, including nickel sulphamate bath, nickel chloride bath and nickel fluoborate bath, are employed for nickel electroplating, which are listed in Table 2.4 [129].

2.3.4.2 Microstructure

Jeong et al. [44] deposited nanocrystalline nickel coatings with the average grain size of 13 nm on mild steel substrates by pulse current electrodeposition in a modified Watt's bath. The bright field and dark field transmission electron microscopy (TEM) images with electron diffraction patterns are shown in Fig. 2.7. The first four rings in Fig. 2.7(c) represent (111), (200), (220) and (311) for the fcc structure.

The typical XRD pattern of nanocrystalline nickel is illustrated in Fig. 2.8. It can be observed that the crystal structure is pure fcc and no characteristic peaks of other structures have been recorded [130].

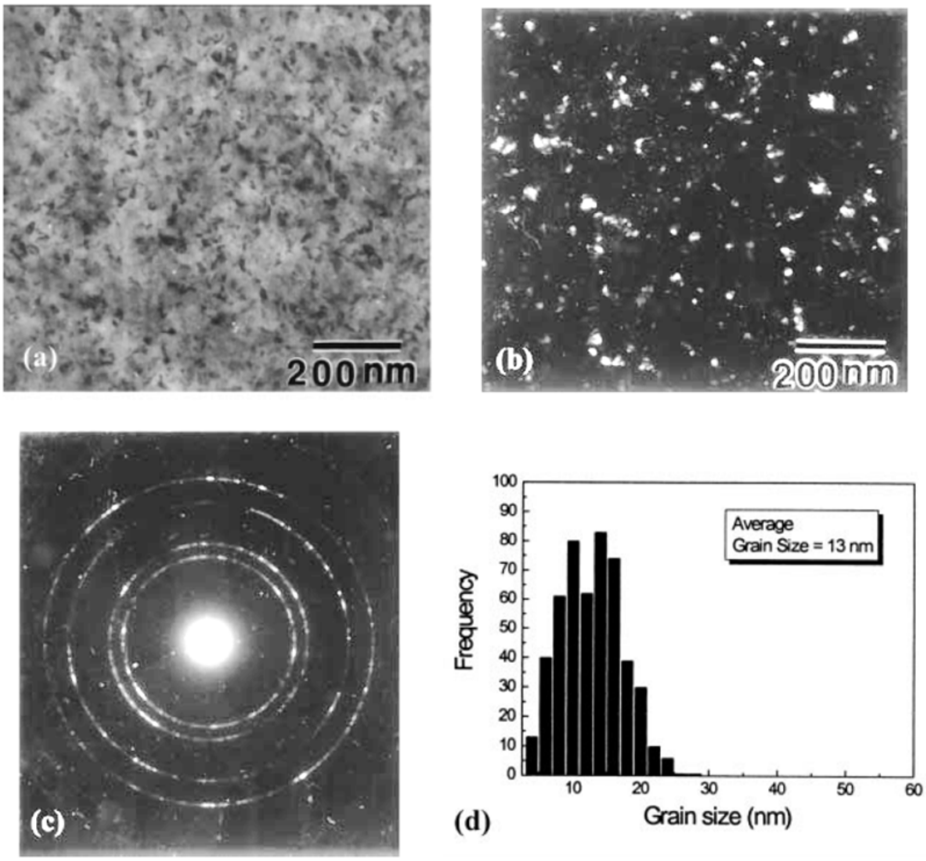

Fig. 2.7. Bright field (a) and dark field (b) TEM micrographs with electron diffraction patterns (c) and grain size distribution (d) of electrodepsited nanocrystalline nickel coating [44].

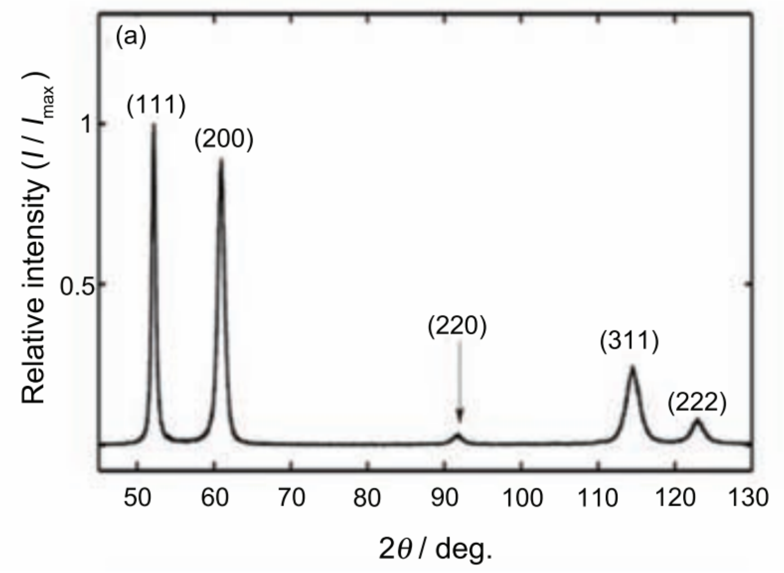

Fig. 2.8. XRD pattern of electrodeposited nanocrytalline nickel with the grain size of approximately 25 nm [130].

2.3.4.3 Microhardness

Jeong et al. [44] reported that the microhardness of coarse-grained polycrystalline nickel with the grain size of 90 µm was approximately 120 HV. As shown in Fig. 2.9, it initially increased with the decrease of grain size. The behaviour is known as the Hall-Petch effect [40], which can be described as

$$H = H_0 + kd^{-\frac{1}{2}} \tag{2.2}$$

where H_0 is the intrinsic hardness, d is the grain size and k is a constant for a particular material. However, at the grain size below 62 nm, the deviation from Hall-Petch relationship was observed. Mishra et al. [46] also reported that by reducing the grain size from 28 nm to 10 nm, the microhardness of electrodeposited nickel coatings increased from around 570 HV to higher than 700 HV, but the deposit with the grain size of 8 nm was softer than its counterpart with the grain size of 10 nm. Erb [48] found Hall-Petch relationship for nickel electrodeposits broke down when the grain size was less than 30 nm, while Wang et al. [43] claimed that the deviation occurred as the grain size was reduced to approximately 45 nm as shown in Fig. 2.10(a). The critical grain sizes of the inverse Hall-Petch relationship are not consistent and the mechanisms are not clear. It may be attributed to a number of factors, including suppression of dislocation pile-ups [46], diffusional creep [48], larger fraction of grain boundaries [42], and increasing porosity of deposits with small grain size [45]. A detailed discussion is given in Chapter 6.

2.3.4.4 Tribological Behaviour

Higher hardness related to grain size reduction has been proven to play a dominating role in the improved tribological behaviour of nanocrystalline nickel coatings. Nanocrystalline nickel with 10-20 nm grain size exhibited higher wear resistance and 45-50% lower coefficient of friction than polycrystalline nickel with the grain size of 90 µm in pin-on-disk tests [44]. It has been reported that electrodeposited nickel of 8 nm grain size with smooth surface had a much lower value of coefficient of friction (0.15) against steel in fretting wear tests compared to that of its counterpart of 61 µm grain size [46]. The wear rate of the nickel coatings produced by Wang et al. [43] decreased from approximately 2.5×10^{-3} mm^3 N^{-1} m^{-1} to around 5×10^{-4} mm^3 N^{-1} m^{-1} by reducing the grain size from 3 µm to 16 nm. This was mainly attributed to the increase of microhardness from 200 HV to 600 HV. Moreover, the morphologies of worn surfaces illustrated that the wear mechanism transformed from severe adhesion wear and plastic deformation with delamination to abrasion and oxidation wear as the hardness increased.

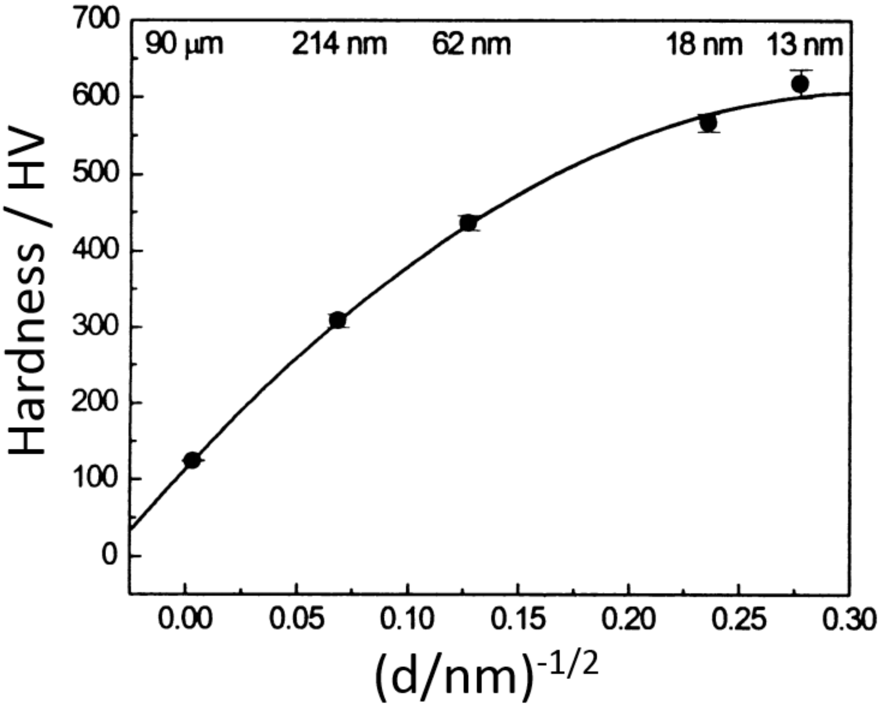

Fig. 2.9. The change of hardness of nickel coatings with the average grain size [44].

2.3.4.5 Corrosion Behaviour

Rofagha et al. [131, 132] investigated the corrosion behaviour of nanocrystalline nickel of 22 nm grain size and coarse-grained nickel of 100 µm grain size in 1 M H_2SO_4. It was found that both could form passive films in sulphuric acid, while the current density of the former in the passive potential range was higher due to a more defective passive film formed on the highly disordered nanocrystalline surface. Mishra and Balasubramaniam [133] also reported the increased passive current density for nanocrystalline nickel compared to microcrystalline nickel in the same corrosion media. However, the increased breakdown potential with the decreasing grain size indicated that the tendency for localised corrosion is lower for nanocrystalline nickel due to the more uniform distribution of the impurities (sulphur). Moreover, it was revealed by Tafel and linear polarisation tests that the corrosion rate of freshly exposed surfaces of electrodeposited nickel decreased with grain size, which indicated greater hindrance to anodic dissolution in nanocrystalline nickel. In alkaline solution, the corrosion resistance of nickel coating considerably increased by reducing the grain size from 3 µm to 16 nm, which can be attributed to faster formation of continuous $Ni(OH)_2$ passive films on nanocrystalline nickel coatings [134]. Although nanostructure may accelerate corrosion by forming more microelectrochemical cells between the large amount of grain boundaries and the matrix, the high density of

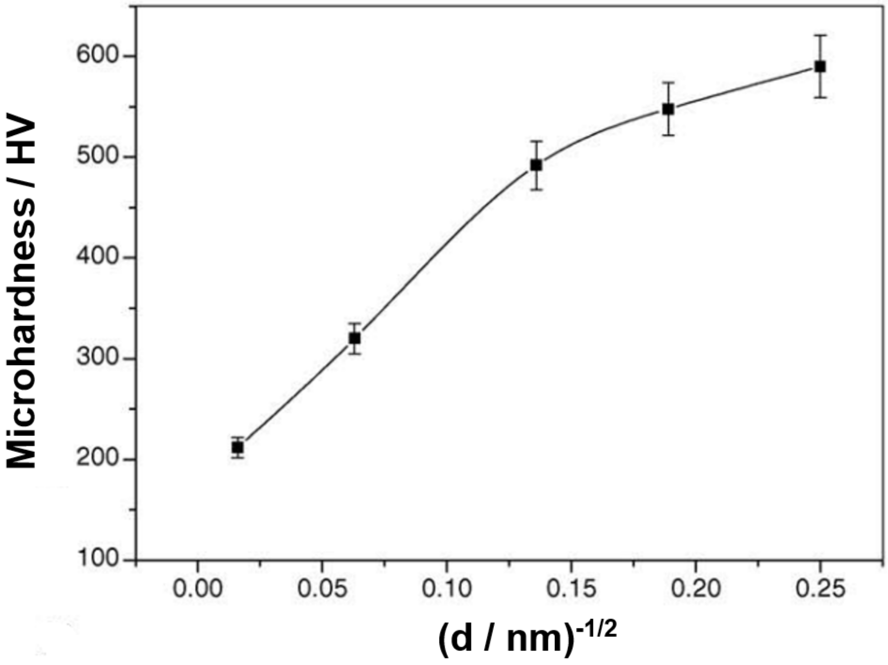

(a)

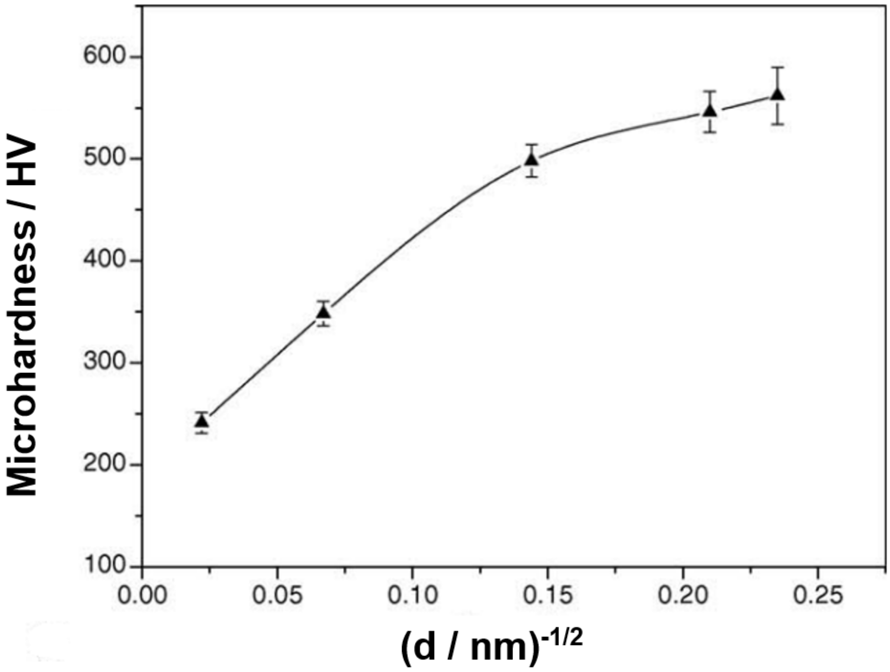

(b)

Fig. 2.10. Hall-Petch plots for as-deposited (a) nanocrystalline nickel and (b) nanocrystalline cobalt [43].

grain boundaries and lattice defects can provide more nucleation sites for passive films, which results in a high fraction of passive layers and low corrosion rate.

2.3.5 Comparison between Electrodeposited Nanocrytalline Ni and Co

Nanocrystalline cobalt can be electrodeposited from baths containing cobalt sulphate and/or cobalt chloride as the source of cobalt ions [135, 136]. The microstructure and properties compared with electrodeposited nanocrystalline nickel are discussed as follows.

2.3.5.1 Microstructure

Rather than the fcc structure of nanocrystalline nickel, the nanocrystalline cobalt coatings with the average grain size of 25 nm exhibited the hcp lattice shown in Fig. 2.11. The characteristic diffraction patterns of hcp Co included the (100), (002) and (101) innermost rings followed by fainter (102), (110), (103) and (200) rings [137].

XRD pattern shown in Fig. 2.12 exhibited a strong basal (002) texture indicating that the majority of grains are oriented with their close-packed plane parallel to the coating surface, which is common in conventional polycrystalline cobalt electrodeposits [137].

2.3.5.2 Microhardness

Wang et al. [43] reported the hardness of both nanocrystalline Ni and Co coatings increased with grain size reduction up to a similar critical value (approximately 45 nm) shown in Fig. 2.10. The same deviation from the Hall-Petch relationship with further reduction of grain size to 16 nm has been observed and the microhardness of nickel and cobalt with the same grain size was comparable. However, Karimpoor et al. [138] claimed that the hardness of cobalt increased from 250 HV to 460 HV with the grain size decrease from 10 µm to 18 nm, which was consistent with the Hall-Petch relationship. The conclusion was drawn based on only three samples, which needs to be confirmed by more experimental work.

2.3.5.3 Tribological Behaviour

Both the nanocrystalline and microcrystalline cobalt coatings with hcp structure exhibited better anti-wear performance compared with nanocrystalline and microcrystalline nickel with fcc structure against a steel ball under the same wear conditions [43]. As shown in Fig. 2.13, with almost the same grain size and hardness, wear rates of cobalt coatings were an order of magnitude lower than those of Ni coatings [43]. Additionally, the

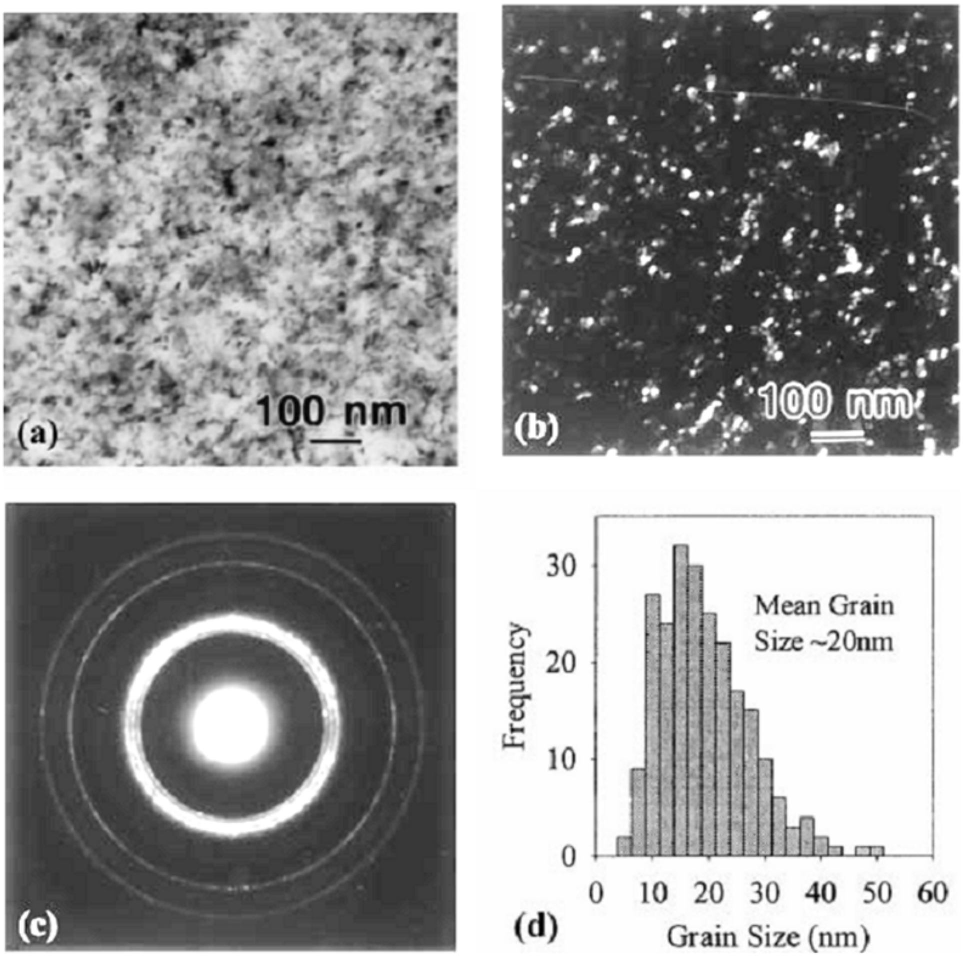

Fig. 2.11. Bright field (a) and dark field (b) TEM micrographs with electron diffraction patterns (c) and grain size distribution (d) of the as-deposited nanocrystalline cobalt [137].

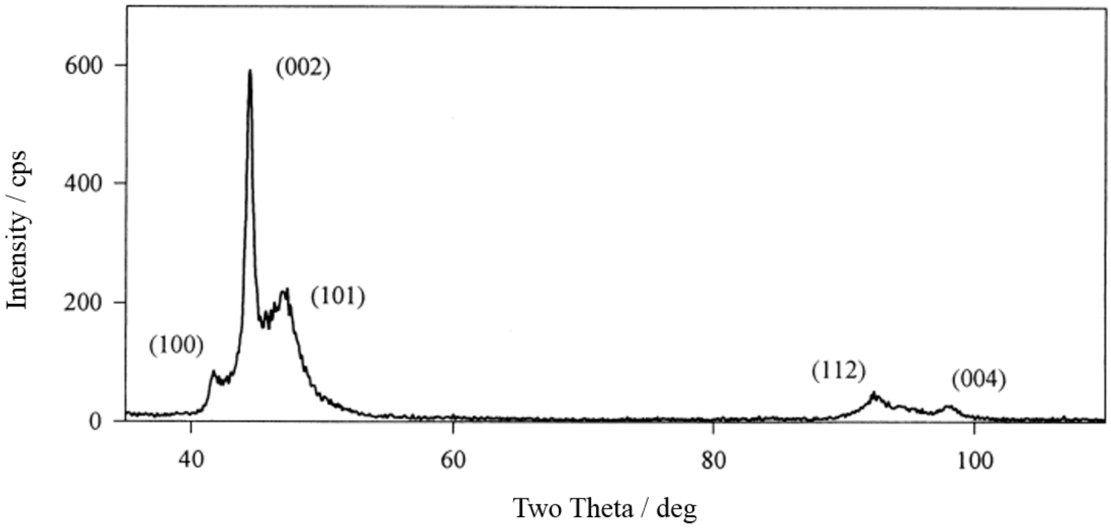

Fig. 2.12. XRD pattern of electrodeposited nanocrytalline cobalt with the grain size of approximately 20 nm [137].

coefficient of friction of nanocrystalline cobalt was 0.2, which was only one third of that of nanocrystalline nickel. The hcp structure has been proven to have a significant effect on friction-reduction by resisting adhesive interactions with the counterface, which is discussed in more detail in Chapter 4. The worn surface morphologies of nickel and cobalt coatings are shown in Fig. 2.14. Although the nickel and cobalt coatings had similar grain size and hardness, the smooth worn surface with fine grooves of cobalt coatings illustrated much lower extent of damage. The tribological properties can be improved by reducing the grain size [43].

2.3.5.4 Corrosion Behaviour

As mentioned in Section 2.3.4.5, both coarse-grained and nanocrystalline nickel coatings exhibited an active-passive potentiodynamic polarisation behaviour in sulphuric acid [132, 133] and alkaline solutions [134]. However, no obviously passive process has been observed for nanocrystalline or microcrystalline cobalt coating in HCl or H_2SO_4 solutions [135, 136]. Consequently, higher grain boundary density of nanocrystalline cobalt will accelerate corrosion due to more active sites for preferential attack. In contrast, in NaOH or NaCl solutions cobalt coatings can form protective passive films [136]. Thus nanocrystalline cobalt coating exhibits improved corrosion resistance than coarse-grained cobalt in alkaline solutions. Wang et al. [136] suggested that the varying corrosion behaviour of nanocrystalline cobalt coatings in different corrosion media could be explained by the effect of a larger number of grain boundaries and defects in nanostructured coatings. As illustrated in Fig. 2.15(a), the high fraction of grain boundaries in nanocrystalline coatings provide a large number of active sites to quickly form a continuous and protective passive film, which increases the difficulty of cobalt ions or electron migration to the surface to participate in further electrochemical reactions. In the case of cobalt coatings in HCl or H_2SO_4 solutions with no formation of passive films, nanostructured surfaces become more electrochemically reactive due to the increasing number of defects as shown in Fig. 2.15(b). It is worth noticing that nanocrystalline cobalt coatings had an order magnitude lower passive current density than that of coarse-grained cobalt coatings, which is inconsistent with the results of nanocrystalline nickel [133] as described in Section 2.3.4.5. Therefore, more factors (e.g. impurities) need to be considered to explain the nature of passive films. Additionally, by comparing the electrochemical behaviour of nanocrystalline cobalt [136] and nickel with similar grain size, 18 nm and 16 nm respectively, it is found that the corrosion resistance of nanocrytalline cobalt was worse than its nickel counterpart in NaOH

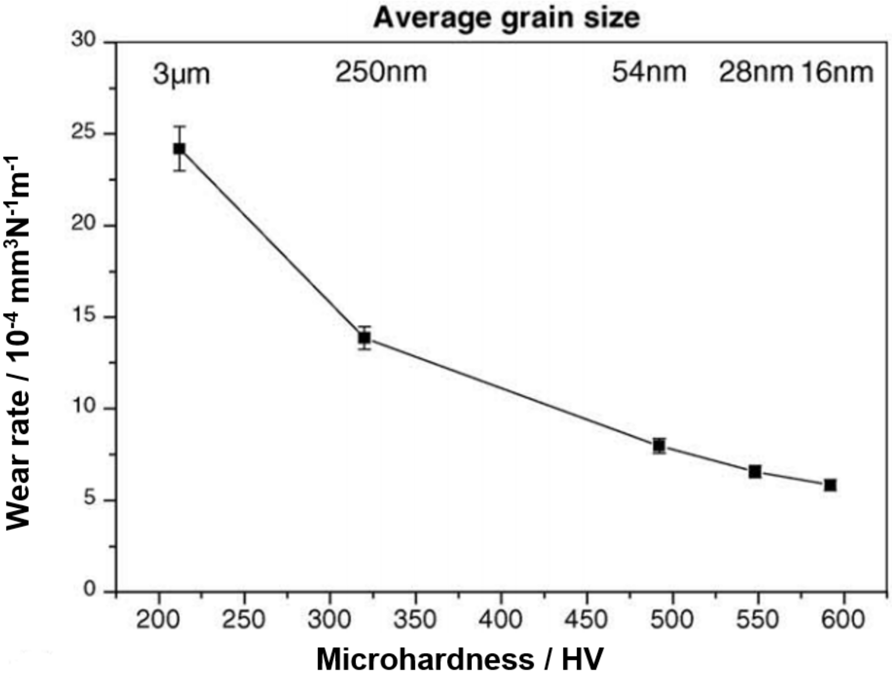

(a)

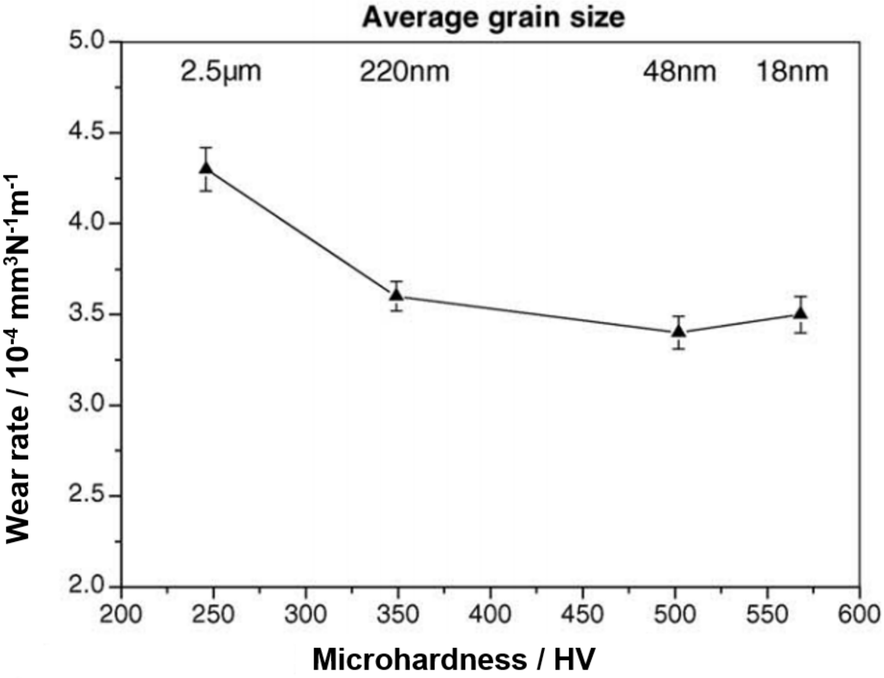

(b)

Fig. 2.13. Variation of wear rates of (a) nanocrystalline nickel and (b) nanocrystalline cobalt [43].

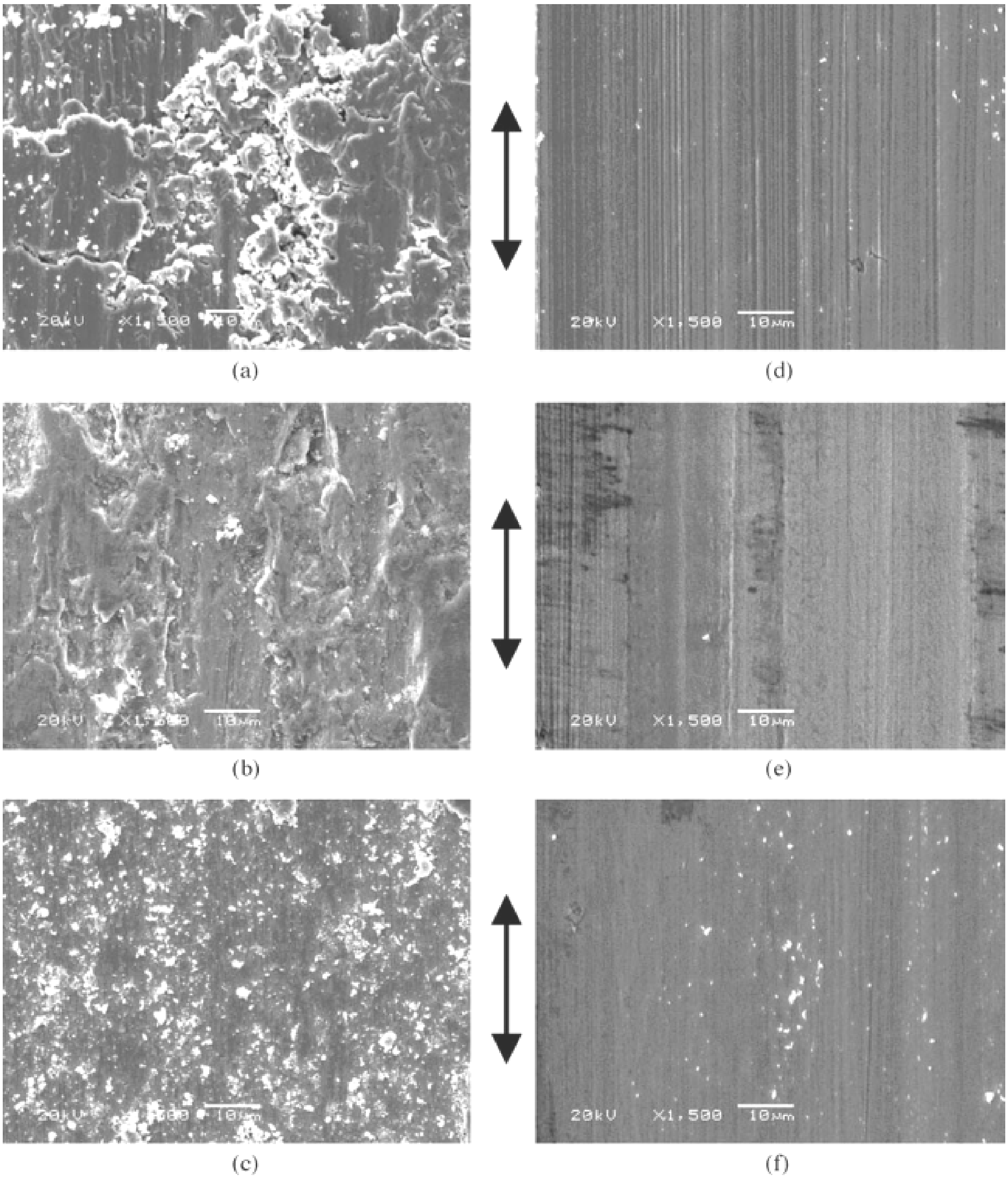

(a) (d) (b) (e) (c) (f)

Fig. 2.14. Worn surface morphologies of nickel coatings with grain size of: (a) 3 µm, (b) 250 nm, (c) 16 nm and cobalt coatings with grain size of (d) 2.5 µm, (e) 220 nm and (f) 18 nm. Double-pointed arrows show the reciprocating sliding direction [43].

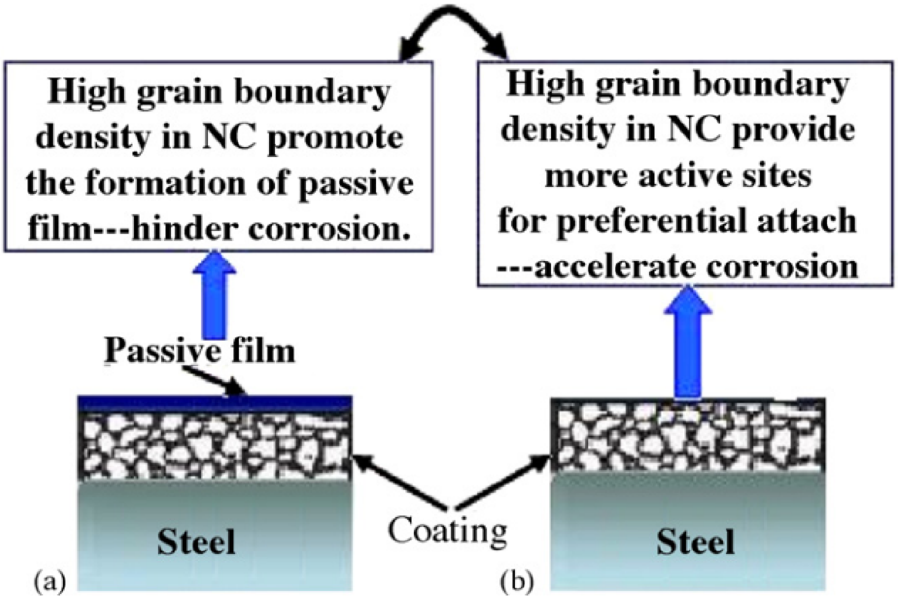

Fig. 2.15. Model for the corrosion mechanisms of nanocrystalline cobalt coatings in different corrosion media; (a) positive effect and (b) negative effect of high grain boundary density [136].

solutions [134, 136].

2.4 Electrodeposited nanocrystalline Ni-Co for Anti-wear and Anti-corrosion Purposes

Nanocrystalline Ni-Co electrodeposits have the potential to be used in aerospace, automobile and general industries as an alternative to hard chromium coatings due to their high hardness, anti-wear and anti-corrosion resistance [24]. Similar to nickel or cobalt coatings, the Ni-Co alloys can be deposited from sulphamate baths, Watts type baths and chloride baths. Tury et al. [21] reported that the coatings plated from the former two baths were homogeneous through the whole cross section, but had much lower microhardness than those produced from chloride baths. In the past few years, the preparation and optimisation of the coatings have drawn extensive attention [22–24, 37, 139], especially the relationship among experimental parameters, microstructure and properties.

2.4.1 Microstructure and Properties

2.4.1.1 Microstructure

The surface morphologies of Ni-Co alloys strongly depend on the cobalt content as shown in Fig. 2.16 [24]. It changed from large polyhedral crystallites to small spherical clusters as the cobalt content increased from 7 wt.% to 66 wt.% Co. The 81 wt.% Co-Ni coating exhibited the branched structure (Fig. 2.16(f)). The phase structure gradually changed from fcc to hcp with the increase of cobalt content [24]. As shown in Fig. 2.17(e), the 66 wt.% Co-Ni coating contained a mixture structure of fcc and hcp, while the 81 wt.% Co-Ni (Fig. 2.17(e)) had a strong hcp (002) texture with pronounced (100) and (101) peaks, similar to the structure of the pure cobalt coating shown in Fig. 2.12. Myung and Nobe [22] reported that the transition from fcc to hcp structure occurred as the cobalt content was in the range of 72-78 wt.%.

2.4.1.2 Microhardness

Generally, the microhardness of nanocrystalline Ni-Co coating with different grain size electrodeposited by direct current was in the range of 300-500 HV depending on the cobalt content as shown in Fig. 2.18 [24]. It was found that the microhardness of Ni–Co alloys increased initially as Co content increased from 0 to approximately 49 wt.%, and then gradually decreased with a further increase of the cobalt content. The similar evolution of microhardness as the function of cobalt content was also reported by Golodnitsky et al. [23] and Srivastava et al. [139]. Wang et al. [24] claimed that the Ni-Co alloys exhibited a nearly constant Hall-Petch gradient. However, it is inappropriate to apply the Hall-Petch relationship to different materials because k in Eq. (2.2) is a material dependant constant [140]. Srivastava et al. [139] attributed the decrease of hardness with the cobalt content higher than 50 wt.% to the formation of fibrous structure and the transformation from fcc to hcp crystal structure. Li et al. [37] reported that the Ni-Co coatings produced by pulse current plating had higher hardness (400-600 HV) than the coatings plated by direct current. The peak current density determined the composition and grain size, which led to the variation of microhardness as shown in Fig. 2.19.

2.4.1.3 Tribological Behaviour

The research conducted by Wang et al. [24] revealed that the cobalt-rich alloys had excellent friction–reduction behaviour against AISI-52100 stainless steel ball under dry sliding conditions compared to nickel-rich alloys. As shown in Fig. 2.20, the coefficient of friction of Ni–Co alloys with cobalt content lower than 49 wt.% was higher than 0.6, similar to that of the pure nickel coating. It started to decrease when the cobalt content was 66 wt.% and the 81 wt.% Co-Ni exhibited a dramatical reduction of coefficient of friction, which was approximately 0.25. The friction reduction of cobalt-rich alloys was

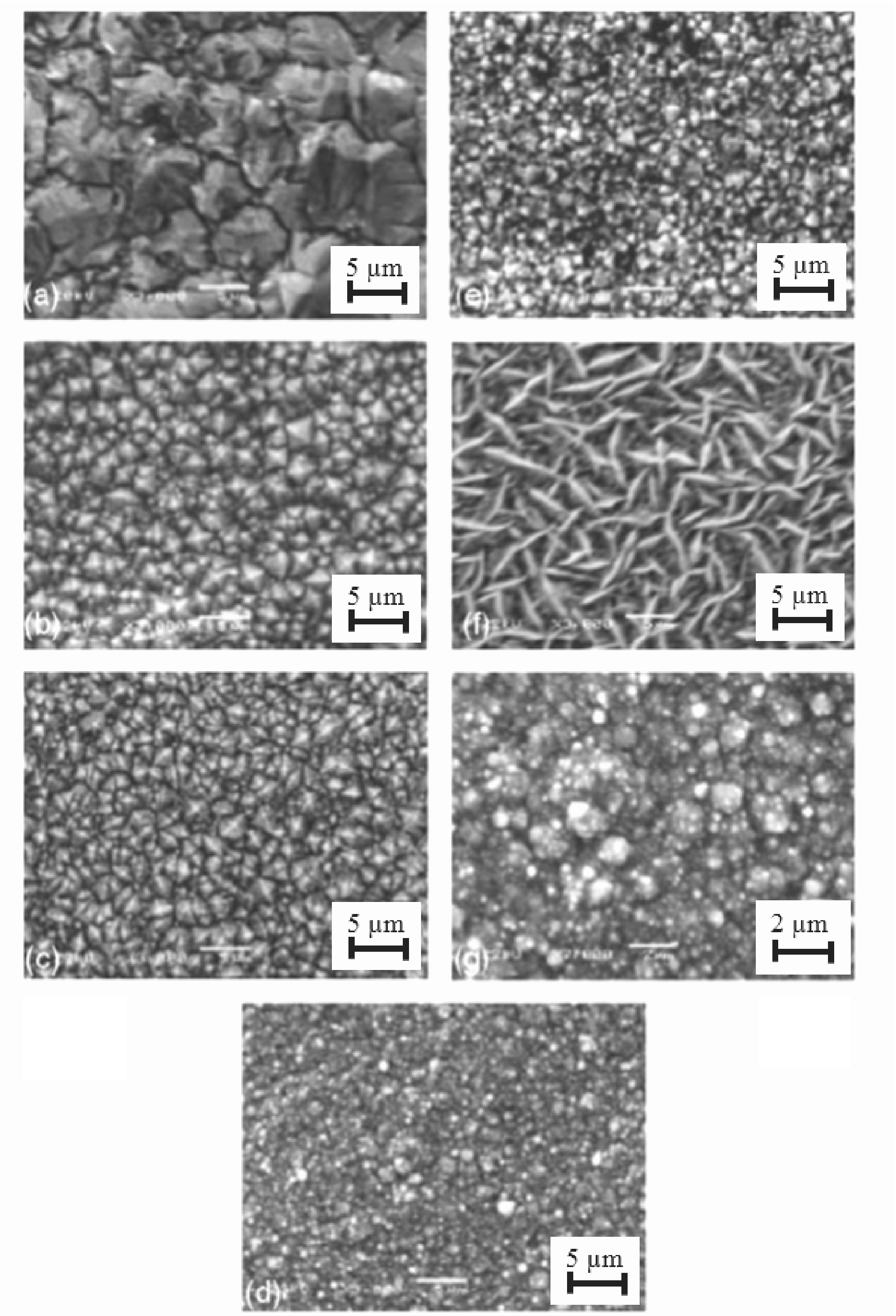

Fig. 2.16. Surface morphologies of Ni–Co alloy deposits with different cobalt contents of (a) 0 wt.%, (b) 7 wt.%, (c) 27 wt.%, (d) 49 wt.%, (e) 66 wt.%, (f) 81 wt.%, and (g) high-magnification of Ni–49 wt.% Co alloy [24].

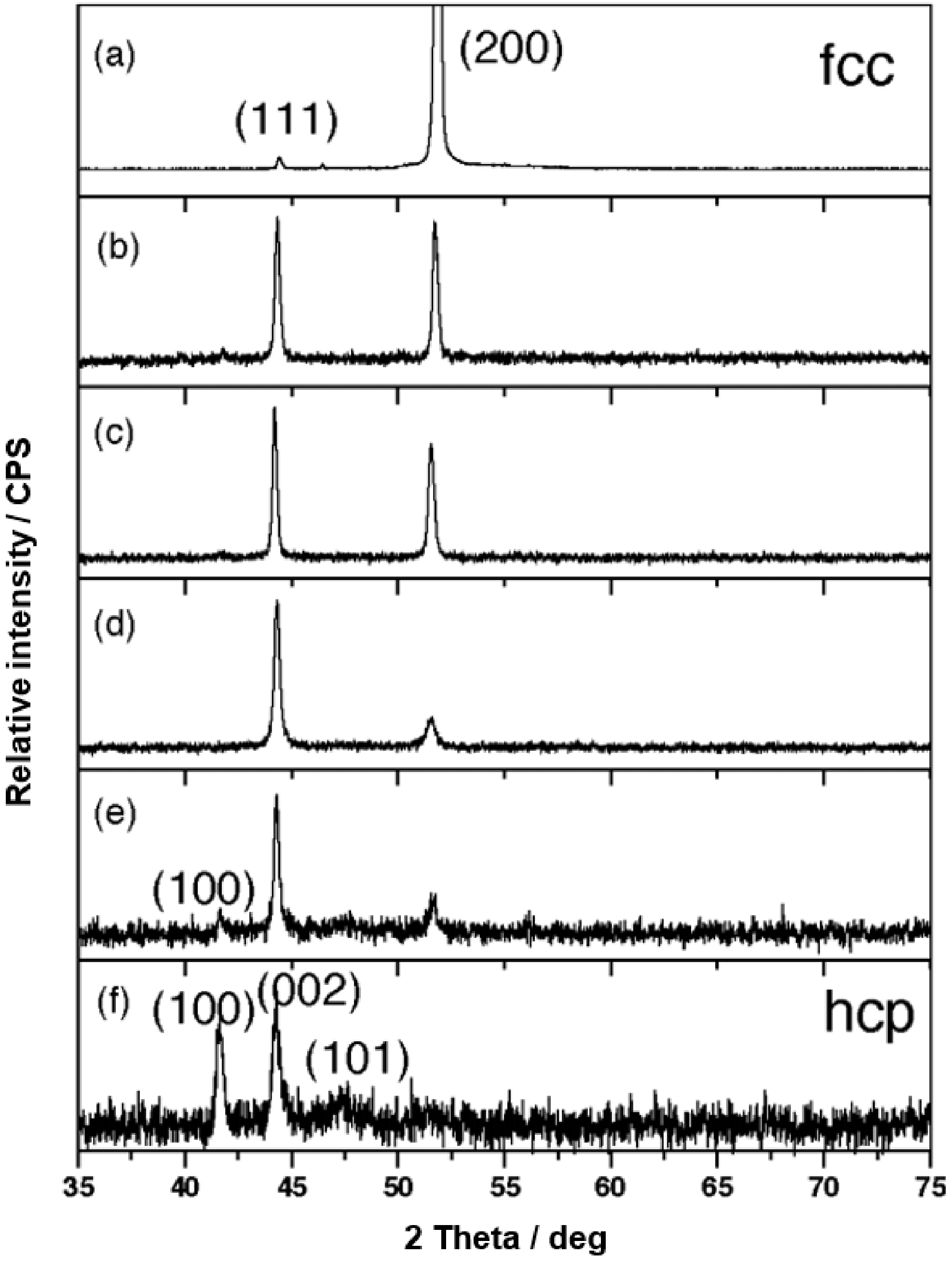

Fig. 2.17. XRD patterns of Ni–Co alloy deposits with different cobalt contents of (a) 0 wt.%, (b) 7 wt.%, (c) 27 wt.%, (d) 49 wt.%, (e) 66 wt.% and (f) 81 wt.% [24].

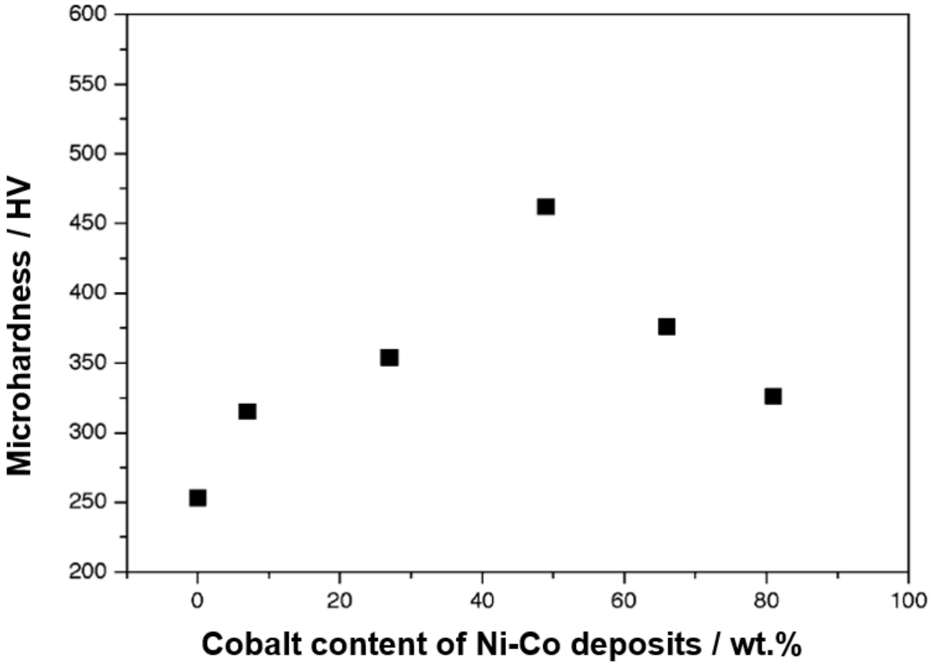

Fig. 2.18. Microhardness as the function of cobalt content [24].

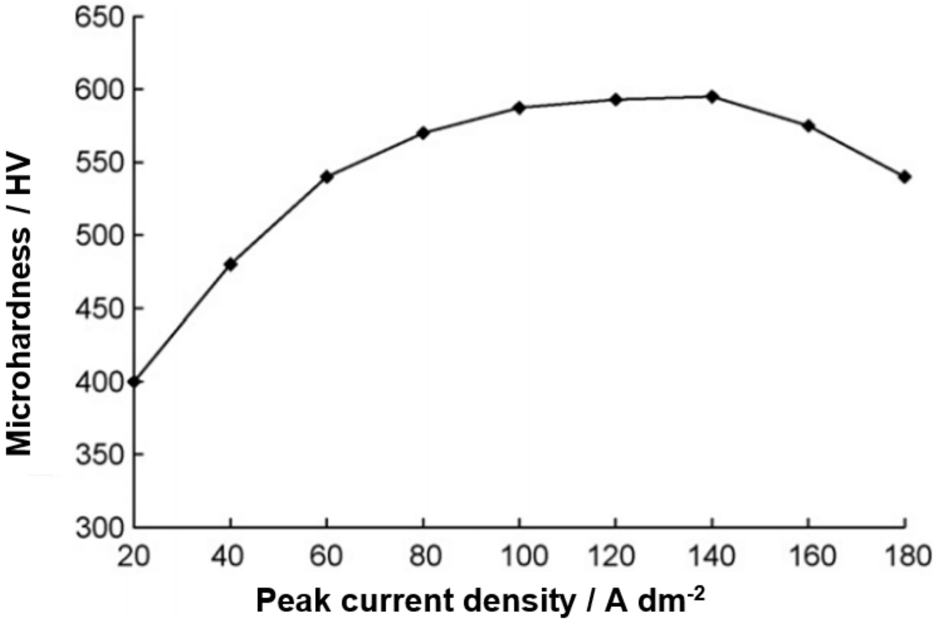

Fig. 2.19. Microhardness of Ni-Co coatings produce by pulse deposition as the function of peak current density [37].

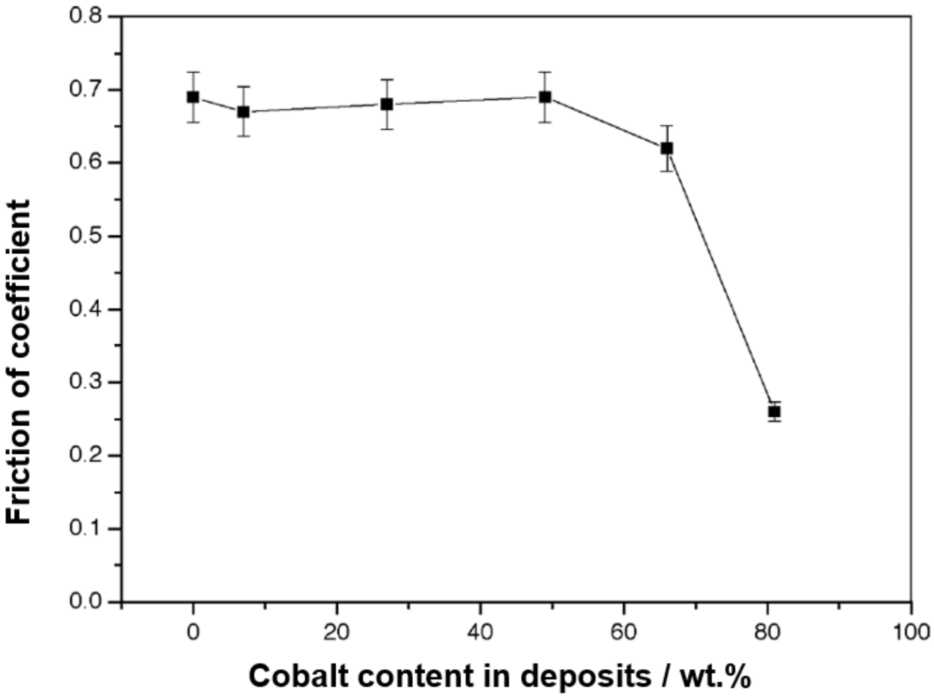

Fig. 2.20. Coefficient of friction as the function of cobalt content in Ni-Co alloys [24].

attributed to the change of crystal structure from fcc to hcp. Fig. 2.21 illustrated the improvement of wear resistance with the increasing cobalt content in the Ni-Co deposits. When the cobalt content was lower than 49 wt.%, the wear rate gradually decreased due to the increase of microhardness. In spite of its lower hardness, the wear rate of 81 wt.% Co-Ni coating was more than an order of magnitude lower than that of pure Ni and Ni-rich alloys. The difference in the wear behaviour of Ni–Co alloys can be verified by the worn surface morphologies shown in Fig. 2.22. The wear tracks of pure nickel (Fig. 2.22(a)) and 27 wt.% Co-Ni (Fig. 2.22(b)) with fcc structure exhibited the larger extent of adhesion wear and severe deformation in the sliding direction under the combined stresses of compression and shear. However, smooth surface with smaller damaged regions, only some light grooves and scars, was observed on the worn surface of the 81 wt.% Co-Ni with hcp structure (Fig. 2.22(c)). It has been found that the hcp structure of cobalt-based alloys (Co-Re, Co-Mo and Co-Cr) leads to lower coefficient of friction and wear rate than their counterparts with fcc structure [25, 26]. A detailed discussion regarding the effect of hcp structure on the tribological properties is given in Chapter 4.

2.4.1.4 Corrosion Behaviour

Myung and Nobe [22] investigated the corrosion resistance of Ni-Co alloys plated from chloride baths with different cobalt contents in 0.5 M NaCl after 1h immersion. As shown

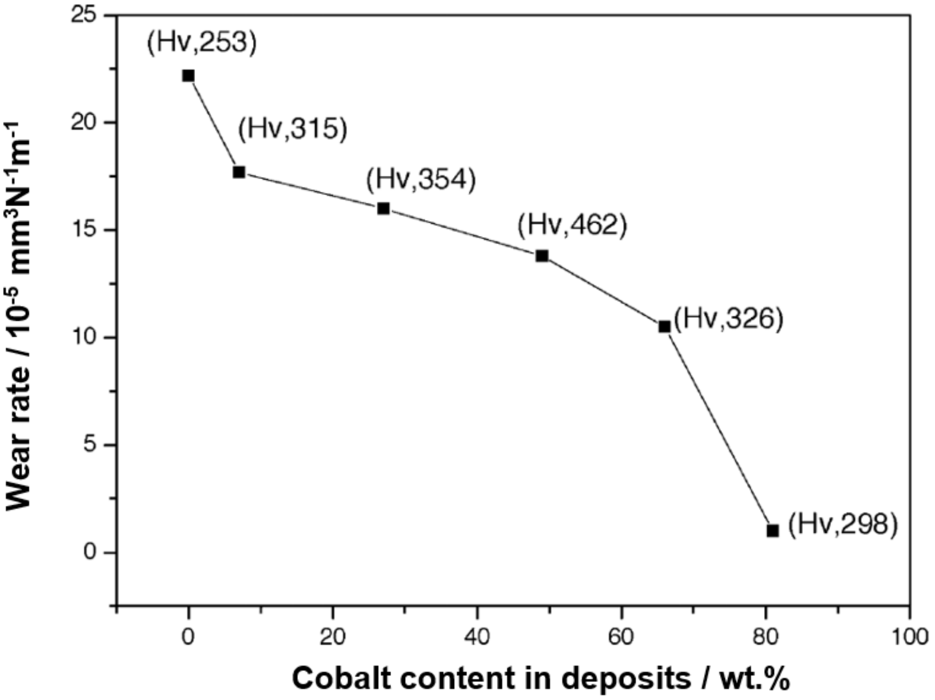

Fig. 2.21. Wear rate as the function of cobalt content in Ni-Co alloys [24].

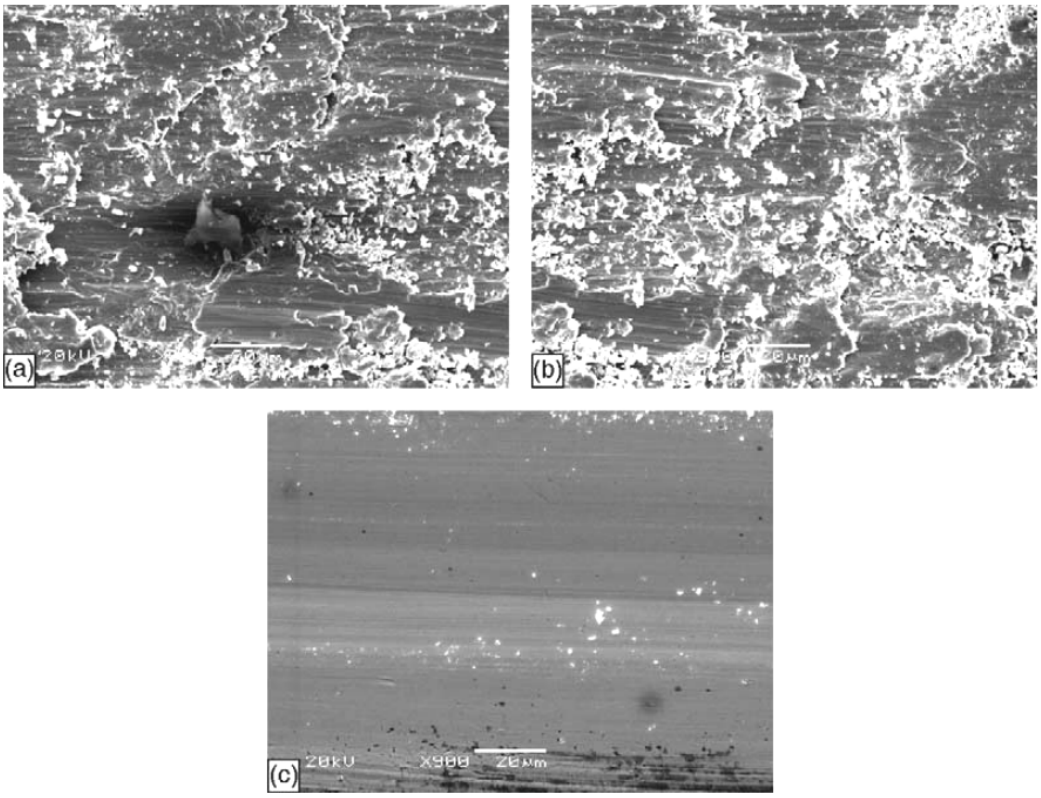

Fig. 2.22. Worn surface of (a) pure nickel and Ni–Co alloy deposits: (b) 27 wt.% Co-Ni and (c) 81 wt.% Co-Ni [24].

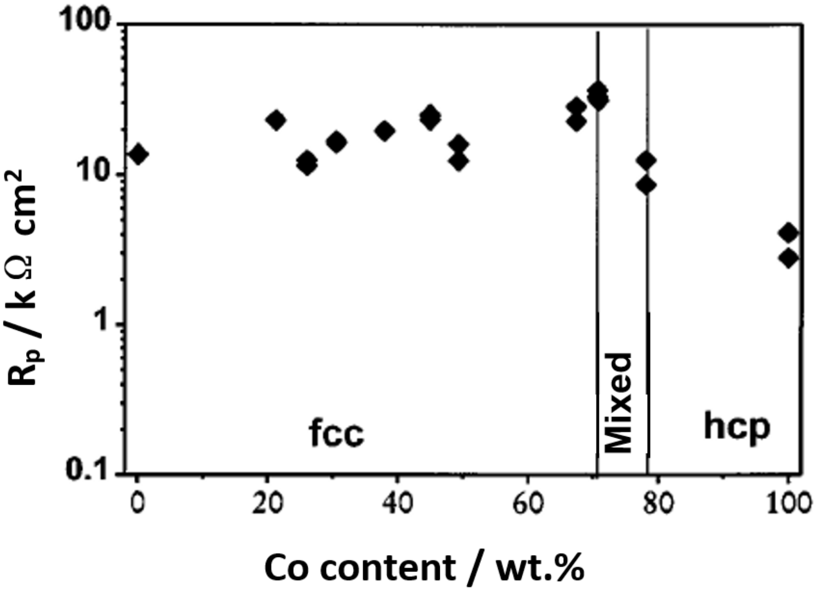

Fig. 2.23. Corrosion resistance of Ni-Co alloys in 0.5 M NaCl after 1 h immersion [22].

in Fig. 2.23, the corrosion resistance increased slightly with the increasing cobalt content until it reached the maximum at 70 wt.% Co and then sharply decreased. The nickel-rich deposits with fcc structure had an order of magnitude higher corrosion resistance than cobalt-rich coatings with hcp structure. Srivastava et al. [139] found that Ni–20% Co alloy plated from sulphamate baths exhibited better corrosion resistance in 3.5% NaCl in comparison to other Ni–Co alloys with higher cobalt content, which was attributed to its dense surface and fcc structure. Hassni et al. [141] reported that the nanocrystalline 5 wt.% Co-Ni alloys with a smooth surface deposited from the bath containing saccharin had higher corrosion resistance in 10 wt.% NaOH compared with the coatings with the same composition plated from additive-free baths.

2.4.2 Experimental Parameters

In order to optimise the properties of nanocrystalline Ni-Co electrodeposition, the electroplating variables, such as cobalt ion concentration, current density, additive, bath temperature and bath agitation, should be appropriately adjusted. Previous studies have shown that these factors had different effects on the microstructure and composition of Ni-Co coatings and consequently led to different hardness, tribological and electrochemical properties, which are discussed as follows.

2.4.2.1 Effect of Cobalt Ions Concentration in Electrolytes

With a fixed concentration of nickel ions, the cobalt content in alloy deposits increased gradually with the increasing Co^{2+} concentration in the electrolyte as shown in Fig. 2.24 [24]. It was found that the percentage of cobalt in alloys was higher than the $Co^{2+}/(Co^{2+}+Ni^{2+})$ ratio in the electrolyte [20, 24]. The less noble metal (Co) was preferentially deposited. Bai and Hu [142] explained the anomalous deposition by the higher adsorption ability of $Co(OH)^{+}$ than $Ni(OH)^{+}$ on the cathode surface. The reaction mechanism of Ni-Co electrodeposition is as follows [142]:

$$2H_2O + 2e^{-} \rightarrow H_2 + 2OH^{-} \tag{2.3}$$

$$M^{2+} + OH^{-} \rightarrow M(OH)^{+} \tag{2.4}$$

$$M(OH)^{+} \rightarrow M(OH)^{+}_{ads} \tag{2.5}$$

$$M(OH)^{+}_{ads} + 2e^{-} \rightarrow M + OH^{-} \tag{2.6}$$

where M indicates nickel and cobalt. The deposition of cobalt is promoted by the surface enrichment of its corresponding adsorbed metal hydroxide ions ($Co(OH)^{+}_{ads}$). The cobalt content has a significant influence on surface morphology, phase structure, microhardness, wear and corrosion resistance, which has been discussed in Section 2.4.1.

2.4.2.2 Effect of Current Density

Fan and Piron [143] reported that the current efficiency for Ni-Co codeposition in chloride baths increased with increasing current density, and reached 96-98% at current densities ranging from 0.5 to 10 A dm^{-2}. It decreased with the further increase of current density. The coating plated with the current density of 100 A dm^{-2} was porous and fragile, and detached partially from the electrode due to vigorous hydrogen evolution during deposition. High current density can be applied to produce nanocrystalline Ni-Co alloys by jet electrodeposition [20] and pulse current deposition [37]. The cobalt content decreased as the (peak) current density increased as shown in Fig. 2.25 [20] and Fig. 2.26 [37]. The increase of cathodic current density leads to the cathodic overpotential which favours the activation-controlled nickel deposition, whereas the diffusion-controlled cobalt deposition

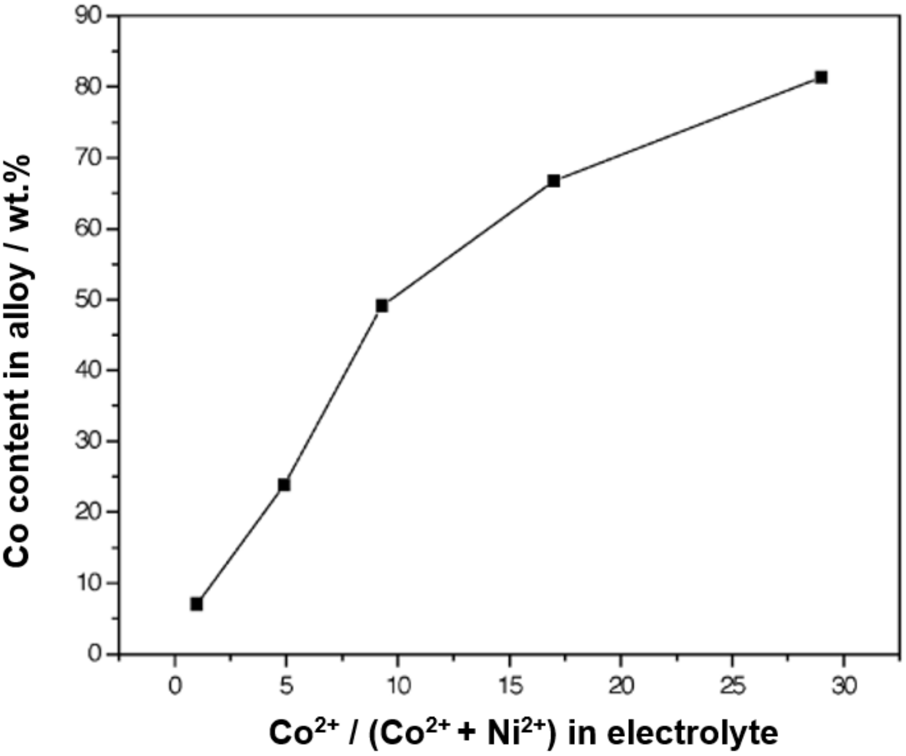

Fig. 2.24. The composition of Ni-Co alloys as the function of the ratio of $Co^{2+}/(Co^{2+}+Ni^{2+})$ in electrolytes [24].

has fewer responses. Therefore, higher current density results in lower cobalt content in deposits [20].

As shown in Fig. 2.27, the grain size of Ni-Co coatings plated by pulse electrodeposition decreased rapidly with the increasing peak current density to around 20 nm at l00 A dm^{-2} and then slowly reduced to 10 nm at l60 A dm^{-2}. The reduction of grain size can be attributed to the higher overpotential η_k, which is related to the crystalline nucleus formation probability W expressed by the following equation [144]:

$$W = A \exp\left(-\frac{b}{\eta_k^2}\right) \tag{2.7}$$

where A and b are constants. The overpotential increases with the increasing current density as described in the following equation [37]:

$$\eta_k = a + b \log i \tag{2.8}$$

where a and b are constants and i is the current density. Therefore, the increasing current density leads to the increasing overpotential, which promotes the formation of crystalline nucleus. The reduction in grain size can be achieved.

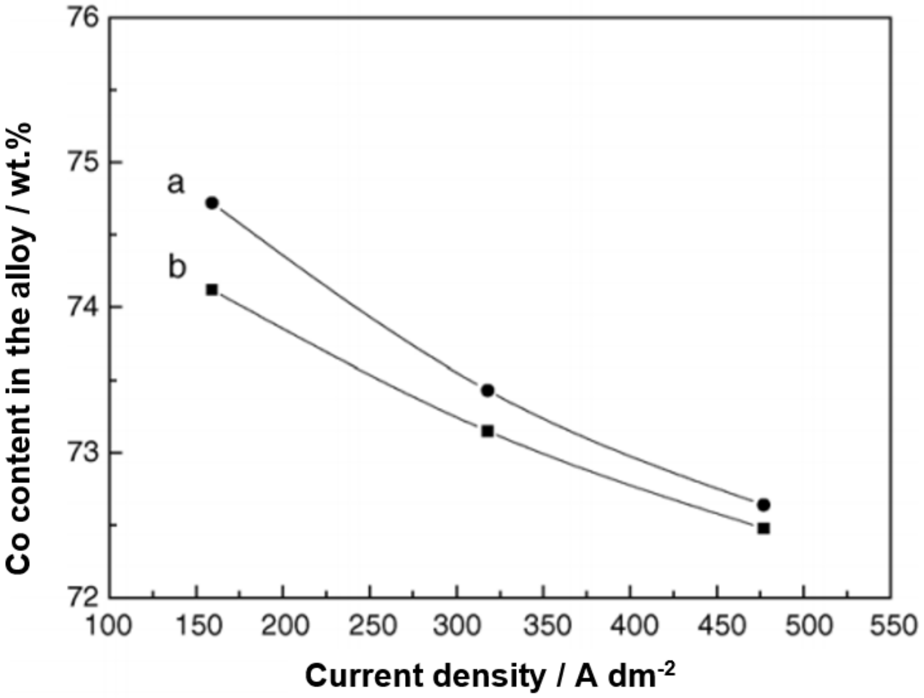

Fig. 2.25. Effect of cathodic current density on the composition of Ni–Co deposits produced by jet electrodeposition (a) without saccharin and (b) with 2.5 g dm^{-3} saccharin [20].

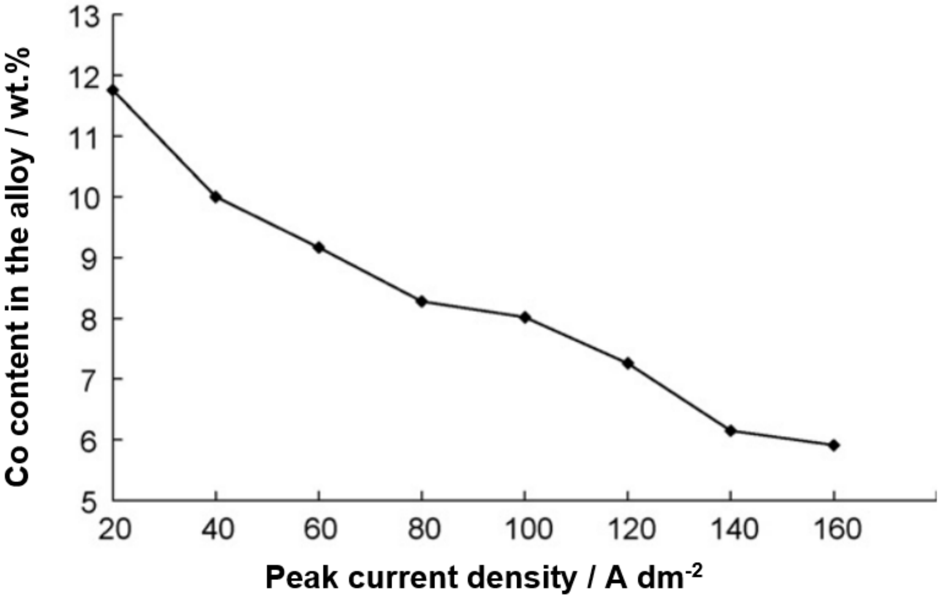

Fig. 2.26. Effect of peak current density on the composition of Ni–Co deposits produced by pulse electrodeposition [37].

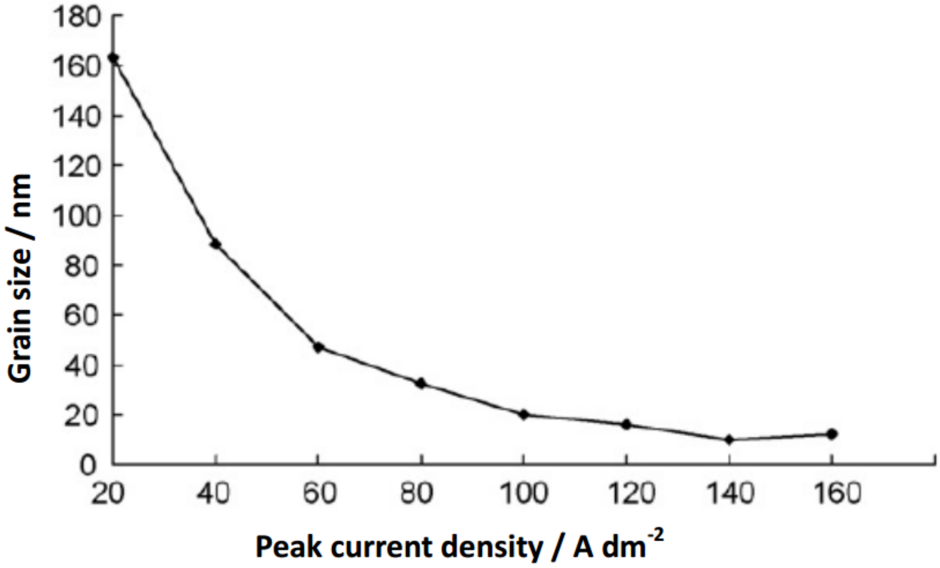

Fig. 2.27. Effect of peak current density on the grain size of Ni–Co deposits produced by pulse electrodeposition [37].

2.4.2.3 Additives

Organic compounds (e.g. saccharin, sodium lauryl sulphate and BD) in small concentrations can be added to Ni-Co plating baths to modify the process of electrocrystallisation for a variety of purposes, including obtaining a mirror-like surface, increasing hardness and improving corrosion resistance [145]. The influences of additives on the composition, grain size, microstructure and properties of Ni-Co deposits have been investigated.

Compared with the coatings obtained from additive-free baths, the addition of saccharine resulted in a slight reduction of cobalt content due to the increasing deposition overpotential as shown in Fig. 2.25, which was in favour of activation-controlled nickel deposition [20]. Li et al. [38] also reported that by increasing the concentration of saccharin from 3 g dm^{-3} to 5 g dm^{-3} in electrolytes containing 6 g dm^{-3} cobalt sulphate, the cobalt content slightly decreased from 8.5 wt.% to 6.1 wt.%. The deposits from saccharin-containing baths inevitably contain certain amounts of sulphur impurities [38, 146], which may lead to poor ductility [147] and corrosion resistance [133].

Saccharin has a significant effect on the reduction of grain size. The grain size of 5 wt.% Co-Ni alloys decreased from 44 nm for the coating plated from the additive-free bath to 22 nm by adding 1 g dm^{-3} saccharin [141]. At the same time, the texture changed from (200) to (111) and the surface was much smoother. These changes led to higher microhardness and improved anti-corrosion properties of coatings. The addition of sodium lauryl sulphate led to a compact surface morphology, which improved the corrosion resistance. Marikkannu et

Table 2.5. Properties of Ni-Co deposits plated from acetate baths in 5% NaCl solution with different additives [145]

Additives	Concentration / g dm^{-3}	E_{corr} vs. SCE / mv	i_{corr} / 10^{-4} A cm^{-2}	Microhardness / HV
Plain	0	-449	3.5	349
Saccharin	2	-501	1.7	385
Dextrin	3	-648	2.5	365
Coumarin	1	-684	2.3	375
Formaldehyde	2$^{\#}$	-460	1.9	379
Glycine	2	-593	3.1	371
Crotonaldehyde	2$^{\#}$	-585	2.9	367

$^{\#}$ ml dm^{-3}

al. [145] investigated the role of additives in Ni-Co deposits from acetate baths containing any one of the additives, including saccharin, dextrin, coumarin, formaldehyde, glycine and crotonaldehyde. As shown in Table 2.5, it was found that the corrosion resistance of Ni-Co deposits with the cobalt content of approximately 45% in 5% NaCl solution was improved by adding these additives. Furthermore, the microhardness of these coatings was higher compared with the deposits from the additive-free bath. Additionally, saccharin and formaldehyde gave the mirror bright deposits.

2.4.2.4 Bath Agitation and Temperature

The common methods used for bath agitation include air agitation, impeller [148], magnetic stirrer [24], high speed jet [20] and peristaltic pump [149] in order to keep the flow of electrolytes at a constant and stable level. The increase of bath agitation results in higher cobalt content in deposits because of the reduction of the diffusion layer thickness accompanied by the rising metal ion concentration in it. As discussed above, diffusion-controlled cobalt is preferentially deposited [20]. In addition, the agitation can increase the limiting current density J_{lim} by reducing the thickness of the diffusion layer δ by the equation [144]:

$$J_{lim} = nFD_i\frac{c_b - c_i}{\delta} \tag{2.9}$$

where F is the Faraday constant; D_{i} is the diffusivity of metal ions, C_b is the metal ion concentration in bulk solution and C_i is the concentration at the interface. The increasing current density results in higher overpotential to produce coatings with finer grain size.

Qiao et al. [20] reported that with the increase of temperature from 30 °C to 50 °C, the cobalt content in Ni-Co deposits decreased from 77 wt.% to 69 wt.%, because higher temperature favoured the activation-controlled Ni deposition.

2.4.3 Approaches to Reduce Internal Stress

Wang et al. [18] reported that the internal stress of Ni-Co electrodeposits depended on the cobalt content. As shown in Fig. 2.28, the internal stress gradually decreased with increasing cobalt content. It changed from compressive to tensile as the cobalt content exceeded 49 wt.%. A very high tensile stress in the range of 40-70 MPa was obtained for the cobalt-rich coatings. The high internal stress can result in lower ductility and adhesion between coatings and substrates [150], which restricts their applications for anti-wear and anti-corrosion purposes. In order to decrease the internal stress, the Ni-Co coatings with continuously graded composition and structure were produced by controlling the cobalt ions concentration in baths during the electrodeposition process [18]. As shown in Fig. 2.29, the composition gradually changed from the Ni-rich region to the Co-rich region as the function of distance from the interface between the coating and the AISI-1045 steel substrate. The phase structure gradually changed from fcc to hcp with thickness due to the increase of cobalt content. As shown in Fig. 2.28, the internal stress of the graded Ni-Co coating was reduced to a much lower level (approximately 5 MPa). The graded coating with the microhardness of 550 HV exhibited a much lower coefficient of friction and improved wear resistance compared with ungraded nickel-rich coatings. Based on it, Wang et al. [151] developed nanocrystalline Ni-Co/CoO graded coatings by a subsequent cyclic thermal oxidation at 300 °C and quenching. As shown in Fig. 2.30, the graded Ni–Co/CoO coating consisted of six sublayers with a different composition varying from 0 to 81 wt.% Co. The coating was approximately 100 µm thick with an oxide layer of 3-4 µm. Compared to as-deposited Ni-Co graded coatings, the graded Ni–Co/CoO coating exhibited significantly enhanced wear resistance under dry sliding conditions and improved corrosion resistance in both 10 wt.% NaOH and 3.5 wt.% NaCl solutions due to the formation of a dense and protective oxide layer.

2.5 Electrodeposited Nanocrystalline Co-Ni-P Coatings

Ternary Co-Ni-P films (from 10 nm to 10 µm thick) have generally been used as magnetic recording media due to their unique magnetic properties [52, 53]. Furthermore, they

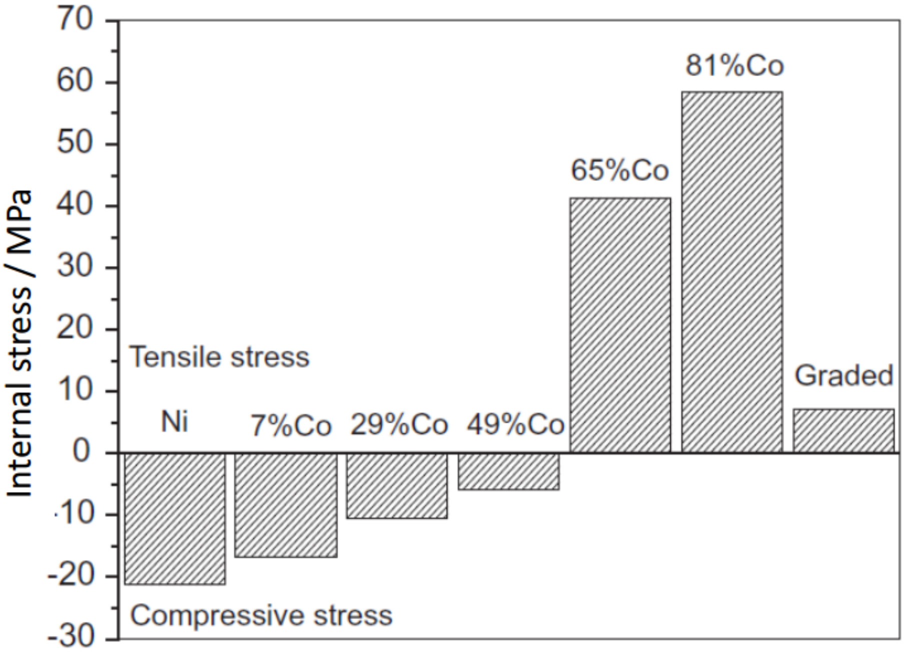

Fig. 2.28. Variation of internal stress with cobalt content in Ni–Co alloys [18].

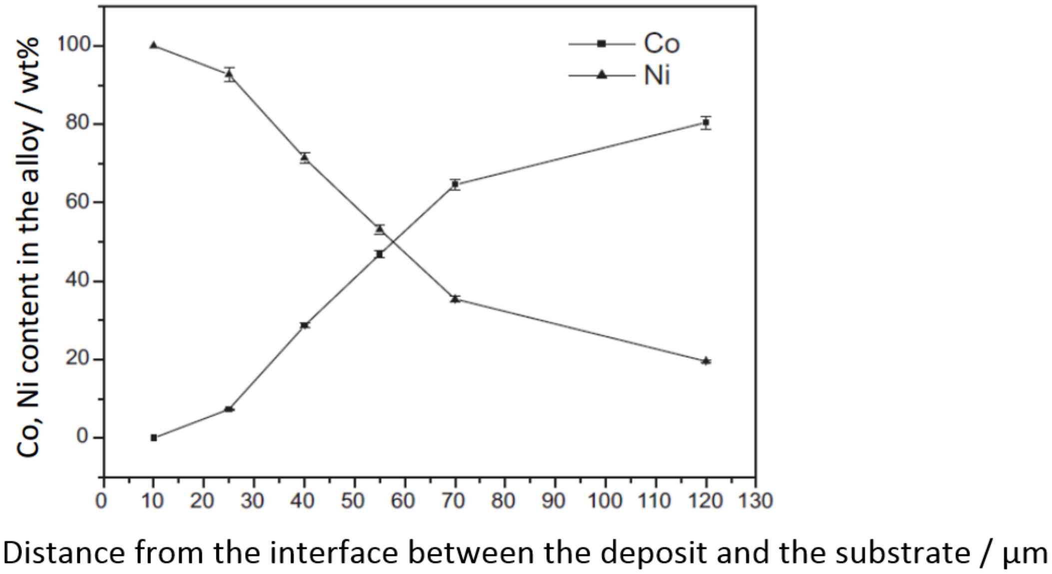

Fig. 2.29. Distribution of cobalt content with thickness of graded Ni–Co nanocrystalline alloys [18].

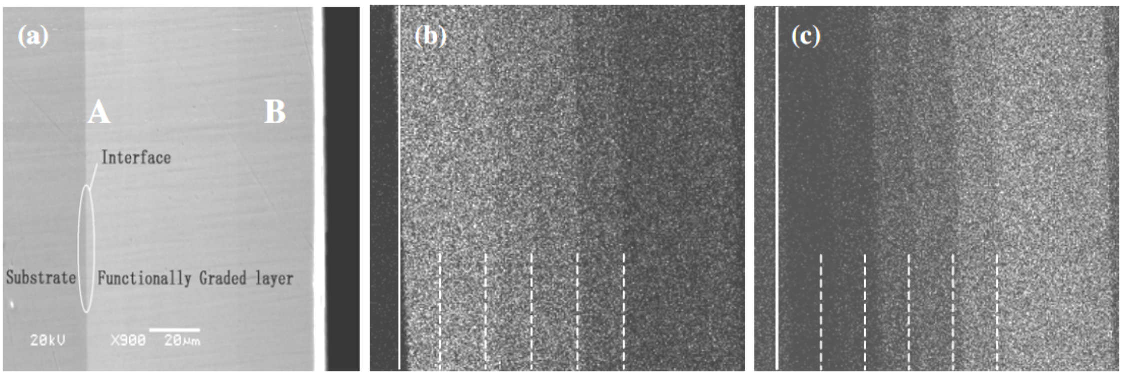

Fig. 2.30. (a) Scanning electron microscopy (SEM) image of the cross section of the graded Co-Ni/CoO coating with corresponding (b) nickel and (c) cobalt element distribution maps [151].

are also applied as anti-corrosion coatings [54], microwave absorptive materials [55] and electrocatalytic materials for water electrolysis [56].

2.5.1 Electrodeposition of Co-Ni-P Coatings

Co-Ni-P films have been produced by electroless deposition [52, 152, 153] and electrodeposition [54, 57–59, 154]. Compared to electroless plating, the electrodeposition has the advantages, including lower cost, faster plating rate and more stable baths. The ternary alloys can be electroplated from a sulphate bath [154], a modified Watts bath [54], a Brenner type chloride bath [57, 58, 155], or a sulphamate bath [59] on copper or mild steel substrates. Sodium hypophosphite is the common source of phosphorus. The electrodeposition of Co and Ni from the sulphate solution as well as the codeposition of phosphorus follows the reactions below [60]:

$$\mathrm{Ni^{2+} + 2e^- \rightarrow Ni} \tag{2.10}$$

$$\mathrm{Co^{2+} + 2e^- \rightarrow Co} \tag{2.11}$$

$$\mathrm{H_2PO_2{}^- + e^- \rightarrow P + 2OH^-} \tag{2.12}$$

Simultaneous hydrogen evolution can be described by:

$$\mathrm{2H^+ + 2e^- \rightarrow H_2} \tag{2.13}$$

2.5.2 Properties and Effect of Experimental Parameters

It has been found that properties of the Co–Ni–P coatings strongly depend on their thickness, composition and microstructure, which are determined by the chemical species present in plating baths and the operating conditions employed. The effects of electroplating variables on the properties of the films are discussed as follows.

2.5.2.1 Composition

Parente et al. [54] reported that the cobalt content in deposits increased with the increase of cobalt ion concentration in the modified Watts bath. However, there was no obvious relationship between phosphorus content and Co^{2+} concentration. Similar phenomenon has been found for the ternary alloys plated from chloride baths [156]. For the Co-Ni-P coatings plated from the electrolyte containing 100 g dm^{-3} cobalt sulphate ($Co^{2+}/(Co^{2+}+Ni^{2+})=0.31$), the cobalt content in deposits increased from 26 at.% to 40 at.% as the current density increased from 30 mA cm^{-2} to 120 mA cm^{-2}. Meanwhile, the P content decreased from 18 at.% to 14 at.%. Kirkwood et al. [157] studied the effect of current density varying from 1 mA cm^{-2} to 50 mA cm^{-2} on the composition of the Co-Ni-P coatings plated from Brenner-type chloride baths with the ratio $Co^{2+}/(Co^{2+}+Ni^{2+})$ of 0.5 at the solution pH of 3.0. As shown in Fig. 2.31, the cobalt content was approximately 72 at.% at a current density of 1 mA cm^{-2}. It jumped to 85 at.% as the current density increased to 5 mA cm^{-2}. Afterwhich, it gradually decreased to around 55 at.% with the corresponding increase of nickel content. The phosphorus content varied slightly around 12 at.%. However, Lew et al. [154] reported that the cobalt content of Co-Ni-P coatings plated from sulphate baths with the same $Co^{2+}/(Co^{2+}+Ni^{2+})$ ratio at the same solution pH initially varied between 52 at.% and 54 at.% with the current density increasing from 5 mA cm^{-2} to 10 mA cm^{-2} , and then the cobalt content gradually decreased to approximately 40 at.% at the current density of 20 mA cm^{-2}, lower than the content of nickel. The P content remained constant at around 6 at.%. In contrast, Djokić et al. [60] found that the P content decreased as the current density increased from 10 mA cm^{-2} to 30 mA cm^{-2} for the Co-Ni-P deposits from modified Watts baths ($Co^{2+}/(Co^{2+}+Ni^{2+})=0.43$) at the pH of approximately 1.5. The authors explained the phenomenon by the increase of partial current for hydrogen evolution reaction due to the increase of current density. According to Eq. (2.13), it led to an increase in the pH near the electrode surface. Therefore, the codeposition of phosphorus was hindered (Eq. (2.12)). Although the results are not consistent depending on different plating baths, it has been accepted that the composition

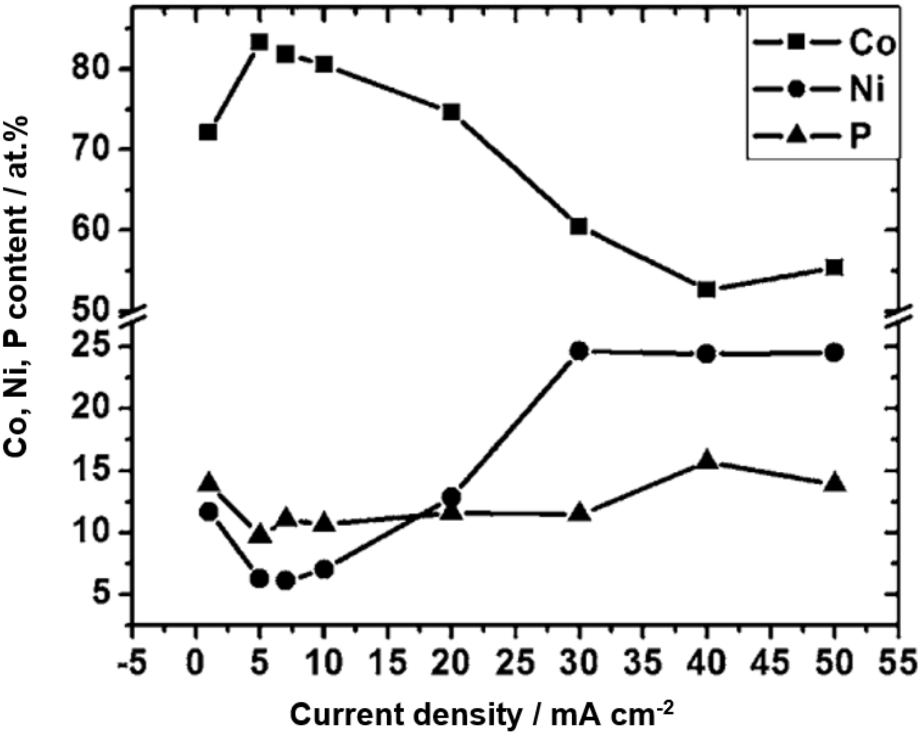

Fig. 2.31. Relationship between current densities and the composition of Co-Ni-P coatings plated from Brenner-type chloride baths with the $Co^{2+}/(Co^{2+}+Ni^{2+})$ ratio of 0.5 at the solution pH of 3.0 [157].

of Co-Ni-P coatings can be tailored by applying different current densities. Additionally, the $Co^{2+}/(Co^{2+}+Ni^{2+})$ ratio [54], the concentration of sodium hypophosphite [156, 158], the solution pH [154] and the bath temperature [59] have an effect on the composition of the alloys.

As shown in Table 2.6, the Co-Ni-P alloy exhibited a gradient in composition with thickness [60]. With the increase of the thickness up to 100 µm, the cobalt content was around 70 wt.%, while the nickel content decreased from 21 wt.% to 10 wt.%. The content of phosphorus continuously increased from 11 wt.% to 20 wt.%. The mechanism is not clear and relevant research is presented in Chapter 7.

2.5.2.2 Microstructure

As shown in Fig. 2.32, the surface morphology changed from a fine granular structure for the Ni-P alloy to a columnar structure for Co-Ni-P coatings plated from a modified Watts bath with the current density of 20 mA cm^{-2}. As the cobalt content increased from 26 at.% (Fig. 2.32(b)) to 40 at.% (Fig. 2.32(c)), this characteristic became more accentuated. Kirkwood et al. [58] reported the Co-Ni-P coating with a thickness of 10 nm was deposited from chloride baths using the current density of 7 mA cm^{-2} , and the

Table 2.6. Composition evolution with thickness for the Co-Ni-P coatings plated from modified Watts baths with the current density of 10 mA cm^{-2} [60]

Thickness / µm	Co content / wt.%	Ni content / wt.%	P content / wt.%
1	68	21	11
50	71	16	13
95	71	11	18
99	70	10	20

morphology was influenced by the substrate as shown in Fig. 2.33(a). In contrast, a 10 µm thick alloy shown in Fig. 2.33(b) exhibited the granular morphology. The composition of the coating was 82 at.% Co-7 at.% Ni-11 at.% P. However, the composition with varying thickness was not given.

The cross-sectional morphologies of Co-Ni-P coatings plated from chloride baths with the different current densities are shown in Fig. 2.34 [58], and the corresponding compositions are shown in Fig. 2.31. The 80 at.% Co-8 at.% Ni-12 at.% P alloy deposited at the current density of 7 mA cm^{-2} exhibited a columnar structure. With increasing current density, the structure changed to a laminar form accompanied by the decrease of cobalt content. The mechanism of the transition of growth mode was not clear.

With low phosphorus content (< 10 at.%), Co-Ni-P films exhibited the transition from fcc structure, to a mixture of hcp and fcc, and then hcp structure depending on the cobalt content [59, 154], which is similar to the structure evolution of Ni-Co alloys mentioned in Section 2.4.1.1. The XRD peaks became broader due to the inclusion of phosphorus atoms as the cobalt content increased [154]. The as-deposited Co-Ni-P coatings with the phosphorus content more than 12 at.% exhibited an amorphous structure [53, 57, 60]. Sankara Narayanan et al. [53] suggested that the presence of phosphorus prevented the nucleation of nickel/cobalt phase and resulted in the amorphous structure. As shown in Fig. 2.35, the broad peak indicated the amorphous structure of the as-deposited ternary alloy. After heat treatment at 500 °C in a N_2 atmosphere for 1 h, the sample showed a typical spectrum of a crystalline structure containing Ni_xP_y phases [54].

Djokić [60] reported that the XRD pattern taken from the top surface of the Co-Ni-P coating exhibited an amorphous structure, while its counterpart taken from the bottom exhibited two sharp peaks (indicating crystalline structure) and one broad peak (indicating amorphous structure) as shown in Fig. 2.36. The change in the structure was related to the

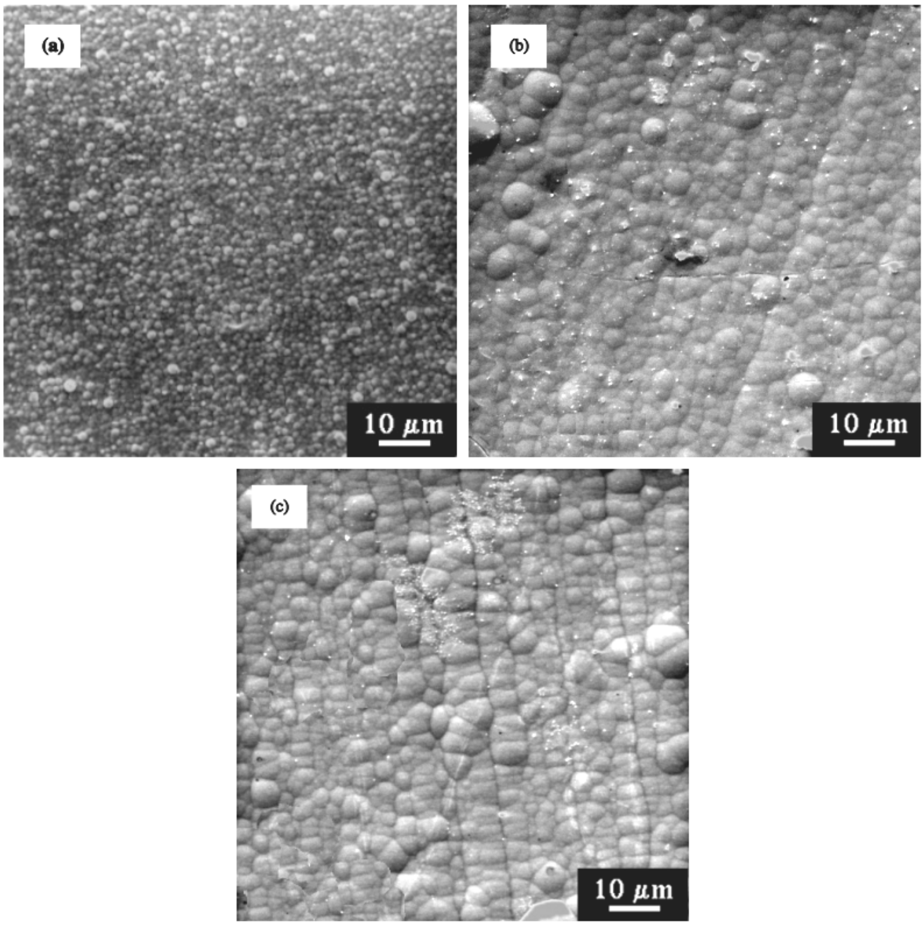

Fig. 2.32. Surface morphologies of (a) 83 at.% Ni-17 at.% P, (b) 26 at.% Co-60 at.% Ni-14 at.% P and (c) 40 at.% Co-46 at.% Ni-14 at.% P coatings deposited from modified Watts baths with the current density of 20 mA cm^{-2} [54].

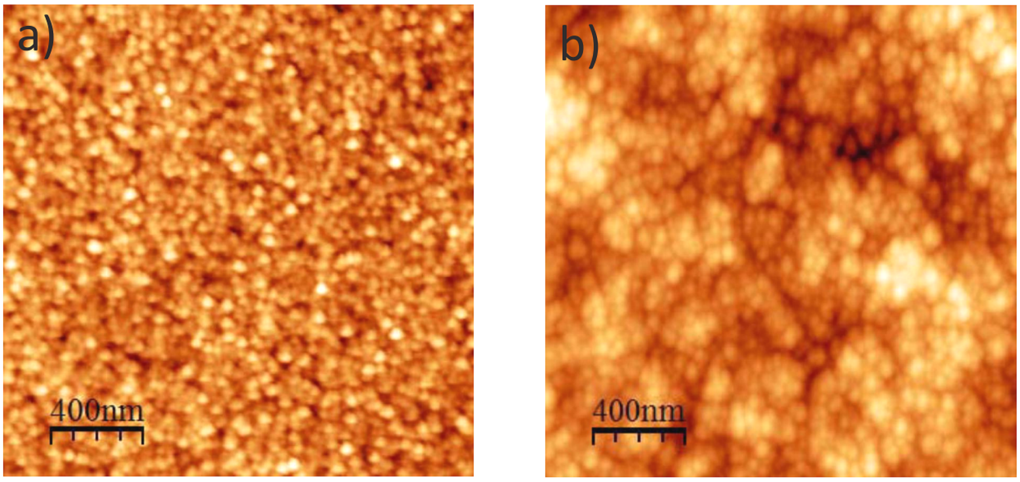

(a) (b)

Fig. 2.33. Surface topographies of Co-Ni-P coatings deposited from chloride baths using the current density of 7 mA cm^{-2} for the thickness of (a) 10 nm and (b) 10 µm [58].

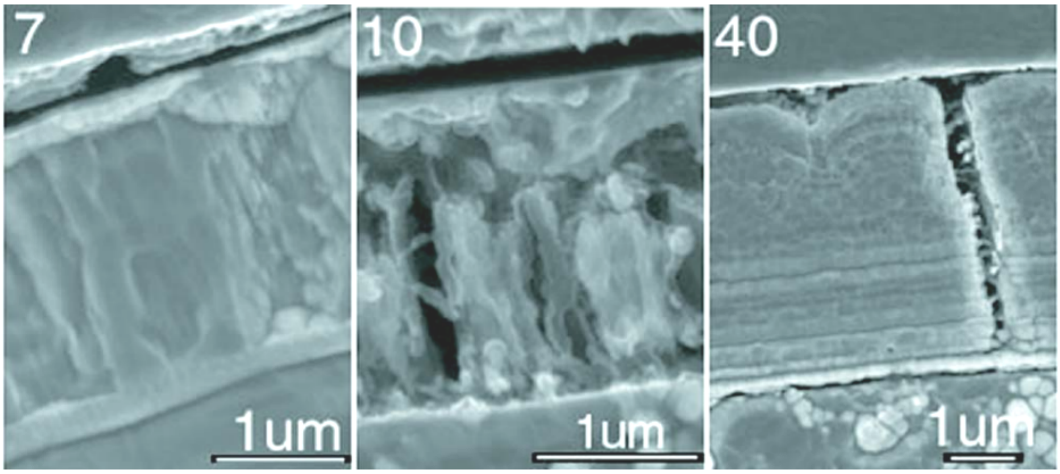

Fig. 2.34. SEM cross-sectional morphologies of Co-Ni-P coatings deposited from chloride baths with different current densities indicated by the numbers at the top left of each figure in mA cm^{-2} [157].

phosphorus content in the coatings. As mentioned above, the phosphorus content increased with the increasing thickness of the deposit. At the beginning of electrodeposition, lower phosphorus content led to the mixture of crystalline and amorphous structure, which transformed to the amorphous structure due to higher phosphorus on the top surface. However, the author did not mention the exact composition of the top and bottom parts of the coating. Although it was suggested that the phosphorus content controlled the transition, its mechanism needs to be clarified.

2.5.2.3 Microhardness

Cojocaru et al. [59] reported that the as-deposited 28 at.% Co-68 at.% Ni-4 at.%P coating plated from a sulphamate bath had the highest microhardness (630 HV) compared to other cobalt-rich coatings obtained with lower bath temperature. The latters were found to be fragile and easy to detach from substrates. Emerson et al. [159] studied the effect of urea on the microhardness of Co-Ni-P coatings with the phosphorus content less than 1 at.% plated from chloride baths. The 83.4 at.% Co-16 at.% Ni-0.6 at.%P coating deposited from an urea-free bath had the hardness of 432±1 HV, which decreased to 366±1 HV by increasing the urea concentration to 5 g dm^{-3}. However, the addition of urea increased the coercivity of the films.

2.5.2.4 Corrosion Resistance

Parente et al. [54] evaluated the effect of structure on the corrosion behaviour of Ni-P coatings with 17 at.% phosphorus and 40 at.% Co-46 at.% Ni-14 at.%P coatings before

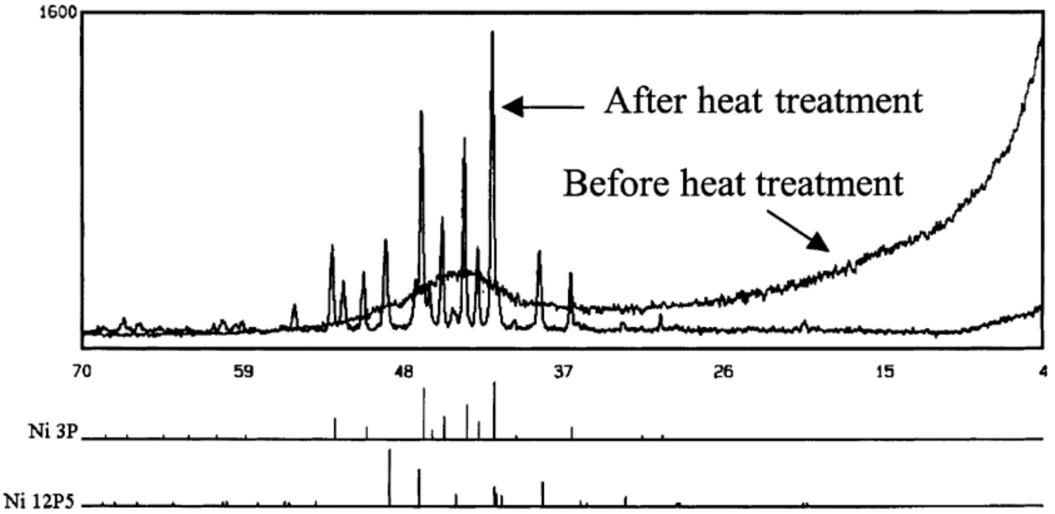

Fig. 2.35. XRD patterns of 55 at.% Co-26 at.% Ni-19 at.% P coatings before and after heat treatment at 500 °C in a N_2 atmosphere for 1 h [54].

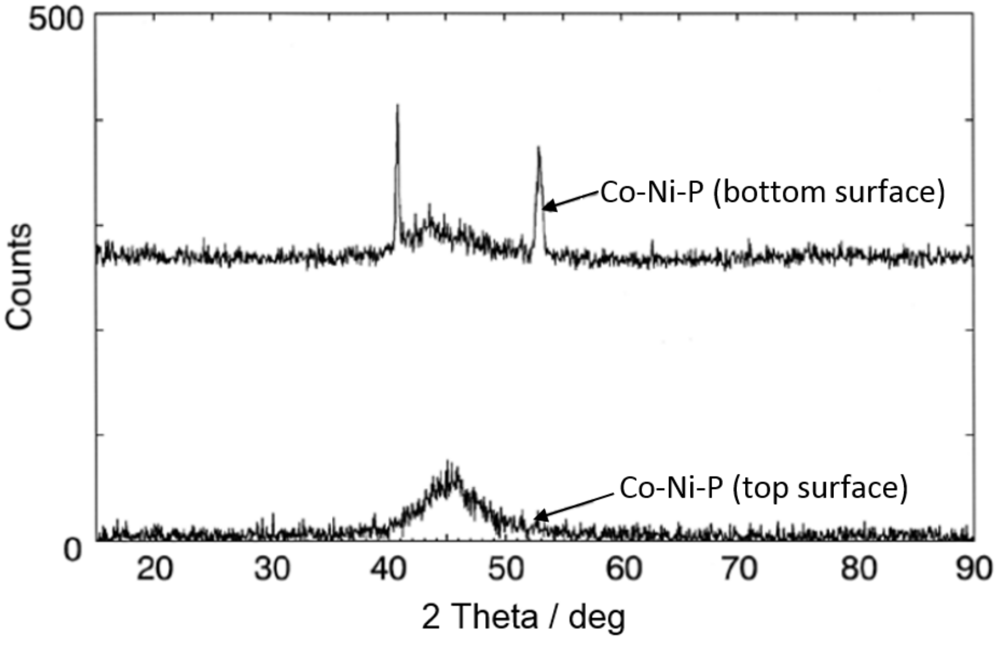

Fig. 2.36. XRD pattern of as-deposited Co-Ni-P coatings (77 wt.% Co-13 wt.% Ni-10 wt.%P) with the thickness of 100 µm: (a) top surface and (b) bottom surface: peak at about 41° (Co_2P), peak at about 53° (CoP_3) [60].

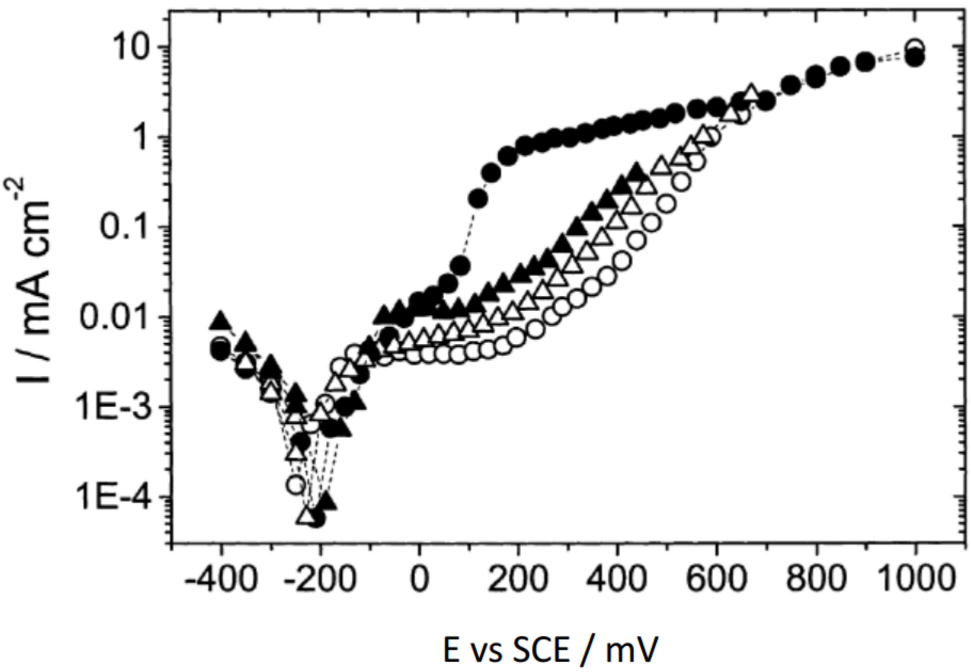

Fig. 2.37. Effects of the structure on the polarisation behaviour of Ni-17 at.% P (amorphous (△) and crystalline (▲)) and 40 at.% Co-46 at.% Ni-14 at.% P alloys (amorphous (○) and crystalline (●)) in 0.1 M NaCl [54].

and after heat treatment at 500 °C in a N_2 atmosphere for 1 h. As shown in Fig. 2.37, both as-deposited Ni-P and Co-Ni-P alloys with amorphous structure exhibited the current plateau due to the formation of passive films in 0.1 M NaCl solutions. The current plateau of the amorphous Co-Ni-P coating was broader than that of the amorphous Ni-P alloy, indicating the improvement of corrosion resistance by the presence of cobalt. It might be associated with a more efficient passivation process. However, the mechanism is not clear. Structure modification produced by heat treatment can affect the polarisation behaviour. For Ni-P alloys, the crystalline structure led to narrower passivation plateau and a shift of the curve to higher current values. The plateau of the crystalline Co-Ni-P coating almost disappeared and a steady current increase was observed with the increase of polarisation, suggesting the non-protective nature of the passive film. The amorphous structure can provide better corrosion resistance to both Ni-P and Co-Ni-P coatings. Raicheff and Zaprianova [160] suggested that it might be due to the homogenous amorphous structure without grain boundaries, dislocations and other surface defects.

2.6 Summary

The chapter began with an introduction of surface engineering techniques, and subsequently discussed the current promising alternatives to hard chromium, including thermal spray, vapour deposition, functional trivalent chromium plating, electroless nickel-based coatings, non-chromium electrodeposited nanocrystalline coatings and welding facing methods. These substitutes have demonstrated the potential to provide equivalent or better properties for anti-wear and/or anti-corrosion purposes. However, they also have some limitations in specific applications as discussed above. Among them, non-chromium electrodeposition is the preferred substitute from the point of view of the balance between cost and performance. The recent studies on electrodeposited nickel, cobalt, Ni-Co binary alloys and Co-Ni-P ternary coatings have been summarised. Further research is needed in order to better understand the microstructure and properties of Ni-Co coatings and to develop novel Co-Ni-P coatings with improved wear and corrosion resistance to replace hard chromium. The key questions are listed as follows and provide the basis for setting the specific aims and objectives of the present research project.

(1) The recent findings showed that electrodeposited nanocrystalline cobalt-rich Ni-Co alloys with hcp structure exhibited better tribological properties than Ni and nickel-rich Ni-Co coatings. It may be associated with the participation of tribofilms and debris. However, no studies on the role of tribofilms and the microstructure of debris have been reported. More experimental work needs to be conducted in order to further understand the tribological behaviours of Ni-Co coatings with different cobalt contents. Besides, the corrosion resistance of Ni-Co alloys in 3.5 % NaCl solutions needs to be examined to compare with that of hard chromium.

(2) It has been reported that cobalt-rich nanocrystalline coatings with improved tribological properties were difficult to be electrodeposited onto steel substrates due to high internal stress. Current methods (developing graded coatings and applying pulse current waveforms) have the limitations including complex equipment and high cost. Moreover, the microhardness needs to be further increased. Thus in the present research single layer Ni-Co coatings with high cobalt content are synthesised on steel substrates by selecting and optimising electrolyte additives. The effect of additives on the microstructure and properties needs to be studied.

(3) Although the effect of baths with different nickel salts on mechanical properties has been studied on coarse-grained (grain size of the order of microns) nickel coatings, a lack of comparable investigation on nanocrystalline Ni-Co coatings was observed. Besides,

numerous mechanisms have been proposed to explain the deviation from the conventional Hall-Petch relationship for nanocrystalline materials when the grain size is reduced to a threshold value. However, none of them focused on the influence of pores on the surface, which are common for electrodeposited nanocrystalline coatings. Deviation from the Hall-Petch relationship may derive from the porosity, which needs to be clarified.

(4) Considering that no studies on the tribological properties of Co-Ni-P coatings has been reported in literature, one of the objective of the present research is to design experiments to deposit Co-Ni-P coatings for anti-wear applications. The novel ternary alloys are expected to combine the lubricity of cobalt-rich Ni-Co coatings and the precipitation hardening found in Ni-P alloys to exhibit comparable or superior wear resistance to hard chromium. Meanwhile, anti-corrosion properties need to be characterised.

(5) The composition gradient and microstructure changes from nanocrystallie to amorphous structure with thickness of Co-Ni-P coatings have been reported in literature, However, the mechanism and the influencing factor are not clear, which need to be investigated in the present research.

Chapter 3

Experimental Methodologies

3.1 Electrodeposition

Ni-Co and Co-Ni-P coatings were electroplated on mild steel substrates by direct current provided by a TTi QL355T power supplier. The bath temperature was maintained at 45 °C by a Grant LTD6G water bath. The electrodeposition arrangement is shown in Fig. 3.1. The solution was continuously stirred by a PTFE-coated magnetic stirrer bar (6 mm diameter × 30 mm length) at 200 rpm. The anode for electrodeposition was a pure Ni sheet (purity 99.99%) with the thickness of 1 mm supplied by Advent Research Materials Ltd. (Oxford, UK). The cathode substrate was 3 mm thick AISI 1020 mild steel with the hardness of 115 HV. The chemical composition of as-received mild steel sheets is given in Table 3.1. Both the anode and cathode were cut by a guillotine in sizes of 80 mm × 10 mm or 80 mm × 30 mm to produce larger coatings for potentiodynamic polarisation measurements. Prior to deposition, the substrate was ground with 320, 800 and 1200 grit SiC paper followed by cleaning to remove any remaining contamination. Subsequently, the substrate was immersed into a 10 % hydrochloric acid bath for 20 s to be activated, and then rinsed by distilled water. As shown in Fig. 3.2, the anode and the substrate were fixed to the holders by polyester tape supplied from Cole-Parmer, UK, leaving an area of 40 mm × 10 mm or 40 mm × 30 mm on one side to be exposed to electrolytes. During the deposition, the cathode was held parallel to the anode with an interelectrode gap of 25 mm. The chemicals in the electrolytes include nickel sulphate hexahydrate $NiSO_4 \bullet 6H_2O$ ($\geq$99.0%), nickel chloride hexahydrate $NiCl_2 \bullet 6H_2O$ ($\geq$98%), cobalt sulphate heptahydrate $CoSO_4 \bullet 7H_2O$ ($\geq$99%), sodium hypophosphite monohydrate $NaH_2PO_2 \bullet H_2O$ ($\geq$99%), boric acid H_3BO_3 ($\geq$99.5%), sodium chloride NaCl ($\geq$99.5%), saccharin $C_7H_5NO_3S$ ($\geq$99%) and BD $HOCH_2C{\equiv}CCH_2OH$ (99%). Sodium dodecyl sulph-

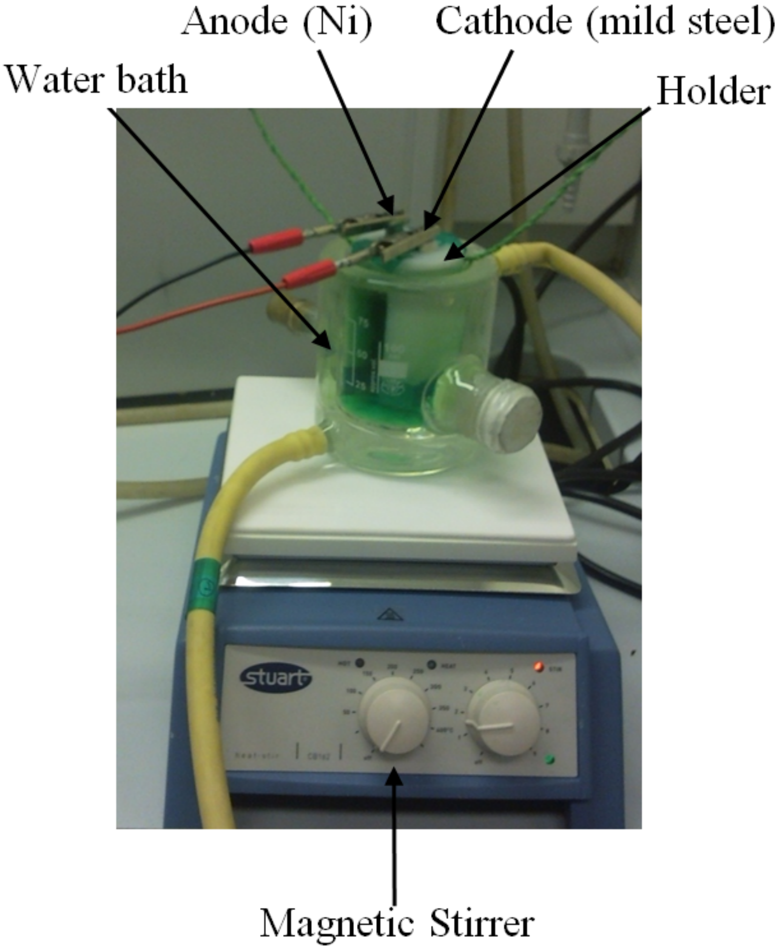

Fig. 3.1. Electrodeposition arrangement for Ni-Co and Co-Ni-P plating. Details of the electrode holders is given in Fig. 3.2.

ate $CH_3(CH_2)_{11}OSO_3Na$ ($\geq$99.0%) was added as a surfactant to lower surface tension between the electrodes and the electrolyte in order to control surface pitting. All the chemicals were from Sigma-Aldrich, UK. The electrolyte compositions can be tailored to meet different functional requirements. In order to further improve the wear and corrosion resistance, the as-deposited Co-Ni-P coatings were subsequently annealed in air at 200 °C, 300 °C, 400 °C and 500 °C for 1 h, respectively. As a comparison, hard chromium coatings with the thickness of 40±5 µm were electrodeposited on AISI 1020 mild steel substrates from a conventional chromic acid bath (CrO_3 160 g dm^{-3}, H_2SO_4 2.5 g dm^{-3}) containing 2 g dm^{-3} $CrCl_3$ with a direct current of 100 A dm^{-2} at 45 °C.

Table 3.1. The chemical composition of as-received AISI 1020 mild steel sheets [161].

Substrate	Element / wt.%					
	C	Si	Mn	P	S	Cr
AISI 1020	0.20	0.189	0.45	0.04	0.050	0.16

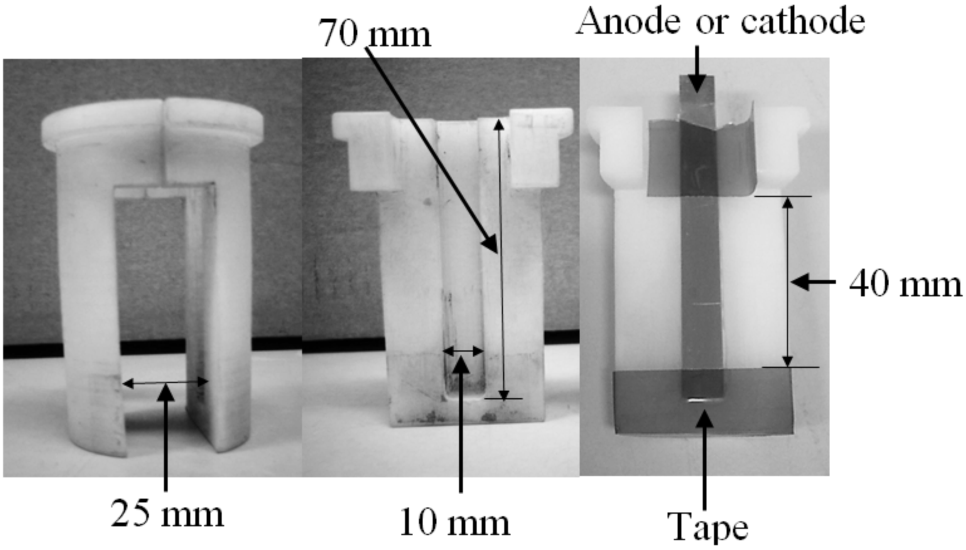

Fig. 3.2. Electrode holders for electrodeposition of Ni-Co and Co-Ni-P coatings.

3.2 Characterisation Techniques

The characterisation techniques used in the research are listed in the Table 3.2. These test methods include microscopy, spectroscopy, mechanical measurements, tribological tests and electrochemical tests.

3.2.1 SEM and Energy Dispersive X-ray Spectroscopy (EDS)

SEM allows observation of the surface morphology on a nanometre to micrometre scale by collecting the imaging signals from secondary and backscattered electrons generated by a finely focused electron beam. The latter can form the image which shows the distribution of elements or compounds within the top micron of the sample. Both qualitative identification and quantitative elemental information can be analysed from characteristic X-radiation emitted as a result of bombardment [162]. A JEOL JSM 6500 SEM was employed for the observation of surface morphologies of as-deposited coatings, as well as worn surface and wear debris. The resolution can attain 1.5 nm at 15 kV, while the magnification is up to 500,000 ×. The composition was studied by an Oxford Instruments INCA 300 EDS equipped in the SEM operating at 15 kV. Backscattered electrons images (BEI) were obtained by detecting the contrast between areas with different compositions.

3.2.2 TEM

TEM was applied in bright field images, dark field images and selected area electron diffraction (SAED) mode to determine the grain size as well as its distribution and to

Table 3.2. Summaries of characterisation techniques

Technique	Principle	Information Gained
SEM&EDS	Secondary electrons, backscattered electrons, characteristic x-rays produced from the interaction of the electron beam with atoms at or near the surface	Surface morphology, distribution of elements or compounds, qualitative and quantitative elemental information
FIB	A gallium ion source employed to remove the material by sputtering	Cross-sectional images
AFM	Conversion of the tip deflection of the repulsive force between the tip and the sample into three-dimensional images of the sample surface	Surface morphology and surface roughness
TEM	Interaction of the electrons transmitted through the specimen	Grain size and its distribution, phases and crystallographic texture
XRD	Diffraction effect of X-ray depended on the periodic structure of material	Average grain size, texture, microstrain, internal stress
Microhardness test	Vickers microhardness indenter	Microhardness
Reciprocating wear test	Reciprocating sliding of steel ball against the surface of samples	Coefficient of friction, wear rate
Potentiodynamic polarisation	Measurement of polarisation behaviour by continuously scanning the potential while monitoring the current response	Corrosion potential, corrosion current density

discriminate phases and crystallographic texture, which can be achieved by changing lens strength or deactivating a lens. A TEM image is formed from the interaction of the electrons transmitted through the specimen [163]. A JEOL JEM 3010 operating at 300 kV with a resolution of 0.21 nm is used to observe thin coatings, which are prepared using twin jet polishing by an electrolyte comprising 10 % perchloric acid, 15 % acetic acid and 75 % methanol at a temperature of -40 °C with a voltage of 30 V [44]. The TEM equipped with Oxford Instruments INCA 100 EDS was employed to study the composition of collected wear debris powders, which were dispersed in absolute alcohol by ultrasonic agitation. A droplet of each suspension was dried on a copper grid with carbon film for subsequent characterisation.

3.2.3 Focused Ion Beam (FIB) Technology

In order to study the morphology change along the growth direction, the cross section of Co-Ni-P coatings was characterised by FIB 1540 XB CrossBeam, Leo/Zeiss. The samples were tilted to align the surface normal to the gallium ion beam. The material can be removed by sputtering, which allows the cross-sectional analysis [164].

3.2.4 Atomic Force Microscopy (AFM)

Agilent 5500 AFM in contact mode is used in the present work to investigate the surface morphology and surface roughness of coatings. It requires neither a vacuum environment nor any special sample preparation. As shown in Fig. 3.3, the AFM tip attached to the end of a cantilever probes the surface of the sample, causing the cantilever to bend, which changes the position of the laser spot reflected on to a position-sensitive photodiode detector. The tip deflection or the repulsive force between the tip and sample can be recorded and then converted into three-dimensional images of the sample surface [165]. A line profile (5 µm) with height measurements was used to determine the surface roughness. Five measurements were performed on each coating.

3.2.5 XRD

A Bruker GADDS diffractometer with a Cu Kα radiation is used to determine the texture of coatings. Besides, the average grain size can be estimated by applying the Scherrer equation [167]:

$$d = \frac{0.9\lambda}{B cos\theta} \tag{3.1}$$

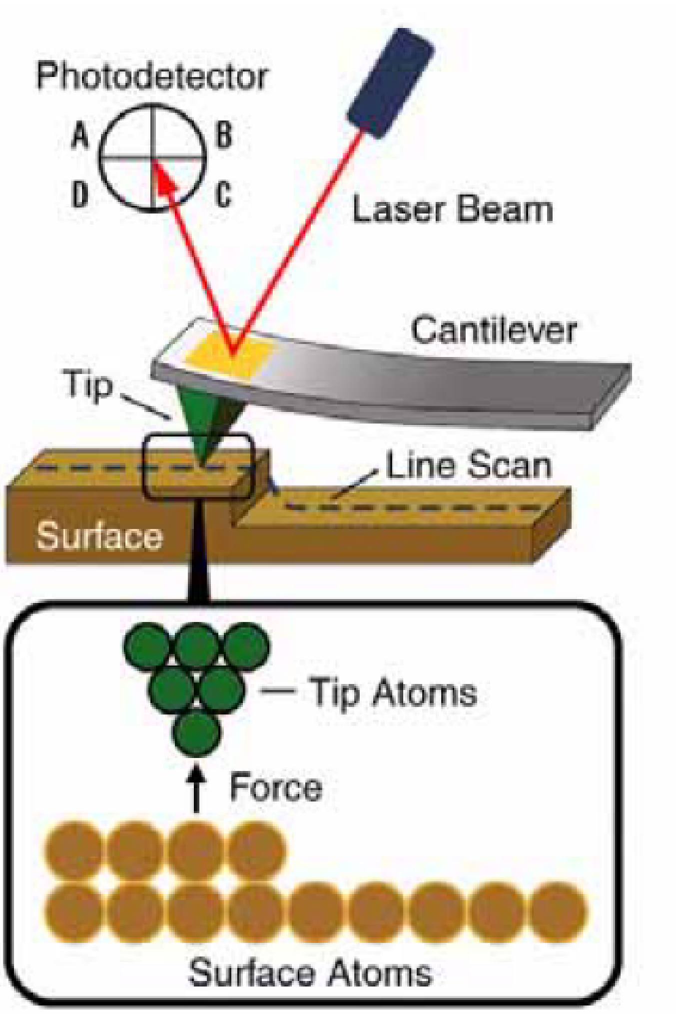

Fig. 3.3. Principles of AFM [166].

where λ is the wavelength of the X-rays (0.154 nm for Cu Kα radiation) and θ is the Bragg diffraction angle. B is the full width at half maximum height of the peak. However, the peak broadening in the XRD pattern may also be caused by internal strain (B_ε). If the microstrain of coatings is not negligible, the grain size calculated by the Scherrer equation is not accurate. A detailed discussion is given in Chapter 5.

The internal stress was measured by a computer programmed Philips X-Pert X-ray diffractometer by the $sin^2\psi$ technique. The d-spacing $d_{\phi\psi}$ of the (hkl) lattice plane can be described as [168]:

$$d_{\phi\psi} = \left(\frac{1+\nu}{E}\right)\sigma d_0 sin^2\psi + (1 - \frac{2\nu}{E}\sigma)d_0 \tag{3.2}$$

where E and ν are the Young's modulus and the Poisson's ratio, respectively. σ is the internal stress, d_0 is the lattice spacing at stress-free condition, and ψ is the off-axis angle with respect to the sample surface normal. The internal stress is related to the slope and the intercept of the plot of $d_{\phi\psi}$ versus $sin^2\psi$. In the present research, the d-spacing measurements were conducted on the (111) plane at ψ ranging from -17° to 17°.

3.2.6 Microhardness Measurement

The hardness of deposits was measured by a MHT-1 Vicker's microhardness indenter under an applied load of 100 g for 15 s. The indenter is a diamond pyramid. An average of five measurements was carried out on each coating. The depth of indentation is less than 3 µm.

3.2.7 Reciprocating Wear Tests

The friction and wear behaviour was tested on a reciprocating TE-77 tribometer (Phoenix, UK) (Fig. 3.4) under the dry sliding conditions with relative humidity of 40-50% at room temperature (25 °C) in air. An AISI-52100 stainless steel ball (diameter 6 mm) with a hardness of 700 HV was used as the counter body. The surface roughness (R_a) of the pin is 0.48 µm. The calibrated load was 14 N corresponding to initial Hertzian contact pressure of 1.12 GPa (see Appendix: A) with the sliding frequency of 1 Hz. The sliding stroke was 2.69 mm, while the average sliding speed was 5.38 mm/s. The total sliding time was 25 min. The friction force was measured by a piezo electric transducer and recorded automatically during the tests. The coefficient of friction was calculated by dividing the friction force by the normal load. The average dynamic friction for the entire test was obtained. The line profile of wear tracks was measured by an Alicona InfiniteFocus Real3D surface profilometer after wear tests, which illustrated the shape and depth of wear tracks for calculating the wear volume. The average cross sectional area was determined by the profiles at five locations perpendicular to the wear track. The wear volume was calculated by multiplying the worn cross sectional area by the sliding stroke (i.e. the wear track length). Subsequently, the specific wear rate (K) in $\mathrm{mm}^3\ \mathrm{N}^{-1}\ \mathrm{m}^{-1}$ can be calculated following the equation:

$$K = \frac{V}{SN} \tag{3.3}$$

where V is the wear volume in mm^3, S is the total sliding distance in metres and N is the normal load in newtons [151]. Additionally, morphology and composition of the worn surface and debris were studied by SEM/TEM and EDS.

3.2.8 Electrochemical Measurements

Potentiodynamic polarisation technique allows the measurement of polarisation behaviour by continuously scanning the potential while monitoring the current response [169]. The electrochemical measurement was carried out in a three-electrode cell as shown in Fig. 3.5. The electrodeposited coating (40 mm × 30 mm × 3 mm) was used as the working electrode (exposed area: 2 mm diameter circular spot), with a platinum counter electrode and a SCE as reference electrode. Polarisation experiments were performed in 3.5% NaCl solution at room temperature with an AUTOLAB PGSTAT30 potentiostat/galvanostat system at sweep rate of 50 mV/s from cathodic to anodic currents in a range of ± 1000 mV vs the rest potential. The scan rate was slow enough to ensure that the capacitance remains fully charged during the experiment. The corrosion potential and the corrosion current density were obtained with the Tafel extrapolation method from potentiodynamic polarisation curves. Additionally, electrodeposition potential-time dependence for the electrodeposition of Co-Ni-P coatings was obtained by the potentiostat/galvanostat system with a nickel counter electrode (40 mm × 10 mm × 1 mm) and a SCE reference electrode.

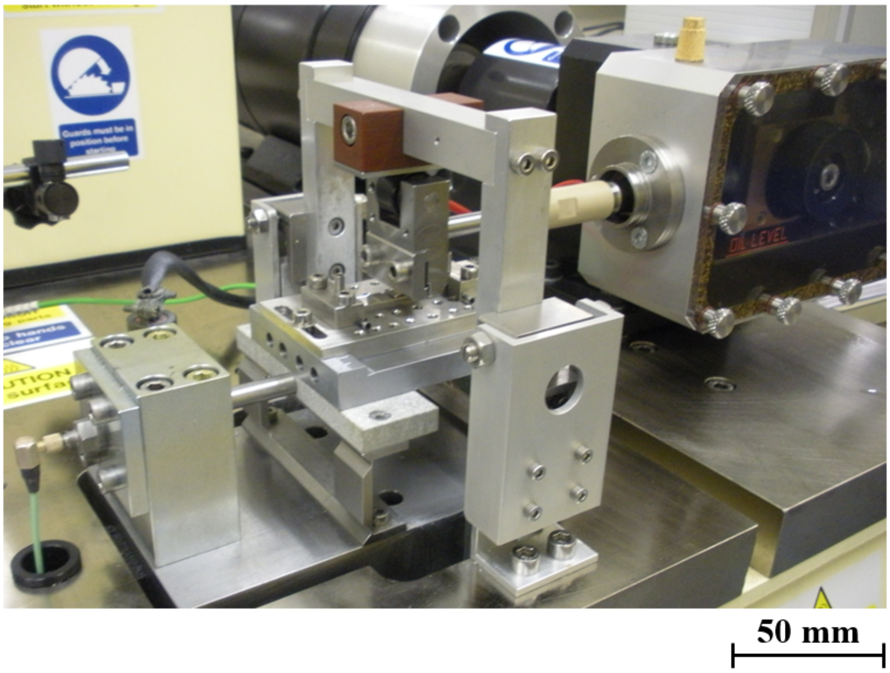

(a)

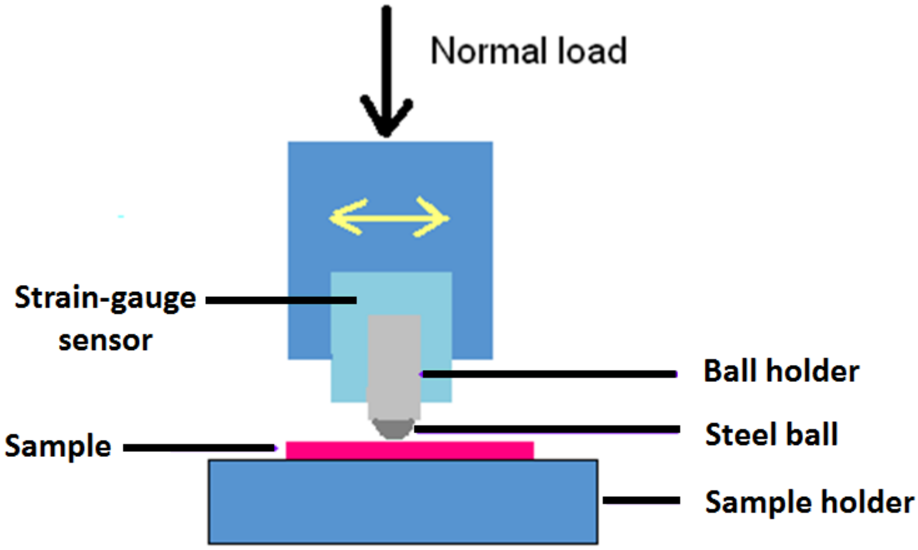

(b)

Fig. 3.4. (a) Image of reciprocating TE-77 tribometer and (b) its schematic diagram.

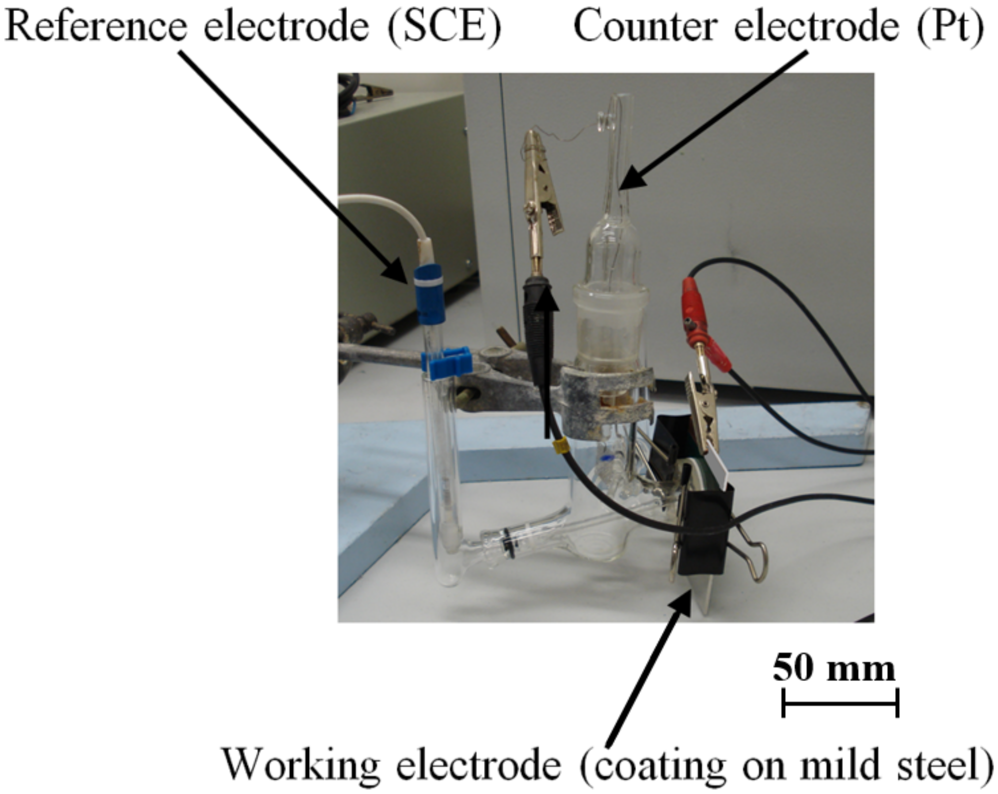

Fig. 3.5. Three-electrode cell employed for potentiodynamic polarisation measurements.

Chapter 4

Wear and Corrosion Properties of Nanocrystalline Ni-Co Coatings with Different Cobalt Contents

4.1 Introduction

Recent studies have shown that electrodeposited microcrystalline cobalt-rich Ni-Co alloys with hcp structure exhibited better tribological properties than Ni and nickel-rich Ni-Co coatings. However, the microhardness needs to be further increased by reducing the grain size. Furthermore, there is a lack of understanding regarding the role of tribofilm and debris on the varied tribological behaviours. Therefore, in the present research, the electrodeposited nanocrystalline Ni-Co coatings with different cobalt contents were prepared. Chemical and structural characterisations of the worn surfaces and debris were conducted by surface analysis techniques. The mechanisms of the tribofilm formation are discussed. Additionally, the corrosion behaviour of Ni-Co coatings in 3.5% NaCl solution has been investigated.

4.2 Experimental Details

Nanocrystalline Ni-Co coatings were electrodeposited from the all-sulphate baths containing varying concentrations of cobalt sulphate. The electrolytic bath composition is listed in Table 4.1. The current density was 4 A dm^{-2}. The electroplating process lasted for 1 h and produced a coating of 50±5 µm thickness.

The surface of the as-deposited Ni-Co coating was investigated by AFM. The composi-

Table 4.1. Bath composition of electrodeposited nanocrystalline Ni-Co coatings.

Chemicals	Concentration / g dm^{-3}
$CoSO_4 \bullet 7H_2O$	0-200
$NiSO_4 \bullet 6H_2O$	200
H_3BO_3	30
NaCl	20
Saccharin	2
BD	0.5

tion of the alloys was studied by SEM equipped with EDS. The hardness and tribological properties of deposits were characterised. Additionally, the morphology and composition of the worn surfaces, debris and the counter body were studied by SEM and EDS. The microstructure of debris was characterised by TEM equipped with EDS. Polarisation experiments were performed in 3.5% NaCl solution. The procedure is described in Chapter 3.

4.3 Results

4.3.1 Composition and Microstructure

Fig. 4.1 shows that the cobalt content in the coatings gradually increased with the increase of the $Co^{2+}/(Co^{2+}+Ni^{2+})$ ratio in the electrolytes. The cobalt content of the coatings was always higher than expected from the bath composition reference line. The anomalous deposition has been explained by the formation and adsorption of metal hydroxide cations on the cathode surface [142]. As the adsorption ability of $Ni(OH)^+$ is lower than $Co(OH)^+$, the formation of a $Co(OH)^+$-enriched film on the substrate surface inhibits the adsorption of $Ni(OH)^+$ and consequently the reduction of cobalt is promoted.

The AFM images of Ni-Co coatings deposited from electrolytes having different concentrations of cobalt sulphate are shown in Fig. 4.2. The coatings deposited from the bath with 0, 40 and 100 g dm^{-3} $CoSO_4$ (Fig. 4.2a-c) are characterised by their smooth surface with a low value of roughness (R_a=15-30 nm). The deposits from the bath containing 150 g dm^{-3} $CoSO_4$ exhibits the same dense and smooth surface morphology. In contrast, 83 at.% Co-Ni alloy produced from the bath with 200 g dm^{-3} $CoSO_4$ has the lens-shaped structure with relatively high surface roughness (R_a=190 nm) as shown in Fig. 4.2(d).

XRD patterns of the as-deposited Ni-Co coatings with different cobalt content are shown in Fig. 4.3. The pure nickel coating (shown in Fig. 4.3(a)) exhibits fcc lattice with (111) growth orientation, indicated by the strong peak at $2\theta \approx 44.4°$. As the cobalt content increases, the intensity of the peak at $2\theta \approx 51.8°$ corresponding to $(200)_{\mathrm{fcc}}$ planes gradually decreases. The 75 at.% Co-Ni alloy has only one peak at $2\theta \approx 44.4°$, which is consistent with the spacing of $(0002)_{\mathrm{hcp}}/(111)_{\mathrm{fcc}}$. At a deposit content of 83 at.% cobalt, the texture of the coating changes to $(10\bar{1}0)_{\mathrm{hcp}}$, indicated by the peak at $2\theta \approx 42°$ as shown in Fig. 4.3(g). With the increase of cobalt content, the phase structure of Ni-Co alloys changes from fcc to hcp structure, which is consistent with previous findings [22, 24]. Compared to the XRD patterns (Fig. 2.17) of Ni-Co deposits reported by Wang et al. [24], two main differences have been observed. Firstly, the pure nickel shown in Fig. 2.17(a) has a strong $(200)_{\mathrm{fcc}}$ texture. And the intensity of the peak corresponding to $(200)_{\mathrm{fcc}}$ planes for the coatings with 7 wt.% and 27 wt.% cobalt (Figs. 2.17(b, c)) is higher than that of the deposits with the similar composition in the present research (Fig. 4.3(b, c)). Secondly, the peaks shown in Fig. 4.3 are much broader. The grain size calculated by the Scherrer equation (Eq. (3.1)) of the present samples is in the range of 12-19 nm. The cobalt-rich coatings have slightly smaller grain size than their nickel-rich counterparts. However, the sharp peaks shown in Fig. 2.17 indicate a larger grain size between 200 nm to 5 µm. The differences can be attributed to the addition of additives in the present research. Saccharin can promote the formation of $(111)_{\mathrm{fcc}}$ texture, which is the most close-packed plane in the fcc structured Ni lattice. Additionally, the additives (saccharin and BD) can modify electrocrystallisation and lead to the grain refinement. The effect of additives is discussed in Chapter 5.

4.3.2 Microhardness

Fig. 4.4 presents the microhardness as the function of cobalt content in the coatings. The microhardness of pure Ni coating is 580 HV. It remains in the range of 470-500 HV as the cobalt content increases up to 82 at.%. However, it drops sharply to 270 HV for the 83 at.% Co-Ni coating deposited from the electrolyte with 200 g dm^{-3} $CoSO_4$. The low microhardness can be attributed to the existence of pores introduced by the loose lens-shaped microstructure [170] as shown in Fig. 4.2(d).

4.3.3 Friction and Wear Behaviour

As shown in Fig. 4.5, the coefficient of friction against a steel ball under unlubricated conditions varies in the range of 0.45-0.5 as the cobalt contents in the coatings increase from 0% to 58 at.%. It is reduced to approximately 0.25 when the cobalt content exceeds 70 at.%. The variation of the wear rate as the function of cobalt content is shown in

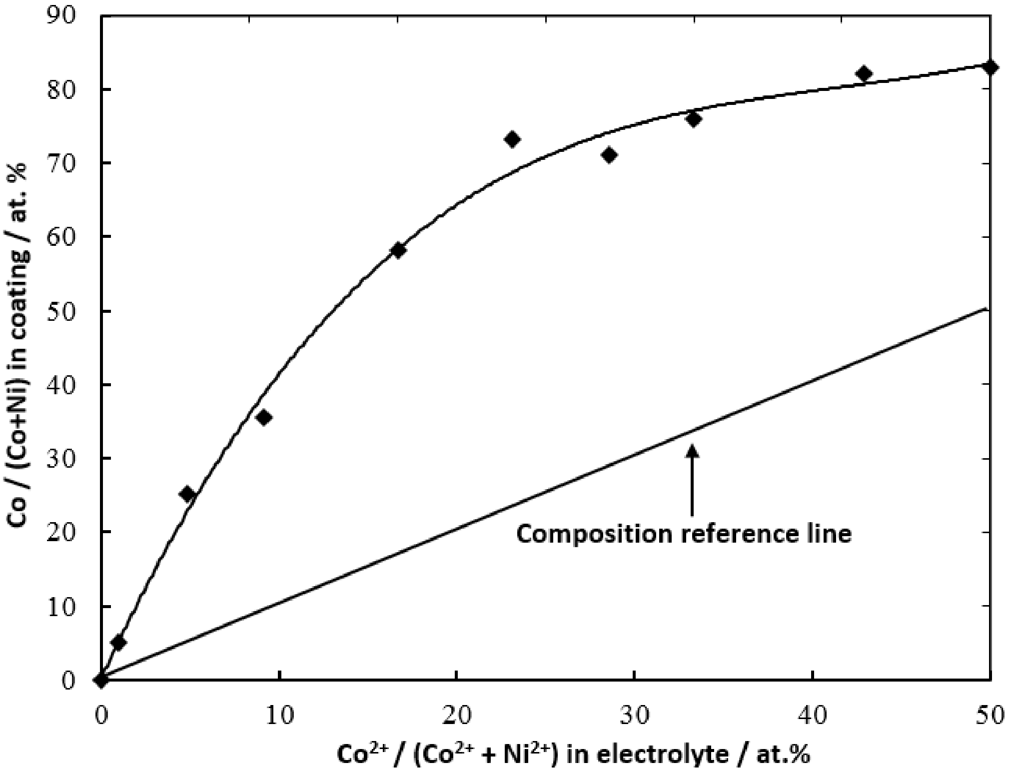

Fig. 4.1. Variation of cobalt content as the function of the ratio of $Co^{2+}/(Co^{2+}+Ni^{2+})$ in the electrolyte. The composition was determined by EDS.

Fig. 4.6. The wear rate of a pure nickel coating with higher hardness is relatively low (approximately 1.2×10^{-4} mm^3 N^{-1} m^{-1}). It increases to approximately 2.5×10^{-4} mm^3 N^{-1} m^{-1} with 5 at.% cobalt and remains constant until it reaches the highest value for a cobalt content at 58 at.%. With a further increase of the cobalt content, the wear rate decreases to 2.2×10^{-5} mm^3 N^{-1} m^{-1}, which is comparable to that of hard chromium coatings under the same conditions. Fig. 4.7 shows the wear track of the 83 at.% Co-Ni coating is much narrower and shallower compared with those of the pure nickel coating and Ni-58 at.% alloy. The worn surface of the pure nickel coating is shown in Fig. 4.8 (a). As listed in Table 4.2, the highlighted area A in the wear track contains a high amount of iron (20 at.%), which was transferred from the pin because of the severe adhesive wear. Fig. 4.9 shows the EDS spectrum of the worn surface compared to that of the as-deposited pure nickel coating (Fig. 4.9(a)). The low-energy peaks O-K$_a$ and the peaks representing Fe were found in the spectrum of the worn surface as shown in Fig. 4.9(b). It is worth mentioning that the analysis depth of EDS at the accelerating voltage of 15 kV is approximately 1 µm. Although the EDS results of the worn surface may contain the signal from the coating beneath the tribofilm, the presence of oxygen and iron confirms the existence of the tribofilm because none of them was detected in the as-deposited coatings. Most of

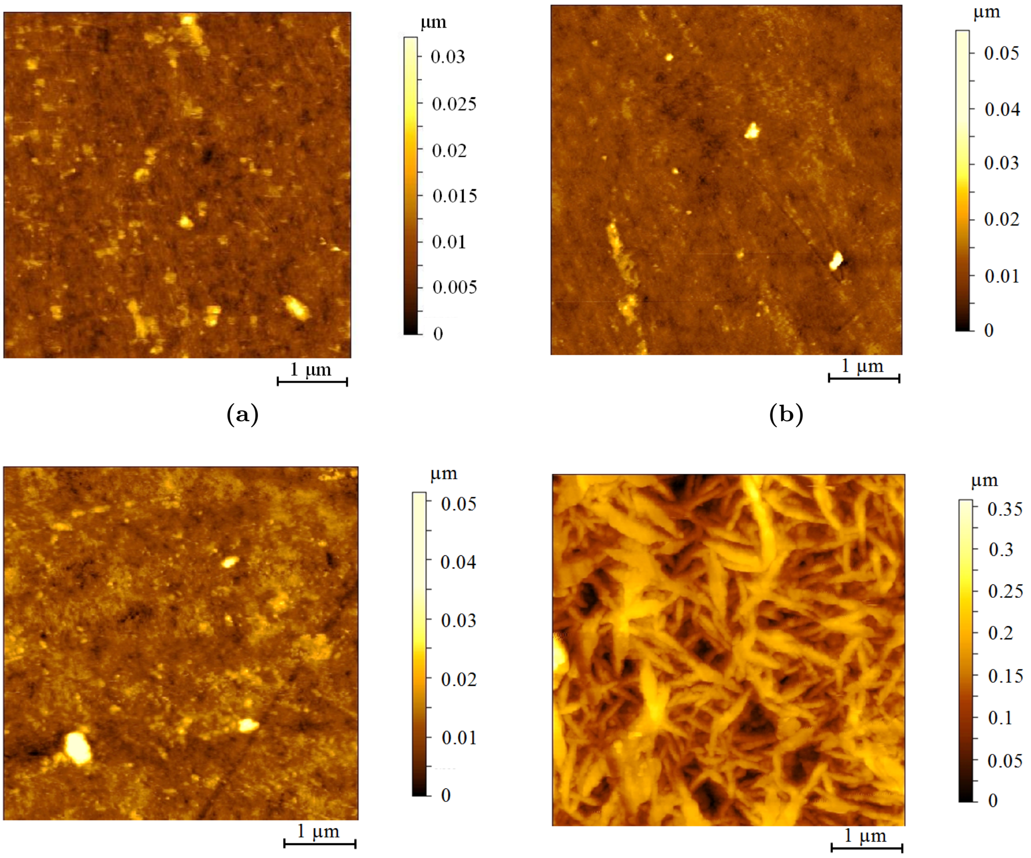

(a) **(b)**

(c) **(d)**

Fig. 4.2. AFM images of as-deposited Ni-Co alloys: (a) pure Ni, (b) 58 at.% Co-Ni from the electrolyte with 40 g dm^{-3} $CoSO_4$, (c) 75 at.% Co-Ni from the electrolyte with 100 g dm^{-3} $CoSO_4$ and (d) 83 at.% Co-Ni from the electrolyte with 200 g dm^{-3} $CoSO_4$.

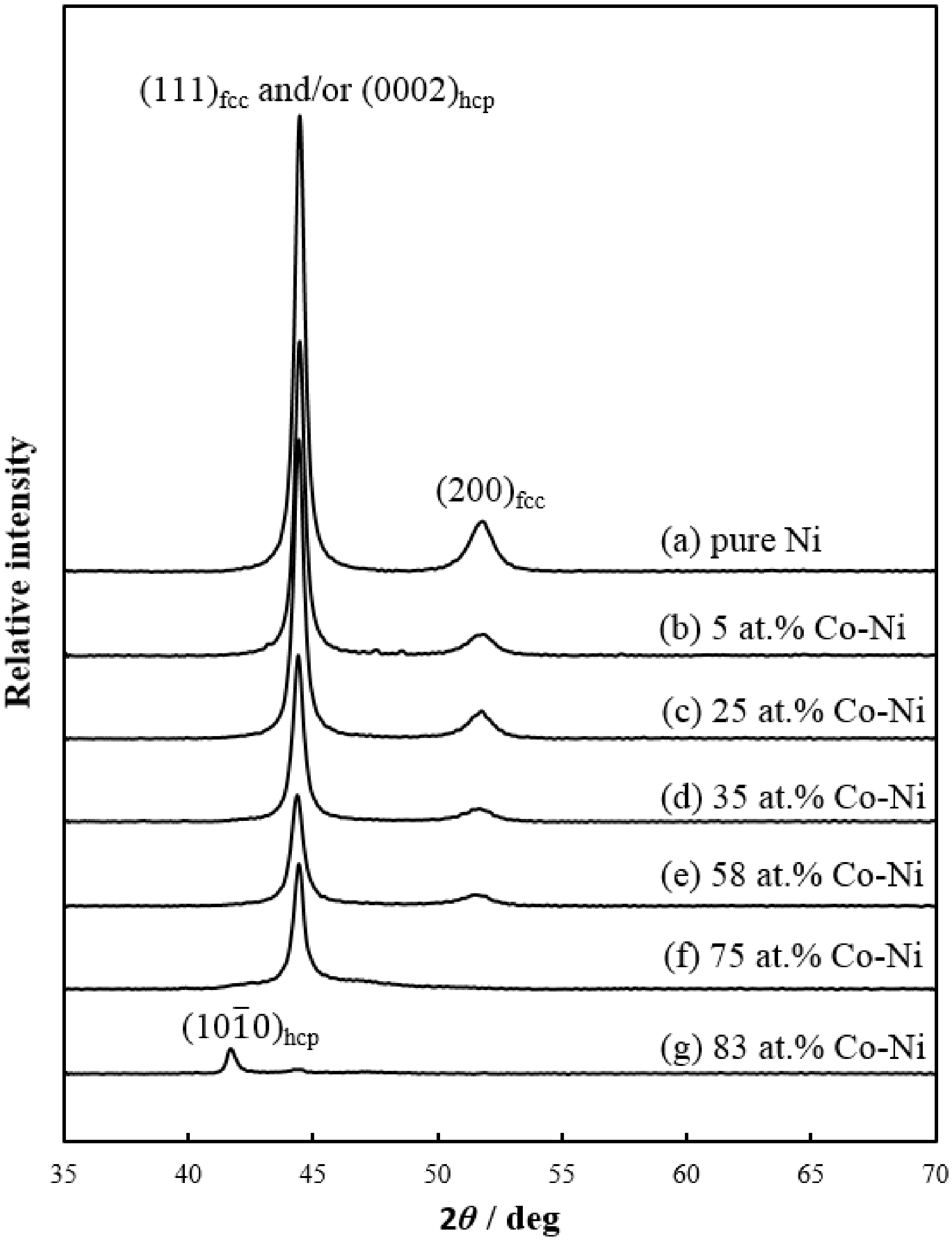

Fig. 4.3. XRD patterns of as-deposited Ni-Co alloys with different cobalt contents.

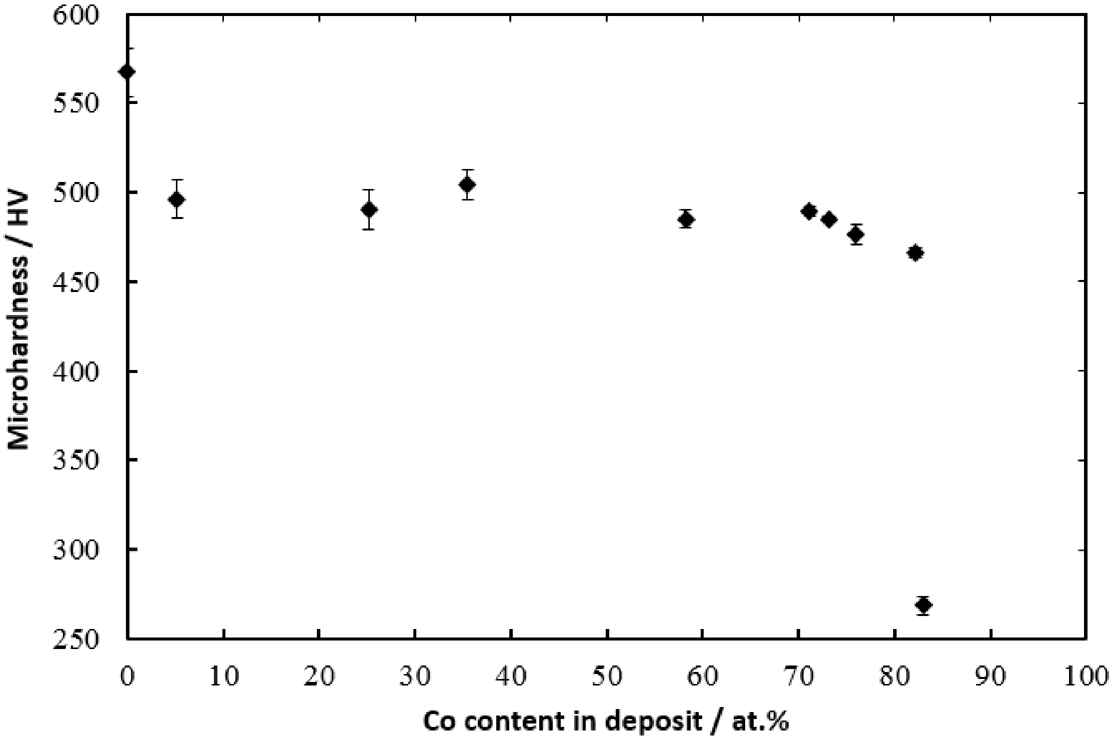

Fig. 4.4. Variation of microhardness with cobalt content. Vertical bars above each mean data point indicate the standard deviation.

the fine debris particles were found at the end of the wear track, and some of them are attached on the wear scar (Fig. 4.8(a)). The debris contains 40 at.% O, 50 at.% Ni and 10 at.% Fe as listed in Table 4.3. The worn surface of the 58 at.% Co-Ni (Fig. 4.8(b)) exhibits three different areas: the smooth area B containing 7 at.% Fe, the transition zone with superficial cracks on it, and the area covered by the debris, which contains 2 at.% Fe. There is more debris on the worn surface. The reason why the 58 at.% Co-Ni coating has a higher wear rate than the Ni-rich coatings can be attributed to its higher internal stress. As more cobalt atoms are accommodated in the fcc lattice of nickel, a larger mismatch of the lattices (0.4%) generates higher internal stress, which causes cracks and more debris on the worn surface shown in Fig. 4.8(b). As the cobalt content increased to 75 at.%, no iron was detected either on the smooth area C as shown in Fig. 4.8(c) or in the much reduced amounts of debris. The EDS spectra shown in Fig. 4.10 confirms that no tribofilm containing oxygen and iron was formed. The worn surface (Fig. 4.10(b)) has similar composition as the as-deposited coating (Fig. 4.10(a)). The 83 at.% Co-Ni coating shows the least debris on the worn track (Fig. 4.8(d)), which corresponds to the lowest wear rate among the present samples. The asperities of the as-deposited coating shown in Fig. 4.8(d) was uniformly removed to form the smooth wear scar. Iron was not found either in the area D or in the debris. Furthermore, there is no evidence of oxidation during

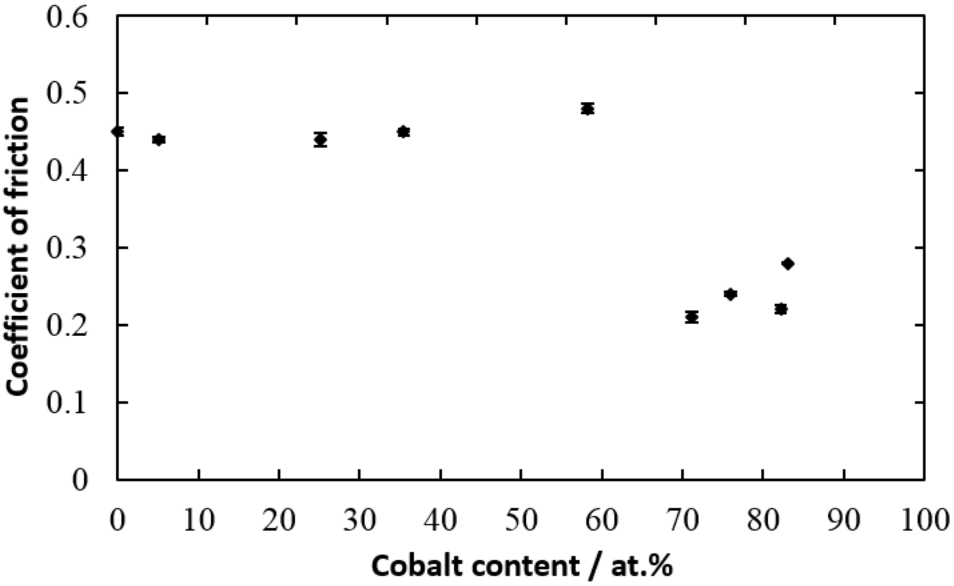

Fig. 4.5. Variation of coefficient of friction with cobalt content during unlubricated reciprocating sliding wear tests against AISI-52100 stainless steel with the sliding stroke of 2.69 mm, the sliding frequency of 1 Hz and the sliding time of 25 min.

the sliding tests in areas C and D. The pin wear scars were also examined by SEM and EDS. The size of the pin wear scar is in accordance with the wear rate. The pin sliding on the 83 at.% Co-Ni coating has the smallest wear scar. The pin surfaces are not totally covered by the transferred debris.

The structure of the debris accumulated at the end of the wear scars was further investigated by TEM. Fig. 4.11 shows the corresponding SAED patterns. The continuous rings indicate the presence of the nanocrystals. As shown in Fig. 4.11(a) a new set of diffraction rings appears compared to the diffraction pattern of nanocrystalline nickel coatings [44]. Based on the calculations of atomic plane spacings, it is found that the debris of the pure nickel coating contains a mixture of two phases: a nickel fcc metallic phase and a NiO fcc oxidised phase. The structure of iron or iron oxide cannot be detected. The patterns are indexed in Fig. 4.12, and all diffraction patterns are consistent with those in Fig. 4.11. While the composition of the debris varies as listed in Table 4.3, the four SAED patterns are similar to each other due to the similar lattice constants of fcc NiO (a=0.4177 nm) and fcc CoO (a=0.4260 nm).

4.3.4 Corrosion Resistance

The comparison of the potentiodynamic polarisation curves of the Ni-Co coatings with different cobalt contents is provided in Fig. 4.13. The corrosion of the alloys involves the following reactions [171]:

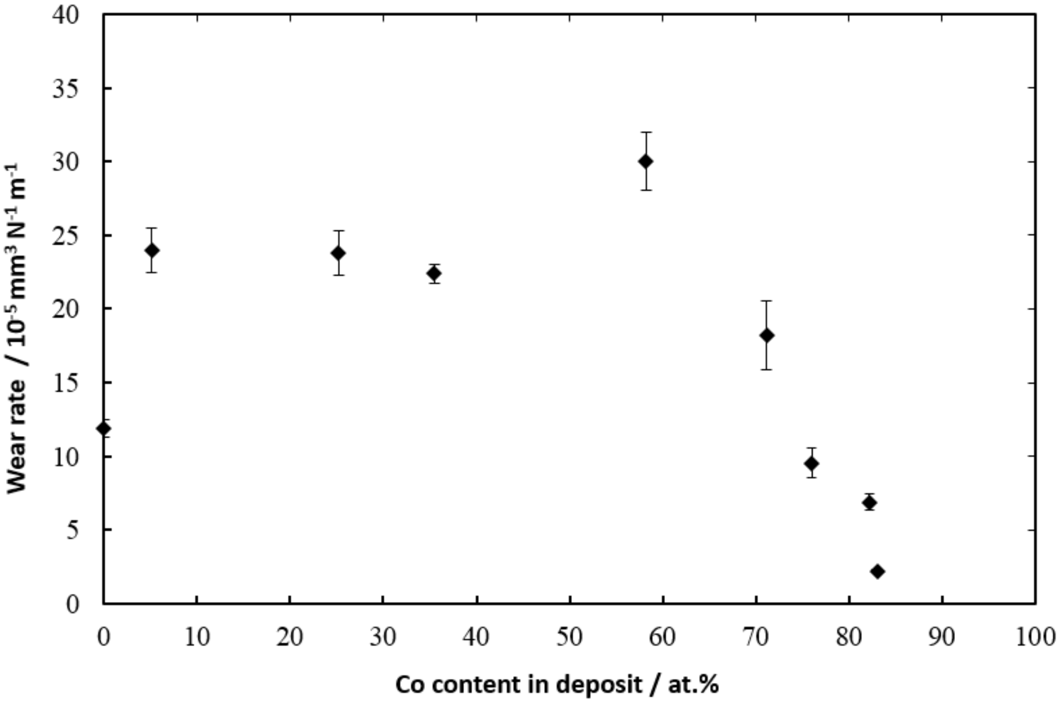

Fig. 4.6. Variation of wear rate with cobalt content after unlubricated reciprocating sliding wear tests against AISI-52100 stainless steel with the sliding stroke of 2.69 mm, the sliding frequency of 1 Hz and the sliding time of 25 min.

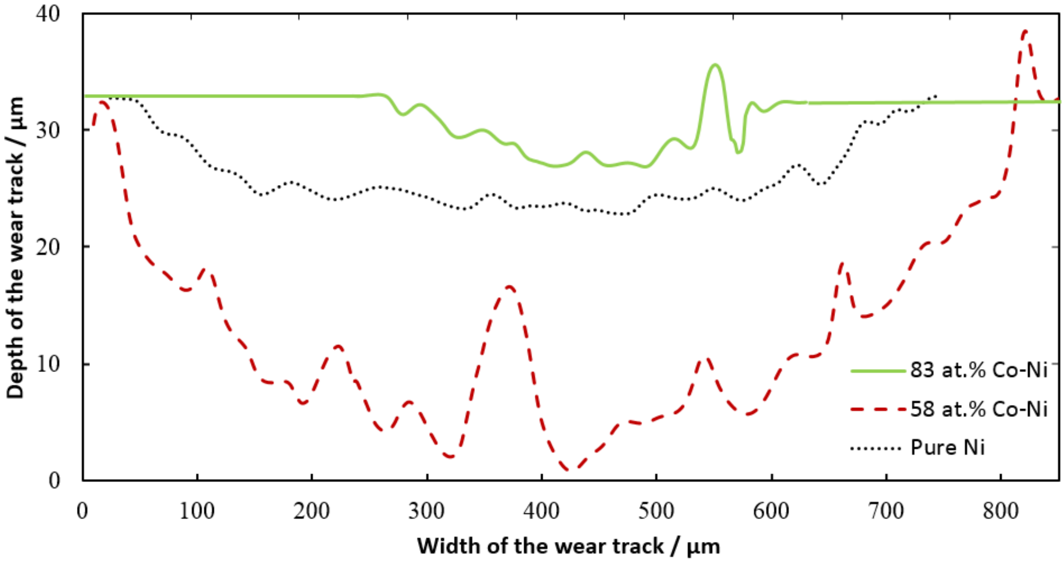

Fig. 4.7. Average surface profile of the wear tracks of pure nickel, 58 at.% Co-Ni and 83 at.% Co-Ni coatings after unlubricated reciprocating sliding wear tests against AISI-52100 stainless steel with the sliding stroke of 2.69 mm, the sliding frequency of 1 Hz and the sliding time of 25 min.

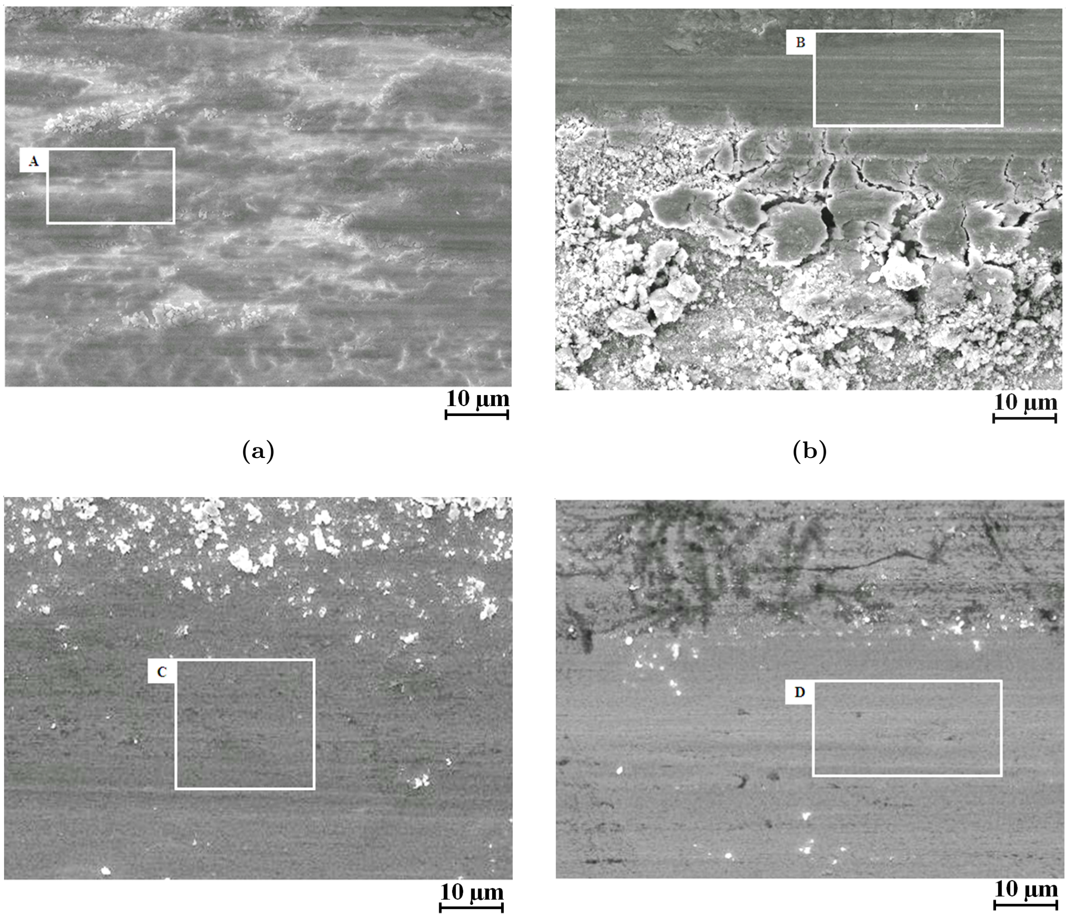

(a) (b) (c) (d)

Fig. 4.8. Worn surface morphology of (a) pure nickel, (b) 58 at.% Co-Ni, (c) 75 at.% Co-Ni and (d) 83 at.% Co-Ni coatings after unlubricated reciprocating sliding wear tests against AISI-52100 stainless steel with the sliding stroke of 2.69 mm, the sliding frequency of 1 Hz and the sliding time of 25 min. The rectangular zones corresponding to the smooth areas were analysed by EDS.

Table 4.2. Composition of the area highlighted in the four white rectangles on the worn surface shown in Fig. 4.8

Content / at.%	worn surface			
	Area A	Area B	Area C	Area D
O	63	48	0	0
Ni	17	18	23	16
Co	0	27	77	84
Fe	20	7	0	0

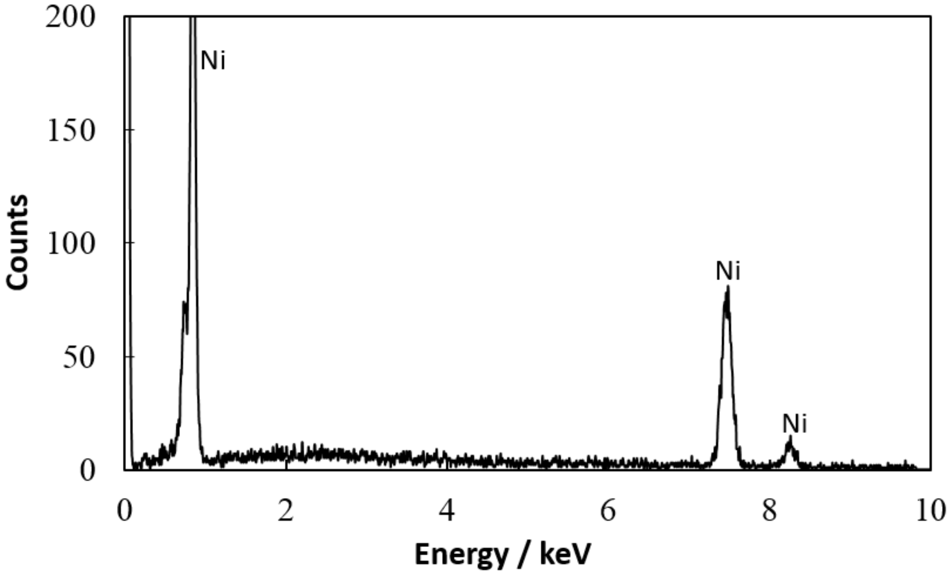

(a)

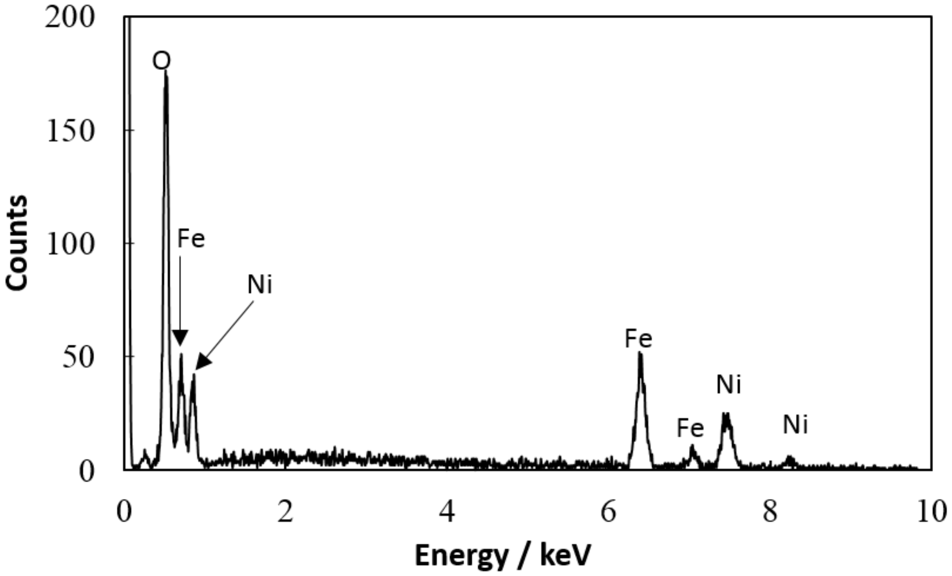

(b)

Fig. 4.9. Comparison of EDS spectra of (a) the as-deposited pure nickel coating and (b) its worn surface.

Table 4.3. Composition of the debris of pure nickel, 58 at.% Co-Ni, 75 at.% Co-Ni and 83 at.% Co-Ni coatings

Content / at.%	Debris			
	Ni coating	58 at.% Co-Ni	75 at.% Co-Ni	83 at.% Co-Ni
O	40	39	36	49
Ni	50	28	16	4
Co	0	31	48	47
Fe	10	2	0	0

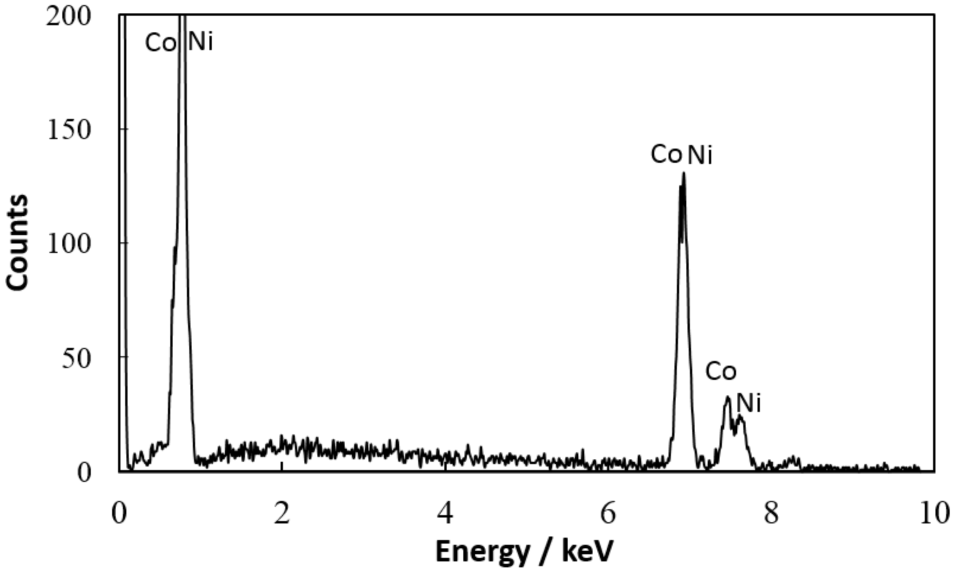

(a)

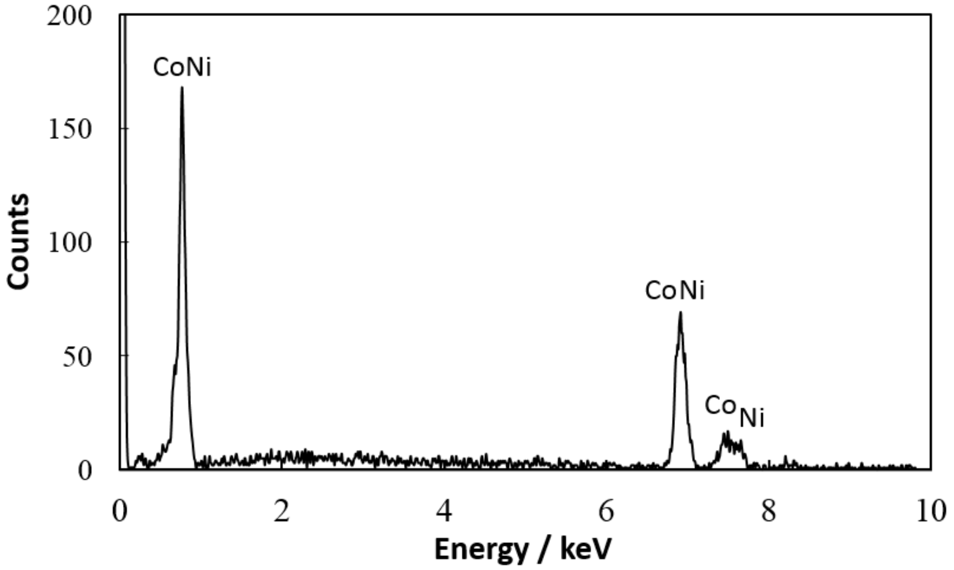

(b)

Fig. 4.10. Comparison of EDS spectra of (a) the as-deposited 75 at.% Co-Ni coating and (b) its worn surface.

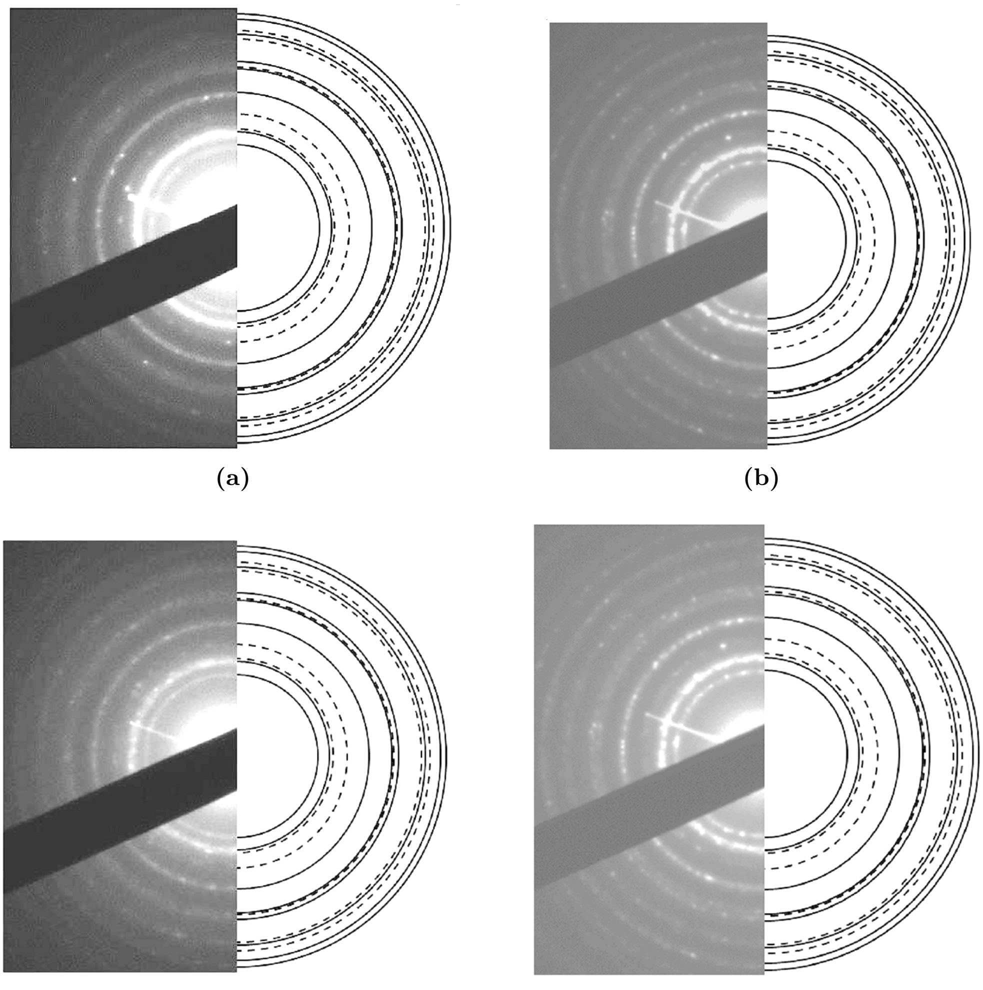

(a) **(b)** **(c)** **(d)**

Fig. 4.11. SAED patterns of the wear debris of (a) pure nickel, (b) 58 at.% Co-Ni, (c) 75 at.% Co-Ni and 83 at.% Co-Ni coatings after unlubricated reciprocating sliding wear tests against AISI-52100 stainless steel with the sliding stroke of 2.69 mm, the sliding frequency of 1 Hz and the sliding time of 25 min.

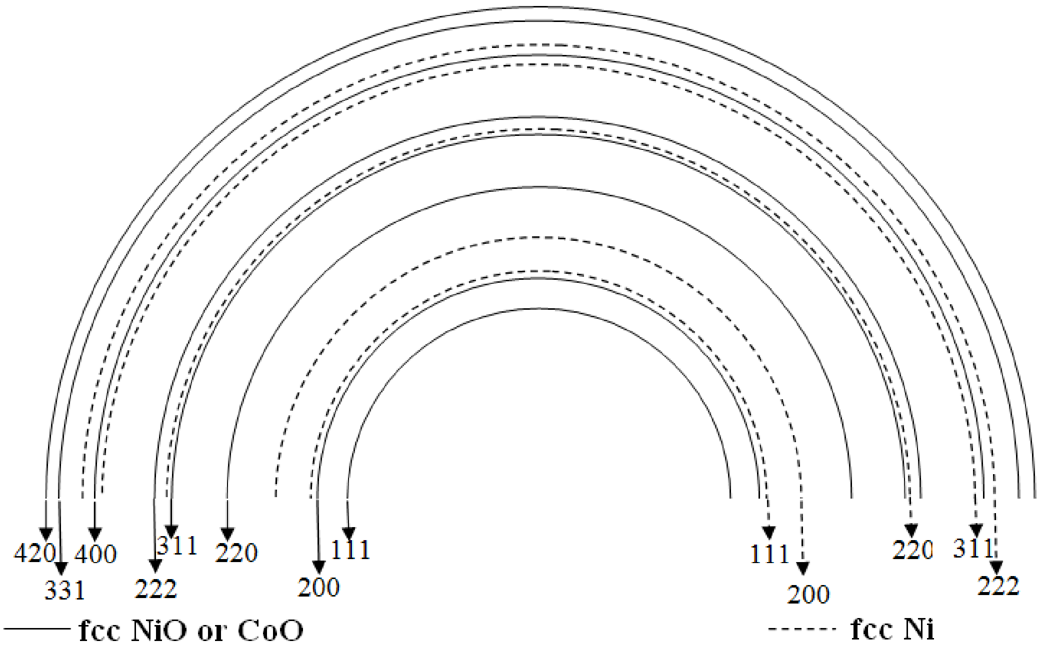

Fig. 4.12. Schematic showing the indices of the diffraction patterns with the solid and dashed lines representing the oxidised phase and metallic phase.

$$\mathrm{Ni} \rightarrow \mathrm{Ni}^{2+} + 2\mathrm{e}^{-} \tag{4.1}$$

$$\mathrm{Co} \rightarrow \mathrm{Co}^{2+} + 2\mathrm{e}^{-} \tag{4.2}$$

$$\mathrm{O}_2 + 4\mathrm{H}_2\mathrm{O} + 4\mathrm{e}^{-} \rightarrow 4\mathrm{OH}^{-} \tag{4.3}$$

The electrode was anodically polarised to a more positive potential whereas the corresponding current remained limited as shown in the rectangle in Fig. 4.13. The passivation behaviour of nickel coatings has been reported in 10 wt.% NaOH solution [134] and in 3.5 wt.% NaCl solution [172]. The passive films can also be formed on the cobalt coating surface in 10 wt.% NaOH solution [136]. In the present research, the four coatings exhibited the active-passive polarisation behaviour in 3.5% NaCl solution. Take the polarisation curve of the 83 at.% Co-Ni coating for example. AB represents cathodic behaviour (Eq. (4.3)), while BC is the active zone. At more positive potential than B, corrosion rate increased and reached a maximum at the passivation potential C. A protective film began to form and therefore the current density was maintained at a steady level until the breakdown of the protective film at D. The formation of the passive film on the electrode surface includes the following steps [134, 173, 174]:

$$\mathrm{M} + \mathrm{H_2O} \rightarrow \mathrm{M(H_2O)_{ads}} \tag{4.4}$$

$$\mathrm{M(H_2O)_{ads}} \rightarrow \mathrm{M(OH)^+} + \mathrm{H^+} + 2\mathrm{e^-} \tag{4.5}$$

$$\mathrm{M(OH)^+} + \mathrm{H_2O} \rightarrow \mathrm{M(OH)_2} + \mathrm{H^+} \tag{4.6}$$

where M represents Ni and Co. The dissolved oxygen in Eq. (4.3) can accelerate the formation of the $\mathrm{M(OH)_2}$ passive film. As the potential increases in the active region, the anodic current density increases because of the dissolution of the adsorbed species $\mathrm{M(H_2O)_{ads}}$ [174]:

$$\mathrm{M(H_2O)_{ads}} + 2\mathrm{Cl^-} \rightarrow \mathrm{MCl_2} + \mathrm{H_2O} + 2\mathrm{e^-} \tag{4.7}$$

As the adsorbed species dissolve, new active sites on the working electrode surface appear which lead to the breakdown of the passive film. The breakdown potential (E_b) of the 25 at.% Co-Ni and 75 at.% Co-Ni are similar, while the anodic current density of the 83 at.% Co-Ni coating with the most negative E_b dramatically increased when the increased potential exceeded E_b. It is found that the 58 at.% Co-Ni coating has the highest breakdown potential. It might be caused by the interaction of nickel and cobalt adsorbed species to stabilise the passive film when the content of nickel and cobalt is close, which needs to be confirmed in a future study.

The corrosion current density calculated by the Tafel extrapolation method and the corrosion potential compared with those of hard chromium coatings on carbon steel are summarised in Table 4.4. It was observed that the corrosion potential vs. SCE positively increased from -603 mV to -487 mV as the cobalt content in deposits decreased from 83 at.% to 25 at.% . The corrosion current density of the 75 at.% Co-Ni and 83 at.% Co-Ni coatings was higher than other two coatings with less cobalt content. The 58 at.% Co-Ni coating had the lowest corrosion current density among the four Ni-Co coatings. Myung and Nobe [22] investigated the corrosion resistance of Ni-Co alloys plated from chloride baths with different cobalt contents in 0.5 M NaCl after 1h immersion. As shown in Fig. 2.23, the corrosion resistance slightly increased with the increasing cobalt content until it reached the maximum at 70% Co and then sharply decreased, which is generally in agreement with the results in the present research. The worst corrosion resistance of 83

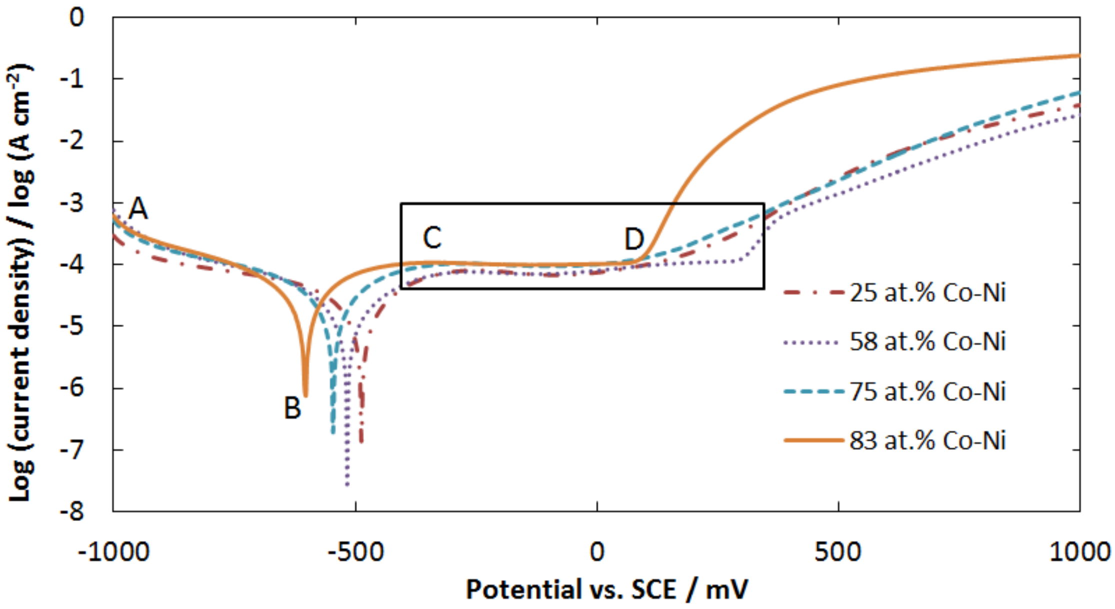

Fig. 4.13. Polarisation curves of Ni-Co alloys with different cobalt content in 3.5% NaCl solutions.

Table 4.4. Corrosion potential and corrosion current of Ni-Co alloys in 3.5% NaCl solutions compared with hard chromium [62]

Parameters	Coatings				
	25 at.% Co-Ni	58 at.% Co-Ni	75 at.% Co-Ni	83 at.% Co-Ni	Hard Cr [62]
Corrosion potential vs. SCE / mV	-487	-517	-546	-603	-299
Corrosion current density / 10^{-6} A cm^{-2}	5.05	2.85	6.85	7.65	3.30

at.% Co-Ni among the present coatings can be attributed to the high porosity of its lens-shaped morphology shown in Fig. 4.2(d), which provides more active areas than the dense surface of the coatings with less cobalt content.

All of the present Ni-Co coatings had more negative corrosion potential than hard chromium [62]. With the exception of the 58 at.% Co-Ni coating, the other three coatings exhibited higher corrosion current density than hard chromium, which indicates that the corrosion resistance of Ni-Co coatings needs to be further improved in order to replace hard chromium for anti-corrosion applications.

4.4 Discussion

4.4.1 Influence of Tribofilm Formation

In the present work, the results show that there is the oxidation product containing Fe on the worn surface of the pure Ni and the 58 at.% Co-Ni coatings showing a higher coefficient of friction and wear rate. However, for the 75 at.% Co-Ni and 83 at.% Co-Ni coatings shown in Fig. 4.8(c) and (d), there is no evidence of oxidation or material transfer from the pin. Without formation of the tribofilm, the latter surprisingly exhibited remarkable friction reduction and improved wear resistance.

For the pure Ni and the 58 at.% Co-Ni coatings, the debris generated by the asperity contact between the pin and the coatings forms a three-body contact. It leads to physical and chemical interactions and the adhesive tribofilms are developed (area A and B in Fig. 4.8 (a, b)). Other debris particles are generated, oxidised, detached and most of them are pushed to the end of the wear scars, i.e. not over-rolled. Formation of the tribofilm depends on the adhesion between the coating and the counterpart. With the strong adhesion, the tribofilm consisting of the oxides of both surfaces is favoured to be generated due to the extensive transfer from the counterpart and the frictional heat [175]. Conversely, no tribofilm is found on the worn surface of the 75 at.% Co-Ni and 83 at.% Co-Ni coatings which have hcp structure with a (0001) preferred orientation [170]. The typical hcp structure has a smaller number of slip systems (one slip plane with three slip directions) than that of fcc-structured metals (four slip planes each with three slip directions). The preferred slip plane in cobalt-rich coatings is the (0001) plane with the largest spacing between planes (c/a=1.623), which leads to less cohesive forces between (0001) planes. Therefore, much lower rate of shearing occurs and the extent of adhesion between the 75 at.% Co-Ni and 83 at.% Co-Ni coatings and the pins is significantly reduced. In this case, the tribofilm cannot be formed under the condition of much weaker adhesion and lower friction heating. No iron transfers from the pin to the worn surface. The enhanced lubricity of the hcp structure of cobalt results in less debris generated and a lower coefficient of friction compared with the that of the pure Ni and 58 at.% Co-Ni coatings. The high friction coefficient of the latter can be attributed to higher ductility of fcc structure [176] and the lack of a low-shear strength lubricious component in the tribofilm [34]. Inman et al. [28] reported that the superior wear resistance of a cobalt-based Stellite 6 alloy was attributed to fewer slip planes and shear-introduced alignment of the operational basal plane of hcp phases, which agrees with the present study. It was also found that at elevated sliding temperature the phase transformation from hcp to fcc led to enhanced material removal of Stellite 6 [177].

4.4.2 Role of the Debris on Friction and Wear Properties

The EDS results and SAED patterns show that the pulverised debris is partially oxidised. As shown in Fig. 4.11, the debris generated on the four coatings with different compositions have a similar fcc phase structure, the performance of which as a solid lubricant is not as good as the hcp structure. Peterson et al. [178] found that the coefficient of friction of Ni-based alloys (Ni-Ta, Ni-W and Ni-Cu) sliding against Al_2O_3 at room temperature was approximately 0.6, much higher than that at 600 °C (0.3-0.4). The reduction of friction at elevated temperatures was attributed to the formation of the metal oxides NiO film. Although the debris could also be oxidised at room temperature because of the high local temperatures in contact areas, the particles could not form an efficient film to eliminate the metallic contact. In the present research, most of the wear debris accumulated at the end of the wear track. The debris left on the wear track was found at the edges of the smooth areas of the pure Ni coating as shown in Fig. 4.8(a). The detached debris of the 58 at.% Co-Ni coating was trapped in the valley of the broken tribofilm as shown Fig. 4.8(b). There was much less debris on the worn surface of 75 at.% Co-Ni and 83 at.% Co-Ni coatings (Fig. 4.8(c, d)). Hence, the loose debris is insufficient to separate the two sliding surfaces. The role of wear debris on the tribological properties depends on the its own performance as a solid lubricant and the formation of a complete oxide film to avoid the metal-to-metal contact. Therefore, the debris have a limited effect on the contact of the rubbing surfaces in the present study.

It is worth noting that no hcp structure has been found in the debris of the 75 at.% Co-Ni and 83 at.% Co-Ni coatings as shown in Fig. 4.11(c) and (d). As mentioned above, the Co-rich alloys mainly contain hcp structure. The absence of hcp structure in debris cannot be explained by the hcp–fcc allotropic phase transformation because the hcp phase is not reformed after cooling to room temperature. Instead, it is suggested that all the cobalt-containing debris has been oxidised prior to the oxidation of nickel. It has been reported that the oxide surface of Ni-Co deposit only consists of CoO after annealing at 300 °C. The CoO layer formed by the outward diffusion of cobalt prevented the oxidation of nickel [151]. This indicates that nickel has better oxidation resistance than cobalt in Ni-Co alloys. In the present research, due to the local temperature rise introduced by the frictional heat, cobalt debris has been fully oxidised and the formed CoO can protect nickel against oxidation. Therefore, no hcp structure is found in debris and fcc nickel is the only metallic phase as shown in Fig. 4.11. The explanation is confirmed by the reduced intensity of the (200) ring of metallic phase as the nickel content decreased. Other rings are closed to those of oxidised phase and difficult to identify their intensity.

4.5 Summary

With an increase in cobalt sulphate concentration in the plating baths, the cobalt content of the electrodeposited Ni-Co coatings gradually increased. The low microhardness of the 83 at.% Co-Ni coating is related to its loose lens-shaped microstructure. By examining the role of the third bodies on the tribological behaviour, the following conclusions have been drawn:

(1) The coefficient of friction dropped from 0.45-0.5 to ca. 0.25 as the cobalt content exceeded 70 at.%. At the same time, the wear rate gradually decreased. The pure nickel coating with high hardness exhibited relatively low wear rate.

(2) A tribofilm consisting of oxides of both the coating and the counterpart was found on the worn surface of the Ni-Co coatings having the cobalt content less than 60 at.%. The formation of the tribofilm was not beneficial to the friction reduction and the wear resistance.

(3) Low coefficients of friction were obtained without the formation of tribofilm on the Co-rich coatings (more than 70 at.% Co) and the stainless steel pin contact. The composition of the smooth worn surface is the same as that of the as-deposited coating. No pin material transfer from the pin to the coating was observed. The improved wear resistance is mainly due to a large portion of hcp structure of the Co-rich coatings, which can act as the solid lubricant.

(4) The debris was nanocrystalline, containing a mixture of two phases: a nickel fcc metallic phase and a nickel oxide/cobalt oxide fcc oxidised phase. No hcp structure has been found in the debris due to the complete oxidation of cobalt. Most of the debris was pushed to the end of the wear scars. At room temperature (25 °C), the loose oxides were insufficient to separate the two sliding surfaces. The debris had a limited effect on the contact of rubbing surfaces.

(5) Ni-Co coatings exhibited the active-passive polarization behaviour in 3.5 % NaCl solution. The worst corrosion resistance of 83 at.% Co-Ni among the present coatings can be attributed to the high porosity of its lens-shaped morphology, which provided more active areas than the dense surface of the coatings with less cobalt content. The corrosion resistance of Ni-Co coatings needs to be further improved in order to replace

hard chromium in anti-corrosion applications.

Chapter 5

Effects of Additives on the Microstructure and Properties of Electrodeposited Nanocrystalline Ni-Co Coatings

5.1 Introduction

The cobalt-rich nanocrystalline Ni-Co coatings exhibit improved tribological properties. However, they were difficult to be electrodeposited onto steel due to their high internal stress. Current methods, e.g. developing graded coatings and applying pulse current waveforms, are expensive and complex. In this chapter, a new approach to electrodeposit single layer Ni-Co coatings with high cobalt content on steel is presented by optimising the concentration of additives (BD and saccharin). High-quality nanocrystalline Ni-Co alloys (78 ±2 at.% Co) containing a large proportion of hcp structure were successfully prepared. Properties of the coatings were investigated including surface morphology, grain size and crystalline texture, hardness and tribological performance against a steel counterpart via a reciprocating ball-on-disc apparatus. The inhibition effect of absorbed additives on electrodeposited nanocrystalline coatings is discussed.

5.2 Experimental Details

5.2.1 Electrodeposition

Nanocrystalline Ni-Co coatings were electrodeposited at 45 °C using a current density of 4 A dm^{-2} from a sulphate bath containing nickel sulphate (200 g dm^{-3}), cobalt sulphate (100 g dm^{-3}), sodium chloride (20 g dm^{-3}), and boric acid (30 g dm^{-3}). BD and saccharin with controlled concentrations were added to the electroplating baths, see Table 5.1. Pure nickel coatings were plated from the three sulphate baths containing different concentrations of additives without adding cobalt sulphate. The plating time was 1 h and the average thickness of the coatings was 50±5 µm. For comparison, a hard Cr coating was electrodeposited onto mild steel from a conventional chromic acid bath as described in Chapter 3.

Table 5.1. The concentration of electrolyte additives to produce Ni-Co coatings

	Sample A	Sample B	Sample C
BD / g dm^{-3}	0.1	0.5	0.5
Saccharin / g dm^{-3}	0.1	0.5	2

5.2.2 Microstructure, Grain size and Microstrain

The surface morphologies of the as-deposited Ni-Co coating and the worn surfaces after wear tests were investigated by SEM while the composition of the alloys was determined by EDS. The crystal structure was studied by XRD and TEM as described in Chapter 3.

The grain size of coatings was estimated via two different approaches. In the first approach, the grain size (*d'*) was measured from TEM bright and dark field images. In the second approach, the grain size (*d*") was calculated by the XRD peak broadening according to the Scherrer equation (Eq. (3.1)) [167]. However, the peak broadening in the XRD patterns may also be caused by internal strain, which can be described by the following relationship:

$$B_{\varepsilon} = 4\varepsilon tan\theta \tag{5.1}$$

where ε is the microstrain [179]. The total XRD peak broadening is attributed to both microstrain and the grain size, which can be expressed as follows:

$$B = 4\varepsilon tan\theta + 0.9\frac{\lambda}{dcos\theta} \tag{5.2}$$

Instead of plotting $Bcos\theta$ vs $sin\theta$ in a Willianson-Hall plot [46, 179] to get the slope as 4ε , the microstrain can be calculated directly with the grain size measured by TEM (d') according to the following equation:

$$\varepsilon = \frac{Bctan\theta - \frac{0.9\lambda}{d' sin\theta}}{4} \tag{5.3}$$

5.2.3 Mechanical and Tribological Properties

The hardness and tribological properties of deposits were characterised as described in Chapter 3. The worn surface and wear debris were studied by SEM and EDS.

5.3 Results

5.3.1 Surface Morphologies and Composition

As shown in Fig. 5.1(a), the sample A deposited from the plating bath with 0.1 g dm^{-3} BD and 0.1 g dm^{-3} saccharin consists of lens-shaped clusters. The size of the clusters is in the range of 150-500 nm. As the amounts of BD and saccharin were increased to 0.5 g dm^{-3}, finer clusters or grains were found between the lens-shaped clusters, shown in the circles in Fig. 5.1(b). Microcracks were observed by an optical microscope on the surface of sample A and B probably due to a high level of internal stress. When the concentration of saccharin was further increased to 2 g dm^{-3}, coating C had dense and smooth surface as shown in Fig. 5.1(c). The EDS shows that the three coatings have the similar composition of 78±2 at.%.

5.3.2 Phase Structure and Grain Size

The phase structure and grain size were studied by XRD. Fig. 5.2 shows the XRD patterns of the Ni-Co coatings from the electrolytes with various additive concentrations. Coating A, electrodeposited from the electrolyte containing 0.1 g dm^{-3} BD and 0.1 g dm^{-3} saccharin, had a strong fibre texture indicated by the peak at $2\theta\approx42°$, which was consistent with the spacing of $(10\bar{1}0)$ in a hcp structured Co lattice. By increasing the concentration of BD and saccharin to 0.5 g dm^{-3}, the fibre texture changed from $(10\bar{1}0)_{\mathrm{hcp}}$ to $(0002)_{\mathrm{hcp}}/(111)_{\mathrm{fcc}}$ indicated by the peak at $2\theta\approx44.4°$ for coating B. The peak for coating C is observed to be slightly higher due to the higher concentration of saccharin. TEM selected area diffraction patterns shown in Figs. 5.3-5.5(c) confirm that the three coatings have a mixed hcp (ϵ) and fcc (a) structure as indexed in Figs. 5.5(c).

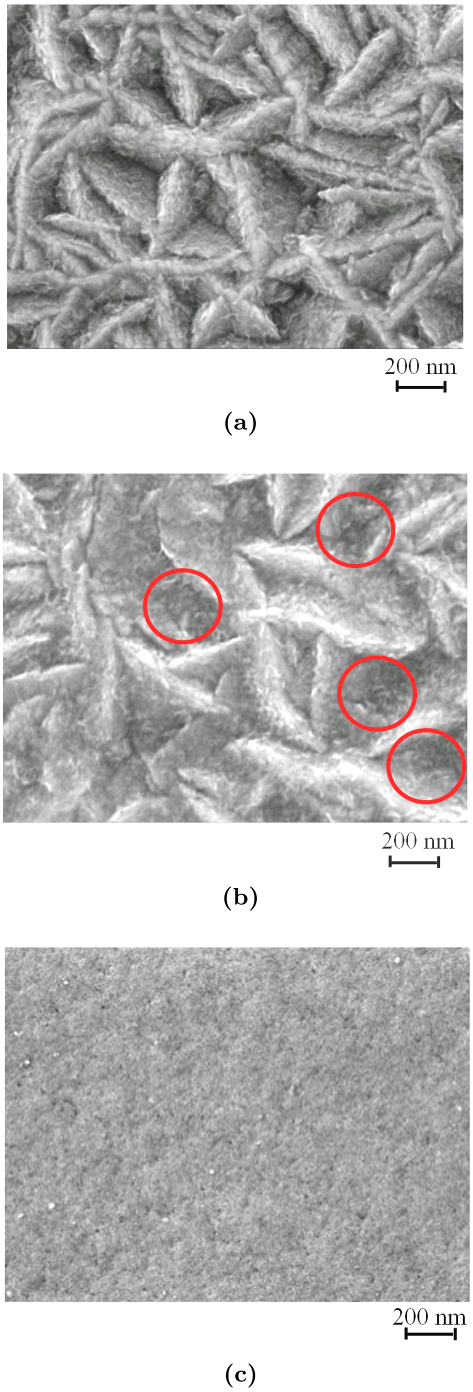

(a)

(b)

(c)

Figure 5.1. SEM morphologies of Ni-Co coatings from the baths containing controlled concentration of BD and saccharin: Sample A (a) 0.1 g dm^{-3} and 0.1 g dm^{-3}, Sample B (b) 0.5 g dm^{-3} and 0.5 g dm^{-3}, Sample C (c) 0.5 g dm^{-3} and 2 g dm^{-3}, respectively.

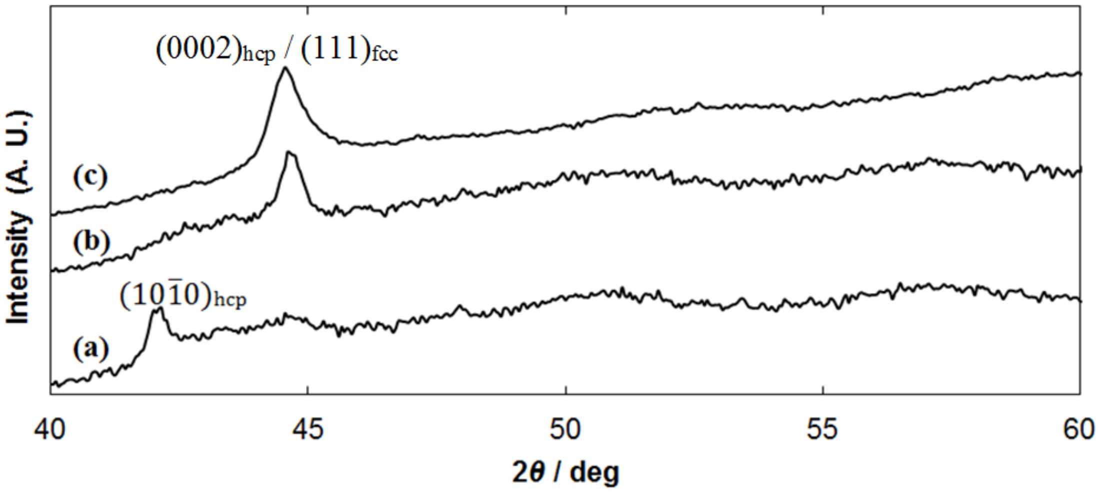

Figure 5.2. XRD patterns of the Ni-Co alloys: (a) Sample A from the bath containing 0.1 g dm^{-3} BD and 0.1 g dm^{-3}saccharin, (b) Sample B from the bath containing 0.5 g dm^{-3} BD and 0.5 g dm^{-3} saccharin, (c) Sample C from the bath containing 0.5 g dm^{-3} BD and 2 g dm^{-3} saccharin.

Grain size was obtained via two different approaches, namely (1) according to the Scherrer equation (Eq. (3.1)), and (2) measured from TEM bright (Figs. 5.3-5.5(a)) and dark field images (Figs. 5.3-5.5(b)). Table 5.2 shows the results of the grain size analysis. The grain sizes of samples A and B obtained from XRD are not consistent with those measured by TEM due to their higher microstrain induced by the stress. The microstrain was calculated by Eq. (5.3) and the results are listed in the last column of Table 5.2. The sample A deposited in the presence of the smallest amount of additives has the highest microstrain. By increasing the concentration of BD and saccharin to 0.5 g dm^{-3}, the tensile microstrain is reduced. The sample C from the electrolyte having a higher concentration of saccharin (2 g dm^{-3}) has a compressive microstrain with the lowest magnitude, which can increase the adhesive strength between the coating and the substrate [180]. Since the microstrain of samples A and B is not negligible, the grain size calculated by the Scherrer equation (Eq. (3.1)) is different from that obtained by TEM analysis. TEM electron diffraction patterns shown in Figs. 5.3-5.5(c) indicate that the grain size decreases as the concentration of additives increases. The rings shown in Fig. 5.3(c) are discontinuous due to large grain size of the sample A, whereas the rings are continuous for sample B (Fig. 5.4(c)) and sample C (Fig. 5.5(c)).

5.3.3 Mechanical and Tribological Properties

No mechanical and tribological tests could be performed on the samples A and B due to the crack propagation and delamination from the substrate. By optimising the amount of

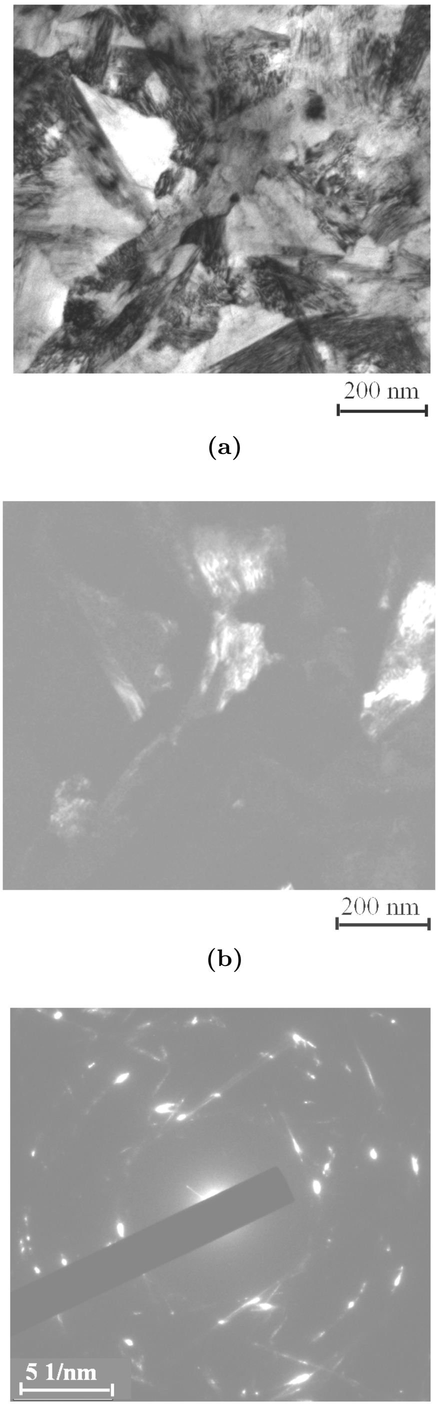

(a)

(b)

(c)

Figure 5.3. Bright field image (a), dark field image (b) and corresponding SAED pattern (c) of the Ni-Co alloy (Sample A) from the bath containing 0.1 g dm^{-3} BD and 0.1 g dm^{-3} saccharin.

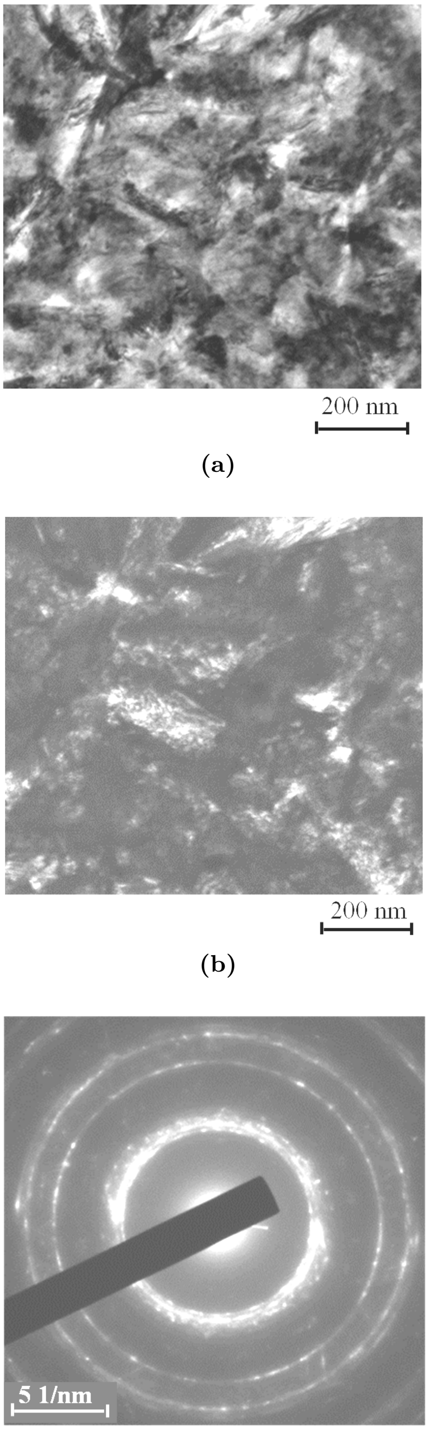

(a)

(b)

(c)

Figure 5.4. Bright field image (a), dark field image (b) and corresponding SAED pattern (c) of the Ni-Co alloy (Sample B) from the bath containing 0.5 g dm^{-3} BD and 0.5 g dm^{-3} saccharin.

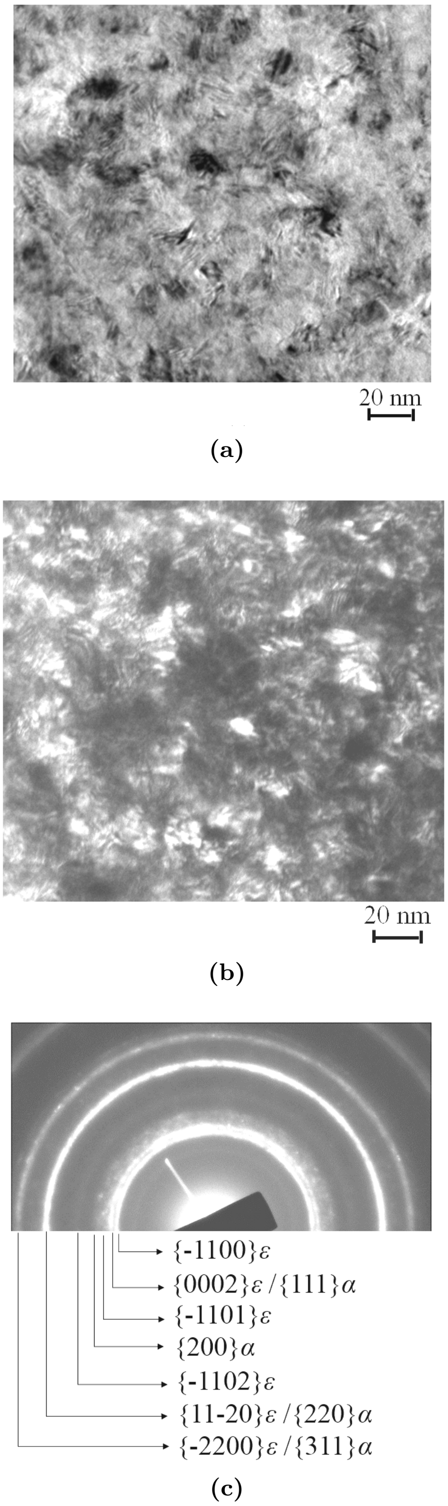

(a)

(b)

(c)

Figure 5.5. Bright field image (a), dark field image (b) and corresponding SAED pattern (c) of the Ni-Co alloy (Sample C) from the bath containing 0.5 g dm^{-3} BD and 2 g dm^{-3} saccharin. SAED patterns indicated that the coatings have a mixed structure of fcc (a) and hcp (ϵ).

Table 5.2. Grain size and microstrain of the coatings deposited on mild steel substrates from the baths containing different concentrations of BD and saccharin

Sample	Grain size, *d"* obtained by XRD / nm	Grain size, *d'* obtained by TEM / nm	Microstrain calculated by Eq. (5.3)
A	16.4	190±5	0.0054 (tensile)
B	17.5	50±7	0.0034 (tensile)
C	11.3	11±2	-0.0002 (compressive)

additives, the sample C exhibits high hardness (503±15 HV), which is much higher than that of the Ni-Co coating with the similar cobalt content produced by Wang. et al [24] (listed in Table 5.3). The increase of hardness can be attributed to the reduced grain size from 2.5 µm to 11±2 nm. However, it needs to be further improved to match that of graded Ni-Co coatings [18, 151] and hard chromium.

As listed in Table 5.3, the coefficient of friction of the sample C is 0.23, which is similar to that of the single-layer 81 wt.% Co-Ni [24] and graded Ni-Co coatings [18, 151]. Fig. 5.6 shows that the coefficient of friction of the sample C (around 0.23) is much lower than that of hard chromium (approximately 0.7). The three Ni-Co coatings [18, 24, 151] exhibit similar coefficient of friction due to a large portion of hcp structure acting as the solid lubricant as discussed in Chapter 4. Due to the lower hardness of Ni-Co coatings, the wear rate is higher than that of hard chromium. The worn surface of hard chromium is shown in Fig. 5.7(a). Numerous debris were produced during the severe wear, which contained 15 at.% oxygen and 4.4 at.% iron from the steel counterpart. Cracks propagated perpendicularly to the sliding direction in the contact zone. In contrast, fine grooves and debris were found on the worn surface of sample C (Fig. 5.7(b)). EDS analysis indicates that the small debris particles contain 36±5 at.% oxygen without iron. A much lower rate of shearing occurred and the extent of adhesion between the Co-rich coatings and the pins was significantly reduced [181]. Under the condition of much weaker adhesion and lower friction heating, no iron transferred from the pin to the worn surface of sample C.

5.4 Discussion

It has been widely reported in the literature that unsaturated organic additives can act as a grain refiner by absorbing on the deposit surface and modifying electrocrystallisation [117]. In this work, BD has the active group C≡C, which can be transformed to cis-2-butene-1, 4-diol then butane-1, 4-diol by reacting with the absorbed atomic hydrogen (H_{ads}) [182]. Hydrogen evolution increases the pH at the cathode followed by the formation of trace amounts of cobalt and nickel hydroxides, which inhibit the crystal growth. Additionally, at

Table 5.3. Mechanical and tribological properties of the single-layer Ni-Co coating (Sample C), compared to the graded Ni-Co deposits and hard chromium

Sample	Hardness / HV	Coefficient of friction	Wear rate / 10^{-5} mm^3 N^{-1} m^{-1}
Single-layer 78 ±2 at.% Co-Ni (sample C)	503±15	0.23	9.6±0.9
Single-layer 81 wt.% Co-Ni [24]	326	0.25#	11#
Graded Ni-Co [18, 151]	550	0.20-0.28†	16†
Hard Chromium	943±47	0.7	2.1±0.2

The tribological behaviour was tested on a reciprocating ball-on-disc UMT-2MT microtribometer tester with an AISI-52100 stainless steel ball (diameter 4 mm) as the counter body under a normal load of 3 N at a sliding speed of 55 mm s^{-1}.

† Under the same condition as above, except the sliding speed of 110 mm s^{-1}.

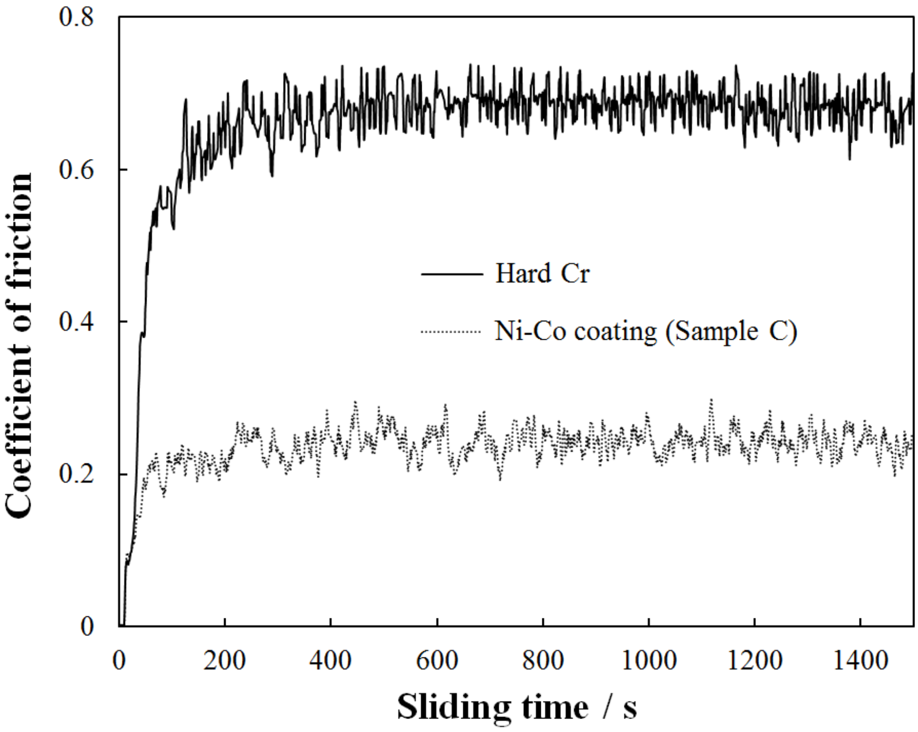

Figure 5.6. Typical coefficient of friction for hard Cr and Ni-Co coating (Sample C) during unlubricated reciprocating sliding wear tests against AISI-52100 stainless steel with the sliding stroke of 2.69 mm, the sliding frequency of 1 Hz and the sliding time of 25 min..

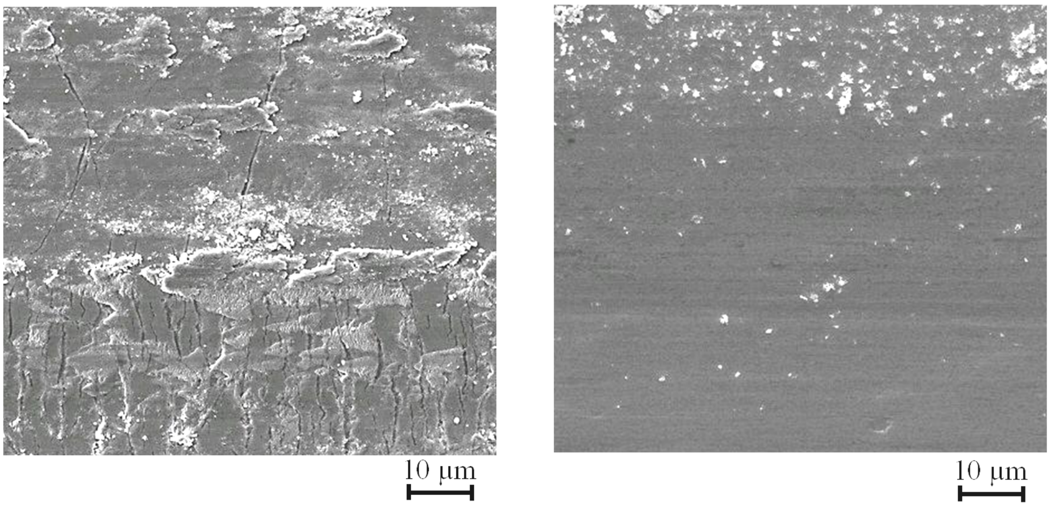

(a) **(b)**

Figure 5.7. Worn surface morphologies of (a) hard Cr and (b) Ni-Co coating (Sample C) after unlubricated reciprocating sliding wear tests against AISI-52100 stainless steel with the sliding stroke of 2.69 mm, the sliding frequency of 1 Hz and the sliding time of 25 min.

a current density below 25 A dm^{-2}, the active groups within saccharin (=C-S and S=O) can react with protons (H^+) to form sulphur anions that can be precipitated as metal sulphides [117]. The process also increases the alkalinity in the cathodic area, which handicaps the discharge of metal ions and significantly increases the overpotential of electroplating. The high overpotential promotes the formation of new nuclei resulting in refined grain size [73]. As shown in Figs. 5.5(a, b), the sample C plated from the bath containing 0.5 g dm^{-3} BD and 2 g dm^{-3} saccharin has the smallest grain size due to the combined effect of BD and saccharin at relatively high concentration. As the concentration of additives decreased (samples A and B), the effect of the grain refinement was restrained, leading to the increasing grain size.

Electrocrystallisation can be strongly influenced by the presence of adsorbed molecules and ions at the surface of the electrode [183]. Amblard et al. [184] reported that the preferred crystal orientation of electrodeposited nickel can be attributed to the inhibition of the electrocrystallisation process by adsorbed chemical species, such as H_{ads} and $(NiOH)_{ads}$, which can slow down propagation steps, block growth site, and/or modify the activity of emerging structural defects. The coverage of absorbed species varies on different crystal faces and the highest coverage with absorbed species leads to the slowest growth rate of the crystal face and the texture can be developed. It has been reported that the activation energy for adsorption of hydrogen is more negative as the distance between adjacent atoms is larger [185]. The phenomenon that different crystallographic planes have different hydrogen adsorption abilities was also reported by Li et al. [186]. They found that the $(110)_{\text{fcc}}$ and $(100)_{\text{fcc}}$ planes were more active in absorbing hydrogen than the $(111)_{\text{fcc}}$ planes, which are the close-packed plane in the fcc structured Ni-20% Fe lattice. In the present research, the $(10\bar{1}0)_{\text{hcp}}$ plane with much lower atomic density has the largest interplanar spacing in a hcp cell. It may allow a more negative free energy of hydrogen absorption, which leads to higher coverage with absorbed atomic hydrogen (H_{ads}) than that on $(0002)_{\text{hcp}}/(111)_{\text{fcc}}$ planes as shown in Fig. 5.8(a). Hence, the $(10\bar{1}0)_{\text{hcp}}$ plane is very likely to be the most catalytic face for hydrogen reduction and to become the lowest growth plane. As discussed above, the BD can react with the absorbed atomic hydrogen (H_{ads}) to inhibit the crystal growth. It may have a significant effect on the growth rate of $(10\bar{1}0)_{\text{hcp}}$ plane with more absorbed atomic hydrogen than that of $(0002)_{\text{hcp}}/(111)_{\text{fcc}}$. It has been reported that, by adding BD, the perfection of [100] preferred crystal orientation for nickel nanocrystalline deposits was slightly enhanced as the relative texture coefficient of $(200)_{\text{fcc}}$ increased from 93% to 99% [182]. In the present study, the addition of BD (0.1 g dm^{-3}) promotes the formation of $(10\bar{1}0)_{\text{hcp}}$ fibre texture of the sample A.

Saccharin can also be absorbed by filling its non-sharing lone pair electrons with the 3*d* electrons of nickel and cobalt atoms to form coordinate bonds [187]. When the concentration of saccharin is low (0.1 g dm^{-3}), its effect is negligible. As the concentration increases to 0.5 g dm^{-3}, the close-packed planes with the highest atomic density favour the absorption of saccharin molecules as shown in Fig. 5.8(b). Therefore, the growth of crystals only leaves the $(0002)_{\text{hcp}}/(111)_{\text{fcc}}$ planes which have the slowest growth rate. Although the concentration of BD was higher in B bath (0.5 g dm^{-3}), the inhibition effect of saccharin was dominant. It has been reported that the fibre texture of electrodeposited nanocrystalline Ni-Fe alloys changed from $(100)_{\text{fcc}}$ to $(111)_{\text{fcc}}$ as the influence of hydrogen adsorption decreased by applying lower current density [186], which is consistent with the present results for Ni-Co alloys. By further increasing the addition of saccharin to 2 g dm^{-3}, the inhibition effect of saccharin was enhanced as shown in Fig. 5.8(c), leading to the higher $(0002)_{\text{hcp}}/(111)_{\text{fcc}}$ XRD peak of the sample C.

As mentioned in Chapter 4, the pure nickel prepared by Wang et al. [24] without adding BD or saccharin has a strong $(200)_{\text{fcc}}$ texture. However, in the present research the nickel deposits plated from the bath containing 0.5 g dm^{-3} BD and 2 g dm^{-3} saccharin (shown in Fig. 4.3(a)) exhibits a $(111)_{\text{fcc}}$ texture. It can be explained by the inhibition effect of additives as discussed above. In the fcc structured nickel, the $(200)_{\text{fcc}}$ plane with lower atomic density is more catalytic for hydrogen absorption than the most close-packed

Table 5.4. Grain size and microstrain of the pure nickel coatings from the baths containing different concentrations of BD and saccharin

Concentration / g dm^{-3}		Grain size, d'' obtained by XRD / nm	Grain size, d' obtained by TEM / nm	Microstrain calculated by Eq. (5.3)
BD	Saccharin			
0.1	0.1	15	30±8	0.0029 (tensile)
0.5	0.5	13	18±2	0.0018 (tensile)
0.5	2	17	15±3	-0.0008 (compressive)

$(111)_{fcc}$. When the concentration of saccharin is low (0.1 g dm^{-3}), the addition of BD (0.1 g dm^{-3}) promotes the $(200)_{fcc}$ texture shown in Fig. 5.9(a), which is consistent with the results reported by Pavlatou et al. [182]. As the concentration of BD and saccharin increased to 0.5 g dm^{-3}, the latter had more influence on the texture formation, as in the case of Ni-Co coatings. As shown in Fig. 5.9(b), the texture changes to $(111)_{fcc}$, which is enhanced by increasing the addition of saccharin to 2 g dm^{-3} (Fig. 5.9(c)). Table 5.4 shows the results of the grain size analysis of the present nickel coatings. Except the sample plated from the bath containing 0.5 g dm^{-3} BD and 2 g dm^{-3} saccharin, the grain size obtained by XRD is smaller than that measured by TEM due to their microstrain, which can be calculated by Eq. (5.3). With the increase of the concentration of additives, the tensile microstrain decreased and changed to compressive stress, which is consistent with the tendency found in Ni-Co coatings with high cobalt content. It is worth noting that the 83 at.% Co-Ni coating plated from the bath containing 0.5 g dm^{-3} BD and 2 g dm^{-3} saccharin exhibits a $(10\bar{1}0)_{hcp}$ texture as shown in Fig. 4.3(g). It might be associated with the absorption of cobalt hydroxide ions. More $Co(OH)^+$ can be formed in the electrolyte with higher concentration of cobalt ions. It has been reported that $Co(OH)^+$ has high adsorption ability [142], which may weaken the inhibition effect of saccharin. Therefore, the texture changed from $(0002)_{hcp}/(111)_{fcc}$ to $(10\bar{1}0)_{hcp.}$

5.5 Summary

Nanocrystalline single-layer Ni-Co coatings having a high cobalt content of 78±2 at.% were successfully electroplated onto mild steel substrates from sulphate baths by optimising the concentration of additives. The coating plated from the bath containing 0.5 g dm^{-3} BD and 2 g dm^{-3} saccharin had a smooth, optically reflective surface. The grain size was reduced to 11±2 nm, which resulted in its high hardness (500 HV). The microstrain can be calculated directly with the grain size measured by TEM according to the total XRD peak broadening equation without plotting the Willianson-Hall plot. As the concentration of

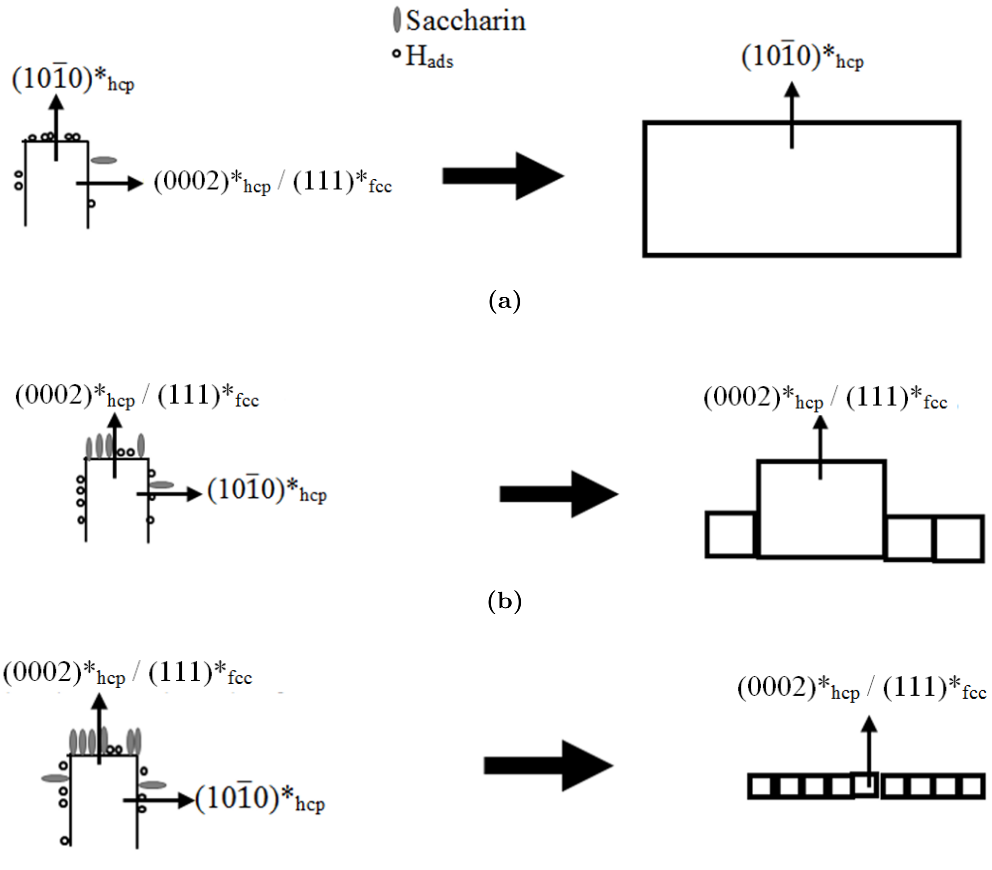

(a)

(b)

(c)

Figure 5.8. Schematic representation of the grain size and the texture of electrodeposited Ni-Co coatings: (a) Sample A from the bath containing 0.1 g dm^{-3} BD and 0.1 g dm^{-3} saccharin, (b) Sample B from the bath containing 0.5 g dm^{-3} BD and 0.5 g dm^{-3} saccharin, (c) Sample C from the bath containing 0.5 g dm^{-3} BD and 2 g dm^{-3} saccharin.

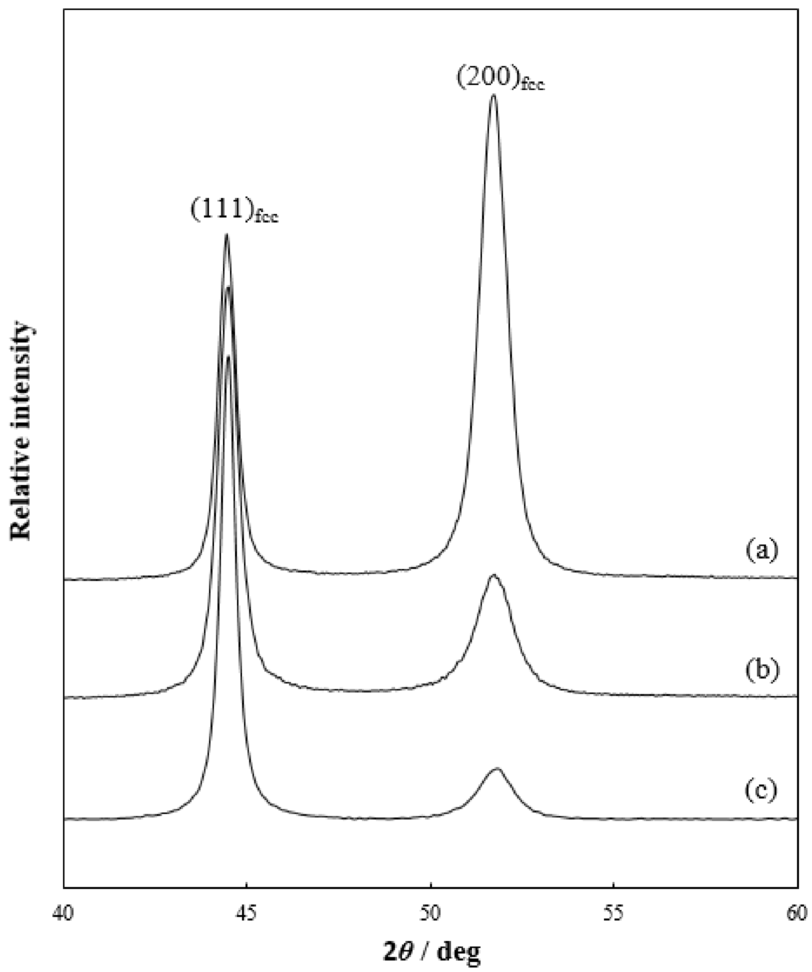

Fig. 5.9. XRD patterns of the pure nickel coatings: (a) from the bath containing 0.1 g dm^{-3} BD and 0.1 g dm^{-3}saccharin, (b) from the bath containing 0.5 g dm^{-3} BD and 0.5 g dm^{-3} saccharin, (c) from the bath containing 0.5 g dm^{-3} BD and 2 g dm^{-3} saccharin.

additives decreased, the microstrain changed from compressive to tensile and its magnitude was significantly increased. In this case, the Scherrer equation cannot be used to calculate the grain size. Although the addition of BD promoted the formation of $(10\bar{1}0)_{\mathrm{hcp}}$ texture, the inhibition effect of saccharin was dominant. The fibre texture of the coating was modified from $(10\bar{1}0)_{\mathrm{hcp}}$ to $(0002)_{\mathrm{hcp}}/(111)_{\mathrm{fcc}}$ as the concentration of saccharin increased. The Ni-Co coating plated from the electrolyte with optimised amount of additives had low coefficient of friction and improved anti-wear resistance due to the high proportion of hcp structure.

Chapter 6

The Hardness of Porous Nanocrystalline Ni-Co Electrodeposits

6.1 Introduction

The Hall-Petch relationship can fail when the grain size is below a critical value of tens of nanometres. This occurs particularly for coatings having porous surfaces. In this study, electrodeposited nanostructured Ni-Co coatings with different porosities were obtained by controlling the concentration of nickel sulphate and nickel chloride within electroplating baths. The influence of porosity on the microhardness was investigated. A cluster-pore mixture model has been proposed to explain the deviation of Hall-Petch relationship for coatings with porous surfaces. Additionally, the effect of different types of nickel salts on the microstructure, composition and microhardness was studied.

6.2 Experimental Details

As shown in Table 6.1, four coatings were deposited from electrolytes containing different concentrations of various nickel salts (A1 - A4). The electrodeposition procedure is described in Chapter 3. All the thicknesses of the coatings were 50±2 µm. The surface of the as-deposited Ni-Co coating was investigated by SEM while the composition of the alloys was determined by EDS. The surface roughness of the as-deposited Ni-Co coating was measured by AFM. The crystal structure, as well as the grain size, was studied by XRD as presented in Chapter 3. The internal stress was measured by the $sin^2\psi$ technique.

Table 6.1. The bath compositions with different concentrations of various nickel salts employed for electroplating Ni-Co coatings

Bath component	Bath concentration / $g\,dm^{-3}$			
	A1	A2	A3	A4
$NiSO_4 \bullet 6H_2O$	200	200	0	50
$NiCl_2 \bullet 6H_2O$	0	50	200	200
$CoSO_4 \bullet 7H_2O$	100	100	100	100
Boric acid	30	30	30	30
Saccharin	2	2	2	2
BD	0.5	0.5	0.5	0.5

A TEM was employed to measure the grain size, while the phase structure was examined by SAED. The hardness of deposits was measured as described in Chapter 3.

6.3 Results

6.3.1 Surface Morphologies and Composition

Fig. 6.1 shows high resolution SEM surface morphologies of four Ni-Co coatings (A1 - A4) deposited from different electroplating baths. Coating A1 deposited from an all-sulphate bath has a dense and smooth surface (Fig. 6.1(a) with low value of roughness (R_a=10 nm). The grain was too fine to be resolved by SEM. With the addition of nickel chloride in the bath, the microstructure of coating A2 has dramatically changed to lens shape (Fig. 6.1(b) and the surface roughness increased to approximately 120 nm. A lens actually consists of a number of fine grains. Both A3 and A4 coatings were deposited from baths with high concentrations of Cl^-, and microcracks were observed by optical microscopy. Their surfaces had clusters consisting of fine grains as shown in Figs. 6.1(c, d) with the surface roughness of 35 nm and 22 nm, respectively. The EDS results confirm that four coatings (A1 - A4) have the similar cobalt content of 77±2 at%, which reveals that the use of baths containing different types and levels of nickel salts has no significant effect on the composition of the Ni-Co coatings.

6.3.2 Microstructure and Internal Stress

The phase structure and grain size were further investigated by means of XRD and TEM. The XRD patterns for all samples (Fig. 6.2) exhibit a single peak. This indicates that all the coatings have a strong fibre texture, i.e. one particular plane is parallel to the coating surface. The peak at 0.205 nm ($2\theta \approx 44.4°$) is consistent with the spacing of $(0002)_{hcp}/(111)_{fcc}$. The TEM electron diffraction patterns of the coatings are similar as

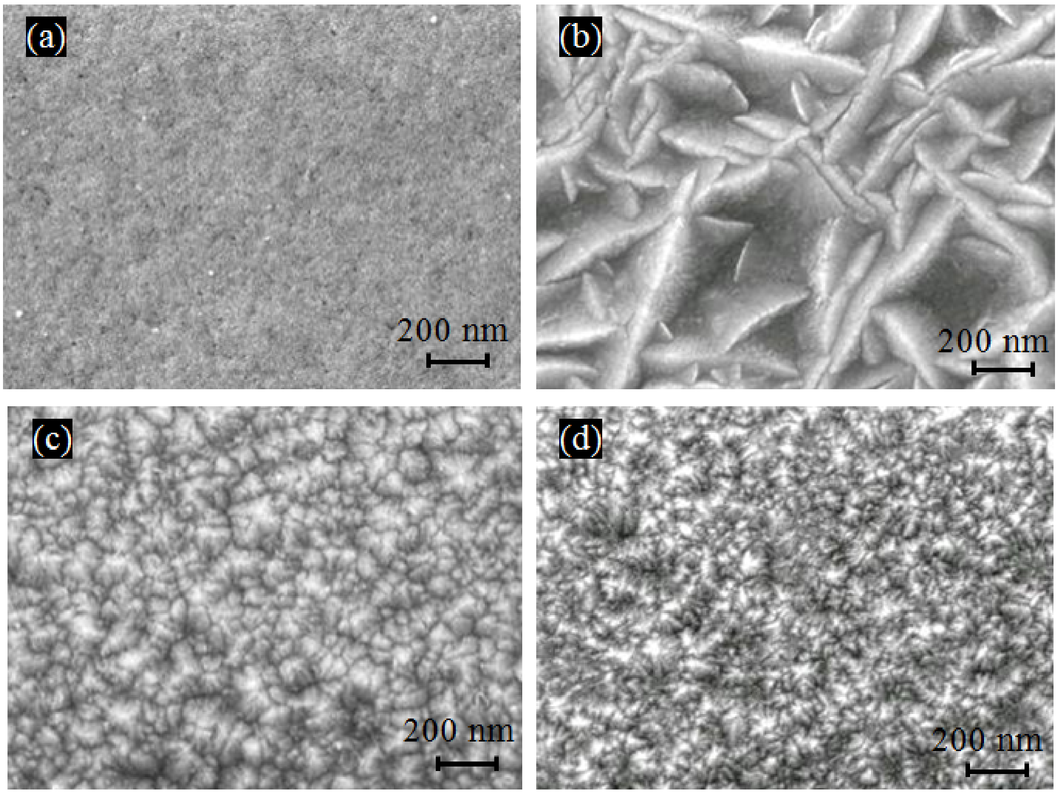

Fig. 6.1. SEM images of as-deposited Ni-Co alloys (a) A1 from the all-sulphate bath with a dense and smooth surface, (b) A2 from the sulphate-dominant bath with the lens-shaped microstructure consisting of smaller grains, (c) A3 from the chloride-dominant bath and (d) A4 from the all-chloride bath showing clusters in the deposits.

Table 6.2. Comparison of grain sizes and hardness of the Ni-Co coatings

	Samples			
	A1	A2	A3	A4
Grain size, *d"* obtained by XRD / nm	11.3	14.5	22.7	22.6
Grain size, *d'* obtained by TEM / nm	10±2	15±1	-	21±2
Measured hardness, H_{m} / HV	503±5	379±20	455±7	469±8
Cluster size, d_{cl} / nm	11	162	30	24
Approximate surface poroxity, p	0	0.225	0.029	0.005
Calculated pore-free hardness, H_{c} by Eq. (6.5) / HV	503	489	468	471

shown in Figs. 6.3(b, d, f). A mixed structure of hcp and fcc has been indexed, as shown in Fig. 6.3(d). The A1 coating deposited from the all-sulphate bath and the A2 deposited from the sulphate-dominant baths have much lower peak intensities than A3 and A4. The XRD peak broadening is attributed to the small grain size, which was calculated by applying Scherrer equation (Eq. (3.1)) [167]. The result of the grain sizes is listed in Table 6.2. TEM dark field images (Figs. 6.3(a, c, e)) were also taken to confirm the grain sizes. The measurements were carried out on at least 50 grains. The A3 coating from the all-chloride bath could not be successfully prepared for TEM foil because of its high brittleness. The comparison of grain sizes in Table 6.2 shows the values calculated by Scherrer equation are consistent with those measured by TEM. It was reported that the total XRD peak broadening is attributed to both microstrain and the grain size, which can be expressed as Eq. (5.2). In the present research, the peak broadening introduced by the microstrain is negligible. It has been widely accepted that nickel coatings deposited from baths containing high concentration of nickel chloride (samples A3 and A4) tend to have a higher internal stress than that from sulphate baths (the sample A1) or sulphamate baths [39]. The internal stress of samples A1 and A3 was measured by the XRD-$sin^2\psi$ analysis method. The A3 coating has lower internal stress of 0.32 GPa than the A1 sample (1.05 GPa). This might be due to microcracks or free boundary clusters which can release the high internal stress.

6.3.3 Microhardness

The measured hardness (H_{m}) of nanocrystalline Ni-Co alloys deposited from the baths containing different nickel salts is listed in the third row of Table 6.2. The Hall-Petch relationship [40] can be described as Eq. (2.2). The measured hardness variation with the grain size of the samples obtained by XRD is plotted in the form of the Hall-Petch relationship in Fig. 6.4(a). The hardness against the reciprocal square root of grain size is not in agreement with the Hall-Petch relationship. In comparison with the sample A1,

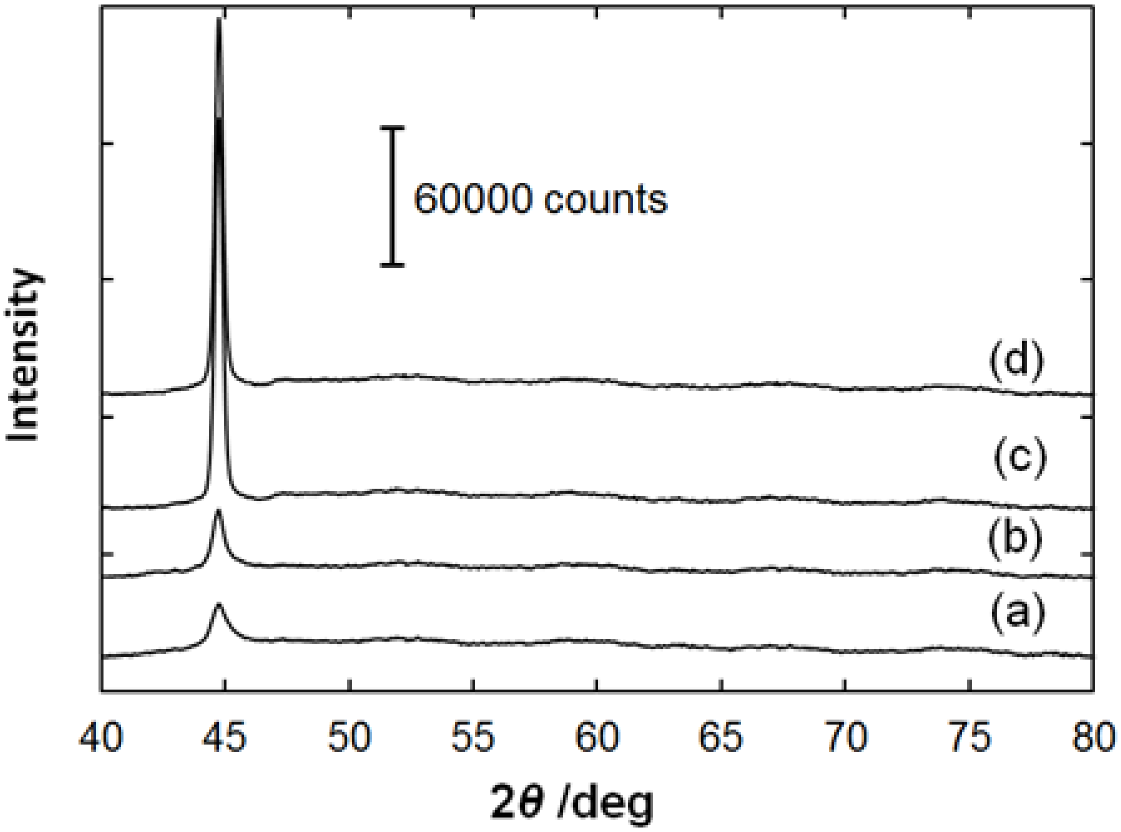

Fig. 6.2. XRD patterns of as-deposited Ni-Co alloys: A1 (a) and A2 (b) coatings deposited from the baths with lower concentration of nickel chloride than the baths of the samples A3 (c) and A4 (d).

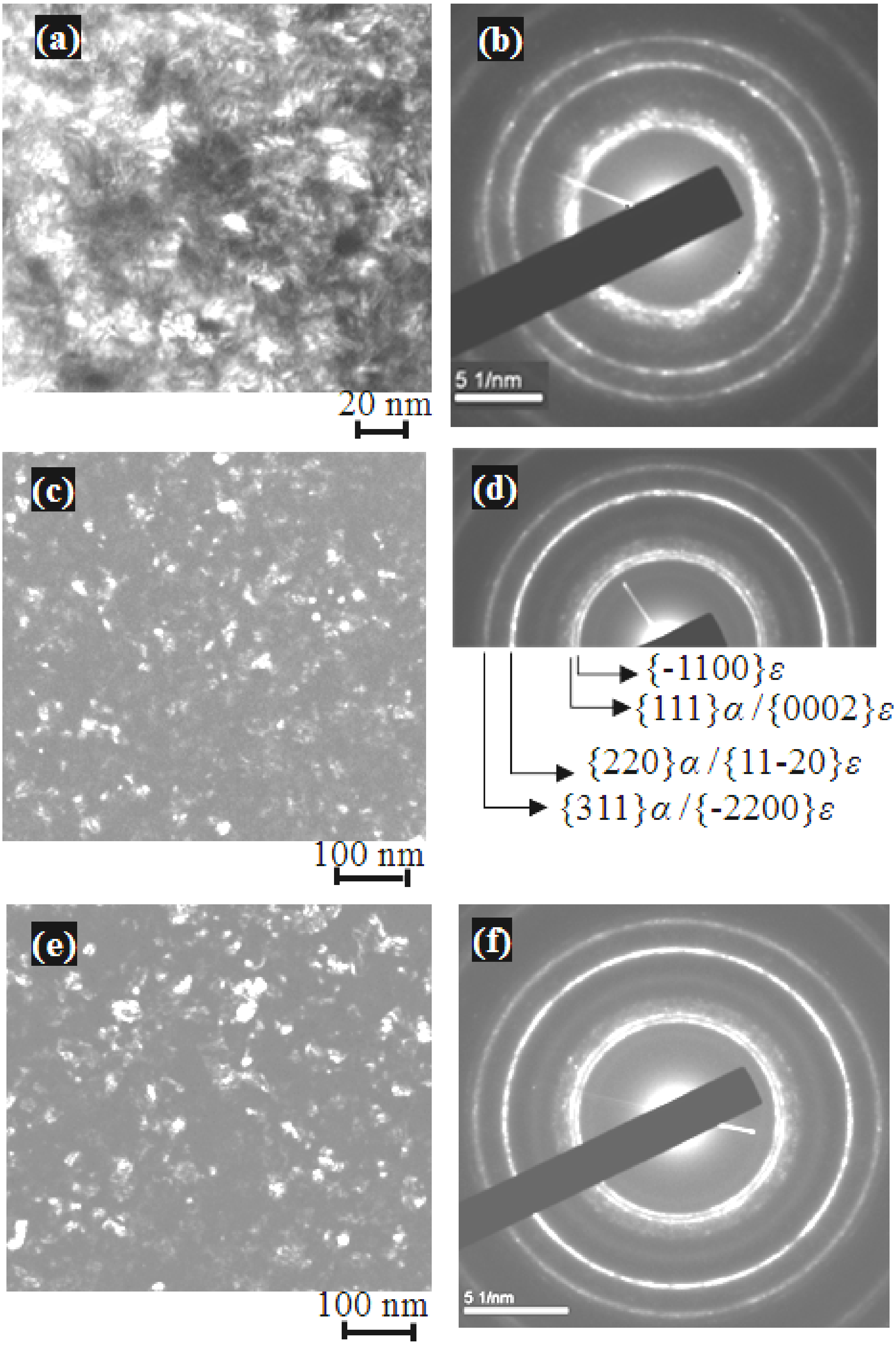

Fig. 6.3. Dark field images, and corresponding SAED patterns of the as-deposited Ni-Co alloys: A1 from all-sulphate bath (a, b), A2 from the sulphate-dominant bath (c, d), A4 from the chloride-dominant bath (e, f). SAED patterns indicated that the coatings have similar mixed structure of fcc (α) and hcp (ϵ).

the coatings A3 and A4 have slightly lower hardness as a result of the increased grain size (23 nm) as shown in Fig. 6.4(a). There is, however, an anomalously low hardness (379 HV) for the sample A2 with the fine grain size of 15 nm.

6.4 Discussion

It is suggested that the anomaly of the coating A2 is caused by a loose microstructure containing high porosity shown in Fig. 6.1(b). Its relatively high standard deviation of hardness measurements shown in Fig. 6.4(a) is due to the porosity. The comparison between the SEM image (Fig. 6.1(b)) and the TEM image (Fig. 6.3(c)) reveals that a lens is not a single grain but a cluster of hundreds of fine grains (around 15 nm). The lens-shaped cluster can be approximated as an ellipsoid. The size of the cluster (d_{cl}) is estimated by calculating the equivalent spherical diameter, which is the diameter of a sphere having the same volume as the cluster [188]. The equation can be described as:

$$d_{cl} = 2\sqrt[3]{r_1 r_2 r_3} \tag{6.1}$$

where r_1 and r_2 are the equatorial radii of the approximated ellipsoid which are equal to each other and r_3 is the polar radius. The weighted average of the cluster size is calculated as 162 nm. The clusters of the sample A3 and A4 shown in Figs. 6.1(c, d) are simplified as spheroids, and the cluster sizes of which are 30 nm and 24 nm, respectively. According to the SEM images (Fig. 6.1), the porosity (p) of the present samples is described as the ratio of the volume of voids to the total volume of the surface layer [189], which can be estimated by:

$$p = \frac{V_t - N' \times \frac{4}{3}\pi(d_{cl}/2)^3}{V_t} \tag{6.2}$$

where V_{t} is the total deposit volume of the top surface and N' is the measured number of clusters. The sample A1 is assumed to be free of pores ($p = 0$) due to its dense microstructure shown in the high resolution SEM image (Fig. 6.1(a). The results are listed in Table 6.2.

According to the phase mixture model [41, 190, 191], for a nanostructured sample, the crystallites, grain boundaries, triple line junctions and quadratic nodes have different contributions to the hardness and the yield strength depending on the volume fraction (f) of each. The composite hardness (H_{com}) can be described as [41, 190]:

$$H_{com} = H_{cr}f_{cr} + H_{gb}f_{gb} + H_{ti}f_{ti} + H_{qn}f_{qn} \tag{6.3}$$

where the subscripts *cr*, *gb*, *tj* and *qn* represent crystallites, grain boundary, triple line junction, and quadratic node, respectively. Based on the phase mixture model, the coatings in the present research can be considered as a mixture of clusters and pores. The volume fraction can be expressed in terms of the porosity. The measured hardness is expressed as:

$$H_m = H_c(1 - p) + H_p p \tag{6.4}$$

where H_{c} and H_{p} are the hardness contribution of clusters and pores, respectively. H_{c} is actually referring to H given by Hall-Petch equation (Eq. (2.2)), which represents the hardness of the dense pore-free coatings. In this cluster-pore mixture model, since the pores have no contribution to the hardness ($H_{\mathrm{p}} \equiv 0$), the hardness of the cluster consisting of fine grains can be determined as:

$$H_c = \frac{H_m}{1 - p} \tag{6.5}$$

The calculated pore-free hardness according to Eq. (6.5) is listed in Table 6.2. After adopting H_{c} as the hardness for Hall-Petch relationship, it can be observed that the hardness increases with a nearly constant slope and there is no obvious deviation even when the grain size is reduced to 11 nm as shown in Fig. 6.4(b). It is worth mentioning that in the Vickers hardness tests no cracking of coatings occurred with an applied load of 100 g. Therefore, these microcracks are not considered as surface pores. The hardness measurements have been found to be sensitive to microstructural flaws in the samples, particularly the porosity. In high-quality copper samples produced by inert-gas condensation and compaction, the hardness is in agreement with the ordinary Hall-Petch relationship when the grain size is reduced to 15 nm, and then plateaued [192]. Sanders et al. [192] explained the deviation of the Hall-Petch relationship by increasing porosity of the samples with smaller grain size, which were produced by lower temperature compaction. Ibañez and Fatás [193] reported the Hall-Petch relationship in electrodeposited Cu coatings broke down when the grain size was less than 80 nm as shown in Fig. 6.5. From SEM images in the paper [193], the surface of the Cu coatings plated at different current densities consisted of clusters of different sizes. The porosity is calculated and the Hall-Petch plot with the pore-free hardness obtained by Eq. (6.5) has been redrawn. As shown in Fig. 6.5, the data fit the relationship well and a high correlation coefficient (R=0.9911) was obtained. Therefore, for the pore-free surface, the relationship between hardness and grain size may satisfy the Hall-Petch equation. However, for coatings with porous surfaces, the porosity effect needs to be taken into consideration for the validation of Hall-Petch equation. The calculated pore-free hardness rather than the measure hardness should be adopted.

6.5 Summary

The Ni-Co coatings (77±2 at% Co) have been successfully prepared by electrodeposition from the baths with different nickel salts (nickel sulphate and/or nickel chloride), which were found to have significant effects on the morphologies, grain sizes and hardness of the coatings. The following conclusions are drawn:

(1) The coating deposited from an all-sulphate bath was characterised by its dense and smooth surface with the finest grain size (approximately 11 nm). By adding nickel chloride in the bath, the coating had the porous lens-shaped microstructure consisting of a number of fine grains (around 15 nm). The surfaces of the coatings plated from the chloride-dominant bath and the all-chloride bath had clusters with much smaller size than that of the lens-shaped clusters. The grain size increased to approximately 23 nm.

(2) The hardness of porous coatings except the dense coating deposited from an all-sulphate bath exhibited the deviation of the Hall-Petch relationship. The extent of deviation depended on the porosity of coatings.

(3) By considering porous materials as composites of clusters and pores, their contribution to hardness has been quantitatively studied. The pore-free hardness (i.e. the hardness of clusters) can be calculated according to the cluster-pore mixture model. By adopting it, the Hall-Petch relationship can be maintained at the nanoscale.

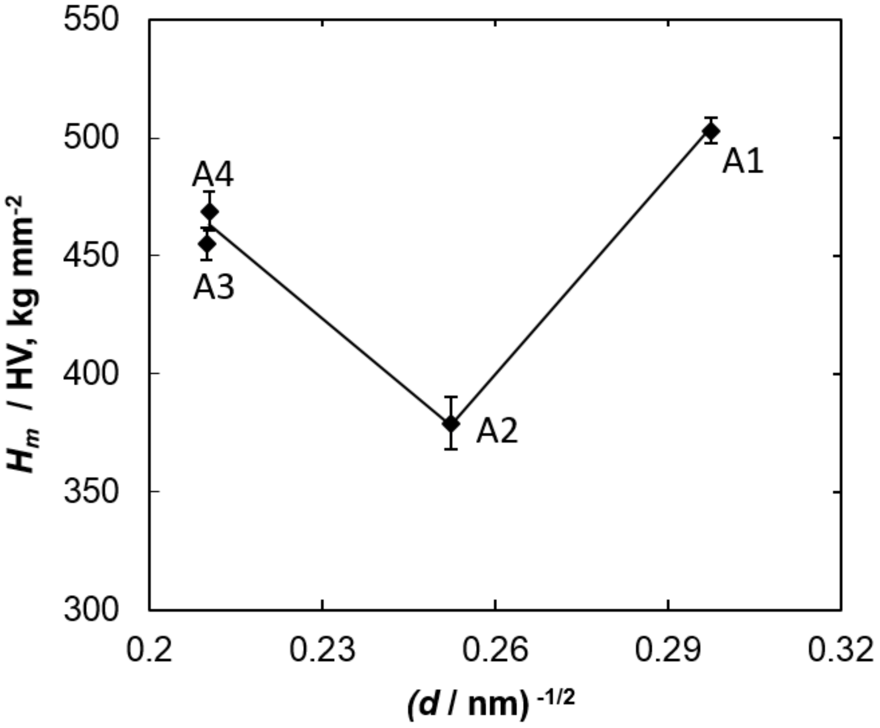

(a)

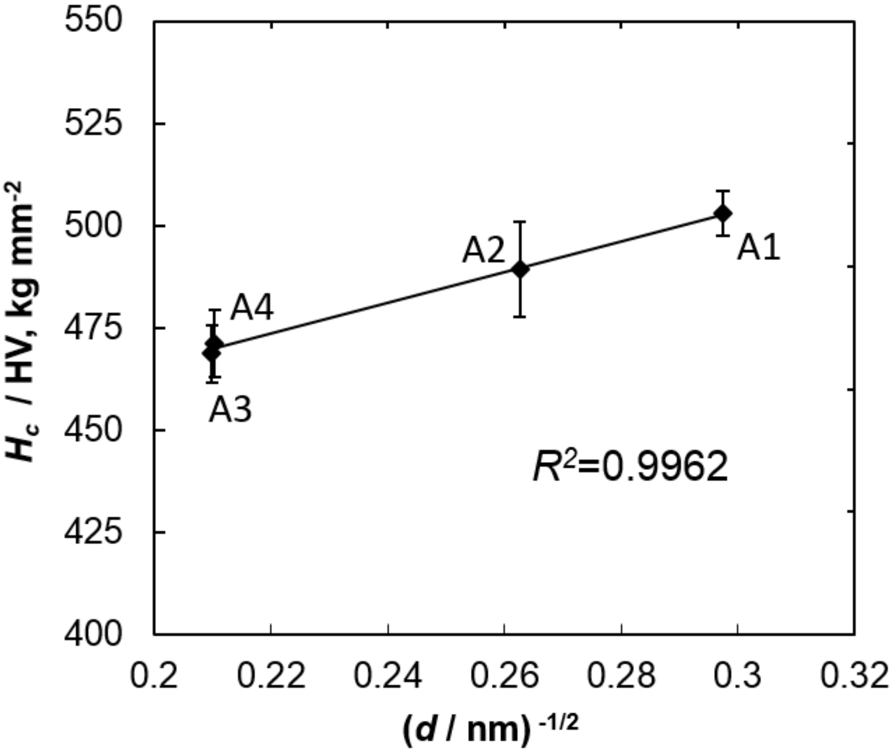

(b)

Fig. 6.4. Hall-Petch plots for as-deposited Ni-Co alloys before (a) and after (b) adopting the calculated pore-free hardness. R is the linear correlation coefficient.

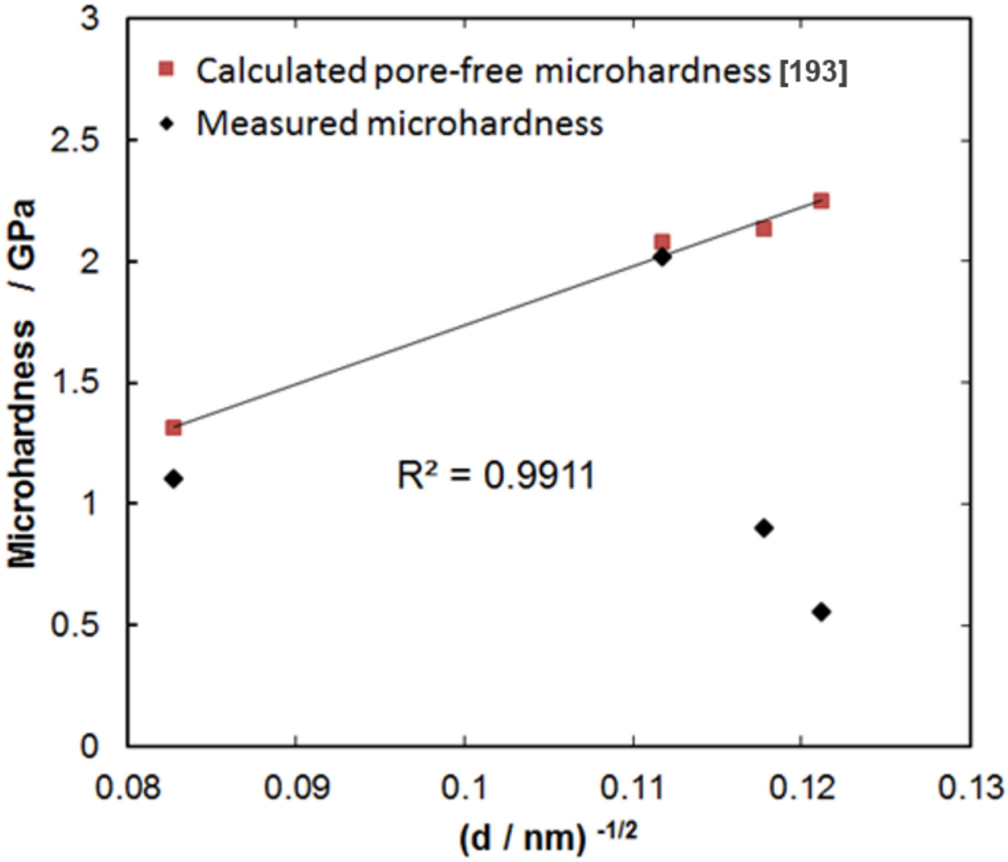

Fig. 6.5. Hall-Petch plots for electrodeposited Cu coatings with the measured microhardness reported by Ibañez and Fatás [193] and with the calculated pore-free hardness according to Eq. (6.5).

Chapter 7

The Electrodeposition and Characterisation of Low Friction and Wear Resistant Co-Ni-P Coatings

7.1 Introduction

Co-Ni-P coatings are expected to possess high hardness derived from the precipitation hardening of Ni-P alloys and improved wear resistance due to the lubricity of cobalt-rich Co-Ni coatings. Although thin Co-Ni-P films (from 10 nm to 10 µm thick) deposited by electroless plating and electroplating have been studied as hard magnetic materials, there is a lack of investigation on their evolution of composition and microstructure, hardness, thermal stability, wear and corrosion resistance. In the present research, a novel Co-Ni-P coating has been electrodeposited from a modified sulphate bath. In order to clarify the mechanism of the composition gradient and microstructure change from nanocrystalline to amorphous structure along the thickness direction as mentioned in Chapter 2, the effect of local pH near the cathode was investigated. The hardness, tribological and electrochemical properties of the coatings after heat treatment were evaluated and compared with those of hard chromium coatings.

7.2 Experimental Details

7.2.1 Electrodeposition

Nanocrystalline Co-Ni-P coatings were electrodeposited from the electrolytes consisting of 40 g dm^{-3} $NiSO_4 \bullet 6H_2O$, 40 g dm^{-3} $CoSO_4 \bullet 7H_2O$, 20 g dm^{-3} $NaH_2PO_2 \bullet H_2O$ and additives. The electrodeposition was carried out with the current density of 5 A dm^{-2} at 45 °C. The plating time was controlled from 1 min to 75 min. The pH of the electrolytic bath was measured before and after the electrodeposition. In situ measurement of the local pH near the cathode was carried out by fixing the pH electrode as close to the cathode surface as possible. The plating time was 75 min. In order to study the influence of the substrate, the plating was repeated on top of the previous Co-Ni-P coating. The as-deposited Co-Ni-P coatings were subsequently annealed in air at 200 °C, 300 °C, 400 °C and 500 °C for 1 h, respectively. As a comparison, hard chromium coatings were electrodeposited onto mild steel from a conventional chromic acid bath as describe in Chapter 3. In order to compare tribological properties, Ni-P coatings with the same P content as the present Co-Ni-P coatings were also plated from the sulphate bath.

7.2.2 Deposit Morphology, Composition and Hardness

The surface morphology and the composition of the as-deposited and annealed Co-Ni-P coatings as well as their cross sections were investigated by SEM equipped with EDS. The surface roughness of the coating was measured by AFM. The crystal structure was characterised by XRD using Cu Kα radiation. The morphology change along the growth direction was further studied by FIB. The hardness of deposits was measured as described in Chapter 3.

7.2.3 Tribological and Electrochemical Evaluation

The tribological and electrochemical behaviours were tested as described in Chapter 3. Additionally, morphology and composition of the worn surface and debris were studied by SEM and EDS.

7.3 Results

7.3.1 Electrodeposition of Co-Ni-P Coatings

Fig. 7.1(a) shows that the pH of the bulk solution decreased from approximately 2.9 to 1.9 during the electroplating process. The pH fell much faster during the first 20 min. The local pH measurements were performed in order to evaluate the pH shift at the electrode surface. It is found in Fig. 7.1(b) that the pH near the cathode immediately jumped from 2.9 to 10 at the very beginning of the electrodeposition. In the following 12 min, it rapidly dropped to 7 and was found to be proportional to $t^{1/2}$. Subsequently, it gradually changed from 7 to 6 at an approximately linear rate.

The electrodeposition of Co and Ni from the sulphate solution as well as the codeposition of phosphorus follows the reactions (2.10), (2.11) and (2.12) accompanied by simultaneous hydrogen evolution (Eq. (2.13)) [60]. The cathodic reactions (2.12) and (2.13) lead to an increase of pH, which explains the sudden pH rise near the cathode shown in Fig. 7.1(b). The following pH decrease may be attributed to hypophosphite oxidation and oxygen evolution near the anode [194, 195]:

$$H_2PO_2{}^- + H_2O \rightarrow H_2PO_3^- + 2H^+ + 2e^- \tag{7.1}$$

$$2H_2O \rightarrow O_2 + 4H^+ + 2e^- \tag{7.2}$$

The positively charged hydrogen ions were generated at the anode and simultaneously diffused through the electrolyte to the cathode. It was suggested that the rate of the proton production at the anode was higher than the rate of the hydroxyl radical production at the cathode. After 12 min, the relative generation rate between hydrogen ions and hydroxyl radicals changed and the local pH was more stable. The net generation of hydrogen ions led to the decrease in pH in the bulk solution.

Fig. 7.2(a) shows the electrodeposition potential (E_{ED})-time (t) dependence for the electrodeposition of the Co-Ni-P coating. The E_{ED}-t curve can be divided into three characteristic regions. In the initial region, the potential rapidly decreased during the first 20 s as shown in Fig. 7.2(b), which corresponded to the process of creating initial nucleus on the mild steel substrate. Similar phenomenons have been reported for nickel [196] and copper [197] electrodeposition, followed by a plateau for the remaining deposition time. However, in the present research, the potential did not converge to a steady-state value. Instead, in the region II from 20 s to 12 min, the potential gradually increased due to the decreasing pH near the cathode. For the electrode reaction $H_2PO_2{}^- + e^- \rightarrow P + 2OH^-$,

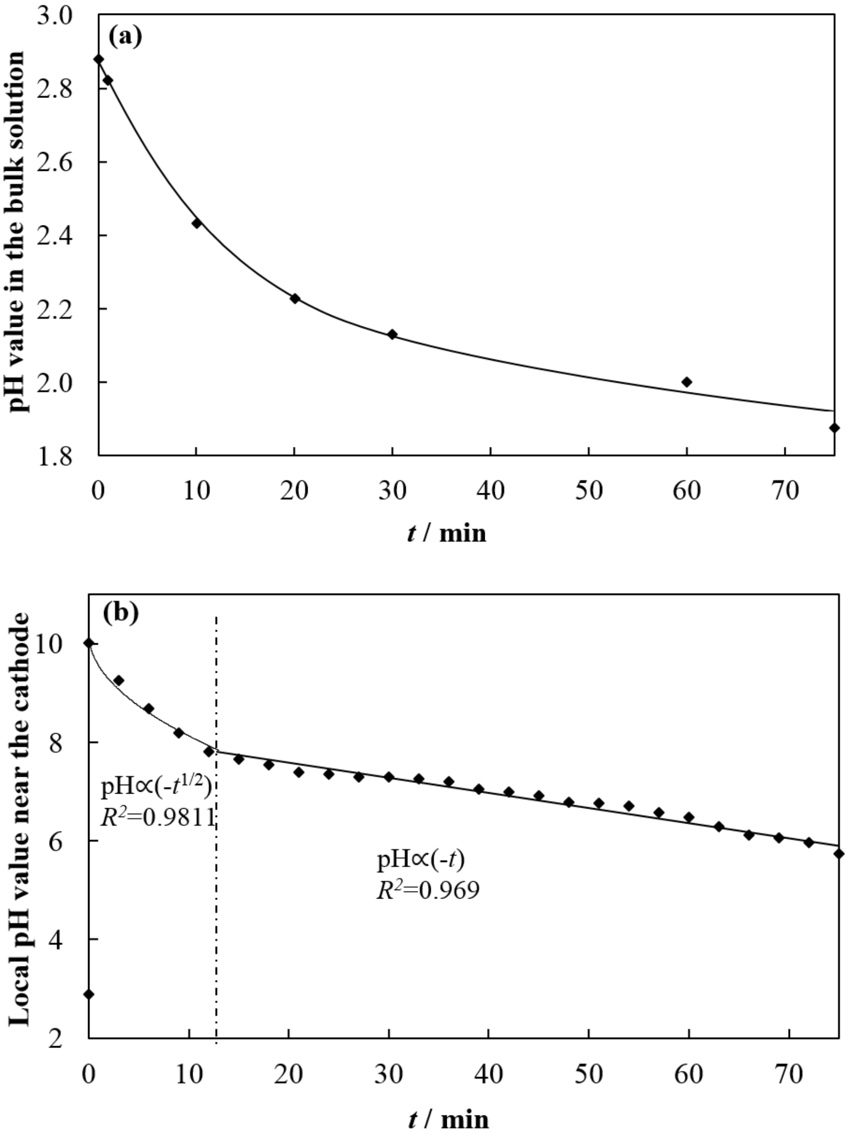

Fig. 7.1. Evolution of (a) bulk solution pH and (b) local pH near the cathode as a function of plating time.

the potential is linearly related to $\ln([\mathrm{H_2PO_2^-}]_*/[\mathrm{OH^-}]_*^2)$, where $[\mathrm{H_2PO_2^-}]_*$ and $[\mathrm{OH^-}]_*$ are the concentration of $\mathrm{H_2PO_2^-}$ and OH- next to the cathode [198]. If the concentration of $\mathrm{H_2PO_2^-}$ is assumed to be constant, it can be deduced that the mixed electrodeposition potential E_{ED} will be proportional to pH, which has a linear dependence on $t^{1/2}$. E_{ED} was plotted against $t^{1/2}$ as shown in Fig. 7.2(c) and the relationship of $E_{ED} \propto t^{1/2}$ was found. After 12 min, the potential linearly increased from -1.31 V to -1.27 V. The potential-time transient changed from $E_{ED} \propto t^{1/2}$ in stage II to $E_{ED} \propto t$ in the stage III due to the varied pH, which indicated different structure and composition of the deposits.

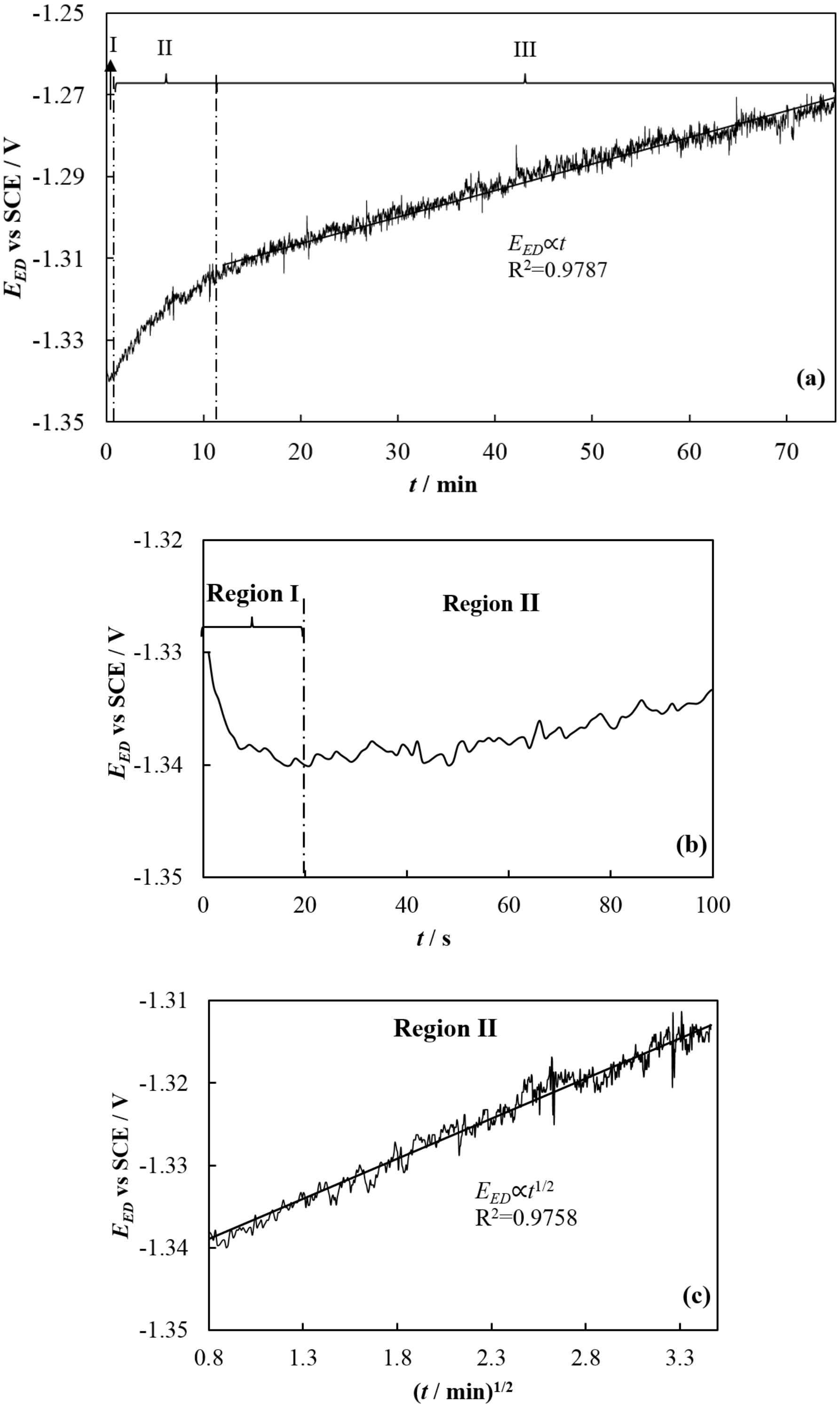

Fig. 7.2. Electrode potential vs. time curves during Co-Ni-P deposition with (b) the enlarged image of the first 100 s and (c) the E_{ED} versus $t^{1/2}$ plot from 20 s to 12 min.

7.3.2 Microstructure and Composition of As-deposited Co-Ni-P Coatings

Fig. 7.3 shows the surface morphologies of as-deposited Co-Ni-P coatings at different deposition times varying from 1 min to 75 min. After 1 min deposition (Fig. 7.3(a)), the surface of the substrate was covered by spherulites consisting of hundreds of grains as shown in the inserted high resolution image. The grain size was very small but clearly resolved at the average of 5 nm. The layer after 10 min plating (Fig. 7.3(b)) consisted of nodular clusters. The grain size measured from the high resolution image was also approximately 5 nm. Gaps were found among aggregations of the crystals. After 20 min, the coating surface was characterised by the adjacent smooth areas with no obvious spherulites as shown in Fig. 7.3(c). There were many small pits with a diameter less than 300 nm distributed along the boundary of the smooth areas. Most of the small pits were covered by the smooth layer after plating for 30 min as shown in Fig. 7.3(d). The smooth area was much bigger with unclear boundaries but with a few larger pits. With the further increase of plating time, no boundaries were observed as shown in Figs. 7.3(e, f). The surface was smoother with shallower pits. The surface roughness was approximately 12 nm.

The SEM cross-section view of the as-deposited Co-Ni-P sample plated for 75 min is shown in Fig. 7.4(a). The thickness of the coating is 25±3 µm. The initial deposit with the thickness of 6 µm grew columnarly, which was confirmed by the secondary ion image of FIB in Fig. 7.4(b). Fig. 7.3(a) and (b) are actually the top views of the columnar structure. As shown in Fig. 7.4(b), when the thickness was more than 6 µm, it suddenly changed to very fine structure, which corresponded to the smooth layer shown in Fig. 7.3(c). Thus, it can be concluded that the structure change occurred during the plating time between 10 min to 20 min. The growth of the columnar structure in Fig. 7.4(b) corresponds to the region II shown in Fig. 7.2(a, c).

The distribution of the elements with thickness of the as-deposited Co-Ni-P coating is shown in Fig. 7.4(c). The cobalt content gradually decreases from 82 at.% close to the substrate-coating interface to 61 at.% on the outer layer of the coating. The nickel content remains uniform at around 10-13 at.%. The phosphorus content increases from 7 at.% to 26 at.% with the increase of the coating thickness. The percentage of the less noble cobalt deposited preferentially, which has been reported in electroplated Ni-Co coatings [24, 181]. The anomalous deposition can be explained by the formation and adsorption of Co(II) and Ni(II) hydroxide ions on the cathode surface [142]. The noble nickel deposition is suppressed in the presence of $Co(OH)^+$ preferentially formed and adsorbed on the cathode. As the plating time increased, the trend of the anomalous deposition was weakened due to the pH decrease as shown in Fig. 7.1. The lower pH inhibits the formation of the metal hydroxide ions, which reduces the difference between $Ni(OH)^+$ and $Co(OH)^+$. Hereby, the preferred cobalt deposition is weakened. The concentration of Co^{2+} is reduced by approximately 5% after electroplating for 75 min, which also partially contributes to the decreasing ratio of Co/Ni. The deposition of P is promoted because of the decreasing pH according to Eq. (2.12).

XRD patterns of the as-deposited Co-Ni-P coatings with different plating times from 1 min to 75 min are shown in Fig. 7.5. The coating deposited for 1 min has a peak at $2\theta \approx 44.4°$ (Fig. 7.5(a)), which is consistent with the spacing of (0002) in hcp structured Co lattice and/or (111) in fcc structured Co (and/ or Ni). As the thickness increases after plating for 10 min, the intensity of the peak at $2\theta \approx 44.4°$ is much higher (Fig. 7.5(b)). The grain size was calculated according to the Scherrer equation (Eq. (3.1)) [167]. The calculated grain size of the coatings plated for 1 min and 10 min is 22 nm. The total XRD peak broadening is attributed to both microstrain and the grain size [179]. Due to the inevitable lattice distortion in the present coatings, the actual grain size should shift away from the calculated value (22 nm). As mentioned in Chapter 5, the grain size measured by XRD was consistent with the one obtained by TEM with the grain size just over 10 nm [170]. However, it seemed that the XRD failed to determine the grain size of a few nanometres for the coatings plated after 1 min and 10 min as shown in the present research.

The layer plated for 20 min with 17 at.% P exhibits the broad peak centred at approximately 44.5° as shown in Fig. 7.5(c), which corresponds to the amorphous structure. With the further increase of the plating time, the microstructure continues to be amorphous (Figs. 7.5(d-f)).

7.3.3 Thermal Stability

Fig. 7.6 shows the surface morphologies of the Co-Ni-P coatings after heat treatment at different temperatures for 1 h. Compared to the as-deposited sample shown in Fig. 7.3(f), there is no significant change in the morphology of the coating annealed at 200 °C (Fig. 7.6(a)), which has a similar composition as the as-deposited sample except for a small amount of oxygen as shown in Fig. 7.7. The oxidation of the coating surface starts from 300 °C, which corresponds to the formation of fibrous oxides shown in Fig. 7.6(b). With

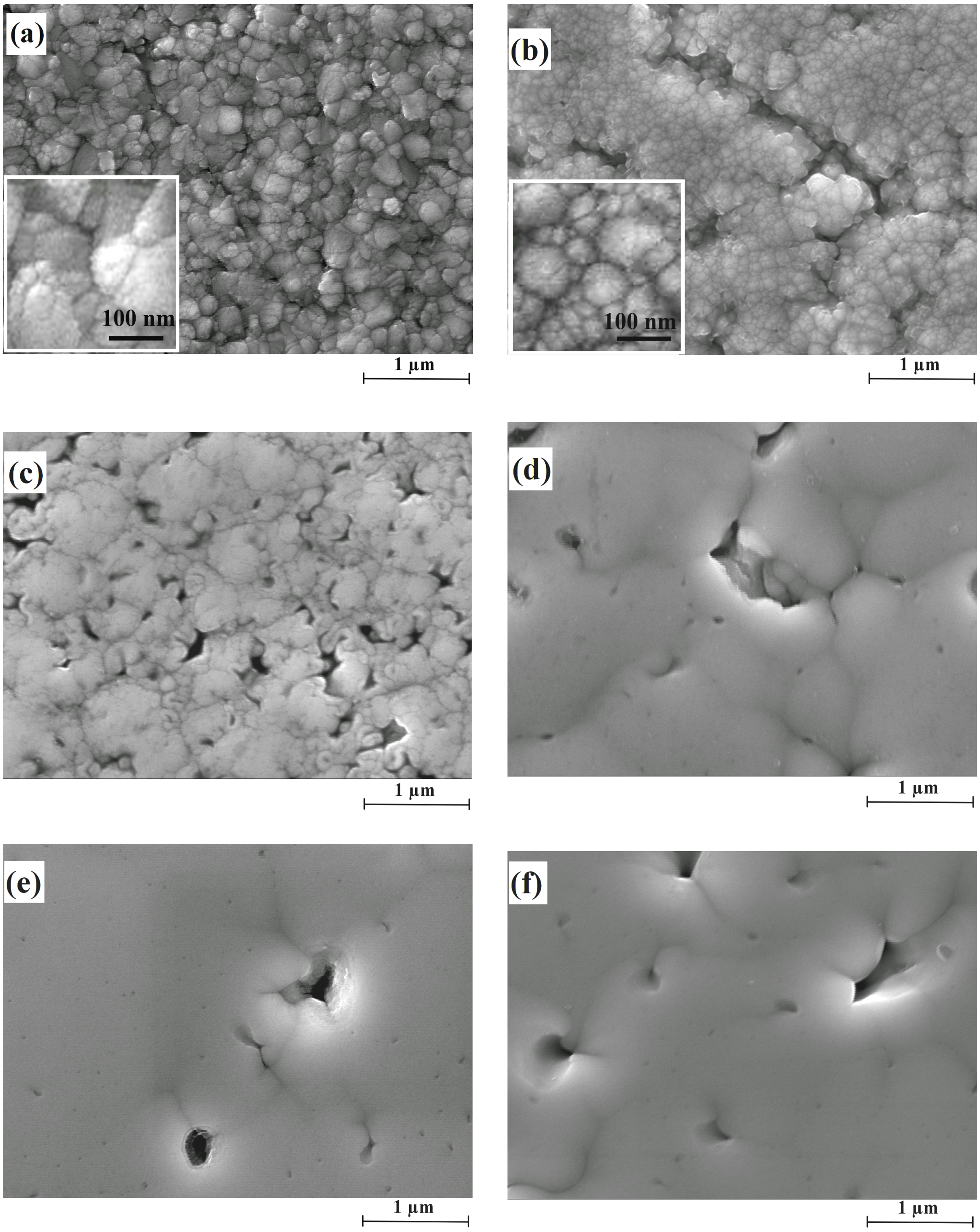

Fig. 7.3. Surface morphologies of as-deposited Co-Ni-P coatings after plating times of (a) 1 min, (b) 10 min, (c) 20 min, (d) 30 min, (e) 60 min and (f) 75 min.

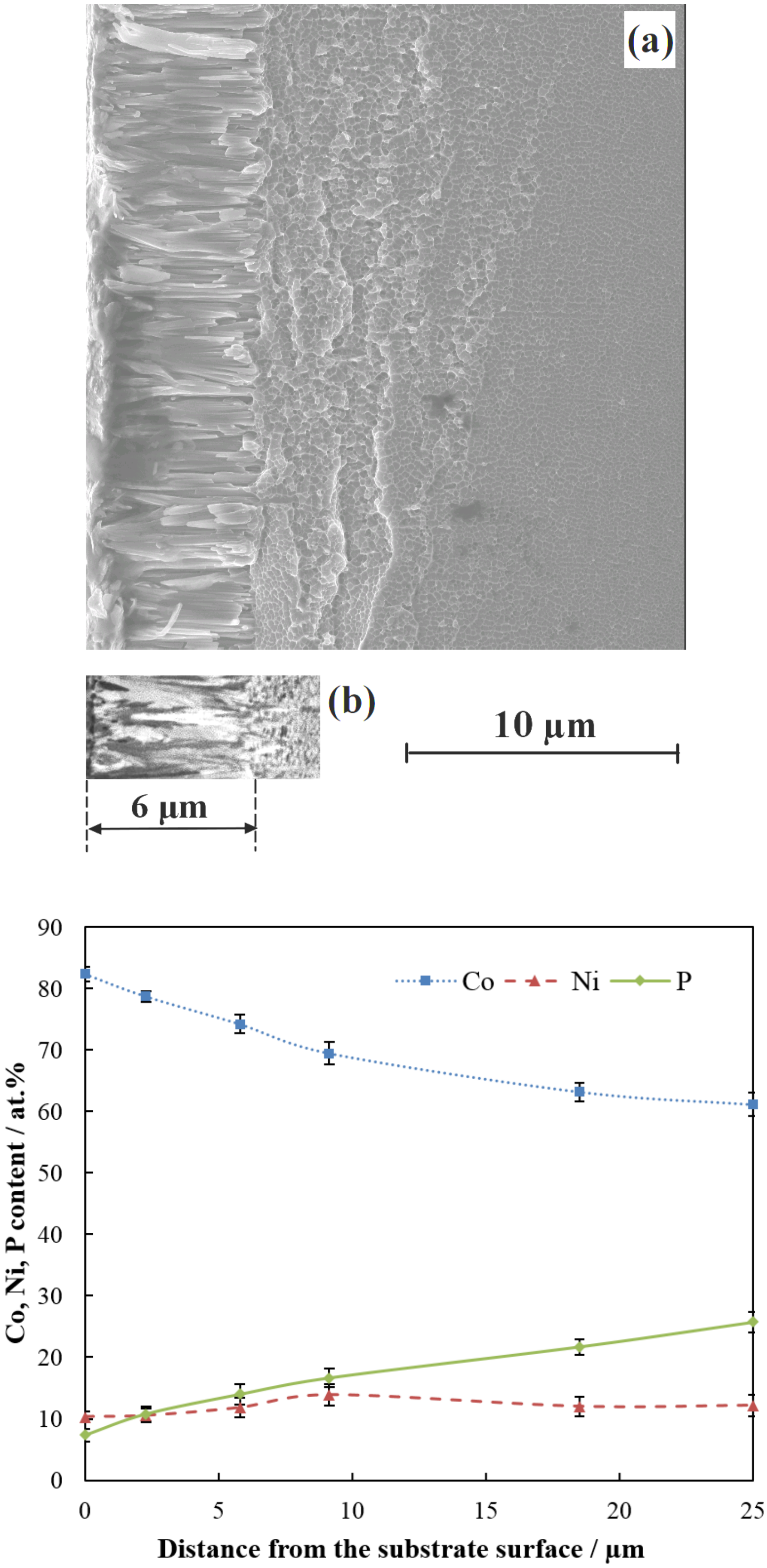

Fig. 7.4. (a) SEM cross-sectional view of the as-deposited Co-Ni-P coating plated for 75 min with (b) the FIB image of the enlarged area, (c) distribution of Co, Ni and P content with thickness.

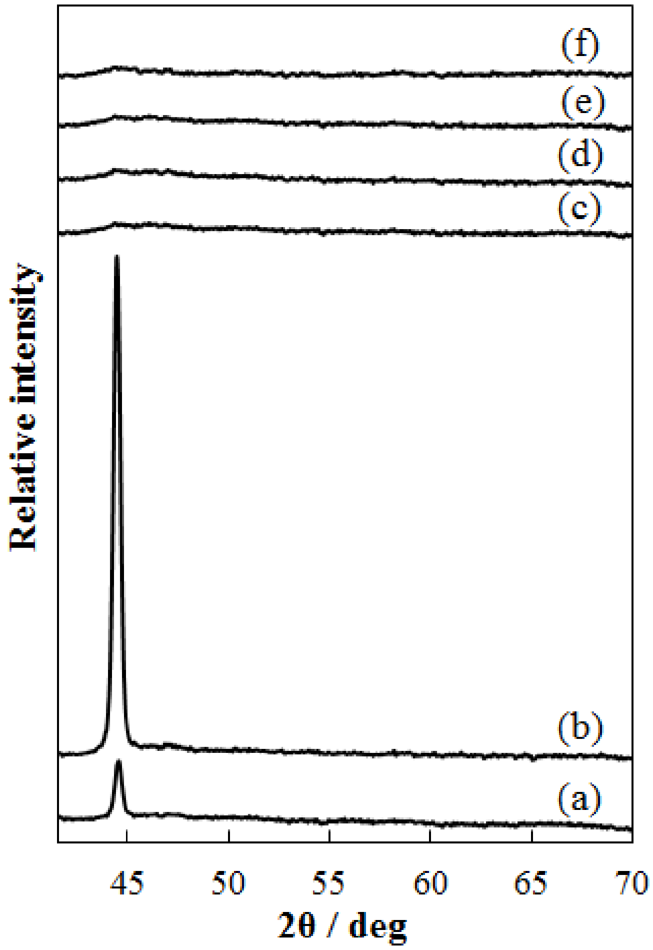

Fig. 7.5. XRD patterns of as-deposited Co-Ni-P coatings after plating times of (a) 1 min, (b) 10 min, (c) 20 min, (d) 30 min, (e) 60 min and (f) 75 min.

the increase of annealing temperature, the content of oxygen increases, while the content of Ni and P in the surface drops to 0 at 500 °C. The top layer of the coating annealed at 500 °C is totally covered by the fibrous cobalt oxides shown in Fig. 7.6(d). The surface roughness increases to approximately 60 nm. As shown in the Fig. 7.8(a) and (b), the 1 µm-thick cobalt oxide layer is followed by the layer depleted in Co, which indicates that the alloys undergo the external oxidation [199]. It had been reported that the oxide film of amorphous $Ni_{77}P_{23}$ oxidised at 300 °C in air mainly consists of NiO because the oxide was formed by the migration of Ni^{2+} ions along grain boundaries in the oxide film [200]. In the present Co-Ni-P ternary alloy, as the activation energy for the motion of Co^{2+} is lower than that of the Ni^{2+} [201], the major oxidation product of the top layer is cobalt oxide.

Fig. 7.9 shows the XRD patterns of the as-deposited Co-Ni-P coating and the samples annealed at different temperatures. No phase transition occurs for the sample annealed at 200 °C. A number of small peaks corresponding to $Ni_{12}P_5$ precipitates emerge as the annealing temperature increases to 300 °C. After annealing at 400 °C, new peaks appear in Fig. 7.9(d), which is consistent with the spacing of (200) and (220) in fcc structured CoO. As confirmed in Fig. 7.9(e), the intensity of the two peaks of the sample annealed at 500 °C increases as the top layer mainly consists of CoO.

7.3.4 Microhardness

The variation of hardness with annealing temperatures is shown in Fig. 7.10. The as-deposited Co-Ni-P coating has the microhardness of 602±15 HV, which is lower than the as-deposited hard chromium coatings. As the heat treatment temperature reaches 400 °C, the microhardness increases to 980±65 HV which is comparable to that of hard chromium coatings, and then decreases to 650±30 HV after annealing at 500 °C. Although no literature addresses on the hardening mechanism of Co-Ni-P coatings, the significant hardening has been reported for Ni-P alloys annealed at 400 °C [107, 202, 203]. It has been accepted that the precipitation of dispersed hard intermetallic compounds ($Ni_{12}P_5$ and Ni_3P) in the nickel matrix (which can impede the dislocation movement) result in increased hardness. Similarly, the formation of $Ni_{12}P_5$ precipitates as shown in Fig. 7.9 is responsible for the significant increase of hardness of the Co-Ni-P coating. The decrease of the hardness after annealing at 500 °C is probably due to the formation of oxide layer, the precipitate coarsening and $Ni_{12}P_5$ intermediate phase transition.

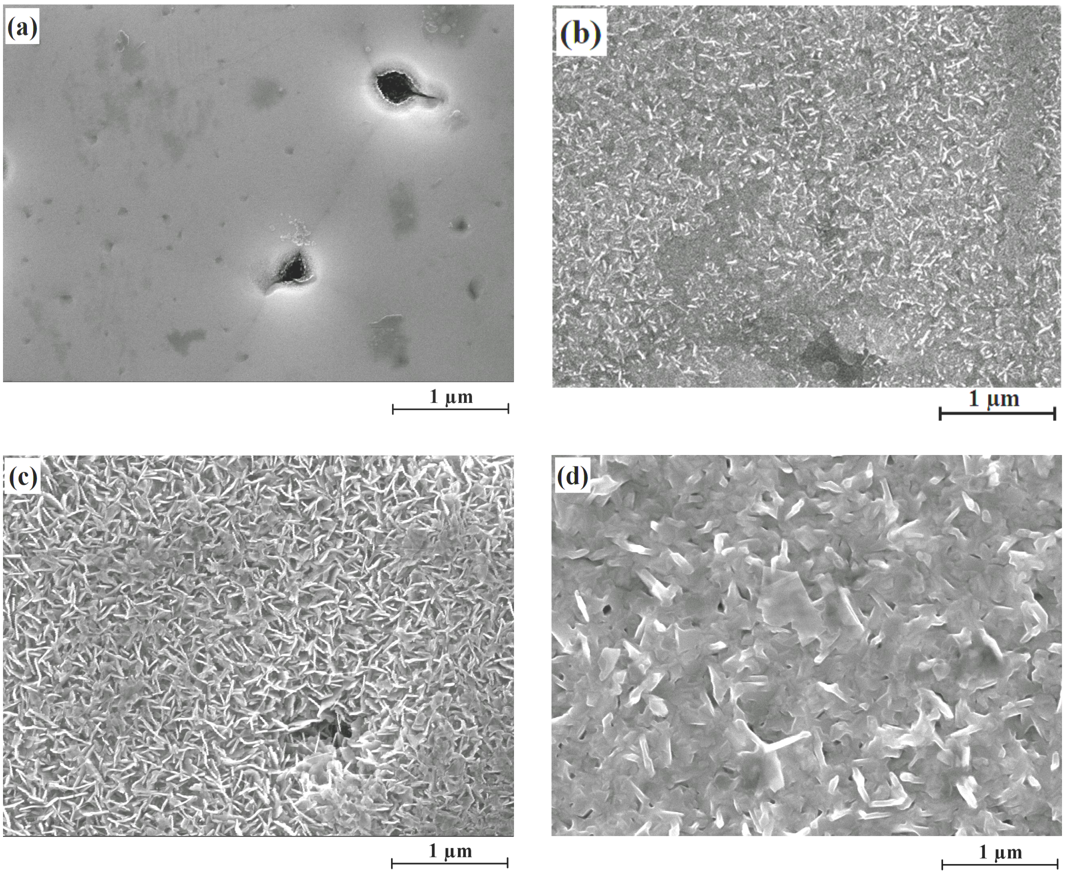

Fig. 7.6. Surface morphologies of heat treated Co-Ni-P coatings at (a) 200 °C, (b) 300 °C, (c) 400 °C and (d) 500 °C for 1 h.

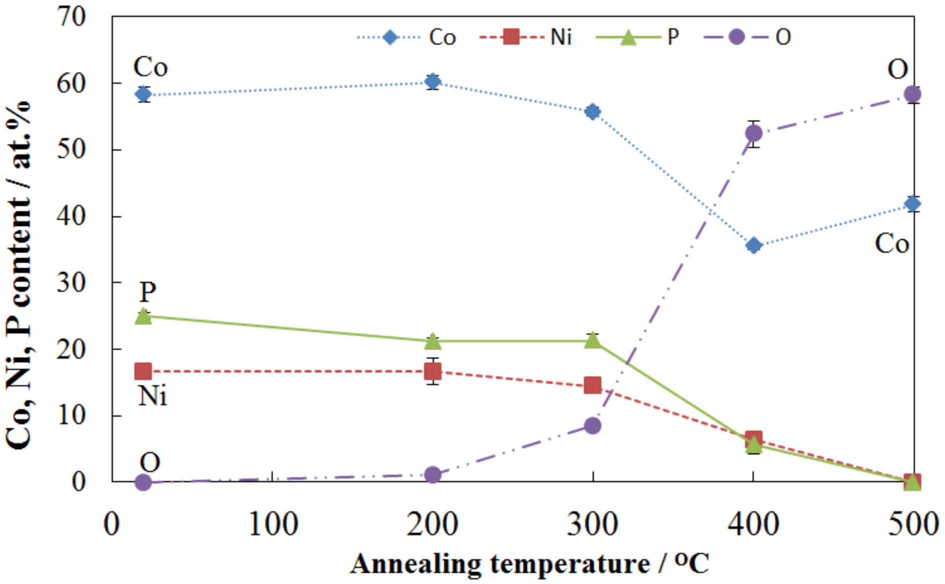

Fig. 7.7. Evolution of the elemental content from the deposit surface with annealing temperature.

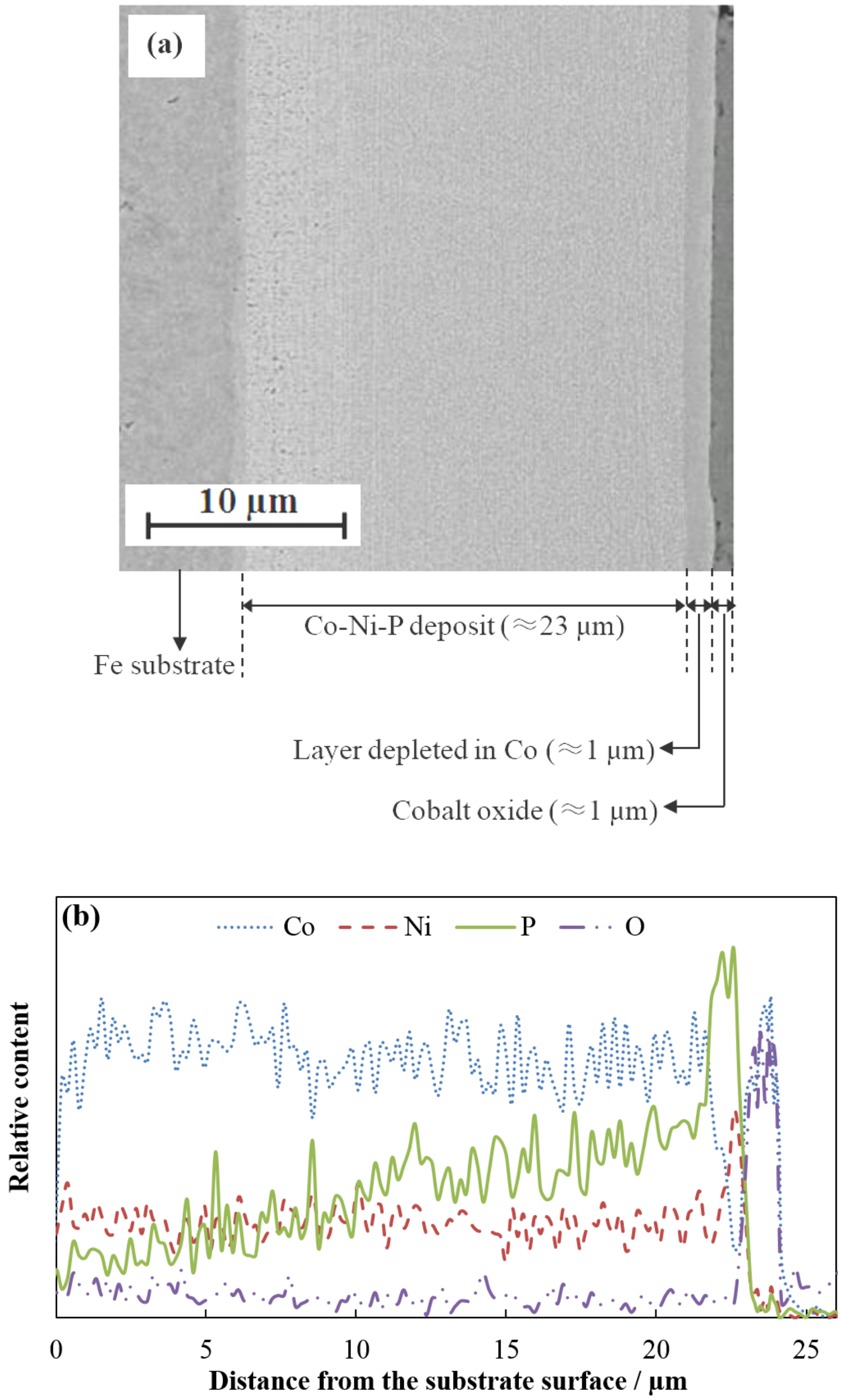

Fig. 7.8. (a) BEI cross-sectional view of the Co-Ni-P coating annealed at 500 °C, (b) distribution of Co, Ni and P content with thickness.

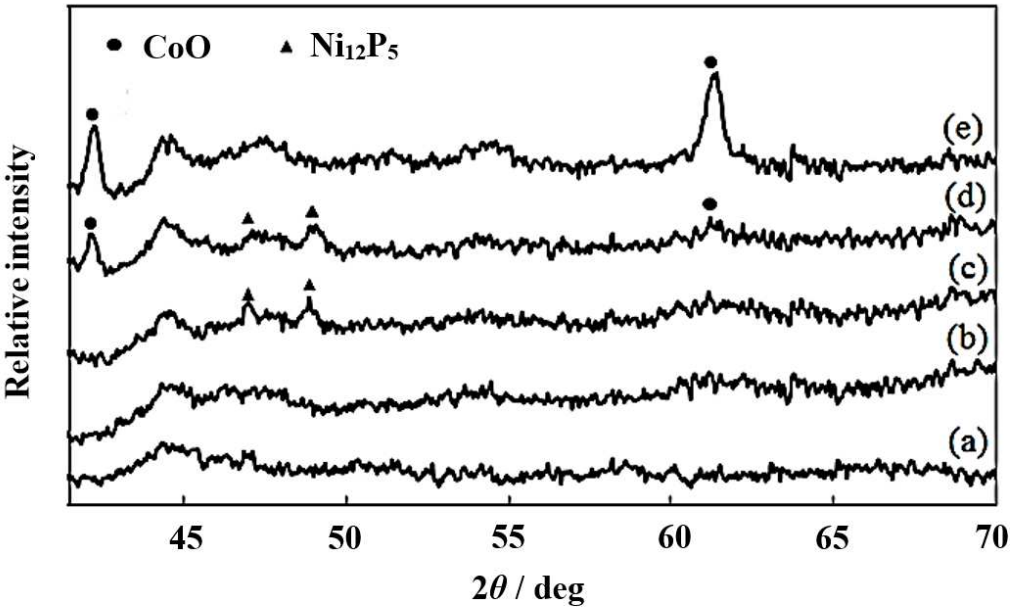

Fig. 7.9. XRD patterns of (a) as-deposited Co-Ni-P coatings plated for 75 min and the coatings annealed at (b) 200 °C, (c) 300 °C, (d) 400 °C, (e) 500 °C for 1 h.

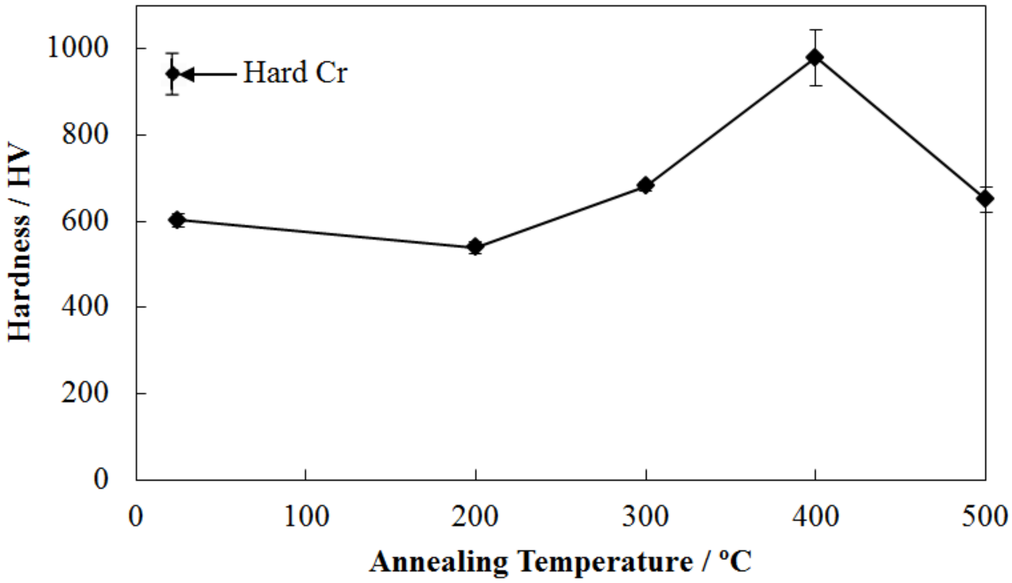

Fig. 7.10. Variation of hardness of the Co-Ni-P coatings annealed at different temperatures for 1 h compared with hard chromium coatings.

7.3.5 Friction and Wear Behaviours

Fig. 7.11 presents the comparison of coefficient of friction between as-deposited hard chromium coating and Co-Ni-P coatings annealed at different temperatures under dry sliding conditions. The coefficients of friction of both the as-deposited Co-Ni-P coating and the heat-treated samples are approximately 0.3 (only half that of hard chromium coatings). Without cobalt, the Ni-P coating with the same P content on the surface (25 at.%) has a higher coefficient of friction (0.5) under the same test conditions. It is found that the presence of cobalt reduces the coefficient of friction. The typical development of the coefficient of friction with time of the as-deposited Co-Ni-P coating and the coating annealed at 500 °C are shown in Fig. 7.12. The difference between the two curves is in the period of the run-in stage, where the curve of the coating annealed at 500 °C is less stable than its counterpart. It is attributed to the formation of cobalt oxide layer with higher surface roughness as shown in Fig. 7.6(d). In the steady-stable stage, the coefficient of friction of the sample annealed at 500 °C is slightly lower than that of the as-deposited sample.

Fig. 7.13 shows the effect of heat treatment temperature on the wear rates of Co-Ni-P coatings compared with hard chromium coatings. There is no significant change in the wear rate of the as-deposited coating and the sample annealed at 200 °C because of their similar surface morphology, composition, microstructure and hardness. As the annealing temperature was raised to 300 °C, the wear rate starts to decrease and the lowest wear rate (2.8×10^{-6} mm^3 N^{-1} m^{-1}) is obtained after the heat treatment at 400 °C due to the precipitation hardening by $Ni_{12}P_5$ precipitates. The wear rates of Co-Ni-P coatings annealed up to 400 °C are 4-7 times lower than that of hard chromium coatings. However, with further increase of the temperature to 500 °C the wear rate increases to 1.3×10^{-5} mm^3 N^{-1} m^{-1}.

The worn surfaces of the samples are shown in Figs. 7.14(a, c, e), indicating mild wear. The grooves and a small amount of wear debris along the sliding direction can be found on the worn track of the as-deposited sample (Fig. 7.14(a)). The worn surface of the sample annealed at 400 °C shown in Fig. 7.14(b) is much smoother with less plastic deformation due to its high hardness. However, the precipitation hardening leads to increasing brittleness. Therefore, the cracks normal to the sliding direction are observed on its worn surface. The wear debris is much less than that of the as-deposited sample. When the annealing temperature increases to 500 °C, wider cracks appear on the worn surface (Fig. 7.14(e)), which result in a higher wear rate. There is more debris than that

Table 7.1. Composition of the debris on the worn surface of as-deposited Co-Ni-P coating and the coatings annealed at 400 °C and 500 °C

Content / at.%	Debris		
	As-deposited sample	Annealed samples	
		400 °C	500 °C
O	37	44	30
Co	36	31	39
Ni	13	9	10
P	14	14	21
Fe	0	2	0

of the sample annealed at 400 °C. The formation of cracks on the worn surface can be attributed to the increase of the brittleness and internal stress. It has been reported that higher internal stress resulted in lower ductility and adhesion between coatings and substrates [150]. The pin wear scars were also examined by SEM and EDS. The size of the pin wear scar is in accordance with the wear rate. The wear debris was attached to the pin surface.

Typical morphologies of the debris are shown in Figs. 7.14(b, d, f) while their composition is listed in Table 7.1. There are two types of oxidised debris randomly distributed on the wear track of the as-deposited coatings (Fig. 7.14(b)), irregular shaped debris and the roll-like debris. The rolls are approximately 150-300 nm in diameter, and the length varies from 0.35 µm to 2.6 µm. As indicated by the arrows, the plate-like flakes start to be detached from the surface. As the heat treatment temperature increases to 400 °C, the plate-like flakes which are about to peel off are more obvious as the worn surface is smoother (Fig. 7.14(d)). Unlike the as-deposited coating, the debris of the sample annealed at 400 °C contains 2 at.% Fe from the pin. This can be attributed to its high hardness. It is interesting to find that most of the roll-like debris of the coating annealed at 500 °C shown in Fig. 7.14(f) is perpendicular to the sliding direction. The morphology of the roll-like debris is shown in the enlarged view in Fig. 7.14(f).

7.3.6 Corrosion Resistance

The polarisation curves measured in 3.5% NaCl of the Co-Ni-P coatings is shown in Fig. 7.15. The corrosion potential and current density compared with those of the hard chromium coating are listed in Table 7.2. It can be clearly observed that the corrosion potential positively increased from -558 mV to -348 mV as the annealing temperature increases. It can be attributed to the formation of the protective oxide layer [151]. The shift in corrosion potential is in accordance with the degree of oxidation. As mentioned

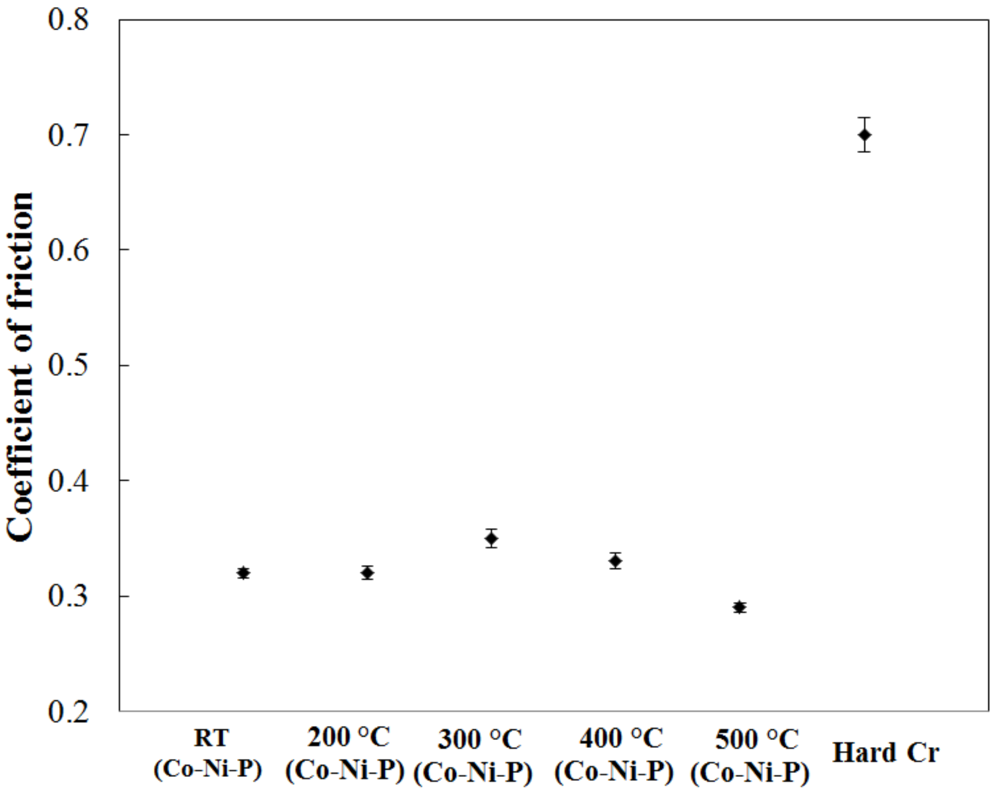

Fig. 7.11. Comparison of coefficient of friction between Co-Ni-P coatings annealed at different temperatures and as-deposited hard chromium coatings during unlubricated reciprocating sliding wear tests against AISI-52100 stainless steel with the sliding stroke of 2.69 mm, the sliding frequency of 1 Hz and the sliding time of 25 min.

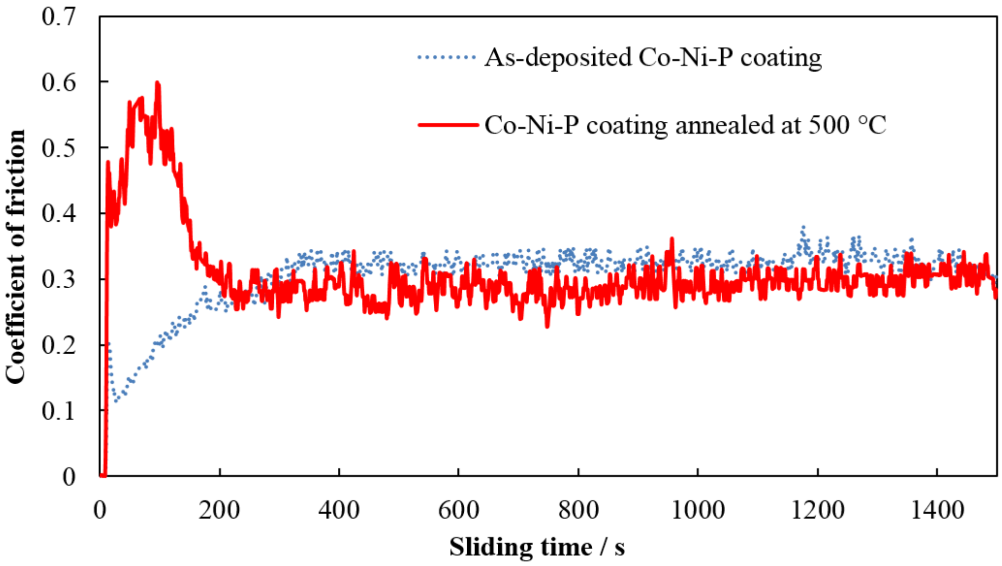

Fig. 7.12. The coefficient of friction of the as-deposited Co-Ni-P coating and the coating annealed at 500 °C for 1 h during unlubricated reciprocating sliding wear tests against AISI-52100 stainless steel with the sliding stroke of 2.69 mm, the sliding frequency of 1 Hz and the sliding time of 25 min.

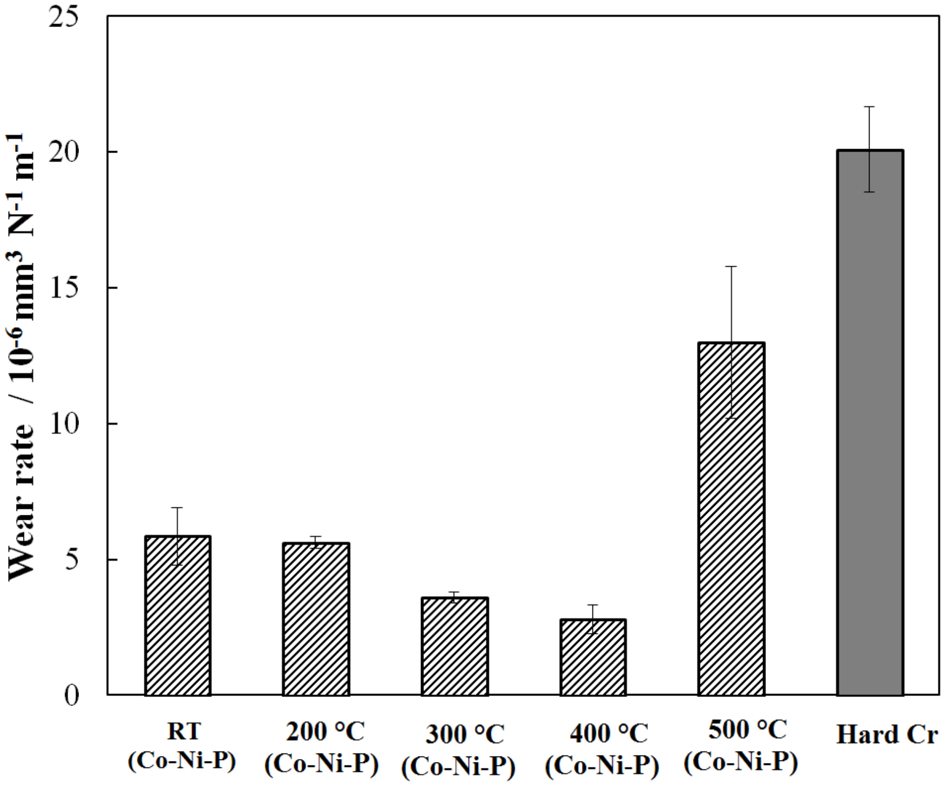

Fig. 7.13. Comparison of wear rates between Co-Ni-P coatings (25±3 µm thick) annealed at different temperatures and as-deposited thick hard chromium coatings (40±5 µm thick) after unlubricated reciprocating sliding wear tests against AISI-52100 stainless steel with the sliding stroke of 2.69 mm, the sliding frequency of 1 Hz and the sliding time of 25 min.

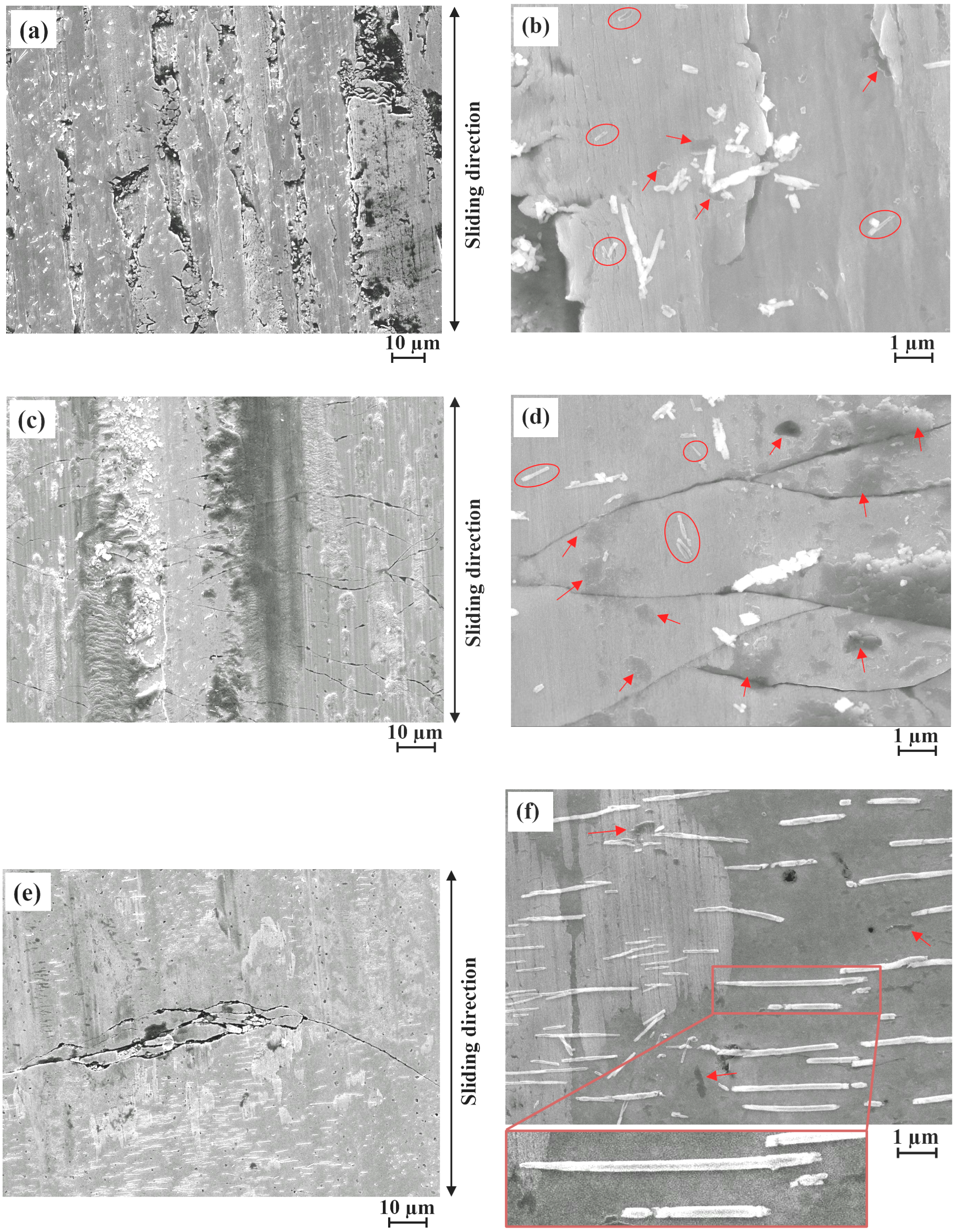

Fig. 7.14. Worn surface morphologies and debris of (a, b) as-deposited Co-Ni-P coating and the coatings annealed at (c, d) 400 °C and (e, f) 500 °C after unlubricated reciprocating sliding wear tests against AISI-52100 stainless steel with the sliding stroke of 2.69 mm, the sliding frequency of 1 Hz and the sliding time of 25 min.

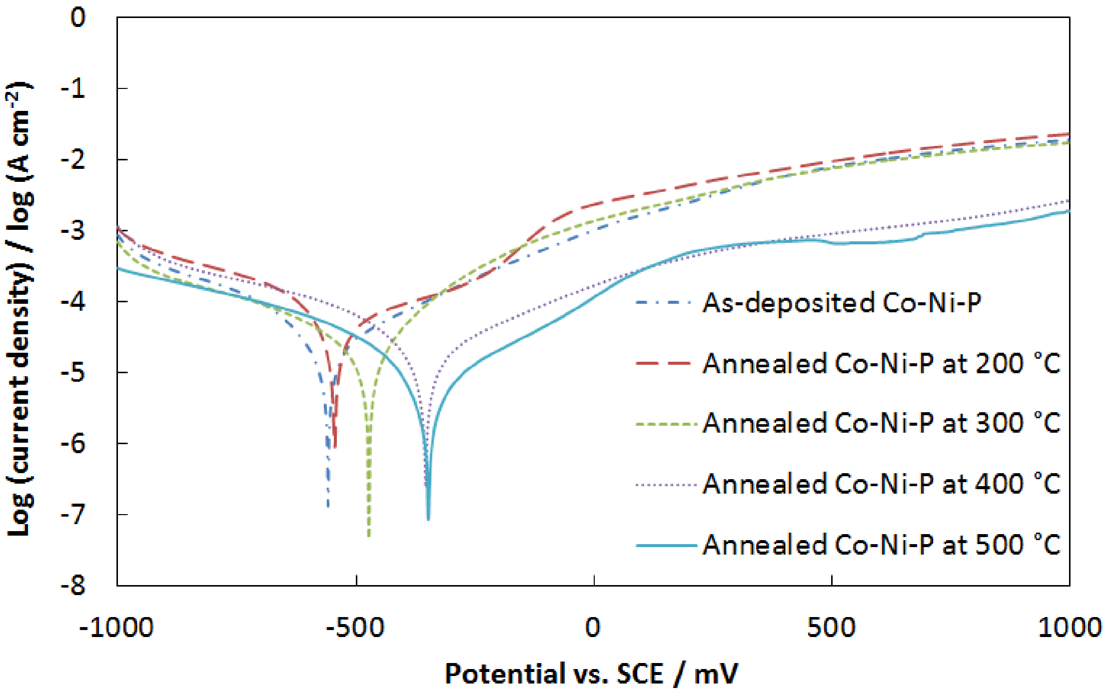

Fig. 7.15. Polarisation curves of Co-Ni-P alloys in 3.5% NaCl solutions.

in Section 7.3.3, the oxidation of the coating surface starts from 300 °C and the corrosion potential increases to -473 mV. When the top layer of the coating is completely oxidised at 500 °C, the corrosion potential reaches its most positive value (-348 mV). Although the corrosion potential of the Co-Ni-P coating annealed at 400 °C is slightly more negative than hard chromium, the corrosion current is only half that for hard chromium. As the annealing temperature is elevated to 500 °C, the corrosion current density increases to 3.8×10^{-6} A cm^{-2}. It can be ascribed to the loose-packed cobalt oxides on the surface shown in Fig. 7.6(d), which provides a more active area than the dense surface.

By comparing the corrosion resistance between the nanocrystalline 83 at.% Co-Ni coating listed in Table 4.4 and the as-deposited 61 at.% Co-13 at.% Ni-26 at.% P coating with the similar ratio of Co/Ni, it can be found that the addition of phosphorus to Ni-Co coatings reduces the corrosion current density from 7.65×10^{-6} A cm^{-2} to 3.58×10^{-6} A cm^{-2}, while the corrosion potentials positively increase from -603 mV to -558 mV. The amorphous structure of the Co-Ni-P coating surface leads to the more homogeneous structure with the absence of grain boundaries, dislocations, kink sites and other surface defects [16, 160, 204]. Therefore, the anti-corrosion properties are enhanced.

Table 7.2. Corrosion potential and corrosion current of Co-Ni-P alloys and hard chromium coating [14] in 3.5% NaCl solution

Coatings	As-deposited Co-Ni-P	Annealed Co-Ni-P				Hard Cr [62]
		200 °C	300 °C	400 °C	500 °C	
Corrosion potential vs. SCE / mV	-558	-544	-473	-354	-348	-299
Corrosion current density / 10^{-6} A cm^{-2}	3.58	2.89	1.50	1.44	3.80	3.30

7.4 Discussion

7.4.1 Microstructure Transition during Electrodeposition

As shown in Fig. 7.4 and Fig. 7.5, the transition from the nanocrystalline structure to the amorphous structure occurred after plating for 12 min, which corresponds to the transition of the E_{ED}-t curve from region II to region III in Fig. 7.2(a). The P content increased from an initial 7 at.% after 1 min plating, to 15 at.% at the transition stage (12 min plating) then to 26 at.% at the end of plating (75 min). Meanwhile, the pH near the cathode decreased from 10, to 8 then 6, respectively. The structure evolution could be due to the atomic mismatch. The Co-Ni solid solution has the atomic diameter of 0.250 nm, whereas the solute P has a much smaller one at 0.217 nm. The mismatch between two different atoms is 13.2%, which is equivalent to a distortion of 1.98% for the 15 at.% P embedded in the Co-Ni solid solution. It appears the Co-Ni matrix can accommodate approximately 2% strain to hold the crystal structure. Above this criterion, Co-Ni-P alloys will favour the amorphous structure to accommodate more solute P. A FIB/TEM combination and simulation could be helpful for the clarification, which will be carried out in future work.

As shown in Fig. 7.16, it is found that the Co-Ni-P film plated on a previous Co-Ni-P coating with the amorphous surface layer has the same morphology evolution. Therefore, the change of the microstructure cannot be attributed to the influence of the substrate. Manna et al. [194] reported that the pH had no effect on the microstructure of the electroless Ni-P-Fe coatings based on the results of the coatings treated for 30 min, 60 min and 90 min. In the present research, the pH is found to play an important role in the surface morphology, composition and microstructure. This contradictory result is, perhaps, due to their lack of deposition data during the first 30 min.

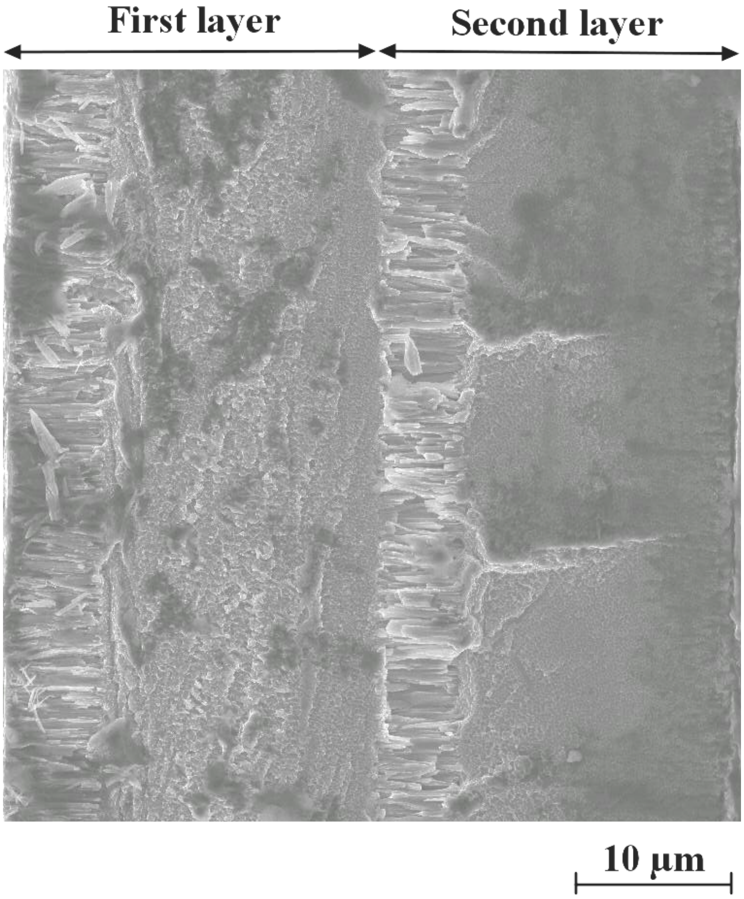

Fig. 7.16. SEM cross-sectional view of the as-deposited Co-Ni-P coating (second layer) on a previous Co-Ni-P coating (first layer).

7.4.2 Formation and Role of Roll-like Wear Debris

The closer inspection of the roll-like debris shown in Figs. 7.14(b, d, f) reveals that the inner part of the smaller roll-like debris highlighted in the circles is darker than the edge, which indicates that the rolls are not solid. As indicated by the arrows, the plate-like flakes start to be detached from the surface and the edge of the flakes has been warped due to the residual stress [205]. Therefore, it is suggested that the rolls are made up of removed sheets. As shown in Fig. 7.14(f), more roll-like debris with more regular shape was observed on the worn surface of the coating annealed at 500 °C. It seemed that the flakes detached from the surface of the coating annealed at 500 °C were easier to roll up than those of the other two coatings, which may be attributed to its different surface composition. The total cobalt oxide layer followed by the layer depleted in Co shown in Fig. 7.8 may introduce more residual stress to form the rolls,

The roll-like debris has been reported by several researchers in ceramics, such as silicon [206], alumina [207], silicon nitride [208], SiC–Al_2O_3 nanocomposites [209], and transition metal nitride coatings [210, 211]. Generally, the formation of roll-like debris is associated with the tribo-chemical reactions of sliding surfaces with the environment species (e.g. water and oxygen) to form a tribofilm [212, 213]. Some authors believe that the cylindrical debris on silicon [212] and TiAlN/VN multilayer coatings [210] was generated by the agglomeration and densification of wear particles which were subjected to opposing tangential forces at the top and bottom. However, the roll-like debris shown in Figs. 7.14(b, d, f) was not solid. Nevertheless, the phenomenon that the plate-like flakes with warped edges start to detach from the worn surface has been observed. Therefore, it is suggested that the rolls in the present research are made up of the removed sheets.

It has been accepted that the presence of the rolls is related to the mild wear regime, but the effect on the tribological properties is controversial. Fisher et al. [207] believed that the rolls on the wear track of a flat Al_2O_3 specimen against an Al_2O_3 ball were generally soft and therefore they were the consequence rather than the cause of the low wear rate. Bajwa et al. [214] found that the rolls formed by the tribochemical wear had limited contribution to the wear rate in the wear testing of SiC-Al_2O_3 composites against alumina balls. However, Zhou et al. [175] reported that the roll-like wear debris formed during the sliding of TiAlN/VN coatings against Al_2O_3 balls was associated with higher friction. By contrast, Zanoria et al. [212] observed that the formation of the cylindrical debris on silicon at 600 °C resulted in the decrease of the coefficient of friction from 0.5 to under 0.2. Moreover, the wear rate was much lower compared to that of the sample tested at 100 °C without the formation of rolls. The authors attributed the reduced coefficient of friction and improved wear resistance to the presence of the rolls which acted as roller bearings. They also found that in the initial stage of the sliding test the coefficient of friction was approximately 0.6 and decreased until it reached a steady state (0.1-0.2). The process is similar to the evolution of coefficient of friction of the Co-Ni-P coating annealed at 500 °C in the present research as shown in Fig. 7.12. It is suggested that the initial fluctuation is due to the high surface roughness of the oxide layer as mentioned above. Additionally, the generation of wear debris and tribofilm leads to the increase of coefficient of friction in the running-in stage of sliding tests [210]. It is noticed that the roll-like debris on the wear track of the coating annealed at 500 °C has much higher population density and more regular shape. The debris is also aligned more closely perpendicular to the sliding direction. They might be related to the slightly lower coefficient of friction than that of the as-deposited sample in the steady-state stage although it was not an evident contribution. It is an interesting topic which requires more experimental work on the composition, hardness and role of roll-like debris and tribofilm in future work.

7.5 Summary

A new Co-Ni-P coating with reduced coefficient of friction and improved wear resistance has been developed by electrodeposition for the replacement of hard chromium coatings. The compositional, morphological, structural, mechanical and tribological properties of the as-deposited and annealed Co-Ni-P coatings were characterised. The following conclusions have been drawn:

(1) Along the growth direction, the microstructure changed from nanocrystalline to amorphous structure as the phosphorus content increased from 7 at.% to 26 at.%. Correspondingly, the surface morphology changed from crystal clusters to smooth surface with low surface roughness (R_a=12 nm). The structural change occurred as the P content exceeded approximately 15 at.% after plating for 12 min due to the atomic mismatch. The local pH rather than the substrate had a significant effect on the evolution of surface morphologies, composition and microstructure.

(2) The oxidation of heat-treated Co-Ni-P coatings started from 300 °C and the top layer of the coating annealed at 500 °C was totally covered by the fibrous cobalt oxide, mainly CoO. The layer depleted in Co was found beneath the oxide layer, which indicated that the Co-Ni-P alloys underwent the external oxidation. $Ni_{12}P_5$ precipitates were formed from the amorphous phase when the coatings were annealed above 300 °C. The hardness

of the as-deposited sample was 602±15 HV. As the heat treatment temperature reached 400 °C, the microhardness increased to 980±65 HV (comparable to that of hard chromium coatings) because of the precipitation hardening. Subsequently, it decreased to 650±30 HV after annealing at 500 °C probably due to the formation of oxide layer, the precipitate coarsening and $Ni_{12}P_5$ intermediate phase transition.

(3) The coefficients of friction of both the as-deposited Co-Ni-P coating and the heat-treated samples under dry sliding conditions against a AISI-52100 stainless steel ball were approximately 0.3, only half of that of hard chromium. As the annealing temperature rose to 300 °C, the wear rate started to decrease and the coating annealed at 400 °C had the lowest wear rate (2.8×10^{-6} mm^3 N^{-1} m^{-1}), which was an order of magnitude lower than that of hard chromium coatings. With a further increase of the temperature to 500 °C the wear rate increased, which may be attributed to its decreased microhardness and high internal stress.

(4) Roll-like debris was found on the worn surface. It was believed to be made up of the removed sheets from the coating surface. More roll-like debris was observed on the worn surface of the coating annealed at 500 °C. Furthermore, the debris was also aligned more closely perpendicular to the sliding direction. It may be related to the slightly lower coefficient of friction compared to that of the as-deposited coating in the stable stage. In the run-in stage, the coefficient of friction of the coating annealed at 500 °C was less stable than that of the as-deposited coating. It was attributed to its higher surface roughness and the formation process of the roll-like debris.

(5) The as-deposited 61 at.% Co-13 at.% Ni-26 at.% P coating with amorphous surface structure exhibited better corrosion resistance in 3.5% NaCl solution than nanocrystalline 83 at.% Co-Ni coating with the similar ratio of Co/Ni. The corrosion current the Co-Ni-P coating annealed at 400 °C was only half of that for hard chromium. The improved anti-corrosion properties can be attributed to the formation of a protective oxide layer.

Chapter 8

Overall Conclusions and Suggestions for Future Work

8.1 Overall Conclusions

In the present research, the tribological and electrochemical properties of nanocrystalline Ni-Co alloys with different cobalt contents have been studied and the role of a tribofilm and wear debris has been examined. Nanocrystalline single-layer Ni-Co coatings with high cobalt content were electrodeposited onto mild steel substrates by optimising the concentration of additives. The effect of additives on the microstructure and properties has been investigated. Different nickel salts (nickel sulphate and/or nickel chloride) have been found to have significant effect on the surface morphology, porosity and hardness of Ni-Co coatings. A cluster-pore mixture model has been proposed to explain the deviation of the Hall-Petch relationship. By combining the lubricity of cobalt-rich Ni-Co coatings and the precipitation hardening of Ni-P alloys, a new Co-Ni-P coating with superior properties to hard chromium coatings for anti-wear and anti-corrosion applications has been developed. The conclusions of the main results can be stated.

(1) A tribofilm consisting of oxides of both the coating and the counterpart was found on the worn surface of the Ni-Co coatings having a cobalt content less than 60 at.%. The formation of the tribofilm was not beneficial to the friction reduction and the wear resistance. As the cobalt content exceeded 70 at.%, the coefficient of friction dropped from 0.45-0.5 to ca. 0.25 . At the same time, the wear rate gradually decreased. No tribofilm was formed on the Co-rich coatings (more than 70 at.% Co) and the stainless steel pin contact. No pin material transfer from the pin to the coating was observed. The improved wear resistance was mainly due to a large portion of hcp structure of the Co-

rich coatings, which can act as the solid lubricant. The nanocrystalline debris contained a mixture of two phases: a nickel fcc metallic phase and a nickel oxide/cobalt oxide fcc oxidised phase. No hcp structure was found in the debris due to the complete oxidation of cobalt. The debris cannot form an efficient lubricative film to promote separation of the sliding surfaces and had a limited effect on the contact of rubbing surfaces. Ni-Co coatings exhibited the active-passive polarisation behaviour in 3.5 % NaCl solution. The corrosion resistance of Ni-Co coatings needs to be further improved in order to replace hard chromium in anti-corrosion applications.

(2) The effect of additives on the microstructure and properties of Ni-Co coatings with high cobalt content is presented in Chapter 5. The 78±2 at.% Co-Ni coatings with the grain size of 11±2 nm plated from the bath containing 0.5 g dm^{-3} BD and 2 g dm^{-3} saccharin had a smooth, optically reflective surface. As the concentration of additives decreased, the microstrain changed from compressive to tensile and its magnitude was significantly increased. Although the addition of BD promoted the formation of $(10\bar{1}0)_{\mathrm{hcp}}$ texture, the inhibition effect of saccharin was dominant. The fibre texture of the coating was modified from $(10\bar{1}0)_{\mathrm{hcp}}$ to $(0002)_{\mathrm{hcp}}/(111)_{\mathrm{fcc}}$ as the concentration of saccharin increased.

(3) The effect of different nickel salts (nickel sulphate and/or nickel chloride) on the morphologies, grain sizes and hardness of the Ni-Co coatings (77±2 at% Co) is present in Chapter 6. The finest grain size, approximately 11 nm, was obtained from a coating with dense and smooth surface developed from the nickel sulphate bath. By adding nickel chloride in the bath, the coating had the porous lens-shaped microstructure consisting of a number of fine grains (around 15 nm). The surfaces of the coatings plated from the chloride-dominant bath and the all-chloride bath had clusters with much smaller size than that of the lens-shaped clusters. The grain size increased to approximately 23 nm. The hardness of porous coatings except the dense coating deposited from an all-sulphate bath exhibited the deviation of the Hall-Petch relationship. The extent of deviation depended on the porosity of coatings. By considering porous materials as composites of clusters and pores, their contribution to hardness has been quantitatively studied. The pore-free hardness (i.e. the hardness of clusters) can be calculated according to the cluster-pore mixture model. By adopting it, the Hall-Petch relationship can be maintained at the nanoscale. The present model can be applied to other porous nanocrystalline coatings, and the Hall-Petch relationship is maintained.

(4) The local pH rather than the substrate had a significant effect on the evolution

of surface morphologies, composition and microstructure of Co-Ni-P coatings. Along the growth direction, the microstructure changed from nanocrystalline to amorphous structure as the phosphorus content increased from 7 at.% to 26 at.%. The structural change occurred as the P content exceeded approximately 15 at.% after plating for 12 min due to the atomic mismatch. The oxidation of Co-Ni-P coatings started from 300 °C and the top layer of the coating annealed at 500 °C was totally covered by the fibrous cobalt oxide; mainly CoO. $Ni_{12}P_5$ precipitates were formed from the amorphous phase when the coatings were annealed above 300 °C. The hardness of the as-deposited sample was 602±15 HV and increased to 980±65 HV (comparable to that of hard chromium coatings) after annealing at 400 °C because of the precipitation hardening. The coefficients of friction of both the as-deposited Co-Ni-P coating and the heat-treated samples under dry sliding conditions against a AISI-52100 stainless steel ball was approximately 0.3, only half of that of hard chromium. The coating annealed at 400 °C had the lowest wear rate (2.8×10^{-6} mm^3 N^{-1} m^{-1}), which was an order of magnitude lower than that of hard chromium coatings. With a further increase of the temperature to 500 °C the wear rate increased, which may be attributed to its decreased microhardness and high internal stress. The roll-like debris was made up of sheets removed from the coating surface. The roll-like debris on the worn surfaces of the coating annealed at 500 °C was oriented perpendicularly to the sliding direction. They may be related to the slightly lower coefficient of friction compared to that of the as-deposited coating in the stable stage. In the run-in stage, the coefficients of friction of the coating annealed at 500 °C was less stable than that of the as-deposited coating. It is attributed to its higher surface roughness and the formation process of the roll-like debris. The Co-Ni-P coating annealed at 400 °C exhibited better corrosion resistance in 3.5% NaCl solution than hard chromium coatings due to the formation of a protective oxide layer.

8.2 Novel Contributions

The obtained results and analysis show up the following novel contributions:

(1) The novel investigation concerning the role of tribofilms and wear debris in the tribological behaviour of nanocrystalline Ni–Co electrodeposits with different cobalt contents shows that no tribofilm or iron transfer from the counterbody pin was found on the Co-rich coatings (more than 70 at.% Co), which exhibited a dramatic friction reduction of 50 % and improved wear resistance. The improved tribological properties is mainly due to a large portion of hcp structure of the Co-rich coatings, which can act as the solid

lubricant. The debris was nanocrystalline, containing an fcc metallic phase and an fcc oxidised phase, irrespective of the coating composition.

(2) A new approach to fabricate single layer Ni-Co coatings with high cobalt content has been developed by appropriate selection and optimisation of additives. Compared to graded coatings [18] and the application of pulse current waveforms [36–38], the present method is more feasible in industry and cost competitive. The high quality 78±2 at.% Ni-Co coating plated from the bath with optimised amount of additives (0.5 g dm^{-3} BD and 2 g dm^{-3} saccharin) exhibited high hardness and improved tribological properties.

(3) The effect of additives (BD and saccharin) on surface morphology, grain size and crystalline texture of Ni-Co has been studied. It was found that the inhibition effect of saccharin resulted in the texture evolution from $(10\bar{1}0)_{\mathrm{hcp}}$ to $(0002)_{\mathrm{hcp}}/(111)_{\mathrm{fcc}}$.

(4) A new cluster-pore mixture model is proposed by considering porous materials as composites of clusters and pores. According to it, the pore-free hardness can be calculated, which is in agreement with the ordinary Hall-Petch relationship at the nanoscale.

(5) A novel friction reducing and wear resistant Co-Ni-P coating with improved corrosion performance has been fabricated by combining the precipitation hardening found in Ni-P alloys and the lubricity of cobalt-rich Co-Ni coatings. Compared to thin Co-Ni-P coatings (from 10 nm to 10 µm thick) as hard magnetic materials reported in the literature, the composition and thickness of the present coating have been optimised by tailoring the bath composition and electroplating parameters for anti-wear and anti-corrosion applications. As summarised in Table 8.1, the Co-Ni-P annealed at 400 °C can match the hardness and anti-corrosion properties of hard chromium. Moreover, it exhibits superior tribological properties compared to hard chromium and other alternative electrodeposited coatings [14]. The formation of the roll-like debris on the worn surfaces of the coating annealed at 500 °C is discussed.

(6) The novel investigation on the composition and microstructure of Co-Ni-P reveals that the local pH near the cathode played an important role in the change of the microstructure from nanocrystalline to amorphous along the growth direction as the phosphorus content increased from 7 at.% to 26 at.%.

8.3 Future Work

The following suggested work should be helpful for the further improvement of the properties of electrodeposited coatings for hard chromium replacement as well as the further understanding of the relationships among electroplating variables, microstructure, micro-

Table 8.1. Comparison of corrosion and tribological properties between alternative electrodeposited coatings and hard chromium

	Hardness / HV	Coefficient of friction	Wear rate / 10^{-6} mm^3 N^{-1} m^{-1}	Corrosion potential$^{\#}$ vs. SCE / mV	Corrosion current density$^{\#}$ / 10^{-6} A cm^{-2}
Hard Chromium	943±47	0.75-0.85	21±2	-299 [62]	3.30 [62]
Co-Ni-P annealed at 400 °C	980±65	0.3	2.8±0.4	-354	1.44
Single-layer 75 at.% Co-Ni	490±17	0.23	95±11	-546	6.85
Graded Ni-P annealed at 400 °C [14]	1000	0.45†	33†	-	-

$^{\#}$ Obtained in 3.5 % NaCl solution.

† The tribological behaviour was tested on a reciprocating ball-on-disc UMT-2MT micro-tribometer tester with a Si3N4 ceramic balls (diameter 3 mm) as the counter body under a normal load of 20 N at a sliding speed of 0.4 m s^{-1}.

hardness, tribological and electrochemical properties.

(1) The cross-section TEM and EDS analysis can be employed to fully characterise the tribofilms on the worn surface of the Ni-Co coatings having a cobalt content less than 60 at.%.

(3) New studies could be carried out to further clarify the microstructure evolution of Co-Ni-P coatings by a FIB/TEM combination and simulation.

(4) The cracks found on the worn surface of the Co-Ni-P coatings annealed at 400 °C and 500 °C can be attributed to the increase of the brittleness and internal stress caused by induced crystallographic mismatch. It would be interesting to determine the effect of residual stress after heat treatment on the tribological properties.

(5) The composition, hardness and role of roll-like debris and the tribofilm formed on the worn surfaces of Co-Ni-P coatings could be further investigated.

(6) There is a lack of information regarding the effect of electroplating parameters on the tribological and electrochemical properties of Co-Ni-P coatings. Most research focuses on their unique magnetic properties. It would be interesting to carry out systematic experiments to determine the optimised conditions to produce Co-Ni-P coatings for anti-wear and anti-corrosion applications.

(7) In order to further increase the microhardness of as-deposited Co-Ni-P coatings to

match that of hard chromium, composite coatings can be developed by co-depositing hard particles, such as boron nitride, silicon carbide and alumina. Other functional particles (such as solid state lubricants, e.g. WS_2) can be added into the Co-Ni-P matrix to expand their applications. This is a challenging topic which requires more experimental work.

References

[1] Z. Zeng, A. Liang, and J. Zhang, “A review of recent patents on trivalent chromium plating,” *Recent Patents on Materials Science*, vol. 2, pp. 50–57, 2009.

[2] D. L. Snyder, “Decorative chromium plating,” *Metal Finishing*, vol. 97, no. 1, pp. 219–226, 1999.

[3] K. Newby, “Functional chromium plating,” *Metal Finishing (USA)*, vol. 95, no. 1, pp. 219–221, 1997.

[4] “Overview of the five chemicals alternatives assessment study (Chapter 6),” Massachusetts Toxics Use Reduction Institute, Tech. Rep., 2006.

[5] S. B. Wilbur, *Toxicological profile for chromium.* US Department of Health and Human Services, Public Health Service, Agency for Toxic Substances and Disease Registry, 2000.

[6] M. A. Polti, R. O. García, M. J. Amoroso, and C. M. Abate, “Bioremediation of chromium (VI) contaminated soil by Streptomyces sp. MC1,” *Journal of Basic Microbiology*, vol. 49, no. 3, pp. 285–292, 2009.

[7] “Directive 2003/108/EC of the European Parliament and of the Council of 8 December 2003 amending Directive 2002/96/EC on waste electrical and electronic equipment (WEEE),” *Official Journal of the European Communities, L*, vol. 345, no. 31, p. 12, 2003.

[8] D. M. J. Psaila-Dombrowski, D. E. Lee, D. J. L. McCrea, and D. U. Erb, “Electroformed nanocrystalline coatings an advanced alternative to hard-chrome electroplating PP-1152,” in *HCAT Meeting, Toronto, Ontario*, 2001.

[9] A. Baral and R. D. Engelken, “Chromium-based regulations and greening in metal finishing industries in the USA,” *Environmental Science and Policy*, vol. 5, no. 2, pp. 121–133, 2002.

[10] B. D. Sartwell, “Status of HCAT/JG-PP program on replacement of hard chrome plating with hvof thermal spray coatings on landing gear,” in *Proceedings of AESF Aerospace Plating and Metal Finishing Forum*, 2000, pp. 131–139.

[11] E. Groshart, “Finishing in the green: chromium plating replacements,” *Metal Finishing*, vol. 95, no. 7, pp. 70–42, 1997.

[12] Z. Zeng, L. Wang, A. Liang, and J. Zhang, “Tribological and electrochemical behavior of thick Cr–C alloy coatings electrodeposited in trivalent chromium bath as an alternative to conventional Cr coatings,” *Electrochimica Acta*, vol. 52, no. 3, pp. 1366–1373, 2006.

[13] E. W. Brooman, “Feature wear behavior of environmentally acceptable alternatives to chromium coatings: nickel-based candidates,” *Metal Finishing*, vol. 102, no. 9, pp. 75–82, 2004.

[14] L. Wang, Y. Gao, Q. Xue, H. Liu, and T. Xu, “A novel electrodeposited Ni–P gradient deposit for replacement of conventional hard chromium,” *Surface and Coatings Technology*, vol. 200, no. 12, pp. 3719–3726, 2006.

[15] R. Johnson, J. Bailey, and J. A. Goetz, “Electro-spark deposited coatings for replacement of chrome plating,” *Pacific Northwest National Laboratory Contract Report ARAET-CR-05002*, 2005.

[16] L. Wang, Y. Gao, T. Xu, and Q. Xue, “Corrosion resistance and lubricated sliding wear behaviour of novel Ni–P graded alloys as an alternative to hard Cr deposits,” *Applied Surface Science*, vol. 252, no. 20, pp. 7361–7372, 2006.

[17] D. Weston, P. Shipway, S. Harris, and M. Cheng, “Friction and sliding wear behaviour of electrodeposited cobalt and cobalt–tungsten alloy coatings for replacement of electrodeposited chromium,” *Wear*, vol. 267, no. 5, pp. 934–943, 2009.

[18] L. Wang, Y. Gao, Q. Xue, H. Liu, and T. Xu, “Graded composition and structure in nanocrystalline Ni–Co alloys for decreasing internal stress and improving tribological properties,” *Journal of Physics D: Applied Physics*, vol. 38, no. 8, p. 1318, 2005.

[19] C. Lupi, A. Dell’Era, M. Pasquali, and P. Imperatori, “Composition, morphology, structural aspects and electrochemical properties of Ni–Co alloy coatings,” *Surface and Coatings Technology*, vol. 205, no. 23, pp. 5394–5399, 2011.

[20] G. Qiao, T. Jing, N. Wang, Y. Gao, X. Zhao, J. Zhou, and W. Wang, “High-speed jet electrodeposition and microstructure of nanocrystalline Ni–Co alloys,” *Electrochimica Acta*, vol. 51, no. 1, pp. 85–92, 2005.

[21] B. Tury, M. Lakatos-Varsányi, and S. Roy, “Ni–Co alloys plated by pulse currents,” *Surface and Coatings Technology*, vol. 200, no. 24, pp. 6713–6717, 2006.

[22] N. V. Myung and K. Nobe, “Electrodeposited iron group thin-film alloys: structure-property relationships,” *Journal of the Electrochemical Society*, vol. 148, no. 3, pp. C136–C144, 2001.

[23] D. Golodnitsky, Y. Rosenberg, and A. Ulus, “The role of anion additives in the electrodeposition of nickel–cobalt alloys from sulfamate electrolyte,” *Electrochimica Acta*, vol. 47, no. 17, pp. 2707–2714, 2002.

[24] L. Wang, Y. Gao, Q. Xue, H. Liu, and T. Xu, “Microstructure and tribological properties of electrodeposited Ni–Co alloy deposits,” *Applied Surface Science*, vol. 242, no. 3, pp. 326–332, 2005.

[25] W. Brainard and D. Buckley, “Preliminary friction and wear studies of cobalt-rhenium solid solution alloy in air and in vacuum,” *NASA Report NASA-TN-D-6165*, 1971.

[26] I. Inman, “Compacted oxide layer formation under conditions of limited debris retention at the wear interface during high temperature sliding wear of superalloy,” Ph.D. dissertation, University of Northumbria at Newcastle, 2003.

[27] I. Inman, S. Rose, and P. Datta, “Studies of high temperature sliding wear of metallic dissimilar interfaces II: Incoloy MA956 versus Stellite 6,” *Tribology International*, vol. 39, no. 11, pp. 1361–1375, 2006.

[28] I. Inman and P. Datta, “Studies of high temperature sliding wear of metallic dissimilar interfaces III: Incoloy MA956 versus Incoloy 800HT,” *Tribology International*, vol. 43, no. 11, pp. 2051–2071, 2010.

[29] D. Persson, E. Coronel, S. Jacobson, and S. Hogmark, “Surface analysis of laser cladded stellite exposed to self-mated high load dry sliding,” *Wear*, vol. 261, no. 1, pp. 96–100, 2006.

[30] M. Godet, “The third-body approach: a mechanical view of wear,” *Wear*, vol. 100, no. 1-3, pp. 437–452, 1984.

[31] H. Kato and K. Komai, “Tribofilm formation and mild wear by tribo-sintering of nanometer-sized oxide particles on rubbing steel surfaces,” *Wear*, vol. 262, no. 1, pp. 36–41, 2007.

[32] S. Gupta, D. Filimonov, V. Zaitsev, T. Palanisamy, and M. Barsoum, “Ambient and 550 c tribological behavior of select max phases against Ni-based superalloys,” *Wear*, vol. 264, no. 3-4, pp. 270–278, 2008.

[33] Z. Zhou, W. Rainforth, Q. Luo, P. Hovsepian, J. Ojeda, and M. Romero-Gonzalez, “Wear and friction of TiAlN/VN coatings against Al_2O_3 in air at room and elevated temperatures,” *Acta Materialia*, vol. 58, no. 8, pp. 2912–2925, 2010.

[34] Q. Luo, Z. Zhou, W. Rainforth, and M. Bolton, “Effect of tribofilm formation on the dry sliding friction and wear properties of magnetron sputtered TiAlCrYN coatings,” *Tribology Letters*, vol. 34, no. 2, pp. 113–124, 2009.

[35] J. Olofsson and S. Jacobson, “The influence of grain size and surface treatment on the tribofilm formation on alumina components,” *Wear*, 2012.

[36] B. Tury, G. Radnóczi, G. Radnóczi, and M. Varsányi, “Microstructure properties of pulse plated Ni–Co alloy,” *Surface and Coatings Technology*, vol. 202, no. 2, pp. 331–335, 2007.

[37] Y. Li, H. Jiang, W. Huang, and H. Tian, “Effects of peak current density on the mechanical properties of nanocrystalline Ni–Co alloys produced by pulse electrodeposition,” *Applied Surface Science*, vol. 254, no. 21, pp. 6865–6869, 2008.

[38] Y. Li, H. Jiang, D. Wang, and H. Ge, “Effects of saccharin and cobalt concentration in electrolytic solution on microhardness of nanocrystalline Ni–Co alloys,” *Surface and Coatings Technology*, vol. 202, no. 20, pp. 4952–4956, 2008.

[39] M. Schlesinger, *Modern Electroplating (5th ed.).* John Wiley & Sons. Inc, New Jersey, 2010, p. 91.

[40] *Strengthening methods in crystals.* Elsevier Publishing Company LTD, Amsterdam-London-New York, 1971, ch. Kelly, A and Nicholson, RB, pp. 333–343.

[41] M. A. Meyers, A. Mishra, and D. J. Benson, “Mechanical properties of nanocrystalline materials,” *Progress in Materials Science*, vol. 51, no. 4, pp. 427–556, 2006.

[42] J. Schiøtz, F. D. Di Tolla, and K. W. Jacobsen, “Softening of nanocrystalline metals at very small grain sizes,” *Nature*, vol. 391, no. 6667, pp. 561–563, 1998.

[43] L. Wang, Y. Gao, T. Xu, and Q. Xue, “A comparative study on the tribological behavior of nanocrystalline nickel and cobalt coatings correlated with grain size and phase structure,” *Materials Chemistry and Physics*, vol. 99, no. 1, pp. 96–103, 2006.

[44] D. Jeong, F. Gonzalez, G. Palumbo, K. Aust, and U. Erb, “The effect of grain size on the wear properties of electrodeposited nanocrystalline nickel coatings,” *Scripta Materialia*, vol. 44, no. 3, pp. 493–500, 2001.

[45] G. C. Hadjipanayis and R. W. Siegel, *Nanophase Materials: Synthesis - Properties - Applications.* NATO Science Series E: Applied Sciences, Vol. 260, 1997, p. 233.

[46] R. Mishra, B. Basu, and R. Balasubramaniam, “Effect of grain size on the tribological behavior of nanocrystalline nickel,” *Materials Science and Engineering: A*, vol. 373, no. 1, pp. 370–373, 2004.

[47] A. Chen, X. Qiu, K. Sridharan, W. G. Horne, R. A. Dodd, A. H. Hamdi, A. A. Elmoursi, G. W. Malaczynski, and J. R. Conrad, “Chromium plating pollution source reduction by plasma source ion implantation,” *Surface and Coatings Technology*, vol. 82, no. 3, pp. 305–310, 1996.

[48] U. Erb, “Electrodeposited nanocrystals: synthesis, properties and industrial applications,” *Nanostructured Materials*, vol. 6, no. 5, pp. 533–538, 1995.

[49] D. H. Jeong, U. Erb, K. T. Aust, and G. Palumbo, “The relationship between hardness and abrasive wear resistance of electrodeposited nanocrystalline Ni–P coatings,” *Scripta Materialia*, vol. 48, no. 8, pp. 1067–1072, 2003.

[50] B. Bozzini, C. Martini, P. Cavallotti, and E. Lanzoni, “Relationships among crystallographic structure, mechanical properties and tribological behaviour of electroless Ni–P (9%)/B_4C films,” *Wear*, vol. 225, pp. 806–813, 1999.

[51] Y. Wu, H. Liu, B. Shen, L. Liu, and W. Hu, “The friction and wear of electroless Ni–P matrix with PTFE and/or SiC particles composite,” *Tribology International*, vol. 39, no. 6, pp. 553–559, 2006.

[52] H. Matsuda, G. Jones, O. Takano, and P. Grundy, “Room-temperature electroless deposition of high-coercivity Co-Ni-P films,” *Journal of Magnetism and Magnetic Materials*, vol. 120, no. 1, pp. 338–341, 1993.

[53] T. Sankara Narayanan, S. Selvakumar, and A. Stephen, “Electroless Ni–Co–P ternary alloy deposits: preparation and characteristics,” *Surface and Coatings Technology*, vol. 172, no. 2, pp. 298–307, 2003.

[54] M. Parente, O. Mattos, S. Diaz, P. L. Neto, and F. F. Miranda, “Electrochemical characterization of Ni–P and Ni–Co–P amorphous alloy deposits obtained by electrodeposition,” *Journal of Applied Electrochemistry*, vol. 31, no. 6, pp. 677–683, 2001.

[55] Y. Li, R. Wang, F. Qi, and C. Wang, “Preparation, characterization and microwave absorption properties of electroless Ni–Co–P-coated SiC powder,” *Applied Surface Science*, vol. 254, no. 15, pp. 4708–4715, 2008.

[56] J. J. Podesta, R. C. V. Piatti, and A. J. Arvia, “The influence of iridium, ruthenium and palladium on the electrochemical behaviour of Co-P and Ni-Co-P base amorphous alloys for water electrolysis in KOH aqueous solutions,” *International Journal of Hydrogen Energy*, vol. 20, no. 2, pp. 111–122, 1995.

[57] G. Pattanaik, D. Kirkwood, X. Xu, and G. Zangari, “Electrodeposition of hard magnetic films and microstructures,” *Electrochimica Acta*, vol. 52, no. 8, pp. 2755–2764, 2007.

[58] D. Kirkwood, V. Zoldan, A. Pasa, and G. Zangari, “Evolution of surface roughness in electrodeposited Co–Ni–P and Co–Ni Films,” *Journal of The Electrochemical Society*, vol. 157, no. 4, pp. D181–D186, 2010.

[59] P. Cojocaru, L. Magagnin, E. Gómez, and E. Vallés, “Electrodeposition of CoNi and CoNiP alloys in sulphamate electrolytes,” *Journal of Alloys and Compounds*, vol. 503, no. 2, pp. 454–459, 2010.

[60] S. Djokić, “Electrodeposition of amorphous alloys based on the iron group of metals,” *Journal of the Electrochemical Society*, vol. 146, p. 1824, 1999.

[61] D. T. Gawne and U. Ma, “Friction and wear of chromium and nickel coatings,” *Wear*, vol. 129, no. 1, pp. 123–142, 1989.

[62] L. P. Wang, “Study on the microstructures and properties of functionally protective nanocrystalline deposits,” Ph.D. dissertation, Lanzhou Institute of Chemical Physics, Lanzhou, China, 2007.

[63] C. Ma, S. Wang, C. Low, L. Wang, and F. Walsh, “Effects of additives on the microstructure and properties of electrodeposited nanocrystalline Ni-Co coatings with high cobalt content,” *Transaction of the Institute of Metal Finishing, under review*, 2013.

[64] C. Ma, S. Wang, L. Wang, F. Walsh, and R. Wood, “The electrodeposition and characterisation of low friction and wear resistant Co-Ni-P coatings,” *Surface and Coatings Technology, under review*, 2013.

[65] E. Rabinowicz, *Friction and wear of materials (2nd ed.).* Wiley Chichester, 1995, pp. 5–8.

[66] J. R. Davis, *Surface engineering for corrosion and wear resistance.* ASM International, Materials Park, OH, USA, 2001, pp. 2–10.

[67] B. G. Mellor, Ed., *Surface coatings for protection against wear.* Woodhead Publishing Limited, 2006, pp. 226–248.

[68] B. Warcholinski, A. Gilewicz, Z. Kuklinski, and P. Myslinski, “Hard CrCN/CrN multilayer coatings for tribological applications,” *Surface and Coatings Technology*, vol. 204, no. 14, pp. 2289–2293, 2010.

[69] Y. Lai, Z. Lin, Z. Chen, J. Huang, and C. Lin, “Fabrication of patterned CdS/TiO_2 heterojunction by wettability template-assisted electrodeposition,” *Materials Letters*, vol. 64, no. 11, pp. 1309–1312, 2010.

[70] S. Tjong and H. Chen, “Nanocrystalline materials and coatings,” *Materials Science and Engineering: R: Reports*, vol. 45, no. 1, pp. 1–88, 2004.

[71] K. Lu and J. Lu, “Surface nanocrystallization (SNC) of metallic materials-presentation of the concept behind a new approach,” *Journal of Materials Science and Technology*, vol. 15, no. 3, p. 193, 1999.

[72] ——, “Nanostructured surface layer on metallic materials induced by surface mechanical attrition treatment,” *Materials Science and Engineering: A*, vol. 375, pp. 38–45, 2004.

[73] C. C. Koch, *Nanostructured materials: processing, properties and potential applications (2nd ed.).* Noyes Publications / William Andrew Publishing, Norwich, USA, 2007, pp. 239–246, 425–438.

[74] K. Legg, “Overview of chromium and cadmium alternative technologies,” *Surface Modification Technologies XV*, 2002.

[75] L. Fedrizzi, L. Valentinelli, S. Rossi, and S. Segna, “Tribocorrosion behaviour of HVOF cermet coatings,” *Corrosion Science*, vol. 49, no. 7, pp. 2781–2799, 2007.

[76] J. Picas, A. Forn, and G. Matthäus, “HVOF coatings as an alternative to hard chrome for pistons and valves,” *Wear*, vol. 261, no. 5, pp. 477–484, 2006.

[77] T. Sahraoui, N.-E. Fenineche, G. Montavon, and C. Coddet, “Alternative to chromium: characteristics and wear behavior of HVOF coatings for gas turbine shafts repair (heavy-duty),” *Journal of Materials Processing Technology*, vol. 152, no. 1, pp. 43–55, 2004.

[78] M. Nascimento, R. Souza, I. Miguel, W. Pigatin, and H. Voorwald, “Effects of tungsten carbide thermal spray coating by HP/HVOF and hard chromium electroplating on AISI 4340 high strength steel,” *Surface and Coatings Technology*, vol. 138, no. 2, pp. 113–124, 2001.

[79] B. Sartwell, P. Natishan, I. Singer, K. Legg, J. Schell, and J. Sauer, “Replacement of chromium electroplating using HVOF thermal spray coatings,” in *AESF Plating Forum*, 1998.

[80] A. Savarimuthu, H. Taber, I. Megat, J. Shadley, E. Rybicki, W. Cornell, W. Emery, D. Somerville, and J. Nuse, “Sliding wear behavior of tungsten carbide thermal spray coatings for replacement of chromium electroplate in aircraft applications,” *Journal of Thermal Spray Technology*, vol. 10, no. 3, pp. 502–510, 2001.

[81] R. J. Wood, “Tribology of thermal sprayed WC–Co coatings,” *International Journal of Refractory Metals and Hard Materials*, vol. 28, no. 1, pp. 82–94, 2010.

[82] L. Fedrizzi, S. Rossi, R. Cristel, and P. Bonora, “Corrosion and wear behaviour of HVOF cermet coatings used to replace hard chromium,” *Electrochimica Acta*, vol. 49, no. 17, pp. 2803–2814, 2004.

[83] S. Kuroda, T. Fukushima, M. Sasaki, and T. Kodama, “Microstructure and corrosion resistance of HVOF sprayed 316L stainless steel and hastelloy C coatings,” *Materials Transactions-JIM*, vol. 43, no. 12, pp. 3177–3183, 2002.

[84] J. Kawakita, S. Kuroda, T. Fukushima, and T. Kodama, "Development of dense corrosion resistant coatings by an improved HVOF spraying process," *Science and Technology of Advanced Materials*, vol. 4, no. 4, pp. 281–289, 2003.

[85] K. Legg and J. Sauer, "Use of thermal spray as an aerospace chrome plating alternative," Rowan Technology Group, Tech. Rep., 2000.

[86] B. Flitney, "Alternatives to chrome for hydraulic actuators," *Sealing Technology*, vol. 2007, no. 10, pp. 8–12, 2007.

[87] B. Sartwell, K. Legg, J. Schell, J. Sauer, and P. Natishan, "Validation of HVOF WC/Co thermal spray coatings as a replacement for hard chrome plating on aircraft landing gear," Naval Research Laboratory, Washington, DC, USA, Tech. Rep., 2004.

[88] B. D. Sartwell, K. O. Legg, A. Nardi, R. Kestler, W. Assink, and J. Schell, "Validation of HVOF WC/Co, WC/CoCr and Tribaloy 800 thermal spray coatings as a replacement for hard chrome plating on C-2/E-2/P-3 and C-130 propeller hub system components," Naval Research Laboratory, Washington, DC, USA, Tech. Rep., 2003.

[89] R. Souza, H. Voorwald, and M. Cioffi, "Fatigue strength of hvof sprayed Cr_3C_2–25NiCr and WC-10Ni on AISI 4340 steel," *Surface and Coatings Technology*, vol. 203, no. 3, pp. 191–198, 2008.

[90] J. Guilemany, N. Espallargas, P. Suegama, and A. Benedetti, "Comparative study of Cr_3C_2–NiCr coatings obtained by HVOF and hard chromium coatings," *Corrosion Science*, vol. 48, no. 10, pp. 2998–3013, 2006.

[91] A. P. Koon, T. B. Hee, M. Taylor, M. Weston, and J. Yip, "Hard chrome replacement by HVOF sprayed coatings," Singapore Institute of Manufacturing Technology, Tech. Rep., 1999.

[92] S. Abdi and S. Lebaili, "Alternative to chromium, a hard alloy powder NiCrBCSi (Fe) coatings thermally sprayed on 60CrMn4 steel. phase and comportements," *Physics Procedia*, vol. 2, no. 3, pp. 1005–1014, 2009.

[93] R. B. Heimann, *Plasma-spray coating.* Wiley-VCH, Weinheim, Gemany, 2008, pp. 17–21.

[94] K. O. Legg, B. D. Sartwell, J.-G. Legoux, M. Nestler, C. Dambra, D. Wang, J. Quets, P. Natishan, P. Bretz, and J. Devereaux, "Investigation of plasma spray coatings as

an alternative to hard chrome plating on internal surfaces," Naval Research Laboratory, Washington, DC, USA, Tech. Rep., 2006.

[95] M. Heydarzadeh Sohi and F. Ghadami, "Comparative tribological study of air plasma sprayed WC–12% Co coating versus conventional hard chromium electrodeposit," *Tribology International*, vol. 43, no. 5, pp. 882–886, 2010.

[96] D. M. Mattox, "Physical vapor deposition (PVD) processes," *Metal Finishing*, vol. 97, no. 1, pp. 417–430, 1999.

[97] B. Navinšek, P. Panjan, and I. Milošev, "PVD coatings as an environmentally clean alternative to electroplating and electroless processes," *Surface and Coatings Technology*, vol. 116, pp. 476–487, 1999.

[98] A. Hurkmans, D. Lewis, and W. Münz, "Runner-up magnetron sputtered CrN_x coatings as alternative to electroplated hard chromium," *Surface Engineering*, vol. 19, no. 3, pp. 205–210, 2003.

[99] K. Brondum and G. Larson, "Low-temperature arc vapor deposition as a hexavalent chrome electroplating alternative," Vapor Technologies Inc., Longmont, USA, Tech. Rep., 2005.

[100] V. S. Sundaram, "Diamond like carbon film as a protective coating for high strength steel and titanium alloy," *Surface and Coatings Technology*, vol. 201, no. 6, pp. 2707–2711, 2006.

[101] Pollution prevention technology profile: Trivalent chromium replacements for hexavalent chromium plating. Accessed on March 28th, 2013. [Online]. Available: www.newmoa.org/prevention/p2tech/TriChromeFinal.pdf

[102] P. Benaben. An overview of hard chromium plating using trivalent chromium solutions. Accessed on April 8th, 2013. [Online]. Available: http://www.pfonline.com/articles/an-overview-of-hard-chromium-plating-using-trivalent-chromium-solutions

[103] A. Baral and R. Engelken, "Modeling, optimization, and comparative analysis of trivalent chromium electrodeposition from aqueous glycine and formic acid baths," *Journal of The Electrochemical Society*, vol. 152, no. 7, pp. C504–C512, 2005.

[104] A. Edigaryan *et al.*, "Chromium plating method," May 30 2006, US Patent 7,052,592.

[105] B. Kagajwala, T. Hall, M. Inman, E. Taylor, B. Griffin, G. Cushnie, R. Taylor, M. Jaworoski, and J. Bonivel. Functional trivalent chromium electroplating of internal diameters. Products Finishing Magazine Online. Accessed on April 15th, 2013. [Online]. Available: http://www.pfonline.com/articles/functional-trivalent-chromium-electroplating-of-internal-diameters

[106] J. Colaruotolo, D. Tramontana, G. Mallory, and J. Hajdu, "Engineering applications of electroless nickel," *Electroless Plating: Fundamentals and Applications*, p. 207, 1990.

[107] R. Agarwala and V. Agarwala, "Electroless alloy/composite coatings: A review," *Sadhana*, vol. 28, no. 3-4, pp. 475–493, 2003.

[108] K. H. Krishnan, S. John, K. Srinivasan, J. Praveen, M. Ganesan, and P. Kavimani, "An overall aspect of electroless Ni-P depositions–A review article," *Metallurgical and Materials Transactions A*, vol. 37, no. 6, pp. 1917–1926, 2006.

[109] Y. Riddle and T. Bailerare, "Friction and wear reduction via an Ni-B electroless bath coating for metal alloys," *JOM*, vol. 57, no. 4, pp. 40–45, 2005.

[110] L. P. Bicelli, B. Bozzini, C. Mele, and L. D'Urzo, "A review of nanostructural aspects of metal electrodeposition," *International Journal of Electrochemical Science*, vol. 3, no. 4, pp. 356–408, 2008.

[111] H. Capel, P. Shipway, and S. Harris, "Sliding wear behaviour of electrodeposited cobalt–tungsten and cobalt–tungsten–iron alloys," *Wear*, vol. 255, no. 7, pp. 917–923, 2003.

[112] D. Facchini, N. Mahalanobis, F. Gonzalez, and G. Palumbo, "Electrodeposition of nanocrystalline cobalt alloy coatings as a hard chrome alternative," in *Department of Defense Corrosion Conference*, 2009, pp. 1–13.

[113] B. Wielage, T. Lampke, M. Zacher, and D. Dietrich, "Electroplated nickel composites with micron-to nano-sized particles," *Key Engineering Materials*, vol. 384, pp. 283–309, 2008.

[114] N. Serres, F. Hlawka, S. Costil, C. Langlade, F. Machi, and A. Cornet, "Dry coatings and ecodesign Part. 1 - Environmental performances and chemical properties," *Surface and Coatings Technology*, vol. 204, no. 1, pp. 187–196, 2009.

[115] N. Serres, F. Hlawka, S. Costil, C. Langlade, and F. Machi, "Dry coatings and ecodesign: Part. 2 - Tribological performances," *Surface and Coatings Technology*, vol. 204, no. 1, pp. 197–204, 2009.

[116] K. Legg, "Choosing a hard chrome alternative," *Availabe: http://www.rowantechnology.com/wp-content/uploads/2012/06/Hard-Chrome-Plating-Alternatives.pdf (accessed on 1st May, 2013).*

[117] M. Schlesinger, *Modern Electroplating (5th ed.).* John Wiley & Sons. Inc, New Jersey, 2010, pp. 84–85.

[118] U. Knock, C. Tome, and H. Wenk, *Texture and anisotropy, preferred orientations in polycrystals and their effect on materials properties.* Cambridge University Press, Cambridge, UK, 2000, pp. 237–238.

[119] T. Watanabe, *Nano plating-microstructure formation theory of plated films and a database of plated films.* Elsevier Science, Oxford, UK, 2004, pp. 50–66.

[120] N. A. Pangarov, "Preferred orientations in electro-deposited metals," *Journal of Electroanalytical Chemistry (1959)*, vol. 9, no. 1, pp. 70–85, 1965.

[121] N. Pangarov, "The crystal orientation of electrodeposited metals," *Electrochimica Acta*, vol. 7, no. 1, pp. 139–146, 1962.

[122] J. James and G. G. Heiniger, "Meeting the pollution prevention challenge at tinker air force base," *Federal Facilities Environmental Journal*, vol. 6, no. 3, pp. 35–48, 1995.

[123] Nickel compounds. Access on May 8th, 2013. [Online]. Available: http://www.epa.gov/ttn/atw/hlthef/nickel.html

[124] Nickel compounds and metallic nickel. Report on carcinogens (12th ed.). U.S. Department of Health and Human Services, Public Health Service, National Toxicology Program. Accessed on May 8th, 2013. [Online]. Available: http://ntp.niehs.nih.gov/ntp/roc/twelfth/profiles/Nickel.pdf

[125] Regulation (EC) No 1272/2008 of the European Parliament and of the Council of 16 December 2008. Accessed on May 8th, 2013. [Online]. Available: http://eur-lex.europa.eu/LexUriServ/LexUriServ.do?uri=OJ:L:2008:353:0001:1355:en:PDF

[126] Nickel and nickel alloy plating operations: Controlling the risk of inhaling mist containing nickel. Suface Engineering Association, Birmingham, UK. Accessed on May 8th, 2013. [Online]. Available: www.hse.gov.uk/surfaceengineering/nickelinhalation.pdf

[127] Nickel and nickel alloy plating operations: Controlling the risk of skin exposure. Suface Engineering Association, Birmingham, UK. Accessed on May 8th, 2013. [Online]. Available: www.hse.gov.uk/surfaceengineering/nickelexposure.pdf

[128] A. Hart, "Substitution issues related to the use of nickel in electrolytic and electroless surface engineering processes," *Transactions of the Institute of Metal Finishing*, vol. 89, no. 4, pp. 181–186, 2011.

[129] J. K. Dennis and T. E. Such, *Nickel and chromium plating (3rd ed.)*. Woodhead Publishing Ltd, Cambridge, England, 1993, pp. 71–76.

[130] A. Rashidi and A. Amadeh, "Effect of electroplating parameters on microstructure of nanocrystalline nickel coatings," *Journal of Materials Science and Technology*, vol. 26, no. 1, pp. 82–86, 2010.

[131] R. Rofagha, R. Langer, A. El-Sherik, G. Palumbo, and K. Aust, "The corrosion behaviour of nanocrystalline nickel," *Scripta Metallurgica et Materialia (USA)*, vol. 25, no. 12, pp. 2867–2872, 1991.

[132] R. Rofagha, S. Splinter, U. Erb, and N. McIntyre, "XPS characterization of the passive films formed on nanocrystalline nickel in sulphuric acid," *Nanostructured Materials*, vol. 4, no. 1, pp. 69–78, 1994.

[133] R. Mishra and R. Balasubramaniam, "Effect of nanocrystalline grain size on the electrochemical and corrosion behavior of nickel," *Corrosion Science*, vol. 46, no. 12, pp. 3019–3029, 2004.

[134] L. Wang, J. Zhang, Y. Gao, Q. Xue, L. Hu, and T. Xu, "Grain size effect in corrosion behavior of electrodeposited nanocrystalline Ni coatings in alkaline solution," *Scripta Materialia*, vol. 55, no. 7, pp. 657–660, 2006.

[135] H. Jung and A. Alfantazi, "An electrochemical impedance spectroscopy and polarization study of nanocrystalline Co and Co–P alloy in 0.1 M H_2SO_4 solution," *Electrochimica Acta*, vol. 51, no. 8, pp. 1806–1814, 2006.

[136] L. Wang, Y. Lin, Z. Zeng, W. Liu, Q. Xue, L. Hu, and J. Zhang, “Electrochemical corrosion behavior of nanocrystalline Co coatings explained by higher grain boundary density,” *Electrochimica Acta*, vol. 52, no. 13, pp. 4342–4350, 2007.

[137] G. Hibbard, K. Aust, G. Palumbo, and U. Erb, “Thermal stability of electrodeposited nanocrystalline cobalt,” *Scripta Materialia*, vol. 44, no. 3, pp. 513–518, 2001.

[138] A. Karimpoor, K. Aust, and U. Erb, “Charpy impact energy of nanocrystalline and polycrystalline cobalt,” *Scripta Materialia*, vol. 56, no. 3, pp. 201–204, 2007.

[139] M. Srivastava, V. Ezhil Selvi, V. William Grips, and K. Rajam, “Corrosion resistance and microstructure of electrodeposited nickel–cobalt alloy coatings,” *Surface and Coatings Technology*, vol. 201, no. 6, pp. 3051–3060, 2006.

[140] M. Gutkin and I. Ovid’ko, *Plastic deformation in nanocrystalline materials.* Springer, Germany, 2004, p. 7.

[141] S. Hassani, K. Raeissi, M. Azzi, D. Li, M. Golozar, and J. Szpunar, “Improving the corrosion and tribocorrosion resistance of Ni–Co nanocrystalline coatings in NaOH solution,” *Corrosion Science*, vol. 51, no. 10, pp. 2371–2379, 2009.

[142] A. Bai and C. Hu, “Composition controlling of Co-Ni and Fe-Co alloys using pulse-reverse electroplating through means of experimental strategies,” *Electrochimica Acta*, vol. 50, no. 6, pp. 1335–1345, 2005.

[143] C. Fan and D. Piron, “Study of anomalous nickel-cobalt electrodeposition with different electrolytes and current densities,” *Electrochimica Acta*, vol. 41, no. 10, pp. 1713–1719, 1996.

[144] C. Karakus and D.-T. Chin, “Metal distribution in jet plating,” *Journal of the Electrochemical Society*, vol. 141, no. 3, pp. 691–697, 1994.

[145] K. Marikkannu, G. P. Kalaignan, and T. Vasudevan, “The role of additives in the electrodeposition of nickel–cobalt alloy from acetate electrolyte,” *Journal of Alloys and Compounds*, vol. 438, no. 1, pp. 332–336, 2007.

[146] A. El-Sherik and U. Erb, “Synthesis of bulk nanocrystalline nickel by pulsed electrodeposition,” *Journal of Materials Science*, vol. 30, no. 22, pp. 5743–5749, 1995.

[147] W. Yin, S. Whang, and R. Mirshams, “Effect of interstitials on tensile strength and creep in nanostructured Ni,” *Acta Materialia*, vol. 53, no. 2, pp. 383–392, 2005.

[148] M. Schlesinger, *Modern Electroplating (5th ed.).* John Wiley & Sons. Inc, New Jersey, 2010, pp. 513–516.

[149] L. Burzyńska and E. Rudnik, "The influence of electrolysis parameters on the composition and morphology of Co–Ni alloys," *Hydrometallurgy*, vol. 54, no. 2, pp. 133–149, 2000.

[150] J. Deng and M. Braun, "DLC multilayer coatings for wear protection," *Diamond and Related Materials*, vol. 4, no. 7, pp. 936–943, 1995.

[151] L. Wang, J. Zhang, Z. Zeng, Y. Lin, L. Hu, and Q. Xue, "Fabrication of a nanocrystalline Ni–Co/CoO functionally graded layer with excellent electrochemical corrosion and tribological performance," *Nanotechnology*, vol. 17, no. 18, p. 4614, 2006.

[152] W. Liu, W. Chen, T. Tsai, S. Hsieh, and S. Chang, "Effect of nickel on the initial growth behavior of electroless Ni–Co–P alloy on silicon substrate," *Applied Surface Science*, vol. 253, no. 8, pp. 3843–3848, 2007.

[153] Y. Huang, K. Shi, Z. Liao, Y. Wang, L. Wang, and F. Zhu, "Studies of electroless Ni–Co–P ternary alloy on glass fibers," *Materials Letters*, vol. 61, no. 8, pp. 1742–1746, 2007.

[154] K. S. Lew, M. Raja, S. Thanikaikarasan, T. Kim, Y. D. Kim, and T. Mahalingam, "Effect of pH and current density in electrodeposited Co–Ni–P alloy thin films," *Materials Chemistry and Physics*, vol. 112, no. 1, pp. 249–253, 2008.

[155] N. V. Myung, D. Y. Park, M. Schwartz, K. Nobe, H. Yang, C. K. Yang, and J. W. Judy, "Electrodeposited hard magnetic thin films for MEMS applications," *Proceedings of the Electrochemical Society*, vol. 20, p. 29, 2000.

[156] D.-Y. Park, N. V. Myung, M. Schwartz, and K. Nobe, "Nanostructured magnetic CoNiP electrodeposits: structure–property relationships," *Electrochimica Acta*, vol. 47, no. 18, pp. 2893–2900, 2002.

[157] D. M. Kirkwood, G. Pattanaik, and G. Zangari, "Electrodeposited CoNiP films with perpendicular magnetic anisotropy," *Journal of The Electrochemical Society*, vol. 154, no. 8, pp. D363–D368, 2007.

[158] C. Byun, G. Rauch, D. Young, C. Klepper, and J. Greggi, "Effects of hypophosphite contents and surface treatment on electroplated Co-Ni-P thin films," *Journal of Applied Physics*, vol. 73, no. 10, pp. 5575–5577, 1993.

[159] R. N. Emerson, C. J. Kennady, and S. Ganesan, “Effect of organic additives on the magnetic properties of electrodeposited CoNiP hard magnetic films,” *Thin Solid Films*, vol. 515, no. 7, pp. 3391–3396, 2007.

[160] R. Raicheff and V. Zaprianova, “Effect of crystallization on the electrochemical corrosion behavior of some nickel-based amorphous alloys,” *Journal of Materials Science Letters*, vol. 19, no. 1, pp. 3–5, 2000.

[161] S. Şahin, “Effects of boronizing process on the surface roughness and dimensions of AISI 1020, AISI 1040 and AISI 2714,” *Journal of materials processing technology*, vol. 209, no. 4, pp. 1736–1741, 2009.

[162] J. Goldstein, D. E. Newbury, D. C. Joy, C. E. Lyman, P. Echlin, E. Lifshin, L. Sawyer, and J. R. Michael, *Scanning electron microscopy and X-ray microanalysis (3rd ed.).* Kluwer Academic/Plenum Publishers, 2003.

[163] R. F. Egerton, *Physical principles of electron microscopy.* Springer, New York, 2005.

[164] S. Reyntjens and R. Puers, “A review of focused ion beam applications in microsystem technology,” *Journal of Micromechanics and Microengineering*, vol. 11, no. 4, p. 287, 2001.

[165] C. R. Blanchard, “Atomic force microscopy,” *The Chemical Educator*, vol. 1, no. 5, pp. 1–8, 1996.

[166] “Agilent Technologies 5500 scanning probe microscope user’s guide,” Agilent Technologies, Tech. Rep., 2008.

[167] D. Lewis, E. Wheeler, and D. Northwood, “The practical application of line-profile analytical methods,” *Journal of Educational Modules for Materials Science and Engineering*, pp. 673–99, 1982.

[168] Q. Luo and A. Jones, “High-precision determination of residual stress of polycrystalline coatings using optimised XRD-$\sin^2\psi$ technique,” *Surface and Coatings Technology*, vol. 205, no. 5, pp. 1403–1408, 2010.

[169] N. G. Thompson and J. H. Payer, *DC Electrochemical test methods.* NACE International, 1998.

[170] C. Ma, S. C. Wang, R. J. K. Wood, J. Zekonyte, Q. Luo, and F. C. Walsh, "The hardness of porous nanocrystalline co-ni electrodeposits," 2013, metals and Materials International, in press, 2013.

[171] K. R. Trethewey and J. Chamberlain, *Corrosion for Science and Engineering.* Longman Scientific & Techincal, Harlow, England, 1995, pp. 75–81.

[172] M. Zamanzad-Ghavidel, K. Raeissi, and A. Saatchi, "The effect of surface morphology on pitting corrosion resistance of Ni nanocrystalline coatings," *Materials Letters*, vol. 63, no. 21, pp. 1807–1809, 2009.

[173] W. A. Badawy, F. M. Al-Kharafi, and J. R. Al-Ajmi, "Electrochemical behaviour of cobalt in aqueous solutions of different pH," *Journal of Applied Electrochemistry*, vol. 30, no. 6, pp. 693–704, 2000.

[174] W. A. Badawy, K. M. Ismail, and A. M. Fathi, "Effect of Ni content on the corrosion behavior of Cu–Ni alloys in neutral chloride solutions," *Electrochimica Acta*, vol. 50, no. 18, pp. 3603–3608, 2005.

[175] Z. Zhou, W. Rainforth, C. Tan, P. Zeng, J. Ojeda, M. Romero-Gonzalez, and P. Hovsepian, "The role of the tribofilm and roll-like debris in the wear of nanoscale nitride PVD coatings," *Wear*, vol. 263, no. 7-12, pp. 1328–1334, 2007.

[176] I. Hutchings, *Tribology: friction and wear of engineering materials.* Butterworth-Heinemann Ltd., 1992, p. 40.

[177] I. A. Inman, P. K. Datta, H. L. Du, J. S. Burnell-Gray, S. Pierzgalski, and Q. Luo, "Studies of high temperature sliding wear of metallic dissimilar interfaces," *Tribology International*, vol. 38, no. 9, pp. 812–823, 2005.

[178] M. Peterson, S. Calabrese, S. Li, and X. Jiang, "Friction of alloys at high temperature," *Journal of Materials Science and Technology*, vol. 10, pp. 313–320, 1994.

[179] A. W. Burton, K. Ong, T. Rea, and I. Y. Chan, "On the estimation of average crystallite size of zeolites from the Scherrer equation: a critical evaluation of its application to zeolites with one-dimensional pore systems," *Microporous and Mesoporous Materials*, vol. 117, no. 1, pp. 75–90, 2009.

[180] C.-J. Chen and K.-L. Lin, "Internal stress and adhesion of amorphous Ni–Cu–P alloy on aluminum," *Thin Solid Films*, vol. 370, no. 1, pp. 106–113, 2000.

[181] C. Ma, S. Wang, L. Wang, F. Walsh, and R. Wood, “The role of a tribofilm and wear debris in the tribological behaviour of nanocrystalline Ni–Co electrodeposits,” 2013, wear, http://dx.doi.org/10.1016/j.wear.2013.01.121, 2013.

[182] E. Pavlatou, M. Raptakis, and N. Spyrellis, “Synergistic effect of 2-butyne-1, 4-diol and pulse plating on the structure and properties of nickel nanocrystalline deposits,” *Surface and Coatings Technology*, vol. 201, no. 8, pp. 4571–4577, 2007.

[183] R. Winand, “Electrocrystallization-theory and applications,” *Hydrometallurgy*, vol. 29, no. 1, pp. 567–598, 1992.

[184] J. Amblard, I. Epelboin, M. Froment, and G. Maurin, “Inhibition and nickel electrocrystallization,” *Journal of Applied Electrochemistry*, vol. 9, no. 2, pp. 233–242, 1979.

[185] S. H. Ahn, S. J. Hwang, S. J. Yoo, I. Choi, H.-J. Kim, J. H. Jang, S.-W. Nam, T.-H. Lim, T. Lim, S.-K. Kim, and J. J. Kim, “Electrodeposited Ni dendrites with high activity and durability for hydrogen evolution reaction in alkaline water electrolysis,” *Journal of Materials Chemistry*, 2012.

[186] H. Li, F. Czerwinski, and J. Szpunar, “Monte-Carlo simulation of texture and microstructure development in nanocrystalline electrodeposits,” *Nanostructured Materials*, vol. 9, no. 1, pp. 673–676, 1997.

[187] X. Y. Yuan, Y. Wang, D. Sun, and H. Yu, “Influence of pulse parameters on the microstructure and microhardness of nickel electrodeposits,” *Surface and Coatings Technology*, vol. 202, no. 9, pp. 1895–1903, 2008.

[188] B. Jennings, K. Parslow, B. Jennings, and K. Parslow, “Particle size measurement: the equivalent spherical diameter,” *Proceedings of the Royal Society of London. A. Mathematical and Physical Sciences*, vol. 419, no. 1856, pp. 137–149, 1988.

[189] C. Bray and D. Karig, “Porosity of sediments in accretionary prisms and some implications for dewatering processes,” *Journal of Geophysical Research*, vol. 90, no. B1, pp. 768–778, 1985.

[190] H. Kim, Y. Estrin, and M. Bush, “Plastic deformation behaviour of fine-grained materials,” *Acta Materialia*, vol. 48, no. 2, pp. 493–504, 2000.

[191] S. Wang, Z. Zhu, and M. Starink, “Estimation of dislocation densities in cold rolled Al-Mg-Cu-Mn alloys by combination of yield strength data, EBSD and strength models,” *Journal of Microscopy*, vol. 217, no. 2, pp. 174–178, 2005.

[192] P. Sanders, C. Youngdahl, and J. Weertman, “The strength of nanocrystalline metals with and without flaws,” *Materials Science and Engineering: A*, vol. 234, pp. 77–82, 1997.

[193] A. Ibanez and E. Fatas, “Mechanical and structural properties of electrodeposited copper and their relation with the electrodeposition parameters,” *Surface and Coatings Technology*, vol. 191, no. 1, pp. 7–16, 2005.

[194] M. Manna, N. Bandyopadhyay, and D. Bhattacharjee, “Effect of plating time for electroless nickel coating on rebar surface: An option for application in concrete structure,” *Surface and Coatings Technology*, vol. 202, no. 14, pp. 3227–3232, 2008.

[195] T. Mimani, S. Mayanna, and N. Munichandraiah, “Influence of additives on the electrodeposition of nickel from a Watts bath: a cyclic voltammetric study,” *Journal of Applied Electrochemistry*, vol. 23, no. 4, pp. 339–345, 1993.

[196] V. Vasilache, G. Gutt, and T. Vasilache, “Electrochemical researches about influence of the aditives of watts’s solutions on throwing power and brightness,” *Revista de Chimie (Bucharest)*, vol. 59, no. 2, pp. 915–920, 2008.

[197] T. Drews, J. Ganley, and R. Alkire, “Evolution of surface roughness during copper electrodeposition in the presence of additives comparison of experiments and monte carlo simulations,” *Journal of the Electrochemical Society*, vol. 150, no. 5, pp. C325–C334, 2003.

[198] C. M. A. Brett and A. M. O. Brett, *Electrochemistry: Principles, Methods, and Applications*. Oxford Science Publications, New York, US, 1993, pp. 209–212.

[199] Y. Li, “The oxidation of NdFeB alloys,” Ph.D. dissertation, University of Birmingham, 2001.

[200] K. Shimizu, K. Kobayashi, P. Skeldon, G. Thompson, and G. Wood, “Oxidation of an amorphous $Ni_{77}P_{23}$ alloy in air and dry oxygen at 300 °C,” *Materials Science and Engineering: A*, vol. 198, no. 1, pp. 35–41, 1995.

[201] V. Chapman, B. J. Welch, and M. Skyllas-Kazacos, "High temperature oxidation behaviour of Ni–Fe–Co anodes for aluminium electrolysis," *Corrosion Science*, vol. 53, no. 9, pp. 2815–2825, 2011.

[202] M. H. Seo, J. S. Kim, W. S. Hwang, D. J. Kim, S. S. Hwang, and B. S. Chun, "Characteristics of Ni–P alloy electrodeposited from a sulfamate bath," *Surface and Coatings Technology*, vol. 176, no. 2, pp. 135–140, 2004.

[203] L. Chang, P. Kao, and C. Chen, "Strengthening mechanisms in electrodeposited Ni–P alloys with nanocrystalline grains," *Scripta Materialia*, vol. 56, no. 8, pp. 713–716, 2007.

[204] H. Ashassi-Sorkhabi and S. H. Rafizadeh, "Effect of coating time and heat treatment on structures and corrosion characteristics of electroless Ni–P alloy deposits," *Surface and coatings Technology*, vol. 176, no. 3, pp. 318–326, 2004.

[205] W. Rainforth, "The wear behaviour of oxide ceramics-a review," *Journal of Materials Science*, vol. 39, no. 22, pp. 6705–6721, 2004.

[206] E. Zanoria, S. Danyluk, and M. McNallan, "Effects of length, diameter and population density of tribological rolls on friction between self-mated silicon," *Wear*, vol. 181, pp. 784–789, 1995.

[207] T. Fischer, Z. Zhu, H. Kim, and D. Shin, "Genesis and role of wear debris in sliding wear of ceramics," *Wear*, vol. 245, no. 1, pp. 53–60, 2000.

[208] T. Fischer and H. Tomizawa, "Interaction of tribochemistry and microfracture in the friction and wear of silicon nitride," *Wear*, vol. 105, no. 1, pp. 29–45, 1985.

[209] H. Chen, W. Rainforth, and W. Lee, "The wear behaviour of Al_2O_3–SiC ceramic nanocomposites," *Scripta Materialia*, vol. 42, no. 6, pp. 555–560, 2000.

[210] Q. Luo, "Origin of friction in running-in sliding wear of nitride coatings," *Tribology Letters*, vol. 37, no. 3, pp. 529–539, 2010.

[211] Q. S. Luo, "Temperature dependent friction and wear of magnetron sputtered coating TiAlN/VN," *Wear*, vol. 271, no. 9, pp. 2058–2066, 2011.

[212] E. S. Zanoria, S. Danyluk, and M. J. McNallan, "Formation of cylindrical sliding-wear debris on silicon in humid conditions and elevated temperatures," *Tribology Transactions*, vol. 38, no. 3, pp. 721–727, 1995.

[213] V. Murthy, H. Kobayashi, N. Tamari, S. Tsurekawa, T. Watanabe, and K. Kato, "Effect of doping elements on the friction and wear properties of SiC in unlubricated sliding condition," *Wear*, vol. 257, no. 1, pp. 89–96, 2004.

[214] S. Bajwa, W. Rainforth, and W. Lee, "Sliding wear behaviour of SiC–Al_2O_3 nanocomposites," *Wear*, vol. 259, no. 1, pp. 553–561, 2005.

[215] R. S. Dwyer-Joyce. (1997) Tribological design data part 3: Contact mechanics. The Tribology Group of The Institution of Mechanical Engineers. Accessed on June 15th, 2013. [Online]. Available: http://www.leonardocentre.co.uk/Media/Default/Documents/Book_3_contact_mechanics.pdf

Appendix A

Determination of Initial Contact Pressure for Reciprocating Wear Tests

The surfaces are assumed to be smooth and frictionless and the coating is considered as an infinite half space as shown in Fig. A.1.

The parameters of the stainless steel ball and the coating are listed in Table A.1.

The effective radius *R'* and the reduced modulus *E** are determined by [215]:

$$R' = \left(\frac{1}{R_1} + \frac{1}{R_2}\right)^{-1} = \left(\frac{1}{3} + \frac{1}{\infty}\right)^{-1} = 3\,\mathrm{mm}$$

$$E^* = \left(\frac{1-\nu_1^2}{E_1} + \frac{1-\nu_2^2}{E_2}\right)^{-1} = \left(\frac{1-0.3^2}{207} + \frac{1-0.3^2}{207}\right)^{-1} = 114\,\mathrm{GPa}$$

The region of contact under the normal load (N) of 14 N is spherical with a radius *a'* given by:

$$a' = \sqrt[3]{\frac{3NR'}{4E^*}} = 0.046\,\mathrm{mm}$$

Table A.1. Parameters of pin and coating

	Pin	Coating
R / mm	3	∞
E / GPa	207	207
ν	0.3	0.3

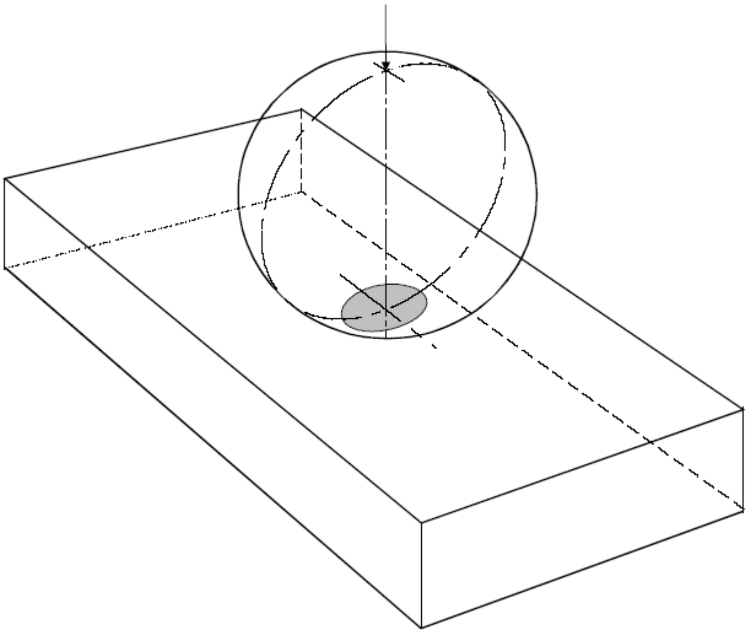

Figure A.1. A ball loaded onto a flat plate [215].

The peak contact pressure *P0* is then given by:

$$P_0 = \frac{3N}{2\pi a'^2} = 1.12\,\text{GPa}$$

The yield stress is about 1/3 of the hardness. Therefore, theoretically no plastic deformation will occur on the coatings with the hardness higher than 3.36 GPa, which is equivalent to approximately 340 HV.

Appendix B

Research Publications

The following are published research papers generated as part of the work presented in the thesis. They are listed in the following order:

(a) C. Ma, S. C. Wang, L. P. Wang, F. C. Walsh, R. J. K. Wood, The role of a tribofilm and wear debris in the tribological behaviour of nanocrystalline Ni-Co electrodeposits, *Wear*, in press. DOI: http://dx.doi.org/10.1016/j.wear.2013.01.121.

(b) C. Ma, S. C. Wang, R. J. K. Wood, J. Zekonyte, Q. Luo, F. C. Walsh, The Hardness of Porous Nanocrystalline Co-Ni Electrodeposits, *Metals and Materials International*, in press.

The following items have been submitted and are currently under review:

(c) C. Ma, S. C. Wang, L. P. Wang, F. C. Walsh, R. J. K. Wood, The electrodeposition and characterisation of low friction and wear resistant Co-Ni-P coatings, *Surface and Coatings Technology*, under review (Minor revision).

(d) C. Ma, S. C. Wang, C. T. J. Low, L. P. Wang, F. C. Walsh, Effects of additives on the microstructure and properties of electrodeposited nanocrystalline Ni-Co coatings with high cobalt content, *Transaction of the Institute of Metal Finishing*, under review (Minor revision).

Additionally, contributions in the field of microstructure characterisation have been made in the following published papers:

(e) M. -H. Evans, J. C. Walker, C. Ma, L. Wang, R. J. K. Wood, A FIB/TEM study of butterfly crack formation and white etching area (WEA) microstructural changes under rolling contact fatigue in 100Cr6 bearing steel, *Materials Science and Engineering: A*, 570(2013) 127-134.

(f) W. Li, S. C. Wang, C. Ma, Z. Wang, An electron microscopy study of the effect of Ce on plasma sprayed bronze coatings, *Journal of Physics: Conference Series* 371(2012)

012085.

(g) W. Li, Y. Liu, Z. Wang, C. Ma, S. C. Wang, Effects of Ce in novel bronze and its plasma sprayed coating, *Transactions of Nonferrous Metals Society of China*, 22, (9), 2139-2145.